ABSTRACT

Title of Document: QUANTIFYING THE ROLE OF CERIUM OXIDE AS A CATALYST IN SOLID OXIDE FUEL CELL ANODES

Steven C. DeCaluwe, Doctor of Philosophy, 2009

Directed By: Associate Professor Gregory S. Jackson, Department of Mechanical Engineering

Solid Oxide Fuel Cells (SOFCs) are an important electrochemical power conversion device, due largely to their high efficiencies and ability to directly oxidize a variety of fuels, including hydrogen, carbon monoxide, and light hydrocarbons. Conventional Ni-based SOFC anodes are prone to failure due to carbon deposition or unwanted metal oxidation. For this reason, ceria (CeO_2) is being explored to replace or supplement Ni in SOFC anodes. CeO_2, a mixed ionic-electronic conductor (MIEC), has been shown to improve SOFC anodes' resistance to carbon deposition and sulfur poisoning. Optimization of ceria-based anodes has proven difficult due to the unknown role of ceria during SOFC operation. The electrochemical mechanisms and reaction rates needed to describe fuel oxidation on ceria anodes are not well understood, and thus it is not clear how to model the coupling between electrochemistry and mass transport in complex SOFC geometries containing ceria. Both Ce^{4+} and Ce^{3+} are present during fuel cell operation, and the ionic and electronic

conductivities are determined by the abundance of Ce^{3+}. The *in situ* spatial distribution of valence states, then, is expected to have a major impact on ceria's role in SOFC anodes.

This work aims to describe the fundamental role of ceria in SOFC anodes by building a numerical SOFC model for the electrochemical oxidation of small molecules. Porous-media SOFC models are developed and validated against experimental data, correcting previous errors in transport equations. The thermodynamic and kinetic parameters for such a model are obtained from experimental measurements on thin-film ceria anodes, including electrochemical measurements and novel *in situ* X-ray photoelectron spectroscopy measurements. Fitting thin-film MIEC model results against experimental data leads to the identification and estimation of several key parameters in the proposed H_2 oxidation mechanism, with results demonstrating the importance of charge transfer, bulk oxide diffusion and adsorption reactions at the electrode surface. This provides a basis for modeling porous media composite SOFC electrodes with distributed electrochemistry as demonstrated in this work.

QUANTIFYING THE ROLE OF CERIA AS A CATALYST IN SOLID OXIDE FUEL CELL ANODES

By

Steven C. DeCaluwe

Dissertation submitted to the Faculty of the Graduate School of the
University of Maryland, College Park, in partial fulfillment
of the requirements for the degree of
Doctor of Philosophy
2009

Advisory Committee:
Dr. Gregory Jackson, Chair
Dr. Hugh Bruck
Dr. Bryan Eichhorn
Dr. Henry Haslach
Dr. Santiago Solares
Dr. Michael Zachariah

Dedication

For Heather.

Acknowledgements

The author would like to acknowledge the great many collaborators who assisted with the completion of this work:

Firstly, I would like to express my deepest gratitude to my advisor, Dr. Greg Jackson, for the opportunity to conduct research in his lab. His constant support, guidance, and encouragement were invaluable, and the strength of his ideas an inspiration.

I am grateful to Dr. Bryan Eichhorn, not only for serving on my dissertation committee but also, along with Dr. Robert Walker, for the many fruitful discussions as part of the SOFC Research Group.

A special thanks to other the members of my committee for their time and attention, and for bringing their high standards to bear on this work to make it the best it can be – Dr. Hugh Bruck, Dr. Henry Haslach, Dr. Santiago Solares, Dr. Michael Zachariah.

Furthermore, I am forever indebted to the many present and former colleagues in the SOFC Research Group and the Jackson Research Group.

My deepest gratitude to Dr. Chunuan Zhang, for her assistance in the fabrication and analysis of single-chamber fuel cells.

Dr. Mary A. Sukeshini has my highest regard, for her assistance with electrochemical testing, ceria sputtering, and film characterization.

Special thanks to Dr. Seyed A-Reihani, for his constant interest and many productive conversations about this work.

Great thanks to Dr. Bahman Habibzadeh, for his friendship and for pioneering the electrochemical testing in the SOFC Research Group.

Many thanks to: Dr. Mike Pomfreit, Dr. Oktay Demerican, Ben Becker, Paul Jawlik, Atul Bhargav, Josh Pearlman, Jenny Hu, Siddharth Patel, Rick Stroman, Brian Eigenbrodt, Chris Maxey, and Anita Maghdouri.

Very special thanks to the Tom Loughran and John Hummel at the University of Maryland Fablab, for deposition and patterning of Au masks.

Sincerest thanks to Dr. Wen-An Chiou and Li-Chun Lai for assistance with SEM.

Deepest gratitude to my collaborators at other institutions:

Dr. Robert Kee and Dr. Huayang Zhu at Colorado School of Mines

Dr. Hendrik Bluhm, Dr. Zhi Liu, Dr. John Newberg, and Dr. Michael Grass at the Advanced Light Source at Lawrence Berkeley National Labs

Dr. Mark Linne, Dr. Roger Farrow, Dr. Kevin McCarty, Dr. Anthony McDaniel, Dr. Farid El-Gabali, and Shu Nie at Sandia National Labs.

Finally, to my loving wife Heather, without whom this would not have been possible. You are a constant source of inspiration who is always there to support me, but also makes sure that I never take myself too seriously. I could never thank you enough.

Table of Contents

Dedication ii

Acknowledgements iii

List of Tables viii

List of Figures ix

List of Figures ix

Chapter 1: Introduction – The Promise and Challenges of Cerium Oxide as an SOFC Electrocatalyst 1
1.1 Introduction to Solid Oxide Fuel Cells 1
1.1.1 Common SOFC Materials 3
1.1.2 General Description of SOFC Processes 5
1.1.3 Sources of Overpotentials in SOFCs 8
1.2 Challenges of SOFC Technology 11
1.3 Cerium Oxide as an Alternative Anode Electrocatalyst 12
1.3.1 CeO_2, Mixed Conduction, and Alternate Oxidation Pathways 15
1.4 SOFC Modeling and Optimization of Electrode Microstructures 17
1.5 Thin-film SOFCs 19
1.6 Objectives and Overview of Current Study 20

Chapter 2: One-dimensional Thin-film SOFC Model with Mixed Ionic-Electronic Conduction 22
2.1 Previous SOFC Modeling Efforts 25
2.1.1 General Approaches to SOFC Simulation 26
2.1.2 Previous Thin-film and MIEC Models 28
2.2 Model Geometry 29
2.3 Model Equations 31
2.3.1 Conservation Equations 31
2.3.1.1 Conservation of Gas-phase Mass/Species 31
2.3.1.2 Conservation of Surface Species 32
2.3.1.3 Conservation of Charge and Calculation of Electric Potential 33
2.3.1.4 Conservation of bulk species 36
2.3.2 Transport and Reaction Rate Equations 41
2.3.2.1 Gas-Phase Transport Equations 41
2.3.2.2 Ion and Polaron Transport in bulk CeO_{2-x} 41
2.3.2.3 Surface and Electrochemical Reactions 43
2.4 Simulation Procedure 46
2.5 Sample Model results for Hydrogen Oxidation 48
2.5.1 Oxidation Mechanism for H_2/H_2O 48
2.5.2 Initial Model Results 53

2.6 Conclusions 56

Chapter 3: Experimental Characterization of Thin-film, Undoped Ceria Electrodes 58
3.1 Previous Studies 60
3.1.1 Characterization of Thin-film Ceria 61
3.1.2 Fabrication of Oxide Thin-films 62
3.1.3 XPS Quantification of CeO_{2-x} Oxidation States 66
3.2 Electrochemical Characterization of CeO_{2-x} Thin Film Anodes 69
3.2.1 Experimental Details 69
3.2.1.1 Button-cell Fabrication 69
3.2.1.2 Instrumentation and Measurement 71
3.2.2 Results and Discussion 74
3.2.2.1 Structural Characterization of CeO_{2-x} Thin Film Anodes 74
3.2.2.2 Electrochemical Characterization of Nanoporous Films 82
3.2.2.3 Electrochemical Characterization of Dense Films 94
3.3 In situ XPS for Evaluation of Ceria Oxidation States 101
3.3.1 Experimental Details 103
3.3.1.1 Ambient Pressure XPS 103
3.3.1.2 Cell Fabrication 104
3.3.1.3 Experimental Set-up and Testing 105
3.3.2 Results and Discussion 109
3.4 Conclusions 116

Chapter 4: Modeling Electrochemical Oxidation on Cerium Oxide Anodes – Validation of Thin-film MIEC Model Results 120
4.1 Previous Research 121
4.1.1 Reduction Thermodynamics in Bulk-phase Ceria 121
4.1.2 Computer Simulations of Ceria Surface Properties 122
4.1.3 Non-ideal Energetic Interactions between Reduced Cerium Cations 123
4.2 Derivation of Baseline Thermodynamic and Kinetic Parameters 129
4.2.1 Thermodynamic Parameters 129
4.2.2 Kinetic Parameters 131
4.2.3 Non-ideal Interaction Potentials 131
4.3 Results and Discussion 134
4.3.1 Comparison of Model Predictions and Experimental Results 134
4.3.2 Effect of Interaction Potential Model 142
4.3.3 Sensitivity of Model Predictions to Parameter Variation 144
4.4 Conclusions 149

Chapter 5: 1-D SOFC Model with Porous Electrodes – The Importance of Microstucture in SOFC Modeling 152
5.1 Previous SOFC Modeling Efforts 155
5.1.1 Characterization of Porous Media Microstructures 155
5.1.2 Gas-phase Transport in Porous SOFC Electrodes 157
5.1.3 Distributed Electrochemistry Models 158
5.2 Model Formulation 159

5.2.1 Gas-phase Mass and Species Conservation 162
5.2.2 Conservation of Surface Species 163
5.2.3 Charge Conservation 164
5.2.4 Gas-phase Transport Equations 167
5.2.5 Surface and Electrochemical Reaction Rates 170
5.3 Simulation Procedure 175
5.4 Results 177
5.4.1 Fixed δ_{util} model 179
5.4.2 Distributed Electrochemistry Model 190
5.5 Discussion 199
5.5.1 Comparison of Predicted and Measured R_{bulk} Values 200
5.5.2 Possible Sources of Model Error 203
5.6 Conclusions 205

Chapter 6: Conclusions and Outlook 207
6.1 Experimental Characterization of Thin-film CeO_2 Anodes 207
6.1.1 Conclusions 207
6.1.2 Looking Forward 210
6.2 Isothermal 1-D Thin-film MIEC Simulations 213
6.2.1 Conclusions 213
6.2.2 Looking Forward 214
6.3 Isothermal 1-D Porous-media SOFC Simulations 215
6.3.1 Conclusions 215
6.3.2 Looking Forward 216

Glossary of Symbols Used 218

Bibliography 224

List of Tables

Table 2.1. Model parameters for baseline cell. Temperature-sensitive parameters v_{O2-} and v_{el} are given for T = 700 °C 47

Table 2.2. Chemical formulas and average Ce valence for ceria surface species. 50

Table 2.3. Thermodynamics of species at 25 °C and 700 °C. 52

Table 2.4. Forward rate parameters for baseline thin-film results, T = 700 ˚C. 52

Table 3.1. Comparison of film thickness for different deposition conditions, as determined by SEM. Deposition time = 165 min. 76

Table 3.2. Capacitance and Warburg coefficient values..... 90

Table 3.3. Characteristics of AP- XPS end station for Beamline 11.0.2 at ALS..... 103

Table 3.4. Shifts in ceria surface electric potential 114

Table 4.1. Baseline forward rate parameters for baseline thin-film results, T = 700 ˚C. 131

Table 4.2. Optimized reaction rate parameters for H_2 oxidation on ceria 135

Table 5.1. Thermodynamics of species at 25 °C and 800 °C. 174

Table 5.2. Reactions and forward rate parameters used in simulations. 174

Table 5.3. Model parameters for baseline cell. 176

Table 5.4. Pressure and concentration gradients in the anode support layer 189

Table 5.4. Model parameters for distributed electrochemistry model. 195

Table 5.5. Thermodynamics of distributed electrochemistry model at 25 and 800 °C. 196

Table 5.6. Reactions and forward rate parameters used in distributed electrochemistry model..... 197

Table 5.7. Comparison of R_{ohm} values from experiment and from model predictions for varying anode microstructures. 202

List of Figures

Figure 1.1. Schematic representation of SOFC components and diffusive processes.. 1

Figure 1.2. Sample polarization curve, with various sources of overpotential (η) subtracted from the open circuit voltage (OCV)..... 8

Figure 1.3. Schematic representation of traditional metal electrocatalysts vs. MIEC electrocatalysts in SOFC anodes..... 13

Figure 2.1. Model geometry for SOFC button cell (thicknesses not to scale) with dense thin-film ceria anode..... 30

Figure 2.2. Illustration of the two species considered in this study for the ceria bulk. 37

Figure 2.3. Illustration of surface species considered for H_2 oxidation mechanism... 49

Figure 2.4. Predicted polarization and power density curve for SOFC with thin-film dense CeO_{2-x} anode. Baseline cell parameters taken from Tables 2.1-2.4. 53

Figure 2.5. Distribution of ceria surface species versus current density 54

Figure 2.6. Predicted electric potential profile through the 110-nm thick ceria anode. 55

Figure 2.7. Oxide concentration versus current density for the Ceria/YSZ boundary (O^{2-}(b)) and for the ceria sub-surface (O^{2-}(sb))..... 56

Figure 3.1. a) Schematic representation of the sputtering process; b) Lesker PVD 75 sputter-deposition chamber used in this study..... 64

Figure 3.2. Sample XPS spectra for Ce*3d*, with labeled Ce^{4+} and Ce^{3+} peaks. 67

Figure 3.3. View of fabricated SOFC MEAs. a) LSM/YSZ cathode on SC-YSZ, b) CeO_2 anode, 2.8 μm thick, on PC-YSZ. 70

Figure 3.4. Sample SEM of thin-film CeO_{2-x} anodes. 72

Figure 3.5. a) Schematic representation and b) photograph of experimental setup... 74

Figure 3.6. SEM of CeO_2 films deposited on glass substrates..... 76

Figure 3.7. XRD data for CeO_2 films on glass substrates with varying film thickness. 77

Figure 3.8. SEM images of 2.5 μm CeO_2 films on varying substrates, deposited in the same batch. 78

Figure 3.9. Effect of annealing in air at 800 °C on CeO_2 deposited on a SC-YSZ substrate. 79

Figure 3.10. Cross-section SEM images for CeO_2 films deposited on SC-YSZ. 80

Figure 3.11. SEM of as-deposited CeO_2 films with process pressure = 15 mTorr. 81

Figure 3.12. SEM of dense CeO_2 films on SC-YSZ with t_d = 30 min. 82

Figure 3.13. Polarization curves for oxidation of CO and H2 on "nanoporous" ceria anodes. 84

Figure 3.14. Impedance with equivalent circuit modeling for nanoporous 2.8 μm thick anode for varying P_{H2} at 700 °C and i_{ext} = 31.6 mA/cm^2. 86

Figure 3.15. Equivalent circuit modeling results for nanoporous 2.8 μm thick CeO_{2-x} anode. 89

Figure 3.16. Estimated oxide diffusion coefficients 92

Figure 3.17. Polarization results on dense, 110 nm thick ceria anode. 95

Figure 3.18. Impedance spectra for H_2 oxidation on 110 nm dense ceria anode. 99

Figure 3.19. Bode plots for varying current density on a 110 nm dense ceria anode. 101

Figure 3.20. Single chamber SOFC. 102

Figure 3.21. Single-chamber SOFC mounted on ALS XPS sample holder 105

Figure 3.22. a) Diagram of ambient-pressure XPS apparatus for testing single chamber SOFC at Advanced Light Source., and b) photograph of single-chamber SOFC operating in XPS chamber. 108

Figure 3.23. Relationship between ceria oxidation state and electrochemical performance. 109

Figure 3.24. Fitting of *Ce3d* core spectra 111

Figure 3.25. Summary of XPS peak fitting 113

Figure 3.26. Comparison of polarization data from single chamber SOFC in ALS XPS chamber ($T \approx 620$ ºC, $P_{H2} = P_{H2O} = 0.25$ Torr) and from two-chamber SOFC results 115

Figure 4.1. Measured values for the Gibbs free energy of ceria reduction..... 125

Figure 4.3. Conceptual plot of non-entropic free energy versus reaction coordinate for transition state theory. 128

Figure 4.4. Free energy change of ceria reduction ΔG_{red}, vs. degree of reduction .. 133

Figure 4.5. Comparison of experimental polarization data (symbols) with model predictions (lines) for H_2 oxidation on dense ceria at $T = 700$ ˚C..... 135

Figure 4.6. Surface and sub-surface species profiles for varying current density. .. 137

Figure 4.7. Ceria bulk electric potential profile $\Phi_{cat}(y)$ with varying current density. 138

Figure 4.8. Average surface valence state during electrochemical oxidation of H_2 140

Figure 4.9. Variation of polarization results with varying free energy of reduction 143

Figure 4.10. Variation of predicted polarization results with varying charge-transfer forward symmetry parameter $\alpha_{fwd.}$..... 145

Figure 4.11. Variation of predicted polarization results with varying oxide ion mobility 146

Figure 4.12. Variation of predicted polarization results with varying forward kinetic rate parameters 147

Figure 5.1. Illustration of key microstructural parameters related to modeling of porous SOFC electrodes. 156

Figure 5.2. Layout of a typical button cell. 160

Figure 5.3. Experimental polarization and power-density measurements with varying anode support porosity 178

Figure 5.4. Simulated polarization and power density with varying anode support porosity but with all other parameters fixed at baseline values. 179

Figure 5.5. Simulated polarization and power density with varying anode support tortuosity. 181

Figure 5.6. Simulated polarization and power density with covarying anode support porosity and tortuosity. 185

Figure 5.7. Simulated polarization and power density with covarying anode support porosity, tortuosity, and utilization thickness. 187

Figure 5.8. H_2, H_2O, and P profiles through the porous anode thickness at selected current densities. 188

Figure 5.9. Predicted YSZ surface species coverages θ_{YSZ} in the electrochemically active region as a function of i_{ext} for baseline cell parameters. 192

Figure 5.10. Simulated polarization and power density with co-varying anode support porosity and tortuosity for distributed electrochemistry model. 194

Figure 5.11. Predicted $\delta_{util,anode}$ values for varying support layer composition..... 198

Figure 5.12. Predicted distribution of faradaic current in the anode functional layer 199

Figure 5.12. Predicted YSZ surface species coverages θ_{YSZ} in the electrochemically active region..... 205

Chapter 1: Introduction – The Promise and Challenges of Cerium Oxide as an SOFC Electrocatalyst

1.1 Introduction to Solid Oxide Fuel Cells

Solid Oxide Fuel Cells (SOFCs) have emerged as a critical power generation technology that offers high efficiencies, fuel flexibility, and minimal environmental impact for a broad array of applications – ranging from small-scale (<100 W) portable power to more centralized (> 1 MW) power plants. SOFCs are electrochemical power conversion devices, converting the chemical potential of air and fuel streams, separated by an electrolyte membrane, into electrical power. Schematically, SOFCs (like all types of fuel cells) consist of three components, depicted in figure 1.1. These components are the anode, where fuel species are

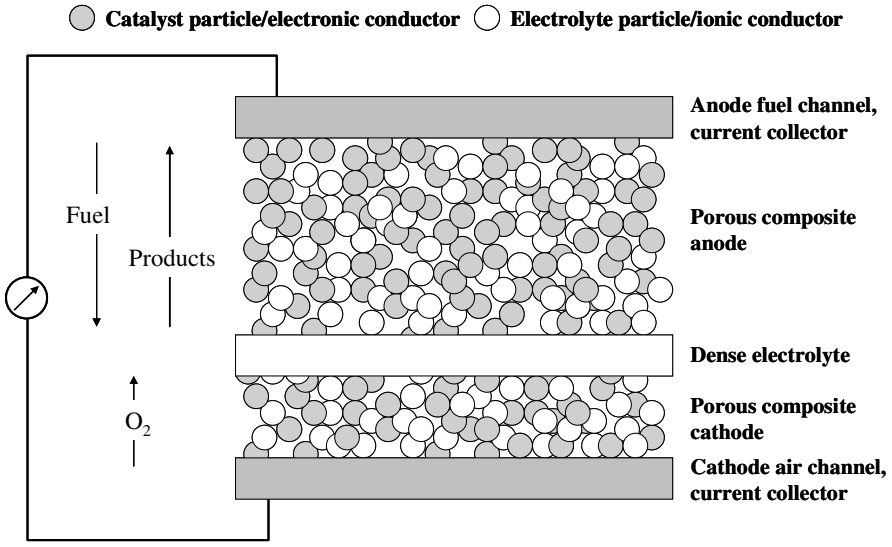

Figure 1.1. Schematic representation of SOFC components and diffusive processes.

oxidized, the electrolyte, which ideally permits neither electron nor gas-phase transport but allows the conduction of ions (oxide ions for SOFCs), and the cathode, where oxygen reduction occurs.

The global fuel cell reaction, presented for hydrogen fuel in reaction 1.1, represents a decrease in total Gibbs free energy, which acts as the driving force for the transport of ions across the electrolyte membrane.

$$H_{2(g),an} + \frac{1}{2} O_{2(g),ca} \Leftrightarrow H_2O_{(g),an}. \qquad \text{(R1.1)}$$

In the presence of an applied load, this chemical driving force transports charged species against an electric potential gradient, and thus electrical work is extracted as electrons flow through an external circuit, as discussed further below.

In SOFCs, the electrolyte is constructed from an oxide-ion (O^{2-}) conducting dense ceramic membrane. SOFCs must be operated at elevated temperatures to give the ceramic membrane sufficient ionic conductivity [1, 2]. This high-temperature operating environment has beneficial impacts on SOFC performance, as discussed below, but also increases material costs and decreases system stability [3]. Although several approaches, including novel materials and thinner electrolytes, have been undertaken with the aim of reducing SOFC temperatures, operating environments in the range of 800 – 1000˚C are still the norm in state-of-the-art SOFCs [3, 4].

Because the dense ceramic electrolyte conducts negatively charged oxide ions (O^{2-}) from the cathode to the anode at high temperatures, direct utilization of carbonaceous fuels in SOFC anodes where fuel is oxidized either electrochemically or via internal reforming reactions is possible. This is likely to play an important role as long as a H_2 infrastructure is not available. The build-up of product water from R1.1 in SOFC anodes humidifies incoming carbonaceous fuel streams, and this promotes non-electrochemical internal reforming reactions, which can prevent damage to SOFC anodes from carbon deposition (discussed below) in the SOFC anode [5-8]. Furthermore, because the SOFC acts as an incidental 'oxygen separator' (oxygen is transported to the anode, while N_2 in the air remains in the cathode), the costs associated with the sequestration of any greenhouse-gas products (notably CO_2) associated with SOFCs drops considerably, making SOFC technology an ideal candidate for hybridization with fossil fuel energy technologies such as coal gasification [9, 10].

1.1.1 Common SOFC Materials

The most common SOFC electrolyte is yttria-stabilized zirconia (YSZ). The doping of zirconia with the trivalent yttria increases the concentration of O^{2-} vacancies, thereby increasing the oxide-ion conductivity of YSZ. While a number of alternate materials have been explored for intermediate-temperature SOFC electrolytes, YSZ remains the most commonly utilized electrolyte material [4, 11],

due in part to its mechanical stability and compatibility with other common SOFC materials.

The high operating temperature of SOFCs removes the need for precious metal catalysts used in lower-temperature fuel cells (such as polymer electrolyte membrane fuel cells). Currently, the most popular electrocatalyst for SOFC anodes is nickel. Nickel's low cost and high catalytic activity for fuel decomposition/oxidation make it an attractive catalyst, despite a host of challenges discussed below. The charge-transfer reactions that are responsible for the oxidation of fuel species (as well as the oxygen reduction reactions in the cathode) depend on the physical intermingling of catalyst, electrolyte, and gas phases in a region known as the three phase boundary (TPB). As such, SOFC electrodes (both anode and cathode) are typically realized as composites, with electrolyte (YSZ) particles mixed in with electrocatalyst particles and significant pore space (to allow for gas-phase diffusion to the active TPB regions). This composite electrode structure also helps to reduce mismatches in the coefficient of thermal expansion (CTE) between elements (anode, electrolyte, and cathode). These Ni-YSZ anodes are typically made thick enough (500 – 1000 μm) such they serve as the physical support for the SOFC membrane-electrode-assembly (MEA) [12-14].

As mentioned, SOFC cathodes are also often realized as porous composite electrodes, with YSZ electrolyte particles typically mixed with a perovskite material, such as lanthanum strontium manganite (LSM) [15]. Due to the high resistances

associated with the O_2 reduction reactions, particularly on LSM, a number of other material combinations have been explored. Among these include mixed ionic-electronic conductors (MIEC) such as lanthanum strontium cobaltite (LSC) and lanthanum strontium ferrite (LSF) [16-18], which have displayed increased catalytic activity, compared to LSM/YSZ cathodes. Despite these performance improvements, issues with long-term degradation and solid-state reactions with YSZ have slowed the introduction of these materials as replacements for LSM in state-of-the-art SOFC cathodes [16, 19].

1.1.2 General Description of SOFC Processes

As stated above, fuel cells convert chemical bond energy into electrical work. A typical single electrochemical cell includes passages for fuel and oxidant streams flowing over and through a porous anode and cathode, respectively, with the two streams separated by a gas-impermeable, ion-conducting electrolyte. This is shown in figure 1.1, which depicts an anode-supported SOFC cell. The global SOFC reaction, shown in reactions 1.2 and 1.3 for H_2 and CO, respectively, represents a net decrease in chemical potential, which acts as a driving force for the transport of ions across the electrolyte:

$$H_{2(g),an} + \frac{1}{2}O_{2(g),ca} + 2e^{-}_{LSM(b)} \Leftrightarrow H_2O_{(g),an} + 2e^{-}_{Ni(b)}; \quad \text{(R1.2)}$$

$$CO_{(g),an} + \frac{1}{2}O_{2(g),ca} + 2e^{-}_{LSM(b)} \Leftrightarrow CO_{2(g),an} + 2e^{-}_{Ni(b)}. \quad \text{(R1.3)}$$

For conventional Ni-YSZ-LSM systems, the subscripts *an* and *ca* represent location in the anode and cathode, respectively, and *g* and *b* represent gas and bulk phases, respectively.

In the cathode, oxygen is electrochemically reduced and incorporated into the electrolyte, which is represented by the global half-cell reaction:

$$\frac{1}{2}O_{2(g)} + 2\,e^{-}_{LSM\,(b)} \Leftrightarrow O^{2-}_{YSZ(b)} \qquad \text{(R1.4)}$$

Meanwhile, in the anode, the electrons donated in the cathode are recovered as the fuel is oxidized. For a H_2 and CO fuels over a Ni/YSZ anode, the global half-cell reactions are:

$$H_{2(g)} + O^{2-}_{YSZ(b)} \Leftrightarrow H_2O_{(g)} + 2\,e^{-}_{Ni\,(b)} \qquad \text{(R1.5)}$$

$$CO_{(g),an} + O^{2-}_{YSZ(b)} \Leftrightarrow CO_{2(g),an} + 2e^{-}_{Ni(b)} \qquad \text{(R1.6)}$$

Over time, as electrons are transferred from cathode to anode, an electric field builds up across the MEA, as depicted in figure 1.1. If the cathode and anode are electrically disconnected, the electric field represents a driving force on the electrons that is equal and opposite the chemical potential driving force. This voltage is known

as the open circuit voltage, or OCV. It is the maximum reversible cell potential for a fuel cell at a given temperature and fuel/oxidant feed. The theoretical OCV can be calculated via the Nernst equation:

$$\Delta\Phi_{\text{cell,OCV}} = -\frac{\Delta G^{o}}{n_{\text{elec}}F} + \frac{\overline{R}T}{n_{\text{elec}}F}\ln\left[\prod_{k}\left(\frac{a_k}{a_k^{o}}\right)^{-v_k}\right] \qquad \text{(eq. 1.1)}$$

where $\Delta\Phi_{cell}$ is the electric potential difference between the anode and cathode (cell voltage), $\Delta G^{o}$is the free energy change for the global reaction (reactions 1.2 and 1.3) at the reference conditions with species activities a_k°, n_{elec} is the number of electrons transferred in the global reaction, F is the Faraday constant, $\overline{R}$ the universal gas constant, T the temperature, and a_k and v_k the activity and net stoichiometric coefficient of species k in the global fuel cell reaction [20].

In order to produce electrical work, the cell potential must be less than the electrochemical driving force. The decrease in cell potential needed to obtain a given current is known as the overpotential (η). The rate of growth of η with regard to current density determines a cell's area specific resistance (ASR), which in turn determines the maximum power density for a cell. These concepts are depicted in figure 1.2, which depicts a sample voltage-current curve from which various overpotentials are subtracted.

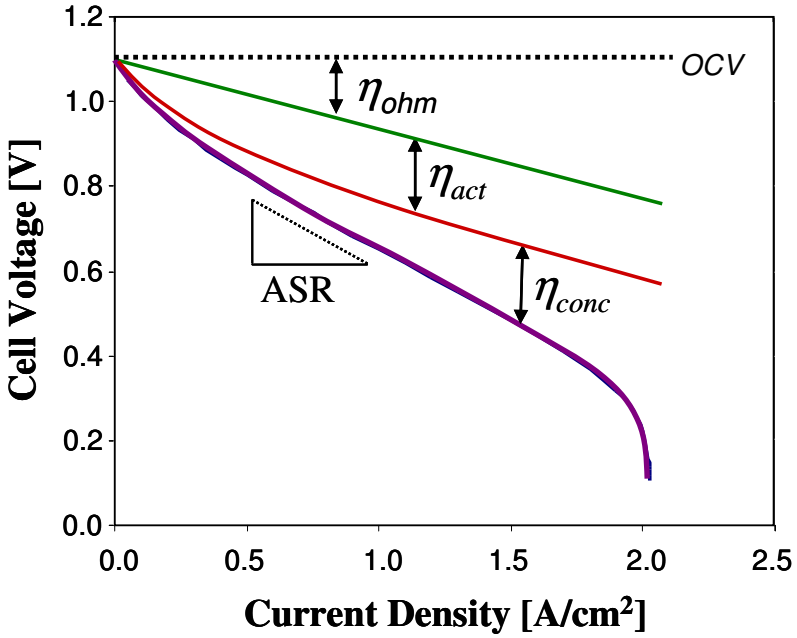

Figure 1.2. Sample polarization curve, with various sources of overpotential (η) subtracted from the open circuit voltage (OCV).

1.1.3 Sources of Overpotentials in SOFCs

Overpotentials in SOFCs (and fuel cells in general) are typically assigned to one of three sources: activation, ohmic, and concentration losses. The various losses depend on operating conditions, materials, and the cell microstructure, and each overpotential evolves with increasing current density, as illustrated in figure 1.2.

Activation overpotentials (η_{act}) in the anode ($\eta_{act,an}$) and cathode ($\eta_{act,ca}$) are associated with changes in electric potential that are needed to drive charge-transfer kinetics. η_{act} increases sharply at low currents, followed by little change at higher currents. Thus, the low-current region of polarization curves are usually referred to

as "activation controlled." Elementary charge-transfer reaction rates are governed by Butler-Volmer kinetics:

$$i = i_o \left[\exp\left(\frac{\alpha_{fwd} n_{elec} F \eta_{ct}}{\overline{R} T} \right) - \exp\left(- \frac{\alpha_{bwd} n_{elec} F \eta_{ct}}{\overline{R} T} \right) \right], \qquad \text{(eq. 1.2)}$$

where i_o is known as the "exchange current density," α_{fwd} and α_{bwd} are forward and backward symmetry parameters, respectively, and η_{ct} is the overpotential associated with the given charge-transfer step. F is the Faraday constant. Non-electrochemical surface reactions can reduce surface coverages that impact the $i_{o,}$ which also depends on the rate parameters for forward and reverse reactions across the TPB. Further discussion on activation overpotentials and Butler-Volmer kinetics are presented in greater detail, below.

Ohmic overpotentials (η_{ohm}) result from the transport of charged particles (ions and electrons). The voltage-current relationship is governed by Ohm's Law:

$$\eta_{ohm} = i R_b, \qquad \text{(eq. 1.3)}$$

where i is the current density and R_b the total resistance of the cell to current conduction. R_b is determined as the sum of the resistivity R_m of each conducting element m (current collector and electrolyte phases in the anode and cathode, plus dense electrolyte) times that element's thickness Δy_m:

$$R_{\mathrm{b}} = \sum_{m} R_m \, \Delta y_m \, . \qquad \text{(eq. 1.4)}$$

These losses are, in general, linearly dependent on the current density, and are most noticeable at intermediate currents, where the nonlinearities of other overpotentials are less prominent. The bulk resistance, and thus the Ohmic overpotential, is typically dominated by the $R_{\mathrm{b,electrolyte}}$ under most SOFC operating conditions.

Concentration overpotentials (η_{conc}) are not "overpotentials" in the strictest sense of the word, but represent losses in the chemical driving force, due to changes in the gas phase near the TPB. N_k, the molar flux of a species k required to sustain a current density i at steady state can be expressed as follows:

$$N_k = \frac{-\nu_k \, i}{n_{\mathrm{elec}} F} \, . \qquad \text{(eq. 1.4)}$$

Here, n_{elec} is the number of electrons produced and ν_{k} the net stoichiometric coefficient for gas species k in the global half-cell reaction (e.g., for $H_2O_{(g),an}$ in R1.2, ν_{k} is 1 and n_{elec} is 2). Concentration gradients across the electrode drive this flux, and grow with the current density. This leads to a decrease in reactant/increase in product concentrations in the electrochemically active regions in both the anode and cathode, and thus a decrease in the reversible cell potential, as per the Nernst equation (eq. 1.1). Since the activities in the Nernst equation (which can be replaced by partial

pressures for ideal gases, appropriate for SOFC operating conditions) are part of a logarithmic term, the effect of η_{conc} is often negligible at low-to-moderate currents, but can dominate at limiting current densities, where fuel utilization near the TPB approaches 100%.

1.2 Challenges of SOFC Technology

While there has been limited success in commercializing SOFCs, researchers have yet to identify a combination of materials and cell architecture that provide stable operation over several thousand hours or reliable performance in large-scale power systems [4, 21]. While high-temperature operation (> 700 °C) in SOFCs has several benefits – including enhanced kinetics and fuel flexibility [22-30] – high operating temperatures pose a significant challenge, in terms of material durability, thermal management, and long start-up times.

Current state-of-the-art anodes utilize a mixture of Ni and YSZ in a porous composite electrode [4, 25]. While this material combination has advantages – the low cost and high catalytic activity of Ni chief among them – the durability of Ni-based systems has proven unsatisfactory in systems running on reformed HCs, particularly for the long-term stability required for central power plants or for the rapid cycling conditions associated with small-scale portable power applications. The Ni/YSZ anodes are prone to failure from oxidation of the Ni catalyst [31, 32], sulfur poisoning [33, 34], and carbon deposition [4, 25, 35].

Carbon deposition (often referred to as coking) has proven particularly deleterious to Ni-based SOFC anodes. A number of strategies have been undertaken to control coking in SOFC anodes by increasing the steam content in the composite anode, including increased steam content in the fuel feed and the use of diffusion barrier layers. However, such strategies reduce the efficiency of SOFC operation, and are generally not effective at preventing coking during long-term operation under low current densities [4, 8]. Because the oxidation potential of Ni generally limits SOFC cell voltages to > ca. 0.7 V [36], feasible conditions for long-term operation of Ni-based SOFCs are rather limited.

1.3 Cerium Oxide as an Alternative Anode Electrocatalyst

One proposed alternate catalyst for SOFC anodes is ceria, (CeO_2). Separate studies in the 1960s by Möbius and Rohland and by Takahashi et al. first demonstrated the use of ceria as an anode catalyst for H_2 and CO oxidation [37-39]. As discussed below, CeO_2 shows activity for electrochemical oxidation in SOFCs, due to reversible redox cycling (between Ce^{3+} and Ce^{4+}) in reducing environments, particularly at temperatures above 500 °C [24, 25, 40, 41]. Ceria also exhibits MIEC behavior due to its ability to transport O^{2-} ions and polarons, and this behavior extends the effective "width" of the TPB, as illustrated in figure 1.3, providing greater surface area and additional pathways for fuel oxidation reactions [42, 43]. Finally, CeO_2 shows a high resistance to carbon deposition and a high tolerance to sulfur poisoning, making it an attractive candidate

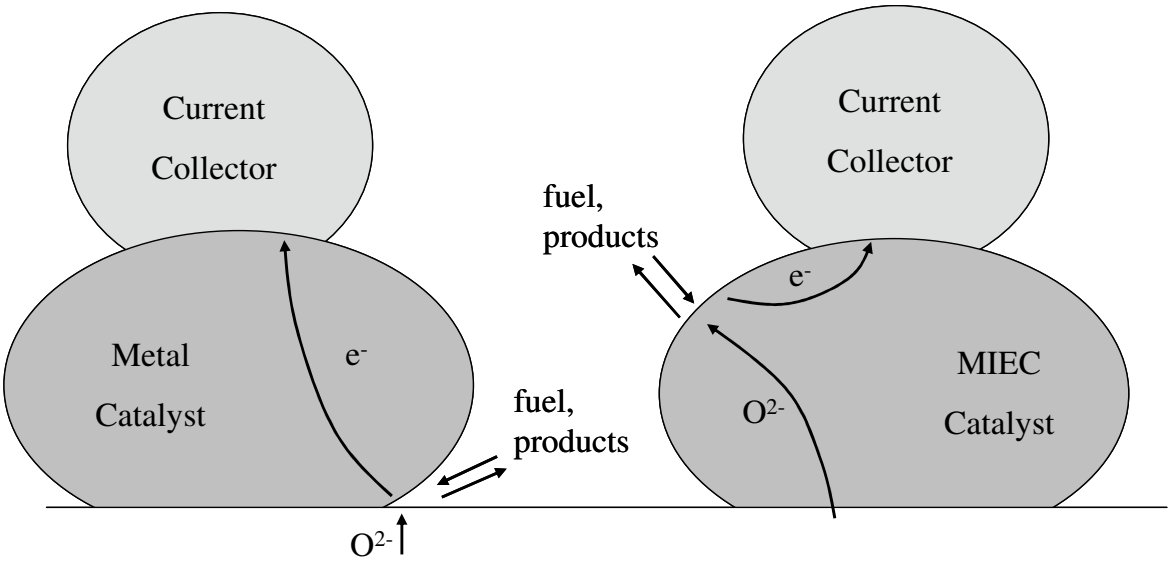

Figure 1.3. Schematic representation of traditional metal electrocatalysts vs. MIEC electrocatalysts in SOFC anodes. In traditional catalysts, reduction reactions are restricted to a narrow three-phase-boundary (TPB) region where gas, catalyst, and electrolyte interact. In MIEC catalysts, fuel oxidation can occur over the entire physical extent of the catalyst surface.

for use in SOFCs, either as the principal electrocatalyst or as an additive to another electrocatalyst [44]

While a large portion of the work regarding CeO_2 in SOFCs centers on the use of ceria in SOFC electrolytes [21, 24, 45-50], interest in ceria-based electrodes has been renewed in recent years. Several recent studies have demonstrated the catalytic activity of CeO_2 in high-temperature SOFC anodes [4, 6, 21, 22, 25, 27-30, 51-55]. As early as 1999, Murray, et al. reported the use of a thin-film Yttria-doped-ceria

(YDC) interlayer in a Ni-YSZ anode operating under a humidified methane fuel feed [22]. These experiments were conducted at temperatures of 550 – 650°C, using Lanthanum-Strontium-Manganite (LSM) cathode-supported SOFCs. The sputtered YDC film between the anode and electrolyte increased resistance to carbon deposition and reduced the polarization resistance by a factor of 7, compared to similar anodes without the interlayer. Also in 1999, Mogensen and co-workers reported the operation of an SOFC with a porous Gadolinia-doped Ceria (GDC) anode [51, 56]. These electrolyte-supported cells were tested at 800 – 1015°C under a range of humidified H_2 and CH_4 feeds. While the power densities under H_2 were lower than for Murray, et al. and the GDC showed little activity for methane oxidation, their results reiterated the feasibility of CeO_2 as an SOFC catalyst. Furthermore, the authors demonstrate the stability of CeO_2 catalysts in SOFCs, operating the cell for 1000 h with rapid thermal and redox cycling, without degradation or carbon deposition.

Since this time, a number of experiments have probed the use of CeO_2 as a catalyst in SOFC anodes. A significant amount of work has been carried out at the University of Pennsylvania, by Gorte and coworkers. Their work focuses on porous YSZ anode structures impregnated with Cu-CeO_2 mixtures, for use in the oxidation of hydrocarbons fed directly into the SOFC. They demonstrate stable operation over 10 hours under humidified fuels ranging from methane to diesel, exploring the effects of various fabrication techniques [25, 29, 52]. Additionally, they demonstrate that inclusion of a steam-reforming catalyst can greatly improve power densities,

implying that CeO_2 has a low activity for C-H cracking [6]. Finally, Gorte and coworkers found that CeO_2-based anodes have enhanced thermal stability and sulfur tolerance, and suppress carbon deposition, compared to traditional Ni-based SOFC anodes [28, 53-55].

Barnett and co-workers have investigated the use of composite SOFC anodes with various levels of GDC, Ni, and Lanthanum Strontium Chromite (LSC). The results provide additional evidence on the stability of ceria-based anodes operating under a variety of HC fuels, including methane, ethane, propane, octane, and butane [21, 27, 28]. While cells showed degradation due to coking, the time scale was much longer than for Ni-based systems and the degradation was reversible [27]. More recently, Barnett and co-workers demonstrated the use of composite Ni-based anodes with a Ru-CeO_2 catalyst layer, achieving power densities up to 1.3 W/cm^2 and 0.65 W/cm^2 under humidified H_2 and an iso-octane/CO mixture, respectively [21, 30]. These cells were also highly resistant to coking [21]. Barnett and coworkers conclude that, while the catalytic activity of CeO_2 by itself is insufficient for HC reforming, its MIEC properties and tolerance to conventional sources of anode degradation coupled with modest catalytic activity make it an attractive candidate for inclusion in composite anodes [4].

1.3.1 CeO_2, Mixed Conduction, and Alternate Oxidation Pathways

The ability of ceria to conduct both O^{2-} ions and electrons, due to reversible redox cycling ($Ce^{4+} \leftrightarrow Ce^{3+}$) in reducing environments, gives it unique catalytic and

electrocatalytic properties, particularly at elevated temperatures [24, 25, 40, 41]. This MIEC behavior of ceria is well documented by Trovarelli [40]. At low temperatures and under the mildest of oxidizing environments, CeO_2 is the most stable state. The Ce^{4+} cations occupy fcc lattice positions, while the O^{2-} anions occupy tetrahedrally-coordinated interstitial sites. In the SOFC anode environment, reactions with adsorbing fuel species can readily perturb this stoichiometry, as indicated here by reaction 1.7, written in Kröger-Vink notation:

$$Ce_{Ce}^{X} + O_{O}^{X} + x\,H_2(g) \leftrightarrow 2x\,Ce'_{Ce} + (1-2x)Ce_{Ce}^{X} + x\,V_{O}^{\bullet\bullet} + (1-x)\,O_{O}^{X} + x\,H_2O(g)\,. \qquad \text{(R1.7)}$$

In reaction 1.7, the variable x represents the degree of non-stoichiometry, with the fully oxidized CeO_2 reduced to CeO_{2-x}. O_{O}^{X} and $V_{O}^{\bullet\bullet}$ represent an O^{2-} anion and a doubly-positive charged oxygen vacancy, respectively. Ce_{Ce}^{X} represents a Ce^{4+} cation and Ce'_{Ce} represents a cerium cation that has been reduced in valence to Ce^{3+}, effectively acting as a localized negative charge or polaron. This polaron can be thermally activated to hop through the CeO_{2-x} as an effective means of electronic conduction. Ion conduction also occurs, as nearby O^{2-} oxides fill in neighboring oxygen vacancies. At temperatures < 500 °C, the polaron concentration is extremely small relative to O^{2-} concentrations, and thus polaron conductivity (proportional to mobility times concentration) is small, despite the relatively high polaron mobility. However, at SOFC temperatures (> 600 °C) and in reducing environments, the concentration of electronic charge carriers increases such that effective electronic conductivity becomes comparable to and eventually greater than ionic conductivity

[38]. It is worth noting that, although ceria provides some electronic conductivity, high-performance SOFCs typically incorporate composite metals into the porous anodes to provide electronic conductivity and, as needed, higher reforming activity for carbonaceous fuels [6].

The MIEC nature of ceria thus opens up new fuel oxidation pathways. Fuel oxidation can occur through TPB surface-mediated processes, as understood for Ni/YSZ anodes. For the ceria composite anodes, the three-phase boundary would exist either at the ceria/electronic conductor interface (ionic conduction in ceria) or at the ceria/electrolyte interface (electronic conduction in ceria). However, with the effective mixed conductivity in the ceria, surface and subsurface processes can provide a pathway for electrochemical fuel oxidation without the interaction of separate electronic and ionic conductors at the TPB, as illustrated in figure 1.3. This MIEC behavior of ceria leads to a degree of uncertainty that has made model-based optimization of ceria-based SOFC anodes difficult, as discussed below.

1.4 SOFC Modeling and Optimization of Electrode Microstructures

Due to the complex interrelation of transport, chemical, and electrochemical processes occurring in composite SOFC electrodes, high power-density operation depends on optimized micro-architectures. Such optimization is best performed with highly accurate physical models, which rely on accurate micro-structural and thermo-kinetic parameters. Recent efforts, both experimental and computational, have improved the ability of physical models to predict performance for traditional Ni-

YSZ anodes. Increased understanding of oxidation mechanisms [20, 57], thermo-kinetic parameters [20, 58], and 3-D microstructures [59-61] have all contributed to the formation of physical models that can more accurately predict the performance of these composite anodes. As discussed more thoroughly in chapters 2 and 5, recent efforts have leveraged this improved understanding to introduce increasingly sophisticated model formulations that incorporate phenomena from a wide range of length scales. These phenomena include the diffusion of gases in porous media (macro-scale) [1, 7, 62, 63], the distribution of electrochemistry into the electrode depth (meso-scale) [64, 65], and the incorporation of thermodynamic consistency in micro-kinetic mechanisms (micro-scale) [20, 66]. Chapters 2 and 5 present a more comprehensive review of previous SOFC modeling efforts.

Optimization of composite ceria anodes, however, has not yet been demonstrated in the literature, due to uncertainties regarding its behavior in the reducing anode environment. While previous efforts have explored ceria catalysis in a number of systems, little quantitative information exists regarding reaction pathways or thermo-kinetic parameters needed for detailed physical models. The MIEC nature of ceria also leads to a degree of uncertainty, in terms of the relative influence of ionic and electronic conduction in SOFC anode conditions. Analysis is further complicated by uncertainties in possible electrochemical oxidation mechanisms, including the role of ceria in composite anodes (whether it contributes directly to electrochemical oxidation or merely serves as an oxygen storage medium) and the roles of the Ce^{3+} and Ce^{4+} oxidation states in SOFC anode operation.

1.5 Thin-film SOFCs

Since the early 1990s, researchers have used simplified electrode geometries to extract kinetic parameters from SOFC experiments. One of the earliest successes in this area was by Mizusaki, who deposited 1-2 micron-thick LSM thin-film electrodes on YSZ [67]. Mizusaki's results demonstrated, and a number of subsequent efforts have confirmed, that even for a poor ionic conductor such as LSM a bulk electrochemical pathway existed, and that the TPB is not strictly necessary [67, 68]. For a more effective mixed conductor such as ceria, this bulk pathway can contribute significantly to the total oxidation current.

Studies by Adler [68] and Baumman, et al. [43] outline methods for determining the source of chemical capacitance in electronic impedance spectra (EIS) data (used to probe the dynamic polarization response of electrochemical systems) for thin-film MIECs. Baumman et al. propose an equivalent circuit model for thin-film MIECs, discussed in greater detail in chapter 3. The authors conclude that differentiating between surface exchange and bulk diffusion processes depends on the film thickness relative to the "characteristic thickness" of the film, which is the ratio of the oxygen tracer diffusion coefficient to the surface exchange rate: $L_c = D/k$, where D and k are the effective diffusion coefficient and surface exchange rates, respectively [43]. Similarly, Adler derives expressions for the chemical capacitance for both adsorption-limited and bulk diffusion-limited systems. Adler also points out that the magnitude of the capacitance can indicate the relative importance of

interface, surface, and/or bulk processes, as the accumulation of electroactive intermediates in the bulk leads to a large chemical capacitance in micron-sized films, on the order of 0.1-1.0 F/cm^2 [68].

1.6 Objectives and Overview of Current Study

The current study represents an initial step in the effort to elucidate the fundamental role of CeO_{2-x} in composite SOFC anodes, by constructing an MEA model of an SOFC with a composite-ceria anode. Key kinetic and thermodynamic model parameters will be derived by experimentally characterizing the electrochemical oxidation of small fuel molecules (H_2, CO) on undoped ceria anodes. While previous experimental efforts have investigated the use of porous, composite ceria anodes [6, 25, 52-54], this work utilizes a dense, thin-film anode geometry, made possible by the MIEC nature of ceria. As with other idealized geometries, the use of thin-film anodes offers three main advantages: 1) isolation of the ceria contributions from other catalyst components, 2) elimination of porous media gas transport effects, and 3) well-defined structural parameters for analysis of electrochemical data [43, 57, 67-69]. The mechanism derived from these thin-film experiments will provide a basis for future SOFC modeling efforts involving ceria-based composite anodes and will form a "core mechanism" for any oxidation mechanism for larger hydrocarbon species.

The following chapters will present a description of the role and electrochemical activity of ceria in SOFC anodes, as well as a framework for the

optimization of the microstructure in ceria-based SOFC anodes. Chapter 2 will describe the governing equations for a 1-D thin-film MIEC SOFC electrode model and interpret some sample results. The fabrication and experimental characterization of button-cell SOFCs with thin-film ceria anodes will be detailed in chapter 3, including the use of *in situ* ambient-pressure X-ray photoelectron spectroscopy (XPS) to identify ceria valence states during SOFC operation. In chapter 4, the model described in chapter 2 will be used to model the kinetics of H_2 and CO electrochemical oxidation on electrolyte-supported SOFCs with thin-film CeO_2 anodes, validating model results against the experimental data presented in chapter 3.

One of the primary objectives of this work is to elucidate the fundamental role of ceria in high-performance SOFC anodes. To this end, chapter 5 describes the governing equations for a 1-D SOFC MEA model with porous composite electrodes, highlighting many fundamental aspects of SOFC operation in the process. Chapter 5 will also illustrate the validation of this model, comparing model results with experimental results for a relatively well understood SOFC anode catalyst system – namely Ni-YSZ operating in H_2/H_2O – to answer several key questions about the relation of porous-media transport to electrochemical performance in SOFCs [70]. By incorporating MIEC kinetics developed in this work into the porous-media model, left as future work, this study provides the foundation for further elucidation of the role of ceria in SOFC anodes and for further design studies to optimize SOFC architectures with ceria catalysts for various applications.

Chapter 2: One-dimensional Thin-film SOFC Model with Mixed Ionic-Electronic Conduction

As mentioned in chapter 1, high-performance ceria-based SOFC anodes are typically realized as porous composite electrodes. While ceria displays mixed ionic and electronic conduction in reducing anode conditions, the magnitude of the electrical conductivity is several orders lower than for metals. For example, at 1000 °C, the conductivity of ceria (0.2 – 2.0 S/cm) is 3-4 orders of magnitude lower than that for nickel ($21.4*10^3$ S/cm) [42, 71]. This discrepancy is due to the low mobility of polarons in ceria, which move by a thermally activated hopping mechanism, compared to the mobility of electrons in a metal. Regardless, a supporting anode (thickness ~ 1 mm) that relies entirely on ceria for electronic current collection will encounter significant Ohmic losses at moderate-to-high current densities. Composite anodes with a mixture of current collector and ceria particles can provide a significant improvement in electrical conductivity.

Another advantage of composite ceria SOFC anodes is the potential for higher catalytic activity than for pure ceria systems. The catalytic activity of ceria for hydrocarbon oxidation (either with O_2 or H_2O) is relatively low at $T \leq 1000$ °C, when compared to Ni and noble-metal catalysts, and a number of studies have shown that ceria limited activity for carbon cracking [6, 56]. Results demonstrate that incorporating a small amount of Pt or Ni can increase the catalytic activity of ceria

systems significantly, for both H_2 and hydrocarbon oxidation [42]. Composite Ni-CeO_2 systems, for example, have been shown to capitalize on the strengths of both constituent materials [72]: Ni performs non-electrochemical reforming of HCs and electrochemical oxidation of smaller fuel species, while ceria increases the resistance to sulfur poisoning and carbon deposition and contributes to the electrochemical oxidation activity.

Generally speaking, composite porous electrodes represent the state-of-the-art for high-performance electrodes of any material class, due to superior microstructural characteristics and adhesion to the dense electrolyte. The inclusion of pore space allows gaseous diffusion toward the dense electrolyte and increases the surface area available for chemical reactions by orders of magnitude, compared to the geometric area [2, 73]. Additionally, the incorporation of electrolyte particles into the porous matrix increases the total available length of three-phase boundary, extending the electrochemically reactive region into the electrode depth, and improves the match in CTE between the ceria anode and electrolyte, improving adhesion between the two layers [38, 42].

However, while porous composite electrodes can provide high electrochemical performance for practical SOFC systems, experimental results on these electrodes are of limited utility for the estimation and validation of micro-kinetic oxidation mechanism parameters. As discussed more thoroughly in chapter 5, the use of porous electrodes introduces significant uncertainty to model results,

regarding porous microstructural parameters such as the porosity, tortuosity, and lengthof TPB, discussed further below, as well as the correct interrelation between gas-phase diffusion and electrochemical activity in porous media. Such parametric and mechanistic uncertainties obscure the oxidation mechanism parameters that this study seeks to estimate, and as such the incorporation of porous electrode phenomena can only serve to increase the uncertainty of model validation results for a given oxidation mechanism. Similarly, the incorporation of an additional catalyst such as Ni or Pt into model results further complicates the determination of rate parameters and relevant surface thermodynamic parameters for ceria. The development of a quantitative understanding of ceria thermochemistry will be an important step in optimizing performance of composite ceria-based SOFC electrodes, and the goal of this study is to begin the development of kinetic models by isolating and characterizing the electrochemical oxidation of small molecules on pure, undoped ceria. Such a mechanism can provide a framework for later modeling studies on ceria-based electrodes.

This study makes use of thin-film ceria anodes to isolate the contribution of ceria surface and bulk processes to electrochemical activity in SOFC anodes. This chapter is devoted to the description of a thin-film SOFC electrode model with MIEC transport phenomena. The model will be used to simulate linear sweep voltammetry (LSV) tests on the thin-film ceria electrodes, which probe the steady-state polarization response as a function of current density. Governing equations are written as a set of differential-algebraic equations (DAE), which are integrated over a

long time span for given boundary conditions to determine the steady state response of the electrode. This chapter describes the governing equations and rate expressions, and presents initial model results to elucidate the operating principles of the dense thin-film electrodes.

2.1 Previous SOFC Modeling Efforts

Many SOFC models have been developed in the past, typically to replicate data from two types of tests: electronic impedance spectroscopy (EIS) and LSV/polarization. Recent studies have demonstrated how results from polarization models can be extended to predict EIS results, with linearized approximations of the impedance response reproduced by manipulation of the numerical Jacobian calculated during LSV simulations [74, 75]. Thus, while the SOFC model described in this chapter can be readily adapted to study EIS, the main goal of this simulation tool is to reproduce LSV data. As mentioned, LSV determines the steady-state response of the system to a given set of boundary conditions: for a given temperature and composition for the oxidant and fuel streams, the test determines the steady-state response for a range of external current densities i_{ext}. For the button-cell tests described in this work, the fuel and air composition in the mixing chambers are assumed constant. As discussed in chapter 1 and depicted in figure 1.2, the individual overpotentials of the various components ($\eta_{ohm,}$ η_{act}, and η_{conc} in both the anode and cathode and η_{ohm} in the electrolyte) adjust such that the total Faradaic current density (due to charge transfer reactions in the electrochemically active regions) is equal to the imposed boundary condition i_{ext}. By adding these various overpotentials η, each

of which are functions of i_{ext}, to the open circuit voltage (OCV), the operating cell voltage for a given current density is determined:

$$V_{cell}(i_{ext}) = V_{OCV} - \sum_{an,ca} \eta_{act}(i_{ext}) - \sum_{an,ca} \eta_{ohm}(i_{ext}) - \sum_{an,ca} \eta_{conc}(i_{ext}). \quad \text{(eq. 2.1)}$$

2.1.1 General Approaches to SOFC Simulation

Many fuel cell models incorporate the notion of an equilibrium Nernst potential into cell voltage calculations, similar to equation 2.1. Overpotentials are calculated independently, as a function of i_{ext}, and subtracted from the Nernst potential to find the cell voltage [76-78]. This approach requires simplifying assumptions about the relationship of the various overpotentials to the current density, and neglects any interrelation between the various overpotentials. As in previous studies [20, 64, 66, 79], the use of reversible elementary charge transfer chemistry in this study eliminates the need to separately evaluate the Nernst potential and the overpotentials. The cell voltage, as detailed further below, is the natural result of thermodynamic consistency. This approach thus presents a consistent method for calculating the cell potential, regardless of the physical phenomena or limiting assumptions included in the model.

Although LSV is a probe of the steady-state SOFC response, most SOFC models are formulated around governing equations that describe the time-derivative of the state variables [2, 63, 66, 80-84]. Models are solved either by setting the residuals of these equations to zero or by integrating the equations over a long time

span and assuming steady state. This latter approach makes use of a technique that Bessler dubs transient numerical simulation [84], and is utilized in this work. Models tend to focus on any or all of the following physical processes: gas-phase diffusion, surface diffusion, and/or chemical and charge-transfer kinetics. In this study, the use of a porous Au current collector in the thin-film experiments introduces some resistance to gas-phase diffusion. However, given the thin nature of the current collector (~50 μm) and the low current densities associated with the thin-film experiments (due to the low catalyst surface area), gas-phase diffusion should not be a significant factor on experimental results. As such, while diffusion through porous media is included in the thin-film model, a more in-depth discussion of the equations governing this process will be handled in chapter 5.

While many past models represent electrochemistry by single-step Butler-Volmer equations, without reference to supporting surface chemistry on the catalyst or electrolyte phases, recent studies have incorporated heterogeneous surface chemistry and electrochemistry with elementary mass-action kinetics. These studies follow the approach outlined separately by Goodwin and Bessler for modeling electrochemistry in patterned SOFC anodes [66, 84], which has recently been applied further to distributed electrochemistry models in porous electrodes [64, 65]. Solving for the coverage of surface species θ_k allows simulations to incorporate the full impact of thermodynamics on charge-transfer kinetics [20] and is a prerequisite for models that write charge-transfer reactions as reversible elementary-step reactions, as in this study.

2.1.2 Previous Thin-film and MIEC Models

A number of MIEC materials, such as perovskites like LSC, LSF, and LSCF, have received considerable attention as SOFC cathode catalysts in recent years. As such, numerous MIEC models have been developed for SOFC cathodes, some of which utilize the dense, thin-film geometry of interest in this study. Coffey and coworkers present a model of an SOFC with a porous MIEC cathode, modeling the pores as cylindrical volumes [85]. Deseure, et al., outline a model for a dense MIEC cathode that closely matches the thin-film geometry to be used in this study [86]. The model explores two rate-limiting processes (bulk diffusion and chemical incorporation of adsorbed oxygen). Mebane and coworkers present a 2-D model of a thin-film MIEC cathode [87]. While that study incorporates charge transfer as a single-step reaction in ways that differ significantly from this study, Mebane's model includes a generalized description for charge transport in MIEC bulk phases that applies to the model formulated here, as discussed below. One important distinction in Mebane's work is that the high P_{O2} in the cathode operating environment leads to a relatively high concentration of oxides in the MIEC. As a consequence, the concentration of electronic charge carriers remains relatively small, a fact that allows these models to simplify (or neglect altogether) the representation of electronic conductivity in ways that are not appropriate for this model. While the limiting assumptions of these models are incorporated into the model formulation in such a way as to reduce the equations' generality, the model results offer insight into the

competition between surface and bulk processes in dense MIECs and establish some of the fundamental equations and principles governing transport in MIEC electrodes.

In addition to MIEC cathode models, the interest in MIEC electrolyte materials such as gadolinium- and samaria-doped ceria (GDC and SDC, respectively) has led to a number of MIEC membrane models [88-90]. The MIEC materials in these electrolyte membranes are typically doped to reduce electronic conductivity and to fix the oxide concentration. This limits the applicability of these models to the anode model discussed herein. However, a series of papers by Riess derive general transport equations for ions and electrons in MIECs [89, 90]. These equations agree with the aforementioned model by Mebane and coworkers [87]. Their formulation is utilized below to describe the transport of O^{2-} ions and polarons in the ceria bulk.

2.2 Model Geometry

The following 1-D model is based on physical conservation laws that are derived as continuum partial-differential equations and then discretized in a finite-volume method and solved computationally. The model is discretized in the through-cell direction (y), with anode properties and state variables averaged over the extent of each volume in the transverse direction (x and z). As depicted in figure 2.1, the thin-film MEA is composed of several distinct elements, reflecting the geometry of the electrolyte-supported MEAs utilized in the experiments described in chapter 3. The anode consists of a porous Au current collector and a dense CeO_2 layer adjacent to the dense YSZ electrolyte. The porous current collector is utilized to allow gas-

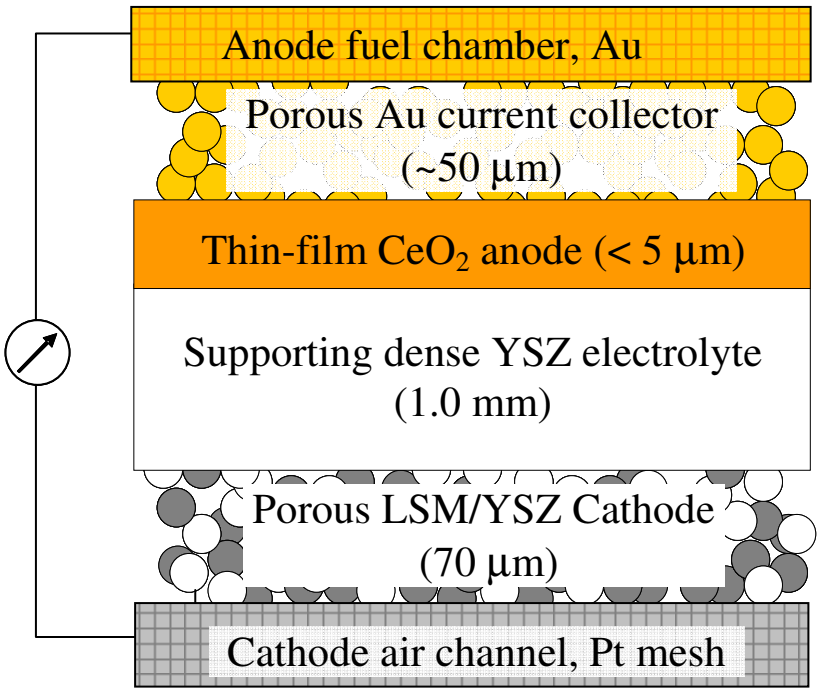

Figure 2.1. Model geometry for SOFC button cell (thicknesses not to scale) with dense thin-film ceria anode.

phase adiffusion to the catalyst surface and to minimize the average path length of polarons conducting on the CeO_2 surface to the current collector (the average pore size in the current collector, as revealed by SEM imaging of the cells described in chapter 3, is ~4 μm).

The LSM/YSZ cathode represents a high-performance composite electrode, as used in the experiments and described with greater detail in chapters 3 and 5. Based on cathode model predictions discussed in chapter 5, the cathode contributes minimally to the total overpotential at the current densities explored, due to its high surface-area and high length of three-phase boundary per unit volume (l_{TPB}). This allows model results to focus on the role of the CeO_2 anode. The cathode is modeled

as a conventional porous LSM-YSZ cathode, as discussed in detail in chapter 5. As such, this chapter will focus on the formulation of the thin-film MIEC anode model. The anode and cathode are in contact with fuel and air mixing chambers, respectively, which are assumed to be at uniform and constant composition, temperature, and pressure. Given the low fuel utilization rates and use of button cell geometry, this assumption is consistent with experimental conditions.

2.3 Model Equations

The MEA governing equations constitute a system of differential-algebraic equations (DAEs), which are discretized in the *y*-direction and integrated in time. Given the aforementioned geometry, the following physical phenomena are included in the anode model: (*i*) convective-diffusive transport from the mixing chamber to the porous medium, (*ii*) gas-phase diffusion through the porous current collector, as described by the Dusty Gas Model [91], (*iii*) reversible gas-phase and surface reactions at the catalyst surface, (*iv*) charge transfer reactions at the catalyst/electrolyte interface, and (*v*) transport of O^{2-} ions and electrons/polarons in bulk ionic solids (YSZ electrolyte, CeO_2 catalyst).

2.3.1 Conservation Equations

2.3.1.1 Conservation of Gas-phase Mass/Species

As noted in previous studies, under SOFC operating conditions the ideal gas equation accurately describes the gas-phase equation of state [92]. Thus, the

temperature T, density ρ, and the mass fractions Y_k can fully describe the gaseous state. Gas phase continuity provides an equation for density:

$$\varphi_g \frac{\partial \rho}{\partial t} = \sum_{k=1}^{k_{\text{gas}}} \left(- \nabla J_{k,g} + W_k \, a_{\text{cat}} \, \dot{s}_{k,g,\text{cat}} \right), \qquad \text{(eq. 2.2)}$$

and gas-phase species conservation equations for all species from $k = 1$ to k_{gas} -1:

$$\varphi_g \rho \frac{\partial Y_k}{\partial t} = -\nabla J_{k,g} + W_k \left(a_{\text{cat}} \, \dot{s}_{k,g,\text{cat}} \right)_k - Y_k \sum_k \left(- \nabla J_{g,k} + W_k \, a_{\text{cat}} \dot{s}_{k,g,\text{cat}} \right), \quad \text{(eq. 2.3)}$$

where $J_{g,k}$ and $\dot{s}_{k,g,\text{cat}}$ are the gas-phase mass flux and the molar production rates from surface reactions on the catalyst, respectively. W_k is the gas phase molecular weight, a_{cat} is the effective surface areas of the catalyst available for surface reactions, per unit total volume, and φ_g is the porosity. With this geometry, the only portion of the catalyst surface not available for reactions is that covered by the porous current collector. Thus, $a_{\text{cat}} = \varphi_g$ in the volume adjacent to the dense anode, and $a_{\text{cat}} = 0$ elsewhere. Finally, in this model, the mass fraction of the last species, $Y_{\text{k,gas}}$, is found by forcing the Y_k to sum to 1.

2.3.1.2 Conservation of Surface Species

Surface site fractions θ_k for species k on the catalyst surface are integrated according to the following relation:

$$\frac{\partial \theta_k}{\partial t} = \frac{1}{\Gamma_{\text{cat}}} \dot{s}_{k,\text{cat}}, \qquad \text{(eq. 2.4)}$$

where Γ_{cat} and $\dot{s}_{k,\text{cat}}$ represent the surface site density (mole sites per area) and molar production rates from surface and reactions, respectively. This formulation assumes that all adsorbed species occupy a single adsorption site. Eq. 2.4 is applied to surface species $k = 1$ to $k = k_{\text{surf,cat,}} - 1$, with $\theta_{k\text{surf,cat}}$ found by forcing the $\theta_{k,m}$ to sum to 1.

2.3.1.3 Conservation of Charge and Calculation of Electric Potential

In the ceria bulk, the currents into and out of a given discretized volume j (with $1 \leq j \leq n_{\text{points,elec}}$) act as charge sinks and sources, respectively:

$$\left.\frac{\partial Q}{\partial t}\right)_j = \frac{\sum i_{j-1/2} - \sum i_{j+1/2}}{\Delta y_j}, \qquad \text{(eq. 2.5)}$$

Where Q is the charge density (in C/m^3), $i_{j+1/2}$ is current crossing the boundary between volumes j and $j + 1$, and Δy_j is the through-cell thickness of volume j. The currents i are summed over the two types of current in the ceria bulk – ionic and electronic – as well as the interfacial currents at the Au and YSZ interfaces.

The location within the ceria dictates which types of current must be considered. The boundary condition at the Ceria/Au current collector interface ($j = 1$) dictates that electrons (polarons) are removed from the ceria at a rate prescribed by the external current, i_{ext}. Furthermore, polarons and oxide ions are exchanged with the next

volume toward the electrolyte, written as $i_{el,3/2}$ and $i_{O2-,\ 3/2}$, respectively. Given the double negative electronic charge of the O^{2-} ion, ion current is related to J_{O2-}, the flux of O^{2-}, by the following, where F is the Faraday constant [C/mol_{e-}]:

$$J_{O2-} = -\frac{i_{O2-}}{2F}. \qquad \text{(eq. 2.6)}$$

At interior points of the ceria ($1 < j < n_{points,\ elec}$), the only currents are i_{el} and i_{O2-}, at the boundaries $j - ½$ and $j + ½$. Finally, at the interface with the electrolyte ($j = n_{points,elec}$), ionic and electronic currents cross the boundary at $n_{points,elec} - ½$, while oxide ions cross the two-phase boundary ($n_{points,elec} + ½$) as Faradaic current i_{Far}, the rate of which is governed by Butler-Volmer kinetics, as discussed below.

At phase interfaces in electrochemical systems, charged double-layers may build up to provide capacitive charge storage. Within the bulk of the ceria, the lack of internal capacitance implies that there is no transient charge storage between separate discretized volumes. Furthermore, *in situ* XPS results discussed in chapter 3 suggest that at the Au/CeO_{2-x} interface the electric potential in the ceria is very close to the Au Fermi level, and that no double-layer develops at the this interface. This implies that there is minimal charge storage at this interface. Therefore, the only double layer present in this system is at the ceria/YSZ interface. Thus, for all volumes $j < n_{points,elec}$ in the ceria:

$$\left.\frac{\partial Q}{\partial t}\right)_j = 0\,. \qquad \text{(eq. 2.7)}$$

Application of eqs. 2.5 and 2.6 requires that at any given point within the bulk of the ceria, the sum of ionic and electronic currents is equal to i_{ext} at all times:

$$i_{O2\text{-},j+1/2} + i_{el,j+1/2} = i_{ext} \left(1 \le j < n_{points,elec}\right). \qquad \text{(eq. 2.8)}$$

As described by Mebane and Riess [87, 89] and depicted in equations 2.15 – 2.18 below, the ionic and electronic currents in the ceria are governed by the gradients in electrochemical potential of the mobile species, which themselves are functions of gradients in species concentration and electric potential. The magnitude of currents is also proportional to the concentration of charge carriers (ions and polarons). At a given time *t*, bulk species concentrations are governed by the differential equations discussed below, while i_{ext} is set as the boundary condition. The bulk catalyst electric potential Φ_{cat}, then, is the only remaining independent variable whose value impacts the solution of eq. 2.8. This equation thus dictates $n_{points,\ elec} - 1$ algebraic equations governing Φ_{cat}. Setting the potential at the current collector interface to a reference value of 0 V fully determines the potential in the ceria bulk.

At the two-phase boundary between the ceria and YSZ, where charged double layers lead to capacitive charge storage, the difference between the anode electric potential Φ_{cat} and the electrolyte electric potential $\Phi_{electrolyte}$ is defined as $\Delta\Phi_{el}$,

$$\Delta\Phi_{\mathrm{el}} \equiv \Phi_{\mathrm{cat}} - \Phi_{\mathrm{electrolyte}} \quad . \qquad \text{(eq. 2.9)}$$

This potential difference is calculated according to the capacitance relationship:

$$C_{dl}\,\frac{\partial \Delta\Phi_{el}}{\partial t} = \frac{\partial Q}{\partial t}, \qquad \text{(eq. 2.10)}$$

where C_{dl} is the double layer capacitance per unit volume. Combining eq. 2.10 with equations 2.5 and 2.8 leads to:

$$C_{dl}\,\frac{\partial \Delta\Phi_{\mathrm{el}}}{\partial t} = \frac{i_{\mathrm{ext}} - i_{\mathrm{Far}}}{\Delta y_{n\mathrm{points,elec}}}. \qquad \text{(eq. 2.11)}$$

The rate equation for Faradaic current density at the YSZ/ceria two-phase boundary is discussed further below. Because Φ_{cat} values in the ceria are fully described by eq. 2.7 and because the boundary condition $\Phi_{\mathrm{cat},1} = 0$, eq. 2.11 determines the evolution of the electric potential of the electrolyte adjacent to the ceria anode. As in other models, the electric potential through the bulk of the YSZ electrolyte is determined for a given i_{ext} by Ohm's law, as discussed in chapter 5.

2.3.1.4 Conservation of bulk species

In doped oxides, such as YSZ or gadolinium-doped-ceria (GDC), the level of doping fixes the ratio of oxides to vacancies at near-constant levels, even in reducing

anode environments [42, 89]. However, the concentration of oxides and vacancies in the undoped ceria explored here can vary considerably with temperature and P_{O2}, as mentioned above. This work considers two bulk species—fully oxidized and fully reduced ceria—both of which are defined in terms of the fcc unit cell (Ce_2O_4 and Ce_2O_3, respectively), as shown in figure 2.2. The Ce_2O_3 bulk species can also be thought of as an oxide vacancy, with two associated polarons. This follows the recommendations from Adler and from Riess who derive a set of rate-laws for MIEC catalysts, and recommend defining reacting species in terms of charge-neutral states [93, 94]. Many intermediate stoichiometric phases of the form Ce_nO_{2n-2m} have been identified [40], and are modeled here as mixtures of these two extreme stoichiometries.

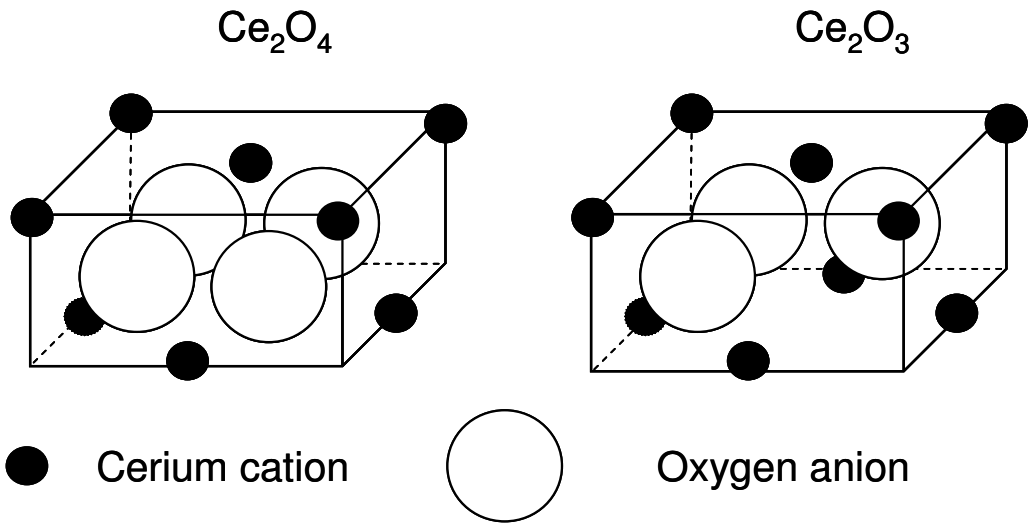

Figure 2.2. Illustration of the two species considered in this study for the ceria bulk. The cations in Ce_2O_4 are 4+ in valence, while the valence of the Ce_2O_3 cations is 3+.

One potential source of complication is the ability of the cerium cation to exist in either the 3+ or 4+ valence states, regardless of the neighboring oxide occupancy. In fact, the movement of charge through the ceria bulk requires, on a transient level, mismatch between the cerium valence state and neighboring oxide occupancy. For example, in non-electrochemical reduction of the ceria, as in reaction 2.1:

$$Ce_{Ce}^{X} + O_{O}^{X} \rightarrow (1-2x)\, Ce_{Ce}^{X} + 2x\, Ce_{Ce}^{\prime} + x\, V_{O}^{\bullet\bullet} + (1-x)\, O_{O}^{X} + \frac{x}{2} O_{2(g)}\,. \qquad \text{(R 2.1)}$$

Here, the two electrons formerly associated with the oxide become "self-trapped" on two local cerium ions, which are reduced from a 4+ valence state to 3+ [40]. However, during oxide diffusion the two electrons remain bound to the oxide, and do not become self-trapped in the cerium lattice positions. For example, consider oxide diffusion from volume *j* to volume *j*+1, with the valence of each cerium cation listed explicitly:

$$Ce_2^{4+}O_4\big)_j + Ce_2^{3+}O_3\big)_{j+1} \rightarrow Ce_2^{4+}O_3\big)_j + Ce_2^{3+}O_4\big)_{j+1}\,. \qquad \text{(R 2.2)}$$

The region formerly occupied by the oxide is now Ce_2O_3, but the cerium ions remain in the 4+ valence state rather than the 3+ valence commonly associated with Ce_2O_3. As such, the $Ce_2^{4+}O_3$ functions like a bulk-phase oxide ion vacancy. Similarly, the oxide ion does not accept two electrons from the cerium ions in its new unit cell, and so these cations remain in a 3+ valence state, despite the fact that the unit cell is now

Ce_2O_4. Similar transient phenomena arise from polaron transport, as well as from charge-transfer reactions at the electrode interfaces.

Although this mismatch between Ce valence state and oxide sub-lattice occupancy implies that the concentration of polarons (Ce^{3+}) is not *a priori* proportional to the concentration of Ce_2O_3 unit cells, this study does not consider such species. Accounting for this mismatch would require the introduction of two additional species: $Ce_2^{3+}O_4$ and $Ce_2^{4+}O_3$, as well as additional kinetic and thermodynamic model parameters, all of which serve to increase the computational cost and uncertainty of the model. However, application of eq. 2.7 in the bulk of the ceria requires that the charge density within each volume remain constant, which implies that the concentration of O^{2-} ions and Ce^{3+} polarons must sum to a constant. Therefore, at any given time the concentrations of such "mismatched" species $Ce_2^{3+}O_4$ and $Ce_2^{4+}O_3$ must be equal. The model further assumes that oxides and polarons can equilibrate infinitely quickly within a given finite volume, which allows all "mismatched" unit cells to return to their more common valence states:

$$Ce_2^{3+}O_4 + Ce_2^{4+}O_3 \rightarrow Ce_2^{4+}O_4 + Ce_2^{3+}O_3 . \qquad \text{(R 2.3)}$$

Assuming a very fast rate of reaction for R 2.3, the concentration of polarons, is therefore dependent on the bulk mole fraction of fully oxidized unit cells:

$$N_{Ce3+} = 2\,\Gamma_{bulk}\left(1 - X_{O2-}\right). \qquad \text{(eq. 2.12)}$$

where N is concentration [kmol-m^{-3}], Γ_{bulk} is the concentration of unit cells in the ceria bulk [kmol-m^{-3}], and X_{O2-} is the mole fraction of Ce_2O_4 unit cells in the ceria bulk. Equation 2.12 assumes that the mole fractions sum to one, and implies that only one mole fraction need be stored as a state variable (without loss of generality, this model stores oxide mole fraction).

The storage of oxide ions in the ceria bulk is determined by the flux of ions into and out of a given volume j, plus any oxides generated by interfacial reactions:

$$\left.\frac{\partial X_{O2-}}{\partial t}\right)_j = \frac{-\nabla J_{O2-,j} + \frac{\dot{s}_{int,j}}{\Delta y_j}}{\Gamma_{cat,bulk}}, \qquad \text{(eq. 2.13)}$$

where J_{O2-} is the flux of oxide ions due to diffusion in kmol-m^{-2}s^{-1}, and $\dot{s}_{int,j}$ is the creation rate of ions due to chemical reactions at the electrode interfaces (ceria/gas and ceria/YSZ), in kmol-m^{-2}s^{-1}. At interior points, $\dot{s}_{int,j}$ is equal to zero.

The preceding equations 2.2 – 2.6, 2.8, 2.9, and 2.11 – 2.13, along with the transport and reaction rate laws derived below, fully specify the state variables of the thin-film CeO_2 anode and associated gas-phase fuel feed for a given external current density i_{ext}.

2.3.2 Transport and Reaction Rate Equations

2.3.2.1 Gas-Phase Transport Equations

For gas-phase transport in the porous current collector, the Dusty Gas Model (DGM), as discussed in ref. [1], is used. $J_{k,g}$ in eqs. 2.2 and 2.3 can be written as:

$$J_{k,g} = -W_k \left[\sum_l \left(D_{DGM,kl} \nabla [X_l] \right) + \sum_l \left(\frac{D_{DGM,kl}[X_l]}{D^e_{Kn,l}} \right) \frac{B_g}{\mu} \nabla P \right], \qquad \text{(eq. 2.14)}$$

where $[X_l]$ is the molar concentration (in kmol-m^{-3}), B_g is the permeability of the porous electrode [m^2], calculated according to the Cozeny-Karman relationship [2], μ is the dynamic viscosity [Pa-s], P is the pressure [Pa], and $D^e_{Kn,l}$ is the effective Knudsen diffusion coefficient for species l [95]. $D_{DGM,kl}$ are the effective binary DGM diffusion coefficients. A more in-depth discussion of the DGM and the $D_{DGM,kl}$ is presented in chapter 5. At the interface with the mixing chamber, $J_{k,g}$ in the porous media matches $J_{k,g}$ from the mixing chamber, as calculated from multi-component diffusion rates multiplied by a constant Sherwood number Sh. As discussed in chapter 5, simulation results were insensitive to variations in Sh, and so an average Sherwood number of 3.0 was used.

2.3.2.2 Ion and Polaron Transport in bulk CeO_{2-x}

As mentioned, previous studies have described mixed conduction in electrochemical systems, for a variety of materials, operating conditions, and with varying levels of detail. Two notable works relevant to this study are by Mebane and

by Riess, who constructed a 2-D model of a MIEC cathode [87] and a 1-D model of an MIEC membrane [89], respectively. Both models attribute the ionic and electronic currents to gradients in electrochemical potential for the respective species, multiplied by the species mobility and the concentration of charge carriers:

$$i_k = v_k \left[X_k\right] \nabla \tilde{\mu}_k, \qquad \text{(eq. 2.15)}$$

where the subscript k refers to either ionic (O^{2-}) or electronic (*el*) current/charged species, v_k refers to the mobility [m^2/V-s], and $\tilde{\mu}_k$ to the electrochemical potential of charged species k:

$$\tilde{\mu}_k = \mu_k + z_k F \Phi_k, \qquad \text{(eq. 2.16)}$$

where μ_k is the chemical potential, z_k is the electric charge/valence (-2 for both species considered here), and Φ_k is the electrostatic potential of the phase for species k. Furthermore, Mebane and Reiss both utilize the dilute solution approximation for the chemical potential μ_k, given by:

$$\mu_k\left(X_k, T\right) = \mu_k^o(T) + \overline{R}\, T \ln\left(\frac{[X_k]}{[X_k^o]}\right), \qquad \text{(eq. 2.17)}$$

where $\mu_k^\circ(T)$ is a temperature-dependent standard-state chemical potential at concentration $[X_k^\circ]$. This simplification only applies if the defect species (Ce_2O_3, in

this study) can be represented as ideal, non-interacting species. Mebane and Riess both use eq. 2.17 to simplify the form of the ionic and electronic currents:

$$i_k = \overline{R}T\, v_k \nabla[X_k] + v_k\, [X_k]\, z_k F\, \nabla\Phi_k . \qquad \text{(eq. 2.18)}$$

In the high-temperature, reducing environment of SOFC anodes, however, the polaron concentration is such that defects can no longer be considered 'dilute.' Previous measurements of ceria conductivity and the free energy of ceria reduction have detected significant interaction potentials between Ce_2O_3 defects at moderate-to high Ce_2O_3 concentrations [38, 42, 96]. These previous measurements, as well as the influence of non-ideal interaction potentials on charge transport and reaction rates, are discussed with greater depth in chapter 4, where model results are validated against experimental data.

2.3.2.3 Surface and Electrochemical Reactions

All chemical reactions are simulated as reversible elementary-step reactions, with rates calculated according to mass action kinetics using the Cantera software package [97]. The net rate of species production $\dot{s}_k$ for gas, surface, and bulk catalyst species depends upon summing the rate-of-progress q_i over all reactions

$$\dot{s}_k = \sum_i v_{i,k} q_i \,, \qquad \text{(eq. 2.19)}$$

where $\nu_{i,k} = \nu'_{i,k} - \nu''_{i,k}$ is the net stoichiometric coefficient of species k in reaction i. The reaction rate-of-progress is evaluated as

$$q_i = k_{\mathrm{i,fwd}} \prod_k^K [X_k]^{\nu'_{ik}} - k_{\mathrm{i,bwd}} \prod_k^K [X_k]^{\nu''_{ik}} \ , \qquad \text{(eq.2.20)}$$

where $\nu'_{i,k}$ and $\nu''_{i,k}$ are the stoichiometric coefficients of species k for reaction i in the forward and backwards directions, respectively, and $[X_k]$ is the generalized activity of species k. The generalized activity for gas-phase species is the molar concentration, and the activity for surface species is the site density [98].

For adsorption/desorption reactions, forward (adsorption) rate coefficients are calculated as sticking coefficients, while all other rate coefficients are described by Arrhenius parameters $A_{\mathrm{fwd/bwd}}$, n_T, and $E_{a,\mathrm{fwd/bwd}}$, as described elsewhere [98]. The forward and reverse reaction rates are related by the equilibrium coefficient K_c, which itself is a function of species thermodynamics. Assuming $n_T = 0$, the reaction rate parameters for a reaction i are thus related to the reaction thermodynamic terms ΔH_i and ΔS_i, the enthalpy and entropy of reaction, respectively:

$$\Delta H_i = E_{a,i,fwd} - E_{a,i,bwd} \ , \qquad \text{(eq. 2.21)}$$

$$\Delta S_i = \overline{R} \ \ln\left(\frac{A_{i,\mathrm{fwd}}}{A_{i,\mathrm{bwd}}}\right). \qquad \text{(eq. 2.22)}$$

A more detailed discussion of these reaction rate parameters is included in chapter 5, which describes the model formulation for a 1-D porous composite SOFC model.

As described by Bessler et al.. [20], the rate expressions for reactions involving charge transfer follow from mass-action kinetics as

$$k_{\text{fwd}} = k_{\text{fwd}}^{*} \exp\left(\frac{\alpha_{\text{fwd}} n_{\text{elec}} F \ \Delta\Phi_{\text{el}}}{RT} \right); \qquad \text{(eq. 2.23)}$$

$$k_{\text{bwd}} = k_{\text{bwd}}^{*} \exp\left(-\frac{\alpha_{\text{bwd}} n_{\text{elec}} F \ \Delta\Phi_{\text{el}}}{RT} \right). \qquad \text{(eq. 2.24)}$$

The thermal components of the rate expression, k_{bwd}^{*} and k_{fwd}^{*}, are expressed in Arrhenius form, as described above. The forward and backward symmetry parameters α_{fwd} and α_{bwd} are related to transition state theory and dictate how the energy shift $\Delta\Phi_{\text{el}}$ is apportioned between the forward and backward reactions. In this study, the charge transfer reaction rates follow the stipulation for elementary reactions that $\alpha_{\text{fwd}} + \alpha_{\text{bwd}} = 1$ [99]. The number of electrons transferred in a reaction is given as n_{elec}. The total Faradaic current is found by multiplying the molar production term $\dot{s}_k$ for the electron by the Faraday constant F. The standard Butler-Volmer form given in eq. 1.2 is related to this mass-action formulation through the exchange current density i_o [20]:

$$i_o = n_{\text{elec}} F l_{\text{TPB}} k_{fwd}^{\alpha_{fwd}} k_{bwd}^{\alpha_{bwd}} \prod_k [X_k]^{\nu_{fwd,k}\alpha_{bwd}} \prod_j [X_j]^{\nu_{bwd,j}\alpha_{fwd}} \quad . \quad \text{(eq. 2.25)}$$

2.4 Simulation Procedure

The simulation of SOFC polarization data involves a series of steady-state calculations for a range of external current density boundary condition values, with a fixed gas state in the anode and cathode fuel and air chambers, respectively. The system of equations described above, after finite-volume discretization of the spatial operators in the *y* direction, represents a system of transient differential-algebraic equations (DAE). Following the example of Bessler's transient numerical simulation [84], simulations integrate the DAE system to steady state for each i_{ext}, calculating the cell voltage V_{cell} as the electric potential difference between the anode and cathode at the electrode interface with the fuel and air chambers, respectively:

$$V_{\text{cell}} = \Phi_{ca,\text{int}} - \Phi_{an,\text{int}} \, . \qquad \text{(eq. 2.26)}$$

The DAE system is solved within the Matlab framework using the function ode15s. For the baseline set of parameters described below, the simulation completed a sweep of 14 steady-state calculations, with $i_{\text{ext}} \leq 40$ mA/cm^2, in a time of 70 min. on a 2.33 GHz processor.

Solving the DAE system described above involves the estimation of numerous model parameters, related to the microstructure of the porous current collector, thermodynamics of surface and bulk species, reaction rate kinetic parameters, and transport parameters in the gas and bulk catalyst phases. Table 2.1 summarizes the geometric and transport parameters for this baseline case. The thicknesses of the various elements are set to match the experimental set-up described in chapter 3. Microstructural parameters for the porous Au current collector are estimated from visual inspection of SEM micrographs and from average literature values for porous transport models [1, 7, 73]. Parameter estimates for the ceria surface site and bulk

Table 2.1. Model parameters for baseline cell. Temperature-sensitive parameters ν_{O2-} and ν_{el} are given for T = 700 °C

Parameter	Value
Average current collector pore radius, $r_{p,cc}$ [μm]	0.5
Average current collector particle diameter, $d_{p,cc}$ [μm]	2.5
Current collector thickness, δ_{cc} [μm]	50
Current collector porosity, $\varphi_{g,cc}$	0.25
Current collector tortuosity, $\tau_{g,cc}$	3.0
Thin-film catalyst thickness δ_{cat} [nm]	111
Sub-surface layer thickness $\delta_{cat,sb}$ [nm]	1
Catalyst surface site density, $\Gamma_{cat,surf}$ [mol/cm^2]	4.05e-10
Catalyst bulk density, $\rho_{cat,bulk}$ [kg/cm^3]	6.2e-3
Catalyst bulk ion mobility, ν_{O2-} [cm^2/V-s]	2.0e-7
Catalyst bulk electron (polaron) mobility, ν_{el} [cm^2/V-s]	7.1e-4
Double layer capacitance, C_{dl} [F/m^3]	0.003

mass density are taken from knowledge of the lattice parameter at moderate degrees of reduction [40], as well as the molecular weights of the constituent atoms. Similarly, the ion and polaron mobilities v_{el} and v_{O2-}, respectively, are taken from previous literature values, as compiled by Trovarelli for moderately reduced ceria [40]. While the mobilities are known to vary with the degree of reduction x (where the ceria composition is CeO_{2-x}), the mobility is most sensitive at values of $x < 0.05$. The mobility reaches a maximum at $x \sim 0.1$, and then reduces more gradually for $x > 0.1$ [38, 40, 42]. For the reducing conditions in this study, x is generally expected to be between $0.1 < x < 0.5$. Thus, the values for v_{io} and v_{el} in table 2.1 are for $x = 0.2$ and 0.23, respectively.

2.5 Sample Model results for Hydrogen Oxidation

2.5.1 Oxidation Mechanism for H_2/H_2O

To illustrate the operating principles of the thin-film MIEC anode model, sample results are presented below for H_2 oxidation. Electrochemical oxidation of H_2 is achieved via the reactions described by R 2.4 to R 2.9. In addition to the gas-phase species $H_2(g)$, $O_2(g)$, and $H_2O(g)$, the mechanism involves four species on the ceria surface ($O_{Ce}(s)$, $Vac_{Ce}(s)$, $OH_{Ce}(s)$, and $H_2O_{Ce}(s)$), two species in the ceria sub-surface ($Ce_2O_4(sb)$, $Ce_2O_3(sb)$), two species in the bulk ceria ($Ce_2O_4(b)$, $Ce_2O_3(b)$) and two species in the YSZ bulk (O^{2-}_{YSZ} and $V_{\ddot{O},YSZ}$). The ceria sub-surface is a thin layer ($\delta_{cat,sb}$ = 1.0 nm in table 2.1) in contact with the ceria surface. Sub-surface thermodynamics will likely vary from bulk values, although the bulk and sub-surface thermodynamics are identical in the baseline results presented below. Oxide ion

exchange between the sub-surface and surface is modeled as a chemical reaction (R 2.10), described by mass-action kinetics, rather than as a diffusive process. Furthermore, the interaction potential of reduced surface species depends on the degree of reduction in the sub-surface, as discussed in chapter 4.

Surface species are associated with a monolayer of Ce_2O_4/Ce_2O_3 unit cells. For the sake of convenient nomenclature, the names of surface species refer only to the occupancy of the reactive oxide. For example, the surface species Ce_2O_3-OH^- is referred to simply as $OH_{Ce}(s)$. Figure 2.3 depicts the surface species considered in this study for H_2 oxidation, while table 2.2 gives the chemical formulas and ceria valence states for all surface species.

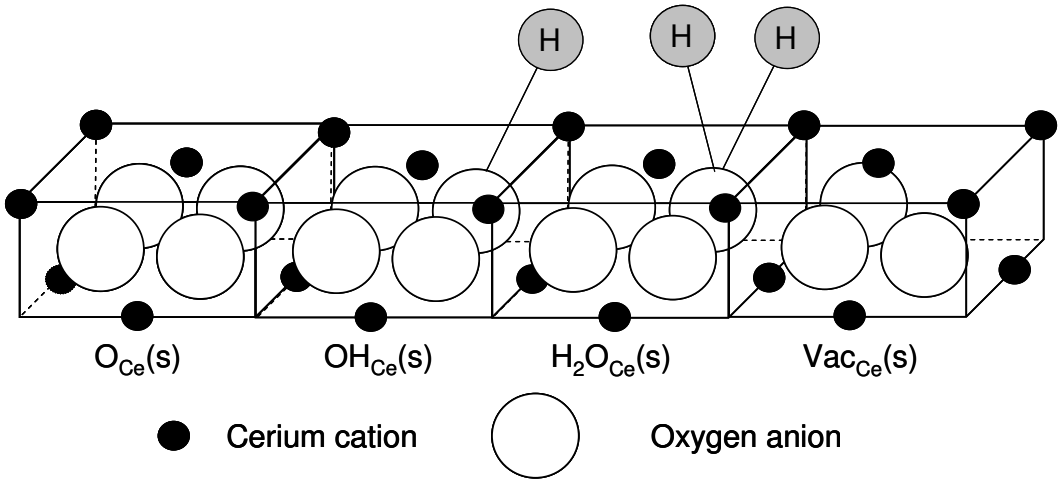

Figure 2.3. Illustration of surface species considered for H_2 oxidation mechanism

Table 2.2. Chemical formulas and average Ce valence for ceria surface species.

Species Name	Unit Cell Formula	Average Ce valence
$O_{Ce}(s)$	Ce_2O_4	4+
$OH_{Ce}(s)$	Ce_2O_3-OH^-	3.5+
$H_2O_{Ce}(s)$	Ce_2O_3-H_2O	3+
$Vac_{Ce}(s)$	Ce_2O_3	3+

It is assumed that each surface unit cell can accommodate at most one defect (vacancy or adsorbed specie bonding to a surface oxide). This is a simplification of what most likely occurs on an atomic level, but given that calculated properties are taken as an average over the physical extent of the anode surface, it should not have a significant effect on the mean-field calculations performed in this study. As mentioned above, all reactions are written as fully reversible. Chemical reactions included in the proposed mechanism are as follows:

- Dissociative hydrogen adsorption on $O_{Ce}(s)$ and $OH_{Ce}(s)$ sites:

$$H_2(g) + 2O_{Ce}(s) \xleftrightarrow{K1} 2OH_{Ce}(s); \qquad \text{(R 2.4)}$$

$$H_2(g) + O_{Ce}(s) + OH_{Ce}(s) \xleftrightarrow{K2} OH_{Ce}(s) + H_2O_{Ce}(s). \qquad \text{(R 2.5)}$$

- Surface water formation from surface hydroxyl:

$$2OH_{Ce}(s) \xleftrightarrow{K3} H_2O_{Ce}(s) + O_{Ce}(s). \qquad \text{(R 2.6)}$$

- Gaseous water adsorption:

$$H_2O(g) + Vac_{Ce}(s) \xleftrightarrow{K4} H_2O_{Ce}(s). \qquad \text{(R 2.7)}$$

- Oxide exchange between ceria surface and sub-surface:

$$Ce_2O_4(sb) + Vac_{Ce}(s) \xleftrightarrow{K5} Ce_2O_3(sb) + O_{Ce}(s). \qquad \text{(R 2.8)}$$

- Charge-transfer via oxide/ hopping at the ceria/YSZ two-phase boundary:

$$O^{2-}_{YSZ} + Ce_2O_3(b) \xleftrightarrow{K6} V_{\ddot{O},YSZ} + Ce_2O_4(b) + 2e^-_{Ce}. \qquad \text{(R 2.9)}$$

While other reactions, such as H_2O adsorption on $O_{Ce}(s)$, are likely to occur, this list represents the set of reactions likely to play the most important roles in the overall global reactions.

For each reaction *i*, the K*i* refers to the forward and backward rate coefficients $k_{i,\text{fwd}}$ and $k_{i,\text{bwd}}$. As described above, the forward and backward rates are coupled via the reaction thermodynamics. While a detailed description of kinetic and thermodynamic parameter estimation is reserved for the discussion of model validation in chapter 4, tables 2.3 and 2.4 present the baseline set of thermodynamic and kinetic parameters, respectively, for the initial model results presented below.

Table 2.3. Thermodynamics of species at 25 °C and 700 °C.

	$h^0_{k,25^\circ C}$ [kJ/gmol]	$s^0_{k,25^\circ C}$ [J/gmol*K]	$h^0_{k,700^\circ C}$ [kJ/gmol]	$s^0_{k,700^\circ C}$ [J/gmol*K]
Gas Phase Species				
O_2	0.00	204.15	25.27	246.06
H_2	0.00	130.68	22.90	168.38
H_2O	-241.83	188.82	-212.77	235.69
Ceria Surface, Sub-surface, and Bulk Species				
$O_{Ce}(s)$	0.00	0.00	18.18	31.87
$OH_{Ce}(s)$	-30.60	37.65	-2.48	86.90
$H_2O_{Ce}(s)$	-49.83	87.27	-17.60	143.20
$Vac_{Ce}(s)$	282.00	-0.12	289.30	13.00
$Ce_2O_4(sb)$	0.00	0.00	18.18	31.87
$Ce_2O_3(sb)$	312.00	24.88	319.30	38.00
$Ce_2O_4(b)$	0.00	0.00	18.18	31.87
$Ce_2O_3(b)$	312.00	24.88	319.30	38.00
YSZ Bulk Species				
$[]_{YSZ(b)}$	0.00	0.00	47.75	78.91
$O^{2-}_{YSZ(b)}$	-182.63	29.54	-122.25	128.91

Table 2.4. Forward rate parameters for baseline thin-film results, T = 700 ˚C.

[a]Sticking coefficient σ^o.

Reaction Rate Parameter	k_{fwd} value
Ceria Surface	
$k_{1,fwd}$[a]	$1.00*10^{-3}$
$k_{2,fwd}$[a]	$4.00*10^{-4}$
$k_{3,fwd}$	$5.00*10^{9}$
$k_{4,fwd}$[a]	$1.00*10^{-4}$
$k_{5,fwd}$	$1.00*10^{6}$
Ceria/YSZ Interface	
$k_{7,fwd}$	$5.00*10^{-8}$

2.5.2 Initial Model Results

Figures 2.4 – 2.7 depict model results for the baseline case presented above, with T = 700 ˚C, P_{H2} = 0.65 atm, P_{H2O} = 0.03 atm, and balance Ar (P_{tot} = 1 atm). Figure 2.4 shows the polarization and power density curves for the baseline case. Aside from the significant bulk resistance due to the supporting electrolyte, the polarization curve mainly appears to reflect the underlying Butler-Volmer (B-V) kinetics governing charge-transfer at the ceria-YSZ boundary. The polarization resistance is highest at open circuit, but decays smoothly and rapidly, consistent with B-V kinetics. For i_{ext} above ~30 mA/cm^2, the polarization curve is almost entirely linear. The power density show maximum of ~17.5 mW/cm^2.

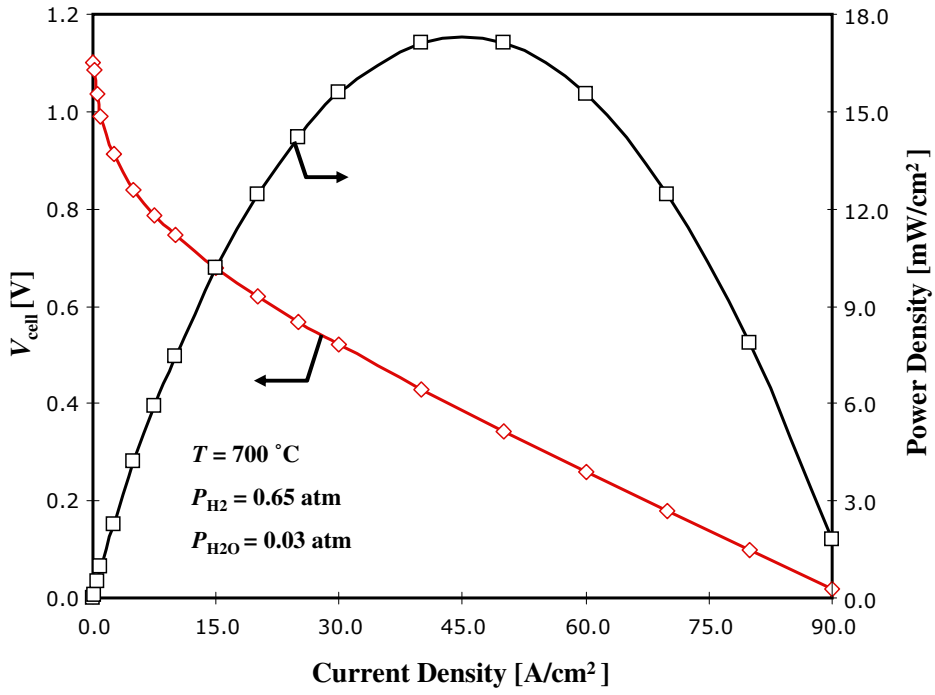

Figure 2.4. Predicted polarization and power density curve for SOFC with thin-film dense CeO_{2-x} anode. Baseline cell parameters taken from Tables 2.1-2.4.

Figure 2.5 shows the distribution of ceria surface species as a function of current density. Model results predict that the surface is dominated by $Vac_{Ce}(s)$, particularly at open circuit, with $\theta_{VacCe(s)} = 0.97$. The surface concentration decreases gradually with increasing current density, to $\theta_{VacCe(s)} \sim 0.8$ at $i_{ext} = 90$ mA/cm^2. As $\theta_{VacCe(s)}$ decreases, $\theta_{OCe(s)}$ and $\theta_{OHCe(s)}$ increase gradually, with covering about 10% of the surface at $i_{ext} = 90$ mA/cm^2. Adsorbed water has a significantly lower coverage than all other species, and never accounts for more than 3% of the available surface sites. It is somewhat curious that $\theta_{H2OCe(s)}$ does not increase more strongly, because the desorption rate of water must increase proportionally to the current. However, the drop in $\theta_{VacCe(s)}$ leads to a significant decrease in the adsorption rate, and so the net desorption rate increases without a significant increase in $\theta_{H2OCe(s)}$.

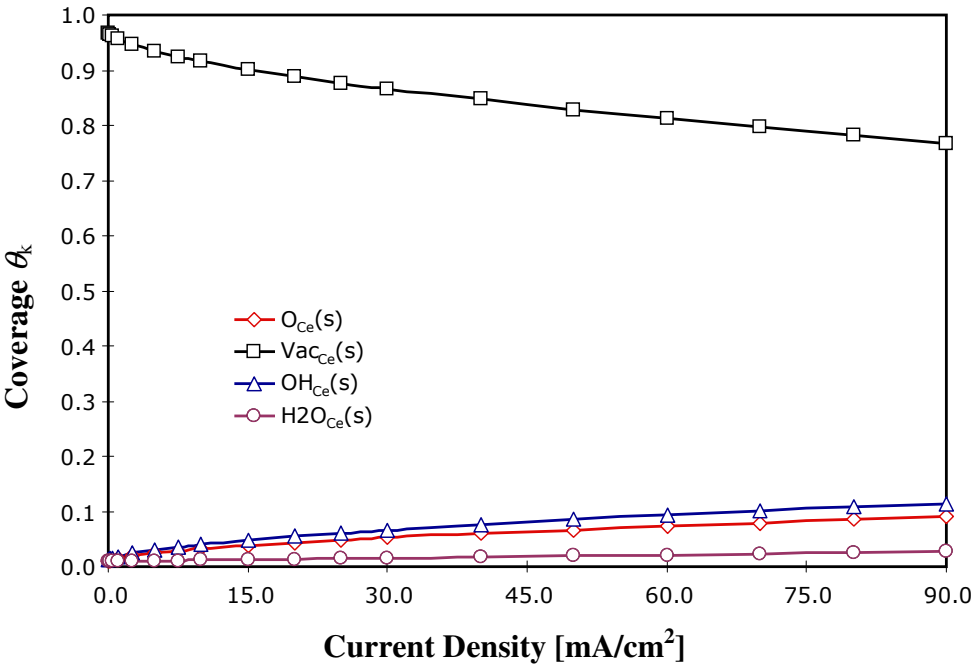

Figure 2.5. Distribution of ceria surface species versus current density

Figure 2.6 illustrates the variation in electric potential through the thickness of the ceria electrode, for several current densities. The electric potential profile shows a high degree of linearity, and the total drop in Φ_{cat} across the electrode is overall rather small—just under 0.8 mV at $i_{ext} = 50$ mA/cm^2.

Finally, figure 2.7 shows the evolution of the O^{2-} concentration at two points in the ceria electrode: in the catalyst sub-surface (labeled O^{2-}(sb) in figure 2.7) and at the ceria/YSZ interface (labeled O^{2-}(b) in the figure). Results show that the bulk oxide concentration increases significantly with increasing current density. Figure 2.7 implies that the overall diffusion resistance is low, with an oxide concentration

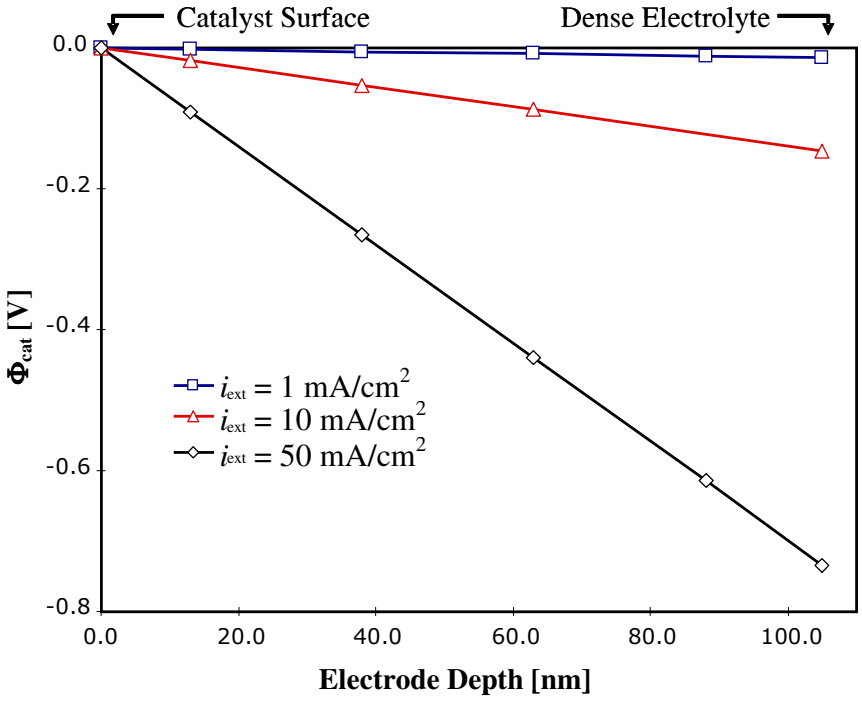

Figure 2.6. Predicted electric potential profile through the 110-nm thick ceria anode.

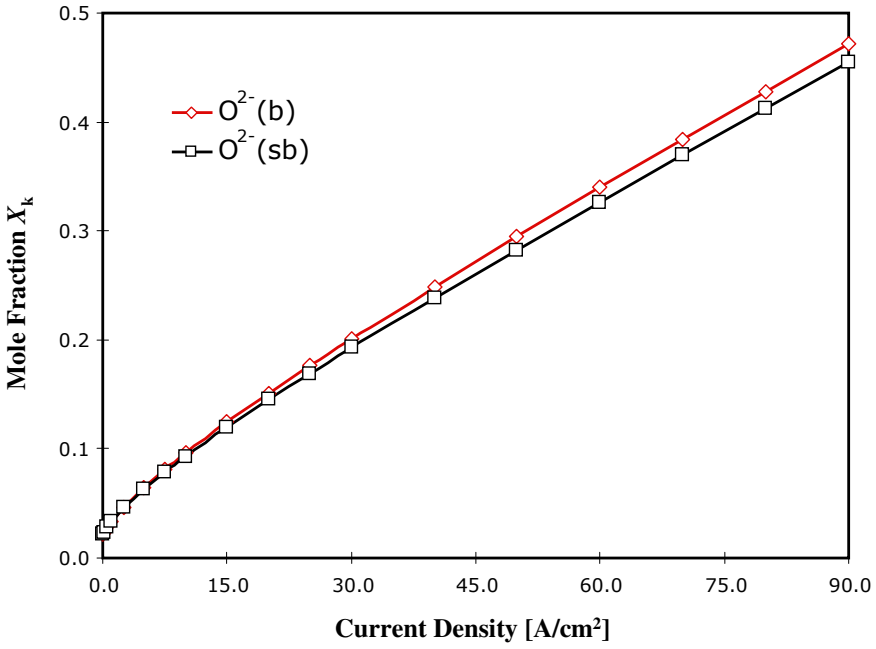

Figure 2.7. Oxide concentration versus current density for the Ceria/YSZ boundary (O^{2-}(b)) and for the ceria sub-surface (O^{2-}(sb))**.**

drop of only ~2% across the film thickness. The significant increase in $X_{O2-(sb)}$, coupled with the modest increase in $\theta_{OCe(s)}$ in figure 2.5 implies that the transfer of oxides between the surface and sub-surface (R. 2.9) has a sizable impact on the electrode polarization characteristics.

2.6 Conclusions

The preceding chapter describes the formulation for an isothermal, 1-D model of a thin-film MIEC SOFC electrode. The model incorporates gas diffusion to the electrode surface, heterogeneous surface chemistry, mixed electronic-ionic

conduction through the catalyst bulk, and charge-transfer kinetics at the catalyst/electrolyte boundary. The model assumes that, while the ceria has a capacitive oxygen storage capability, it does not store charge, but maintains charge neutrality outside of the charged double layer at the ceria/YSZ interface. Species in the ceria bulk and on the surface are thus defined in terms of a charge neutral Ce_2O_4 unit cell. Also, this assumption requires that the ceria electric potential is set as an algebraic variable such that the local current is always equal to the external current density i_{ext}.

To get a sense of the operating principles of the thin-film MIEC electrode, the simulation was run with a set of "baseline" kinetic, transport, and thermodynamic parameters. For T = 700 ˚C, P_{H2} = 0.65 atm, and P_{H2O} = 0.03 atm, results demonstrate the importance of charge transfer at the ceria/YSZ boundary, oxide exchange between the ceria surface and sub-surface, and the bulk resistance of the supporting electrolyte. The parameter space of this model will be more fully explored in chapter 4, in which the model results are fit against experimental polarization data for electrolyte-supported thin-film ceria anodes, presented in the upcoming chapter.

Chapter 3: Experimental Characterization of Thin-film, Undoped Ceria Electrodes

Previous experimental investigations into the role of ceria as an SOFC anode catalyst have primarily made use of composite anode systems that combine ceria with other materials, such as copper for current collection, YSZ for ion conduction, or reforming catalysts such as Pt or Ni [6, 25, 52-54]. Although ceria provides some electronic conductivity and modest catalytic activity, composite metals are often incorporated into the porous anodes to provide increased electronic conductivity and, as needed, higher reforming activity for carbonaceous fuels [6]. While these previous studies more accurately reflect the state-of-the-art in high-performance SOFCs, the multi-component porous electrodes in these studies complicate analysis – due to uncertainties in microstructural parameters such as porosity (φ_g), tortuosity (τ_g), and available surface area (a_{cat}) – and thereby make it extremely difficult to isolate the contributions of the ceria and to identify oxidation mechanisms or estimate rate parameters for fuel oxidation on ceria electrocatalysts.

As such, this study makes use of thin-film ceria anodes to isolate the contribution of ceria surface and bulk processes to electrochemical activity in SOFC anodes. This chapter describes the fabrication and testing of button-cell SOFC MEAs with thin-film ceria anodes. Ceria anodes are sputter-deposited onto 1.1 mm thick

supporting YSZ (8% by mole yttria) electrolytes with high surface-area LSM-YSZ porous cathodes. Varying sputtering conditions led to two distinct ceria-film morphologies, which had a significant impact on electrochemical performance. The cell is characterized electrochemically using linear sweep voltammetry (LSV) and electronic impedance spectroscopy (EIS) under a variety of gas environments for temperatures T from 650 to 850 °C. The analysis of these experiments provides a basis for developing a microkinetic mechanism for the oxidation of small fuel species on ceria anodes in chapter 4. The data presented in this chapter will be used to validate the model described in chapter 2. The mechanism in chapter 4 will provide a basis for future SOFC modeling efforts involving ceria-based composite anodes, forming a "core mechanism" for any oxidation mechanism for larger hydrocarbon species.

Additionally, this chapter will describe the use of *in situ* ambient-pressure x-ray photoelectron spectroscopy (AP-XPS) to characterize the distribution of valence states in operating ceria SOFC anodes. Initial polarization results produced profiles not readily explained by traditional electrochemical models, while impedance spectra demonstrated a highly non-linear dependence of process resistances on the partial pressure of H_2 (P_{H2}) [100]. Furthermore, previous measurements have shown significant non-ideal defect interactions that vary greatly with the degree of ceria reduction [38, 42, 93, 96]. It is thus of great interest to describe the distribution of ceria valence states during SOFC operation, both spatially and as a function of operating conditions. The experiments were performed at the Advanced Light Source

(ALS) at Lawrence Berkeley National Labs (LBNL). These results represent one of the first ever uses of *in situ* AP-XPS in an operating SOFC, and demonstrate that shifts in the ceria oxidation state correlate with changes in SOFC polarization characteristics, as discussed further below.

3.1 Previous Studies

As mentioned in chapter 1, ceria-based electrodes were first demonstrated in the 1960s for SOFC systems [42]. Since this time, a large number of studies have explored the use of ceria for a wide variety of SOFC applications, including dense electrolytes [19, 69, 101-110], dense anode catalyst interlayers [19, 22], porous single-component electrodes [42, 51, 56], and as an element in porous composite electrodes [6, 16, 27, 28, 54, 55]. The results show that ceria has significant activity for H_2 oxidation, but poor carbon-cracking activity. Furthermore, addition of CeO_{2-x} to composite systems has been shown to reduce polarization resistance, while increasing sulfur tolerance and resistance to carbon deposition [3, 6, 8, 23, 25, 53, 54, 111]. The review in chapter 1 provides a comprehensive discussion of previous experiments on ceria-based electrodes and contains an overview of previous thin-film electrode studies relevant to this work. The literature review here focuses on experiments that elucidate the properties of ceria, deposition techniques for oxide thin-films, and previous XPS results on ceria.

3.1.1 Characterization of Thin-film Ceria

Doping ceria with aliovalent anions creates a high concentration of oxygen ion vacancies, increasing the ionic conductivity at intermediate temperatures [45]. Ceria-based electrolytes have thus been extensively explored for intermediate-temperature (500 – 650 °C) SOFCs [21, 112]. While not directly related to the research proposed herein, the information from these studies can still be useful in understanding the role of ceria as an oxidation catalyst.

Important fundamental experiments were conducted by Anderson and coworkers, who explored the use of thin gadolinium-doped-ceria (GDC) electrolytes in SOFCs [46-50]. Their work also includes research on the electronic (σ_e) and ionic (σ_i) conductivity of undoped nanocrystalline CeO_2. In these experiments, thin CeO_2 films were fabricated on sapphire substrates and their conductivities σ were studied as a function of temperature, P_{O2}, and film grain size [46, 48-50]. The authors present a defect-based model of conduction in CeO_2 thin films that allows them to deconvolute the electronic and ionic conductivities (σ_{elec} and σ_{O2-}, respectively) from experimentally measured conductivities and explore the dependence of σ on P_{O2} [46-49]. Results confirm the dependence of σ_{elec} on P_{O2} ($\sigma_{elec} \propto P_{O_2}^{-1/6}$) predicted by their defect model and other previous studies [38, 46, 47], and demonstrate that previous measured deviations from this dependence are likely due to extrinsic defects associated with dopants and/or impurities in the sample. Most significantly, experimental results show a significant influence of microstructure on electrical conductivity. The authors conclude that the enthalpy of formation for oxide

vacancies decreases with grain size δ_g, particularly below δ_g = 100 nm. The resulting increase in vacancy concentration with decreasing grain size leads to a significant increase in conductivity with decreasing grain size, as described by the defect model [46-49].

This last conclusion confirms earlier preliminary findings by Chiang and co-workers on fully dense CeO_{2-x} with nanometer-scaled grain size δ_g ~ 10 nm [113]. Analysis of impedance spectra reveals separate arcs for bulk-film and grain-boundary contributions to the electronic conductivity. By comparing nanocrystalline CeO_{2-x} results to those with δ_g = 5 μm, the authors demonstrate that bulk electronic conductivity increases by over 4 orders of magnitude, grain boundary resistance is negligible, and the heat of reduction decreases by half in the nanocrystalline samples. The authors theorize that the defect thermodynamics of the ceria surfaces/interfaces are observed in the bulk of the nanocrystalline samples, due to the high specific surface area, and that the grain-boundary resistance is due to size-dependent segregation effects. The authors also note that similar behavior is expected in other ceria geometries, including "very thin films" [113].

3.1.2 Fabrication of Oxide Thin-films

Previous thin-film studies have utilized a variety of materials and fabrication techniques. Common deposition techniques include, but are not limited to: RF magnetron sputtering [57, 69, 110, 114-116], chemical vapor deposition (CVD) [117], electron beam (e-beam) evaporation [114], and pulsed laser deposition (PLD)

[114]. Brosha, et al compare the quality of oxide thin films ($La_{1-x}Sr_xCrO_3$) deposited by three separate pressure vapor deposition (PVD) techniques – sputtering, e-beam, and PLD [114]. While their results focus primarily on the high-temperature sintering and densification of lanthanum chromite, the results show that RF magnetron sputtering gave the highest quality oxide films, of the techniques studied. Films deposited by sputtering were mechanically and thermally stable, relatively dense, free of pinholes, and could be deposited at low temperatures, permitting the use of simple lift-off masking materials such as Kapton tape. While e-beam was successful in depositing thin oxide films, film stoichiometry was very sensitive to the deposition temperature [114]. Jiang and coworkers obtained a similar result for the chemical vapor deposition of samaria-doped ceria (SDC) films – film stoichiometry and surface uniformity depended on precise control of the deposition temperature [117].

Baertsch and coworkers characterized the mechanical stability of free-standing oxide thin films, deposited via evaporation and sputtering [69]. Their analysis of mechanical stress in thin films concluded that sputtering led to compressive bi-axial stresses in films, which beneficially compensated for the tensile stresses introduced during annealing. The authors propose that the compressive stresses account for the superior adhesion achieved by sputtering deposition relative to evaporative deposition, which introduces tensile stresses in deposited films.

Furthermore, studies have shown that gas pressure, composition, and temperature, as well as 'throw distance' from target to substrate can control the

deposition rate and characteristics of the deposited film [57, 69, 110, 115, 116]. In general, dense and stable oxide films of sub-micron thickness have resulted from a process pressure of 5-20 mTorr, a throw distance of 40-50 mm, and P_{O2} of ~ 5-10% [69, 110, 115, 116]. The superior mechanical stability of deposited oxide films and the ability to fine-tune film properties according to deposition conditions make RF magnetron sputtering an ideal deposition technique for films in this study.

The RF sputtering process for ceria deposition on a YSZ substrate is shown schematically in figure 3.1, along with a photo of the deposition chamber of the Lesker PVD 75 sputtering unit used in this study. An RF power source introduces a bias between the target and substrate, which are held under vacuum, creating an ion plasma. Ions are accelerated toward the power source and strike the target, transferring momentum to the target and ejecting target particles upon impact. The

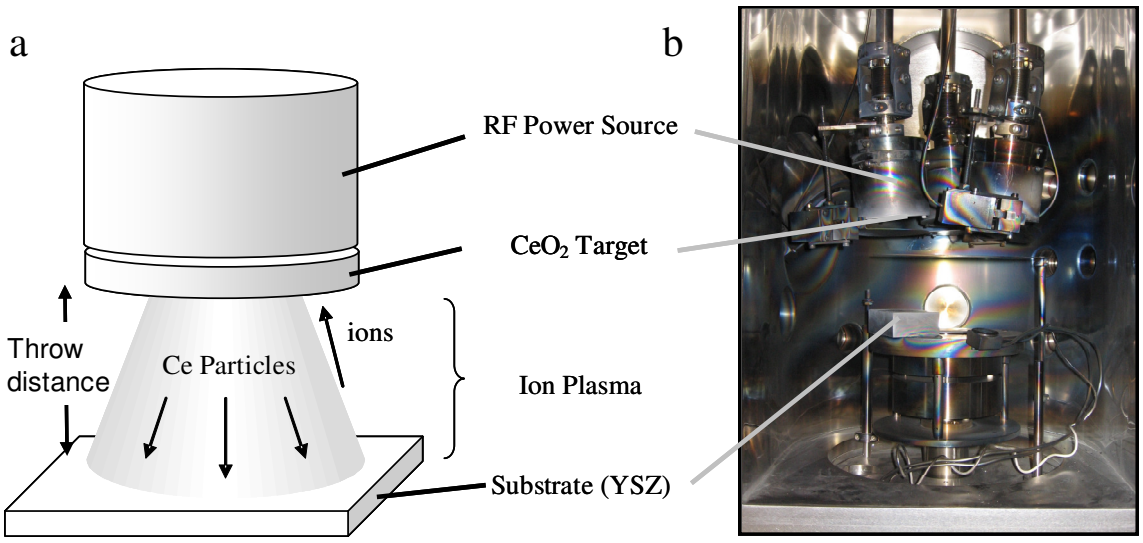

Figure 3.1. a) Schematic representation of the sputtering process; b) Lesker PVD 75 sputter-deposition chamber used in this study

very low pressure (base pressure is ~10^{-8} Torr) increases the average path length of these displaced particles, allowing them to reach the substrate. The displaced particles radiate out from the target surface to coat the substrate and surrounding surfaces. Sputtering is thus a rather inefficient deposition technique, with film growth rates on the order of ~1000 Å/hr [114]. While this growth rate makes sputtering unsuitable for batch-processing, it allows for a high degree of control over film thickness, and micron-thick films can be deposited over the course of several hours. The specific deposition conditions utilized in this study are described further below.

In ceria thin-films, the relatively low electronic conductivity and small film thickness lead to high resistance to lateral conduction of electronic charge. In working SOFC electrodes this requires a unique method of current collection. The current collector must be distributed over the entire electrode surface, to minimize lateral charge conduction. However, the current collector must also be permeable to gaseous reactants and products, allowing access to the electrode surface. Previous thin-film studies have primarily used porous metallic pastes [56], or a combination of metallic gauze meshes pressed onto screen-printed current collectors [118] for effective current collection This study utilizes an inert gold current collector, with gold mesh pressed onto a layer of porous gold paste, the fabrication of which is described below.

3.1.3 XPS Quantification of CeO_{2-x} Oxidation States

In situ synchrotron-based XPS is attractive for coupling with electrochemical studies because of its capability for surface chemical measurements in the presence of gases at significant pressures (several Torr). So-called AP-XPS has been recently applied to *in situ* characterization of catalytic systems at elevated temperatures [119], and this study on ambient-pressure XPS on a high-temperature electrochemical system at elevated temperatures is a unique extension of such studies. XPS can be used to determine electron binding energy (B.E.) from peaks in the XPS spectrum, which can be assigned to specific atoms based on their core-level binding energies and to specific chemical bonding orbitals based on "chemical shifts" of the core-level peak. For electrochemical systems, it is also possible to measure relative surface electric potentials by observing a constant shift of XPS spectral peaks resulting from the contribution of the surface potential. Because photoelectrons from synchrotron X-ray source emerge from surface and near surface layers only a few nm thick, the XPS measurements are capturing the composition very near the surface of the material.

In the current study, ten selected peaks from the Ce*3d* spectrum are analyzed in the range of binding energies (B. E.) 870 eV $\leq$ B. E. $\leq$ 930 eV to determine the degree of reduction in thin-film CeO_{2-x} electrodes, as is typical for XPS studies of ceria [120]. Burroughs was the first to describe this spectrum in detail, and introduced the standard nomenclature used to label the peaks of the Ce*3d* spectra [120, 121]. There is some disagreement as to the exact theoretical model of the CeO_2

ground state related to the possibility of mixed valence – both Ce^{4+} and Ce^{3+} present – in fully oxidized CeO_2, although Ce^{4+} is still generally used to describe the CeO_2 valence [120]. Despite this uncertainty, there is general agreement on the shape and causes of features seen in the Ce*3d* spectra. As summarized by Conesa et al, the features are due to the convolution of spin-orbital splitting [120]. This splitting leads to a pair of peaks for each possible electronic state. In Ce^{4+}, three possible electronic states lead to three pairs of peaks, generally referred to as $v''' - u'''$, $v'' - u''$, and $v - u$, as labeled in the sample spectra of figure 3.2. In the reduced cation (Ce^{3+}), there are just two possible electronic states, leading to the pairs $v' - u'$ and $v_0 - u_0$, also

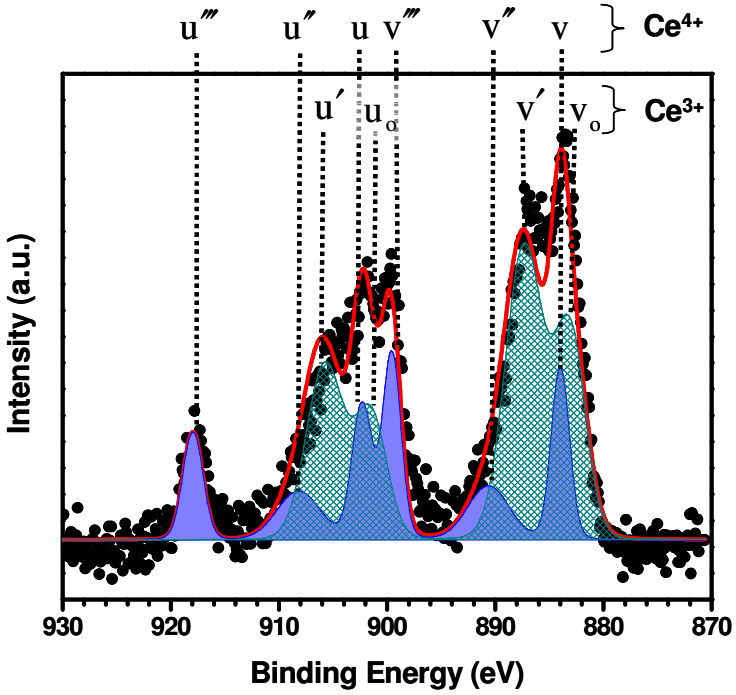

Figure 3.2. Sample XPS spectra for Ce*3d*, with labeled Ce^{4+} and Ce^{3+} peaks. Filled symbols are experimentally measured data from ALS, the solid line is the least-squares fit to the data, the filled spectra is the Ce^{4+} reference spectra, and the cross-hatch is the self-generated Ce^{3+} spectra.

labeled in figure 3.2. The fractions of Ce^{3+} and Ce^{4+} contained at the sample surface and near-surface are calculated as the percentages of the total integrated spectrum intensity attributed to each of the two oxidation states.

As illustrated in figure 3.2, the analysis of Ce*3d* spectra is complicated by the significant overlap in binding energies of the various peaks mentioned above. Among the ten peaks mentioned, only the u‴ peak, B.E. ~ 916.5 eV, is significantlyisolated fromall other peaks. As such, the u‴ peak is frequently used to quantify the oxidation state of the ceria sample [120, 122-127]. Early efforts have utilized the fact that the u‴ peak constitutes 17% of the total integrated spectrum intensity for pure unreduced CeO_2 to calculate the fraction of Ce^{4+} in the spectrum [120, 127]. However, later studies by Romeo et al. showed that reduction of the ceria increases the intensity of the v′ and u′ peaks long before the u‴ reduces in intensity, thus limiting the accuracy of this approach [126]. Other quantification methods include the decomposition of the spectrum into individual peaks via least squares fitting [126] and the use of statistical methods such as factor analysis (FA) [123-125].

FA analysis indicates that a linear combination of two fixed states (corresponding to the two oxidation states) is sufficient to reproduce the range of Ce*3d* spectra obtained [120]. Based on this conclusion, analysis of XPS spectra presented in this study follows the work of Appel and coworkers, who subtract the Ce^{4+} reference spectra (obtained from pure CeO_2 samples) from the Ce*3d* spectra such that the u‴ peak is eliminated entirely. In this manner, the Ce^{3+} and Ce^{4+} signal

fractions of the total integrated intensity are obtained [122]. It is noted that this approach neglects the observed discrepancies between degree of oxidation and the u‴ intensity noted above, which FA has attributed to Ce^{3+} "satellite peaks" that overlap with u‴ [120]. Nonetheless, results have demonstrated that this linear approximation provides a reasonably accurate correlation [128].

3.2 Electrochemical Characterization of CeO_{2-x} Thin Film Anodes

3.2.1 Experimental Details

3.2.1.1 Button-cell Fabrication

Figure 3.3 depicts the single-cell SOFC samples fabricated for this study. Single-cell membrane electrode assemblies (MEAs) are supported on a fully dense, poly-crystalline (PC) YSZ electrolyte. While tests were also conducted on single-crystal (SC) YSZ electrolytes, the data reported herein focus on results for PC-YSZ samples. PC-YSZ discs are fabricated using a static cold-press process. 3.0 g of 8-YSZ powder (purchased from Tosoh) is held at 150 MPa inside a cylindrical die for 10 minutes, and then sintered in air according to the following schedule: heat from 25 ºC to 1450 ºC at 0.5 ºC/min, hold at 1450 ºC for 3 hours, and then cool to 25 ºC at 1 ºC/min. This sintering process fully densifies the PC-YSZ discs (as revealed by SEM images), which are 1.1 mm thick and have a diameter of 23 mm.

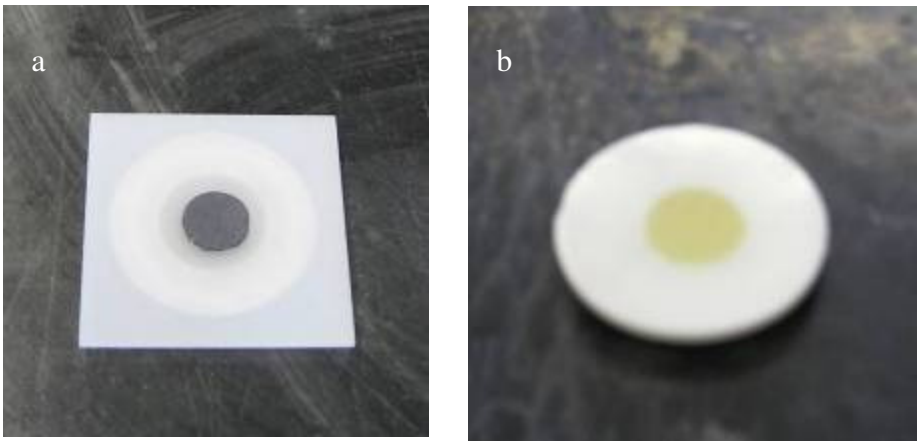

Figure 3.3. View of fabricated SOFC MEAs. a) LSM/YSZ cathode on SC-YSZ, b) CeO_2 anode, 2.8 μm thick, on PC-YSZ.

The electrolyte supports a high-surface area porous cathode, which is slurry-coated as a 50 μm thick layer with a circular area, according to methods described elsewhere [129]. The cathode consists of a 50/50% mixture of La0.85Sr0.15MnO3-δ (LSM) and YSZ (8% by mole yttria). The cathodes are sintered in air with the following schedule: heat from 25 ºC to 400 ºC at 0.3 ºC/min.; hold at 400 ºC for 1 hour; heat to 1300 ºC at 3 ºC/min; hold at 1300 ºC for 1 hour; cool to 25 ºC at 3 ºC/min. Figure 3.3a depicts a sintered LSM-YSZ cathode supported on a SC-YSZ electrolyte.

Thin-film CeO_2 anodes are fabricated via RF magnetron sputtering in a PVD 75 sputtering unit from the Kurt J. Lesker Corporation. To deposit the anode, a Kapton tape mask is placed on the YSZ disc, such that the anode/electrolyte interface area matches with the cathode/electrolyte interface area. Substrates are placed in the PVD unit, which is sealed and pumped down overnight to a base pressure of ~10^{-8}

Torr. After pump-down, the process gas (5% O_2, Ar balance) is introduced at a pressure of 5 mTorr. RF power is gradually supplied to the chamber, up to 150 W. The substrate and target shutters are left closed for a 1 hour "pre-sputter," to remove any possible contaminants from the target surface. Finally, the shutters are opened for a specified time (< 4 h) depending on desired film thickness and on deposition rate. Figure 3.3b depicts a CeO_{2-x} anode supported by a PC-YSZ electrolyte.

Varying deposition conditions led to two distinct film morphologies. Sample scanning electron microscope (SEM) images of these two morphologies for as-deposited films are displayed in figure 3.4. SEM images of thicker films (with thicknesses $\delta_{film} > 1$ μm) show columnar growth structure, which is indicative of mechanical stability, with column widths ranging from 100-300 nm. Thinner films replicate the grain-boundary structure of the YSZ substrate, as shown in figures 3.4b and 3.4c. As thickness increases, so do the column width and surface roughness, with the thickest films (figure 3.4a) no longer replicating the YSZ grain-boundary structure. The CeO_{2-x} films were characterized as-deposited, after annealing in air at T = 800 °C, and after electrochemical testing to determine the impact of sample history, with results presented further below.

3.2.1.2 Instrumentation and Measurement

The MEAs tested in this study are instrumented with a K-type thermocouple pasted onto the electrolyte with a high temperature zirconia-based ceramic paste, near

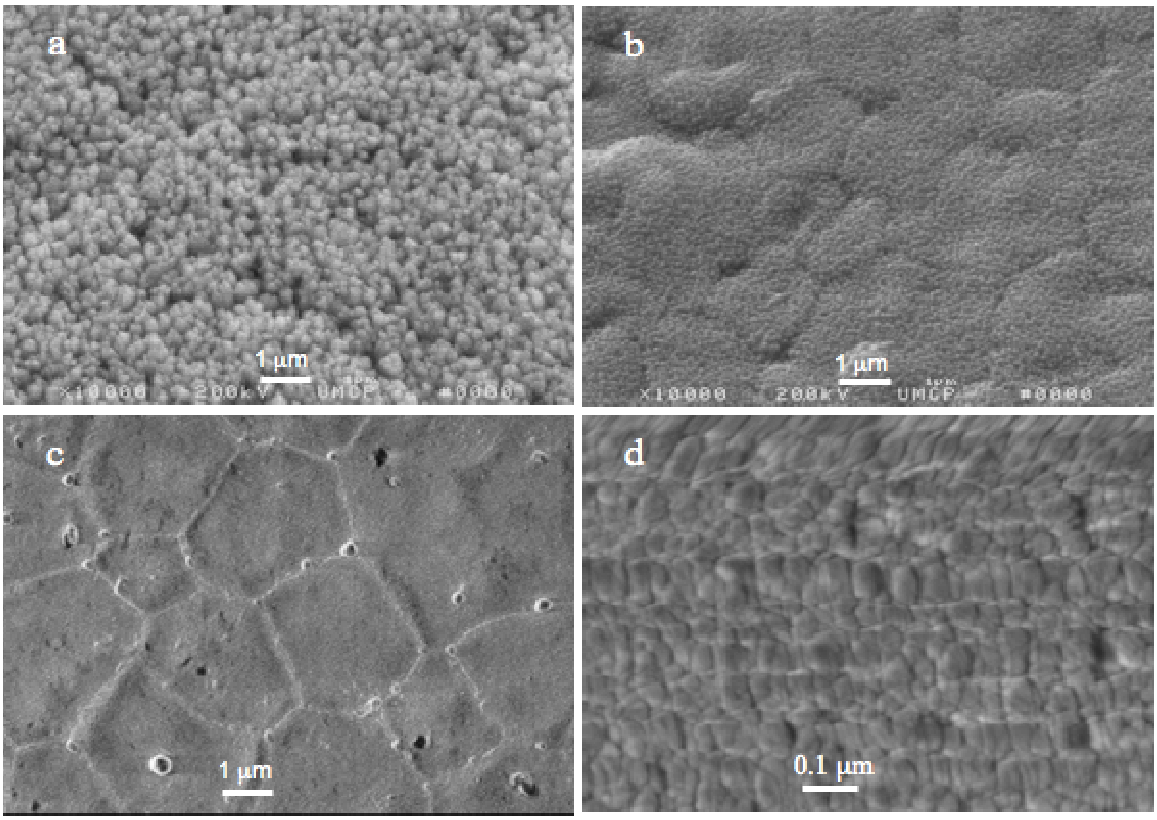

Figure 3.4. Sample SEM of thin-film CeO_{2-x} anodes. a) and b) are separate nano-porous films; c) and d) are a single dense film deposited. Deposition times (t_d) and film thicknesses (δ_{film}) were: a) t_d = 120 min., δ_{film} = 2.8 µm; b) t_d = 60 min., δ_{film} = 1.6 µm; c) and d) t_d = 30 min., δ_{film} = 250 nm.

the cathode. Electrical leads are attached to the electrodes using gauze mesh and metallic pastes. The anode leads, mesh, and paste are Au (wire lead: 0.25 mm diameter, 99.9%; gauze: 52 mesh, 99.9%, both from Alfa Aesar), while the cathode uses Pt (wire lead: 0.25 mm, 99.99%, gauze: 52 mesh, 99.9%, both from Sigma-Aldrich). The MEAs are attached to an alumina tube (15.9 mm ID) with a high temperature zirconia-based ceramic paste. Concentric alumina feed tubes (3.2 mm ID) are passed down the center of the outer tubes such that the feed exit is 5.0 mm

from the outer MEA surface, to provide stagnation flows impinging on both electrodes. The entire assembly is placed inside a temperature-controlled furnace, as pictured in figure 3.5. Electronic mass flow (Brooks 5850E) controls the flow rates of fuel and oxidizer streams. Data from mass flow controllers and thermocouples are collected by a National Instruments SCXI data acquisition system.

The cell is heated at a rate of 1 ºC/min to the cell operating temperature (T between 650-850 ºC) under 30 sccm Argon and air flows on the anode and cathode sides, respectively. After heating, 210 sccm of fuel mixtures containing varying fuel partial pressures with balance Ar are sent either directly to the SOFC anode or through the temperature-controlled humidifier (from Fuel Cell Technologies, Inc.), as pictured in figure 3.5.

Electrochemical tests are carried out with electrochemical work stations (potentiostat/ frequency-response analyzer) from Gamry Instruments and Autolab/Eco Chemie. Previous testing of LSM/YSZ cathodes fabricated at UMD has indicated that these cathodes exhibit improved performance after a short period of polarization. Therefore, before electrochemical measurement at a given condition, a moderate "conditioning current" is passed through the cell until successive polarization curves converge. After conditioning, electrochemical tests are carried out. LSV is used to measure the steady-state polarization response of the cell, while EIS probes the transient cell response to a sinusoidal perturbation superimposed on a constant signal (either current or cell voltage).

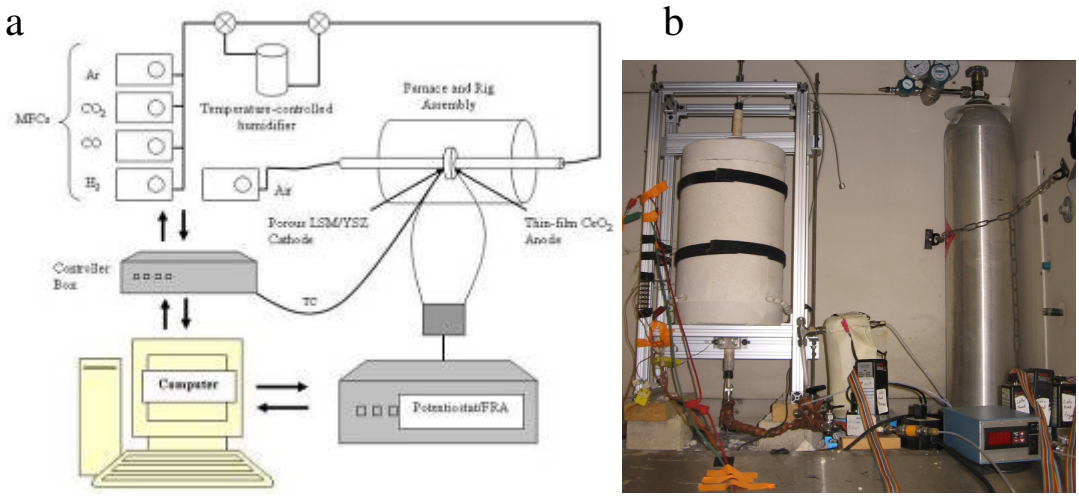

Figure 3.5. a) Schematic representation and b) photograph of experimental setup.

3.2.2 Results and Discussion

3.2.2.1 Structural Characterization of CeO_{2-x} Thin Film Anodes

Initial films were sputter-deposited with a target-to-substrate throw distance of 47 mm and a process pressure of 15 mTorr, unless otherwise noted. Deposition times t_d ranged from 30 min. to 4 hours, with film thicknesses δ_{film} ranging from 1-4.5 μm. As shown in figures 3.4a and 3.4b, these initial films show increasing surface roughness with increasing thickness, with nanometer-scale pores forming at the boundaries of the columnar growth structures. SEM images of films post-electrochemical testing show an even greater degree of "nanoporosity." This film morphology complicates analysis, due to uncertainties in catalyst surface area, porosity for gas transport, and oxide ion conduction lengths in the ceria bulk. As

discussed below, electrochemical results for these films (henceforth referred to as "nanoporous" films) show strong sensitivity to surface morphology, with complex relationships to film thickness and low repeatability for cells fabricated under nominally identical conditions. Characterization of these nanoporous films was carried out by coworkers at UMD. SEM was used to study the morphology/ microstructure of the films. SEM images of nanoporous films were acquired using a Hitachi S-3400. X-ray diffraction (XRD) was used to assess the structure and phase purity of anode films before and after electrochemical studies. X-ray diffractograms were recorded using the Bruker D8 Advanced X-ray diffractometer with Cu K_α-radiation in the range of 2θ from 20-80°. Figures 3.6 – 3.10 give an overview of the structural analysis.

Figure 3.6 shows the top-view SEM data for four nanoporous films deposited on glass substrates with varying throw distance and gas pressure. As in figure 3.4, images reveal significant surface roughness, associated with the growth of columnar structures. This is confirmed by cross-section SEM images (figure 3.10). Film thicknesses in Table 3.1 reveal that the roughness is correlated with thicker films, or possibly higher deposition rates. The increase in film roughness with decreasing throw distance is possibly an effect of film growth with thickness or an effect of substrate heating (due to higher deposition rates), which increases mobility of the deposited film, enabling growth of larger columnar structures. Furthermore, increasing the process pressure also leads to significantly slower deposition rates and thus smoother films, as in figure 3.6d and table 3.1.

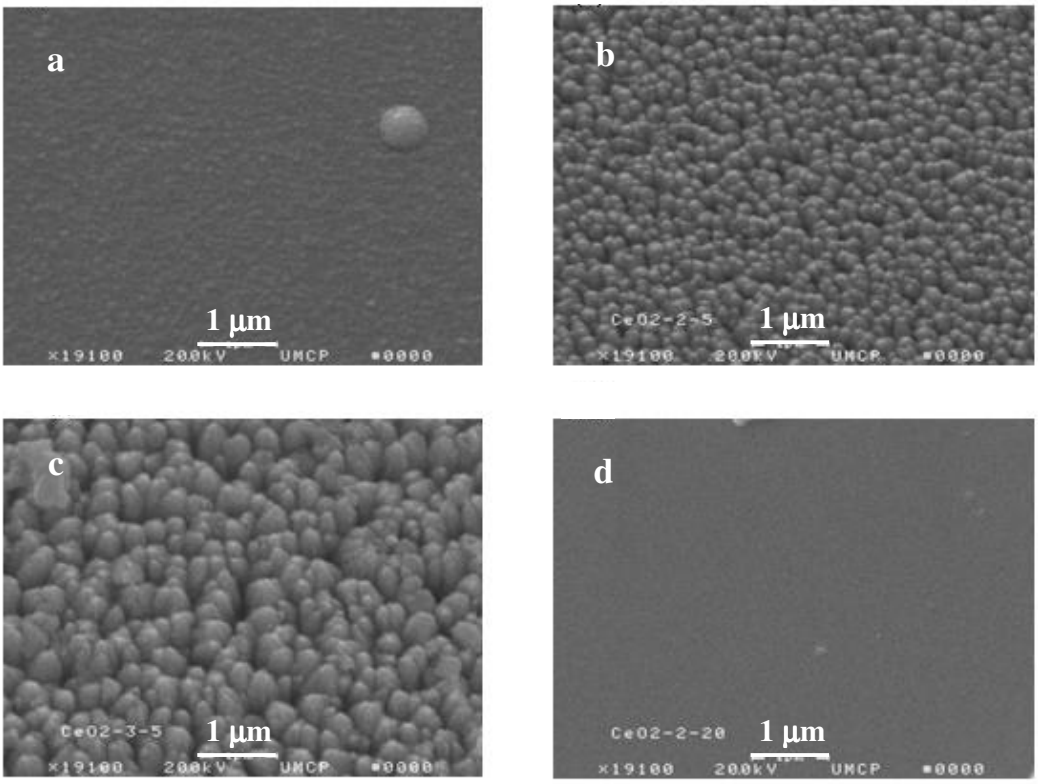

Figure 3.6. SEM of CeO_2 films deposited on glass substrates at a process pressure of 5 mTorr and a throw distance of a) 11 cm, b) 8.5 cm, c) 6 cm; d) at a process pressure of 20 mTorr and a throw distance of 8.5 cm

Table 3.1. Comparison of film thickness for different deposition conditions, as determined by SEM. Deposition time = 165 min.

Throw Distance [cm]	Process gas Pressure [mTorr]	Film Thickness [µm]
11	**5**	**0.4**
8.5	**5**	**2**
6	**5**	**5**
8.5	**20**	**0.15**

Figure 3.7 shows XRD data for CeO_2 films deposited on glass, δ_{film} = 2 and 5 μm. Results confirm the presence of (111) and (222) crystal orientations of CeO_2. While XRD data was not affected by film thickness, comparison with data for CeO_2 on SC-YSZ (figure 3.9a), reveals a significant impact of substrate on crystallographic orientation. This effect is also illustrated in the SEM images of figure 3.8, which depict 2.5 μm films deposited simultaneously on glass and PC-YSZ substrates. The results show the significantly rougher PC-YSZ substrate leads to increased disorder and surface roughness in the films, with clusters of columnar structures forming larger structures (figure 3.8d). The images confirm that CeO_2 films on PC-YSZ substrates mimic the underlying grain boundary structure, as shown in figure 3.8c.

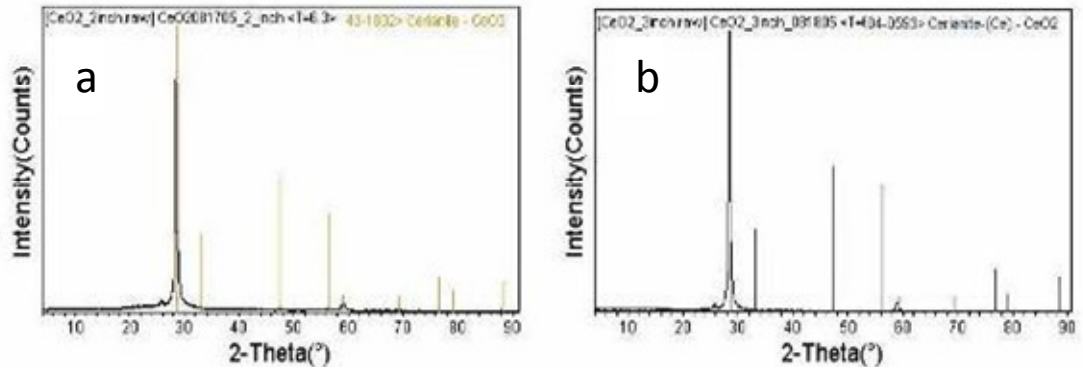

Figure 3.7. XRD data for CeO_2 films on glass substrates with varying film thickness. a) 2 μm b) 5 μm. The peak at (2 – θ) = 27° represents an as-yet-unidentified impurity phase.

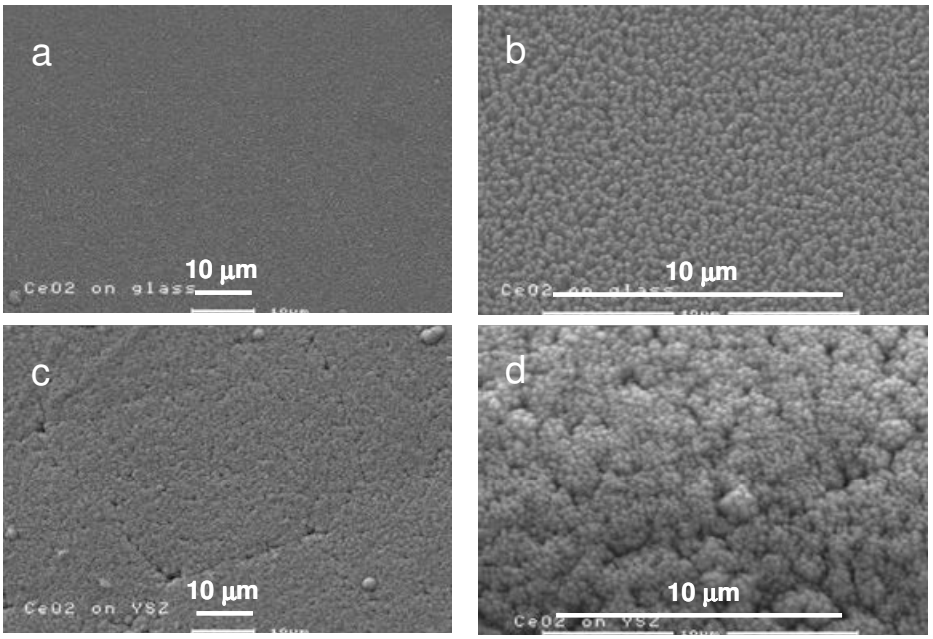

Figure 3.8. SEM images of 2.5 µm CeO_2 films on varying substrates, deposited in the same batch. Substrate: a) and b) glass; c) and d) PC-YSZ. Images reveal the impact of underlying substrate roughness and grain-boundary structure on films.

To assess the impact of annealing at relevant SOFC temperatures, films were deposited on PC-YSZ and SC-YSZ substrates and annealed in air at 800 °C. SEM images taken before and after annealing reveal growth in the average grain size for columnar structures with annealing, as shown for SC-YSZ substrate in figures 3.9a-b. The XRD data in figures 3.9c-d, meanwhile, reveal significant crystallographic reorientation with annealing.

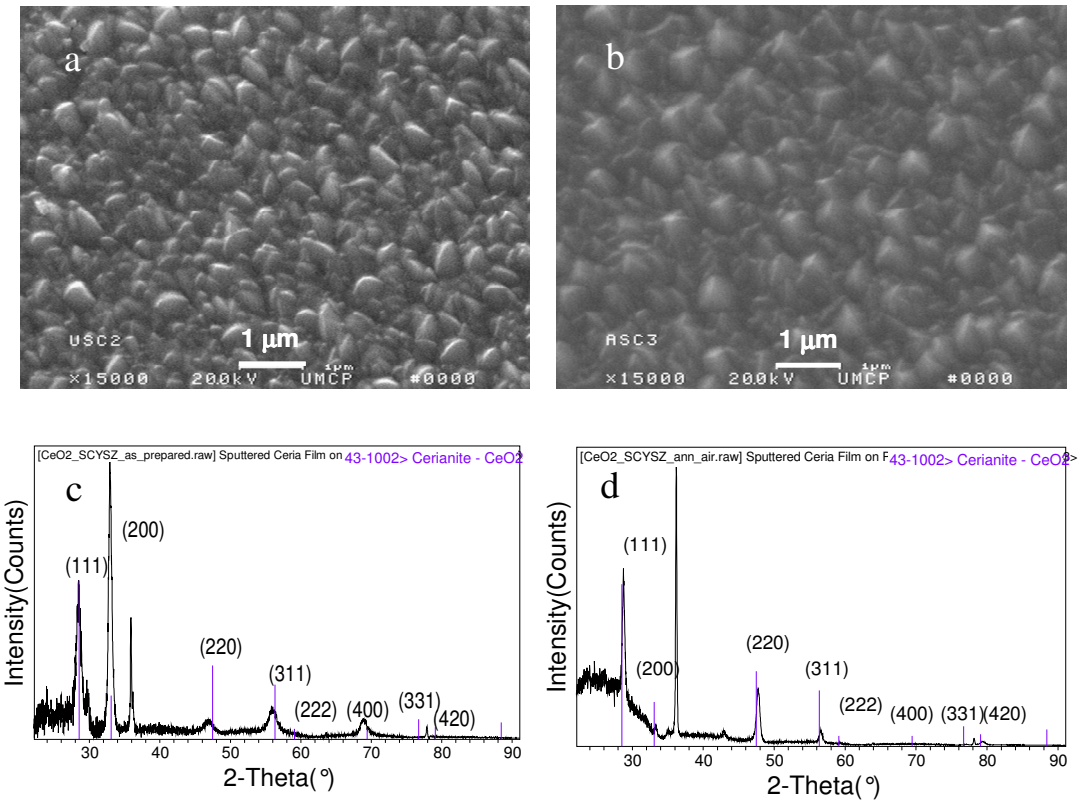

Figure 3.9. Effect of annealing in air at 800 °C on CeO_2 deposited on a SC-YSZ substrate. a) and c) SEM and XRD data for pre-annealed film. b) and d) SEM and XRD data for post-annealed film.

Finally, figure 3.10 shows cross-section SEM images for CeO_2 films on SC-YSZ, before and after electrochemical testing. Pre-test images reveal a relatively dense electrode, free of pinholes, while post-electrochemistry images depict the formation of significant porosity throughout the anode depth. Similar results were obtained for PC-YSZ substrates. As with the columnar structures in general, these nano-pores are most likely beneficial to the catalytic activity and overall performance of these SOFCs, by increasing the total catalyst surface and allowing gas-phase diffusion toward the electrode/electrolyte interface. However, such improvements in

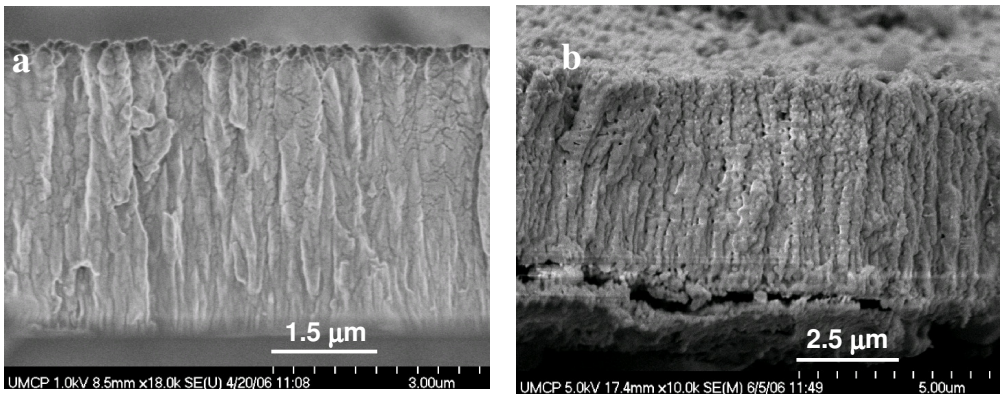

Figure 3.10. Cross-section SEM images for CeO_2 films deposited on SC-YSZ. a) pre-electrochemistry, and b) post-electrochemistry. Post-electrochemical images reveal the formation of visible nano-scale pores in the CeO_2 films.

electrochemical activity negate many of the benefits of thin-film anodes by introducing significant ambiguity to the structural and mechanistic description of these anodes in the SOFC simulations described in the previous chapter.

To more fully leverage the promise of the idealized thin-film geometry, deposition parameters were varied in order to deposit smoother, denser films as suggested by the trends in figure 3.6 and table 3.1. Several films were deposited with a process pressure of 15 mTorr. However, as illustrated in figure 3.11, increasing the process pressure increased the effective vapor pressure in the film bulk, introducing an even greater degree of porosity to the films. Films showed no evidence of columnar growth structure (figure 3.11c). Instead, the major structural elements were irregular-shaped particles with a diameter of approximately 20 nm (figure 3.11a).

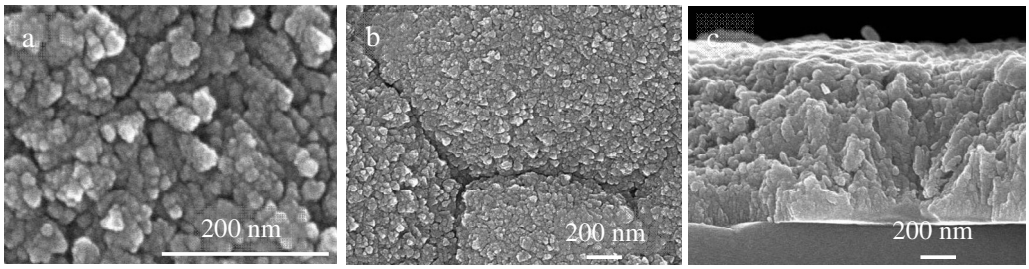

Figure 3.11. SEM of as-deposited CeO_2 films with process pressure = 15 mTorr. Images reveal increased porosity without columnar growth for the increased process pressure.

Later films were deposited with a throw distance of 65 mm, resulting in lower deposition rates. The time of deposition t_d ranged from 15-30 min., with δ_{film} ranging from 110-250 nm. SEM images of these films (henceforth referred to as "dense" films) are shown in figures 3.6c-d and 3.12. SEM images for dense films are acquired with a Hitachi SU-70 Field Emission (FE)-SEM, at the University of Maryland's NISP lab, which is equipped with the Bruker XFlash Silicon Drift Detector for energy dispersive X-ray spectroscopy (EDS). This instrument is able to obtain high-resolution images for secondary electrons with a decelerated electron beam (1.0 kV), which reduces the charging effect on nonconductive samples. CeO_2 films could thus be imaged without the conductive Pt-Au coating required for Hitachi S-3400. Elimination of the coating allows for direct observation of the nano-scale surface structures, as well as elemental analysis with EDS. It is noted, however, that the instrument does not eliminate surface charging entirely, as seen in the image distortion/drift in figures 3.6c-d and 3.12

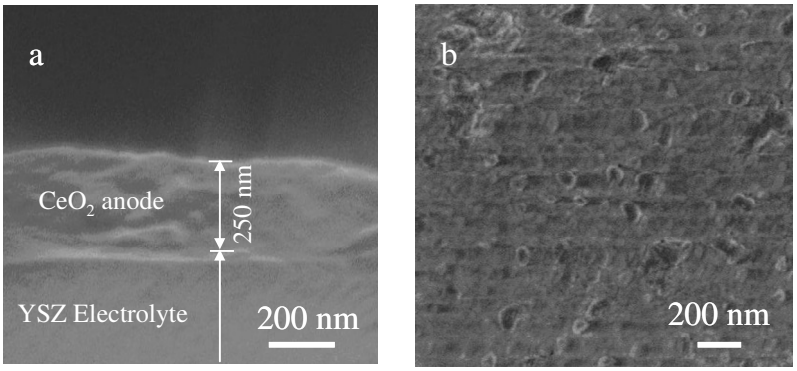

Figure 3.12. SEM of dense CeO_2 films on SC-YSZ with t_d = 30 min. a) cross-section of fracture surface, δ_{film} = 250 nm; b) top-down view of film on SC-YSZ substrate after electrochemical testing, revealing that the dense nature of film is intact.

As shown in figures 3.6c-d, dense films replicate the underlying substrate grain-boundaries, but show smoother surfaces. Images reveal that the average ceria feature size is ~ 40 nm, compared to 100-300 nm for the nanoporous films. Furthermore, images reveal a denser film (figures 3.6d and 3.12a), with no apparent pore space at the grain boundaries. Post-electrochemical SEM images (as in figure 3.12b) reveal that the dense structure is maintained during electrochemical testing.

3.2.2.2 Electrochemical Characterization of Nanoporous Films

Polarization and EIS experiments and analysis for H_2 and CO electrochemical oxidation on the nanoporous ceria anodes, with δ_{film} from 1.0 to 4.5 μm were carried out at temperatures between 650 and 850 ˚C. Figure 3.13 shows full cell polarization results for H_2 and CO on nanoporous ceria anodes of varying thickness. Figure 3.13a

shows data for H_2 and CO on a 4.5 μm thick ceria film. Results show mostly linear polarization curves, with similar total resistances (R_{tot}) for both H_2 and CO. For H_2 oxidation, comparison of polarization data on the 4.5 μm ceria anode to that on two separate 2.8 μm films (figure 3.13b) reveals several stark contrasts. Maximum current densities are higher on the thinner film, but LSV profiles are no longer linear, with R_{tot} decreasing with increasing current density for one film (labeled "cell 1" in figure 3.13b). For the other thin-film anode ("cell 2"), apparent transport limitations, even for relatively high fuel concentrations (i.e., P_{H2} = 0.32 atm), lower the maximum current density. It is unclear what causes the variation between cells with identical fabrication conditions. Furthermore, results show significant sensitivity to fuel composition, with maximum currents depending non-linearly on P_{H2}.

Comparison of P_{H2} = 0.32 atm data for figure 3.13a and cell 2 in figure 3.13b reveals the complicated nature of these nanoporous films. The thinner film has a shorter conduction length for oxide ions through the bulk of the ceria film, resulting in lower resistance to ionic conduction (R_{ion}). This may account for the lower R_{tot} in the 2.8 μm films near OCV. Apparent concentration limitations, meanwhile, can be due either to reduced catalytic surface area with decreasing film roughness (which drops with film thickness, as illustrated in figures 3.4 and 3.6) and/or to higher resistance to diffusion in the nano-scale pores. The complex coupling of these phenomena and the inability to directly measure their contributions to cell overpotentials make it difficult to analyze polarization data in a quantitative manner on these films.

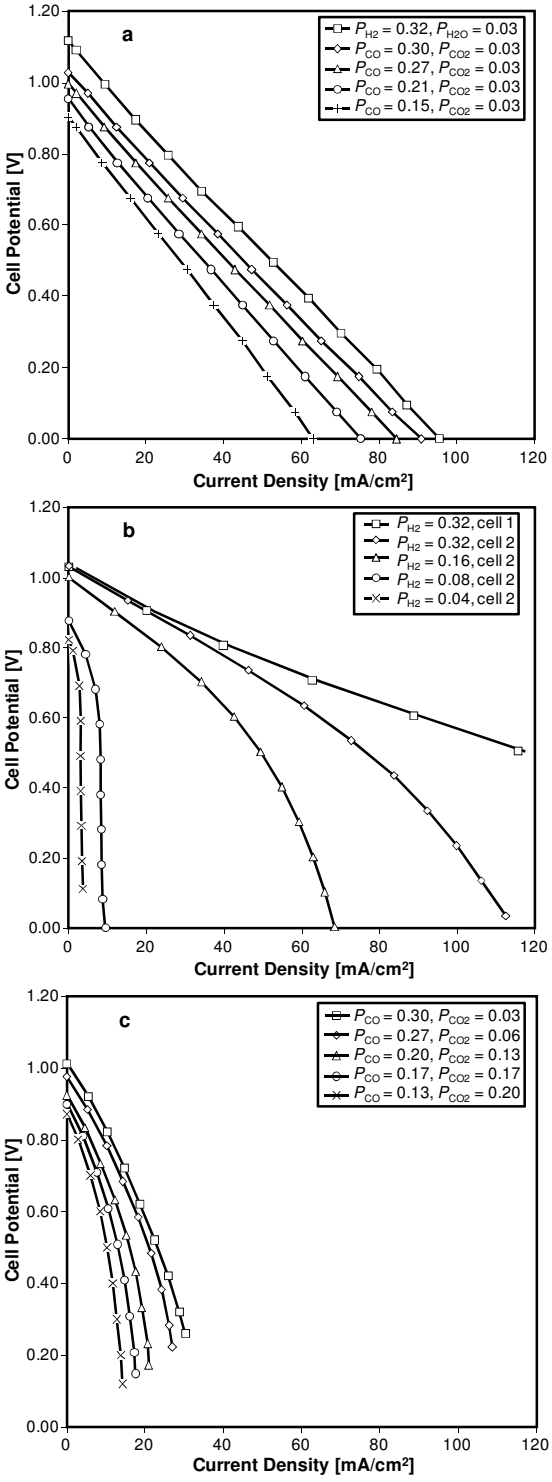

Figure 3.13. Polarization curves for oxidation of CO and H2 on "nanoporous" ceria anodes. T = 850 °C, pressures in atm. a) CO and H_2 on a 4.5 µm thick anode; b) H_2 oxidation on two separate 2.8 µm anodes; c) CO oxidation on a 1.0 µm thick anode.

CO polarization data on thinner anode films (1.0 μm thick in figure 3.13c) show nonlinear LSV profiles. For these thin films, the effect of CO concentration on the polarization curves appears to be both a thermodynamic shift in the open circuit potential (OCV) and an almost linear decrease in the apparent limiting current. Polarization curves for H_2 electrochemical oxidation for these thinner anode films indicates significantly higher current densities, and in general H_2 electrochemical oxidation polarization curves do not depend as strongly on film thickness as do the CO polarization curves.

To further analyze the processes contributing to cell overpotentials, impedance spectra were taken for the full range of temperatures and fuel compositions studied. While EIS results showed little sensitivity to P_{CO} (not shown), results were sensitive to T and P_{H2}. Nyquist plots reveal two dominant arcs – a smaller high frequency arc and a larger low frequency arc. The low frequency arc likely incorporates a small contribution from the cathode, based on previously published cathode characterization data [9]. All the same, the primary resistance of this arc is likely controlled by anode processes because of its strong dependence on P_{H2}, particularly at low P_{H2}, where this arc becomes dominant and develops an inductive low-frequency tail. Representative EIS data at 700 ˚C on a 2.8 μm anode are shown in figure 3.14.

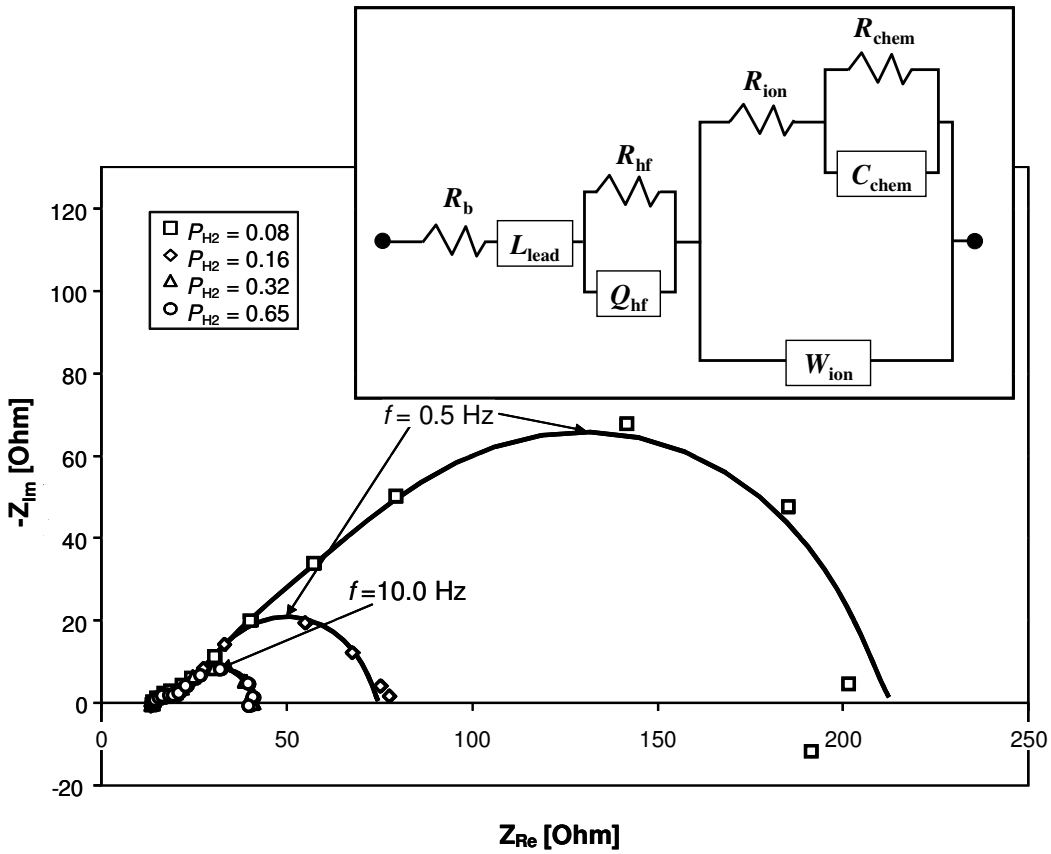

Figure 3.14. Impedance with equivalent circuit modeling for nanoporous 2.8 μm thick anode for varying P_{H2} at 700 °C and i_{ext} = 31.6 mA/cm^2.

To discover the dependence of rate-limiting processes on operating conditions, impedance spectra for δ_{film} = 2.8 μm are analyzed via equivalent circuit modeling. The equivalent circuit modeling adapts a thin-film MIEC equivalent circuit model from Baumann et al.. [43]. Their original model – for use with thin-film LSCF cathodes – includes a resistor/constant phase element (R_i-Q_i) pair related to ion transfer at the electrolyte/micro-electrode interface, with the R_i branch also including in series an (R_s-Q_s) pair related to surface exchange and chemical capacitance in the electrode bulk. The equivalent circuit model used here – as

pictured in figure 3.14 (where R_i becomes R_{ion} and R_s becomes R_{chem}) – adds both an (R_{hf}-Q_{hf}) element in series to the original model in order to account for the observed high-frequency arc and an inductive element L_{lead} to account for lead inductance. While the strongly oxidizing cathode environment and micro-electrode geometry of the previous study differ from the current study in ways that may affect the magnitudes and physical correlations of the resulting circuit element fits, the common thin-film geometry and MIEC behavior will likely dominate the characteristics of this electrode, and the proposed circuit should reasonably model the results reported here.

For the circuit pictured in figure 3.14, the constant phase elements (which have a general impedance model of $|Y|(j\omega)^{-n}$) in the original model from Baumann et al.. have been adapted based on the fits derived here. For all fits in this study, the frequency exponents n for the Q_{ion} and Q_{chem} elements were very close to 0.5 and 1.0, respectively. Since n = 0.5 and n = 1.0 correspond specifically to Warburg (W) and capacitive (C) elements, respectively, the Q_{ion} and Q_{chem} elements were changed to W_{ion} and C_{chem} accordingly and the fits were rerun.

The final equivalent circuit model fits are shown by the solid line curves in figure 3.14 for 700 ˚C. The fits are not exact, but track the measurements well except for the low P_{H2} data at low frequency. Analyzing the variation of the different circuit elements as a function of T and P_{H2} provides a basis for interpreting the behavior of the ceria thin-film anodes. To this end, figure 3.15 reveals the variation of the resistive elements with respect to T and P_{H2}. Initial analysis found that R_{bulk} and R_{ion}

are insensitive to variations in P_{H2}, while R_{hf} and R_{chem} depend strongly on P_{H2}, but are somewhat scattered with regard to T. Since R_{ion} acts in parallel to R_{chem}, which also depends on P_{H2}, and since the source of R_{bulk} is well understood, it is unlikely that any of the features identified can be attributed principally to processes in the cathode. This supports the assumption that cathode contributions to cell overpotentials are relatively small, compared to the thin-film anode contributions.

Figure 3.15a shows the variation of R_{bulk} and R_{ion} with $1/T$ on a semi-log plot. Assuming Arrhenius-type behavior, the results suggest activation energies (E_{act}) of 70.5 and 93.8 kJ/mol associated with R_{bulk} and R_{ion} respectively. The E_{act} value for R_{bulk} compares favorably to the range of literature values (76.2 – 80 kJ/mol) for the ionic conductivity of YSZ [63, 130], and moreover, the magnitude of R_{bulk} values agree with those measured by standard four-probe conductivity measurements [130]. As Warburg impedances are typically associated with solid-state diffusion, the associated resistance R_{ion} is assumed to correspond to resistance to O^{2-} diffusion in the ceria bulk. While the reported E_{act} values for ion conduction in CeO_{2-x} in this temperature range vary greatly across several studies (49.82 – 103.83 kJ/mol), the value reported here lies within this range [40].

Figure 3.15b shows the variation of the inverse resistances $1/R_{chem}$ and $1/R_{hf}$ with P_{H2} at 700 °C. The inverse resistances represent effective conductivities, σ_{chem} and σ_{hf}, and as such figure 3.14b indicates that σ_{chem} and σ_{hf}, depend linearly on P_{H2} at low values, before becoming independent of H_2 partial pressure for $P_{H2} \geq 0.32$ atm.

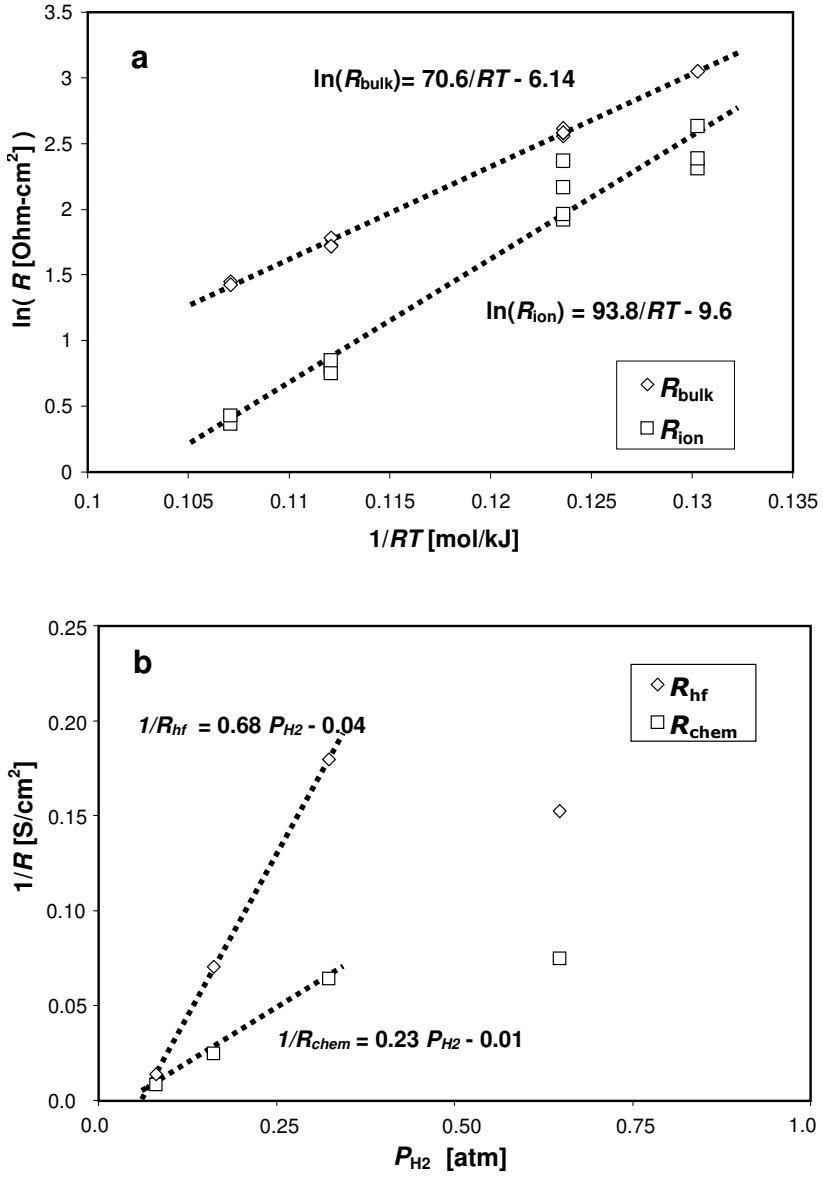

Figure 3.15. Equivalent circuit modeling results for nanoporous 2.8 μm thick CeO_{2-x} anode. a) variation of R_{bulk} and R_{ion} with T; b) variation of R_{hf} and R_{chem} with P_{H2}.

This insensitivity at high P_{H2} values is confirmed visually by figure 3.14, where impedance curves for P_{H2} = 0.32 and 0.65 atm are practically identical. Additional

analysis is required to definitively assign these phenomena to physical processes. While the capacitive nature of R_{chem} suggests that it may be related to the buildup of a capacitive double layer at the ceria surface, the value of C_{chem} (shown in Table 3.2 for T = 700 °C, along with the Warburg coefficient σ_{ion} and the so-called "pseudo-capacitance" C_{hf}, calculated as in the original model [43]) is orders of magnitude larger than values typically associated with charged double layers [43, 68]. The high relaxation frequency for R_{hf} (~18.0 Hz), meanwhile, suggests some process related to surface chemistry.

As a means of confirming the physical interpretation of R_{ion}, the ionic diffusion coefficient was estimated from the Warburg element fitting. For a mixed conductor of oxide ions and polarons, σ_{ion} can be written as follows [131]:

$$\sigma_{ion} = \frac{\overline{R}\,T}{n_{elec}^2\,F^2\,A\sqrt{2}}\left(\frac{1}{D_{O2-}^{1/2}\left[X_{O2-}\right]}+\frac{1}{D_{p}^{1/2}\left[X_{P}\right]}\right), \qquad \text{(eq. 3.1)}$$

where n_{elec} (= 2 here) is the number of electrons associated with diffusion, A the conductor area, D_k the diffusion coefficient for species k (O^{2-} for the oxide, p for the

Table 3.2. Capacitance and Warburg coefficient values. δ_{film} = 2.8 μm, T = 700 °C

P_{H2} [atm]	0.08	0.16	0.32	0.65
C_{hf} [mF/cm^2]	1.8	6.3	11.1	13.1
C_{chem} [mF/cm^2]	6.8	18.5	23.5	26.8
σ_{ion} [kΩ*s$^{-1/2}$]	36.2	13.9	12.4	8.5

polaron), and $[X_k]$ the bulk concentration of species k. The Warburg element σ_{ion} is calculated according to [131]:

$$\sigma_{\text{ion}} = \frac{1}{Y_{\text{ion}}\sqrt{2}} \quad , \qquad \text{(eq. 3.2)}$$

where Y_{ion} comes from the circuit-fitting for the Warburg element with its effective impedance of $|Y_{ion}|(j\omega)^{-0.5}$. In reducing SOFC anode environments, the ionic conductivity is at most only 3% of the total conductivity [132]. As such, the contribution of the polaron to the Warburg element is neglected here, leading to the following estimate for D_{O2-}:

$$D_{O2-} = \left(\frac{Y_{\text{ion}}\,\overline{R}\,T}{n_{elec}^2\,F^2\,A\left[X_{O2-}\right]} \right)^2 . \qquad \text{(eq. 3.3)}$$

For these calculations, bulk oxide concentration $[X_{O2-}]$ is held fixed at the value for $CeO_{1.9}$ (18.87 mol/m^3), according to reported lattice parameters [40]. Furthermore, this value for $[X_{O2-}]$ assumes that only one oxide per Ce_2O_4 unit cell is available for diffusion. As such, eq. 3.3 neglects changes that occur with varying non-stoichiometry, and underestimates D_{O2-} for nonstoichiometric ceria by up to 25%. This analysis is thus intended only to provide approximate analysis of D_{O2-} values.

Figure 3.16 shows estimated values for D_{O2-} compared to previously reported values [40]. Previous values are measured for a range of ceria non-stoichiometry at

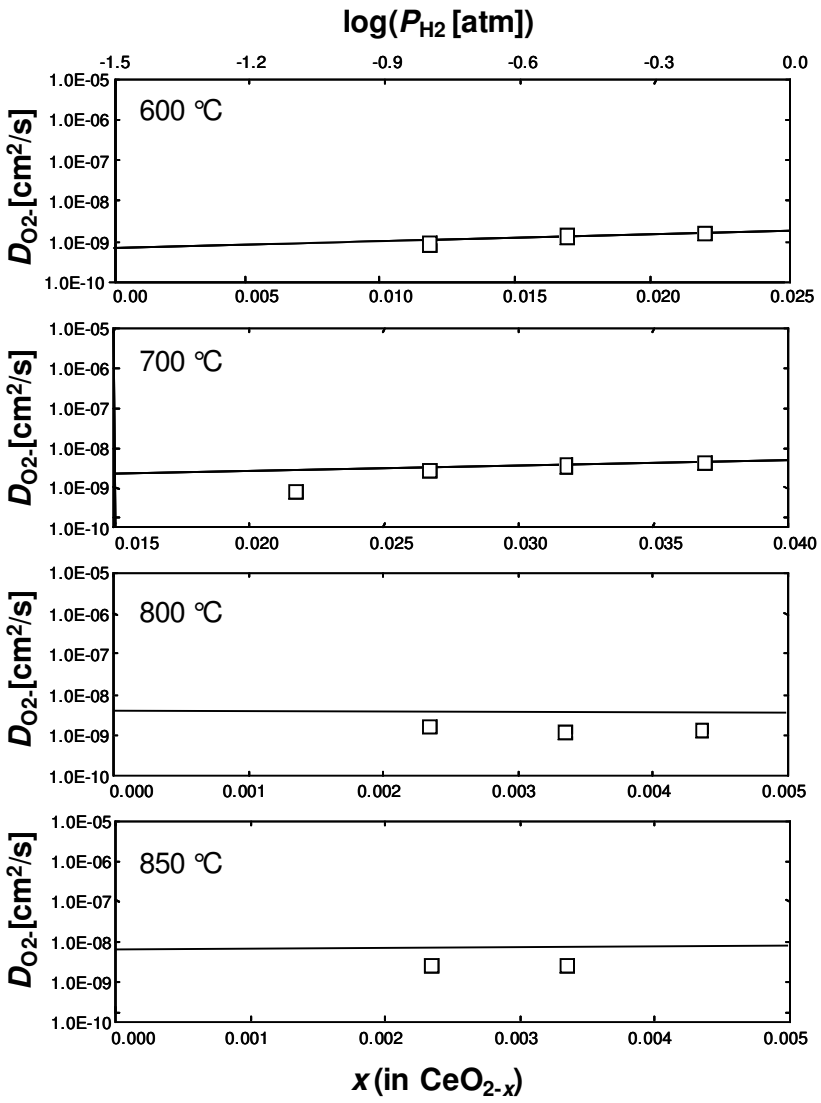

Figure 3.16. Estimated oxide diffusion coefficients D_{O2-} (symbols) as a function of $\log(P_{H2})$, compared to previously measured D_{O2-} values (lines) as a function of x [40]. T = 650 – 850 °C. Note the changing range for x in the lower axis of each plot.

high temperatures (850 – 1150 °C) and reported as Arrhenius parameters, providing correlation to temperatures relevant to this study. Previous data (solid lines) are given as linear fits of the provided data, as a function of non-stoichiometry (x in the formula CeO_{2-x}, displayed on the lower axis of each plot). Estimated D_{O2-} values (discrete

points) are reported as a function of experimental P_{H2} (in log[atm], displayed on the upper axis). The range of the lower axis (degree of non-stoichiometry) is modified for each temperature to give the best match to the estimated D_{O2-} values. In this manner, it is possible to estimate the degree of reduction as a function of operating environment (T, P_{H2}).

Results show a good match between previous and current values for $T \leq 700$ °C. Increasing P_{H2} correlates with an increasing degree of reduction, as is expected. The degree of reduction also varies with T, with $0.01 < x < 0.025$ for $T = 650$ °C and $0.02 \leq x \leq 0.04$ for $T = 700$ °C. For $T > 700$ °C, previous and current values do not correlate, with values in this study significantly smaller than previous values. The closest match is given for fully oxidized CeO_2, in contrast to the prediction that the degree of reduction increases with T. One possible explanation for this discrepancy is the fact that the positive correlation between D_{O2-} and the degree of reduction only holds at low values of x [40]. D_{O2-} is maximized at some moderately low x value (~0.1), after which D_{O2-} decreases with increasing x. For the higher-temperature conditions (T = 800, 850 °C) in this study, greater degrees of reduction become favorable and may lie within the region of negative correlation between x and D_{O2-}. This is confirmed by visual inspection of figure 3.15, where predicted D_{O2-} values are invariant or correlate negatively with $\log(P_{H2})$. Previously measured D_{O2-} values, meanwhile, are for relatively low degrees of reduction ($x \leq 0.2$), and do not capture the decrease in D_{O2-} with increasing x. It is, furthermore, important to re-emphasize

that the constant [X_{O2-}] value assumed in this analysis can underestimate D_{O2-}, and as such likely underestimates the degree of reduction for $T \geq 700$ °C.

3.2.2.3 Electrochemical Characterization of Dense Films

For the dense-film ceria anodes, deposited with a throw distance of 65 mm, polarization results are shown for various gas environments, including H_2/H_2O, CO/CO_2, $CO/CO_2/H_2O$, and C_4H_{10}/H_2O at various partial pressures and T from 600 to 800 °C. Impedance spectra were taken for all fuels, but are displayed for humidified H_2 only, as with the nanoporous films. Figure 3.17 shows polarization results for a 110 nm thick dense anode. For 800 °C, cell performance degraded rapidly, as indicated by an R_{bulk} value that was higher than the corresponding value at 700 °C. The cause of this degradation is likely the loss of active cell area due to liftoff of the Au current collector. Continued degradation prevented the collection of additional data at 800 °C. In order to compare the data taken at 800 °C to other T, as in figure 3.13a, an effective cell area was calculated, by calculating the ratio of the measured R_{bulk} to an estimated value assuming Arrhenius-type behavior. The current densities for the 800 °C polarization curve shown in figure 3.17a are calculated according to this effective area. While the resulting plot shows a large increase in maximum current from 700 °C to 800 °C, such variation is consistent with data from nanoporous films. Measurements prior to operation at 800 ˚C showed no evidence of degradation, as revealed by invariance of R_{bulk} as a function of time, for a given T and gas composition.

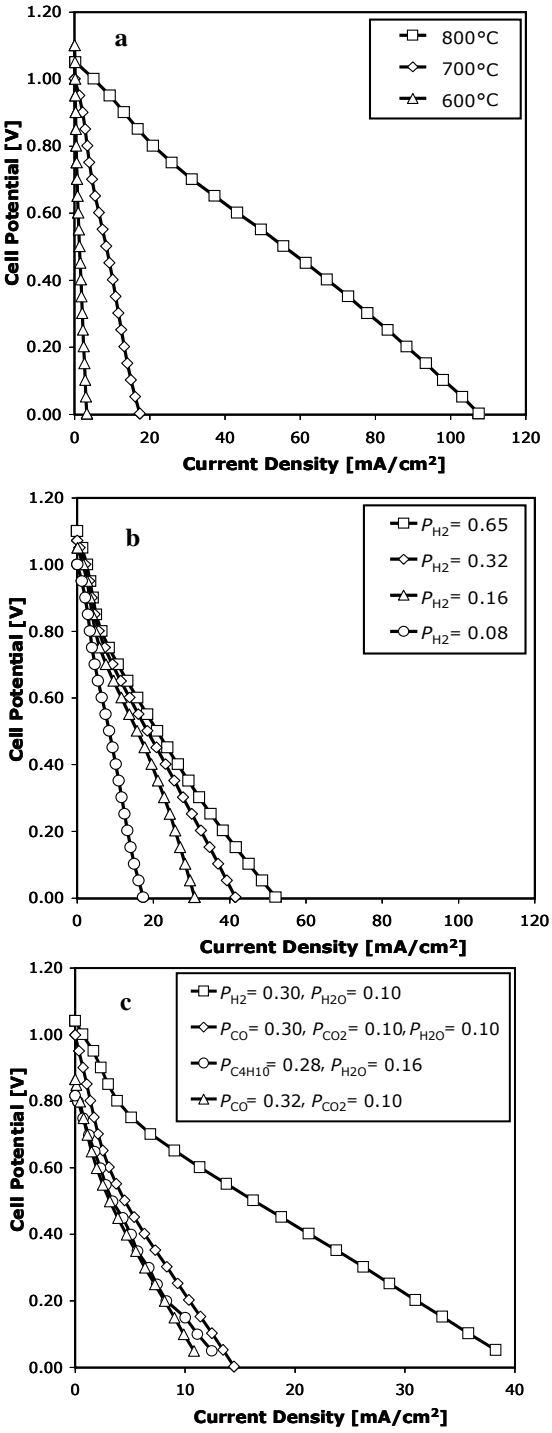

Figure 3.17. Polarization results on dense, 110 nm thick ceria anode. T = 700 °C, unless otherwise noted. a) H_2 oxidation for varying temperatures, with P_{H2} = 0.08 atm, P_{H2O} = 0.03 atm; b) H_2 oxidation for varying P_{H2} (in atm) with P_{H2O} = 0.03 atm; c) comparison of polarization curves for n-butane, H_2, and CO oxidation.

Polarization curves on the dense films show a qualitatively different profile than those from the nanoporous films. The LSV profiles exhibit a region of high resistance near open circuit, followed by a region of lower resistance at intermediate and large current densities. This is in contrast to results on nanoporous films, which were either highly linear or demonstrated the lowest resistance at open circuit, often with apparent concentration-limited maximum current densities. Furthermore, this decrease in resistance occurs at a distinct current density in the polarization curve (most readily seen in the H_2 data in figure 3.17c), rather than increasing gradually. The shape of these polarization curves, then, is not readily explained by traditional Butler-Volmer kinetic relationships for the activation overpotentials η_{act}. From 700 to 800 °C the current densities for P_{H2} = 0.08 atm are significantly higher than the corresponding maximum current density at 850 °C on the nanoporous ceria film (figure 3.13b).

Figure 3.17b depicts polarization results for varying P_{H2}. Results show a clear trend of increasing current density with increasing P_{H2}. However, the variation in currents does not show the significant non-linearity seen in the nanoporous films, nor does P_{H2} have a significant impact on current densities in the high-resistance region near open circuit.

The shift in polarization data with varying P_{CO} on dense films (not shown) is primarily a result of the thermodynamic shift in open circuit potential. Figure 3.17c compares the polarization results for humidified H_2, CO/CO_2, humidified CO/CO_2,

and humidified n-C_4H_{10}. The most striking feature of this comparison is the superior performance of humidified H_2 to all other fuels tested. Also noteworthy is the similarity between CO and C_4H_{10} oxidation data.

Addition of 10% H_2O to a CO/CO_2 feed (figure 3.17c) increases the OCV by ~150 mV to 1.0 V, only 40 mV less than the OCV for H_2 oxidation. This provides evidence of significant water-gas shift (WGS) activity on the ceria anode:

$$H_2O + CO \leftrightarrow H_2 + CO_2 . \qquad [R\ 3.1]$$

In the $CO/CO_2/H_2O$ environment in question, the movement of this reaction toward equilibrium favors the reaction products, leading to hydrogen production. As the current density increases, however, the cell potential drops rapidly, and the $CO/CO_2/H_2O$ system behaves very similar to the CO/CO_2 system depicted in figure 3.17c, albeit with a thermodynamic shift to higher cell potentials. This implies the hydrogen production rate by reaction 3.1 is not sufficient to sustain higher current densities observed for humidified H_2. Thus, CO oxidation is likely a critical pathway for the generation of electrochemical current, either via direct oxidation or via reaction 3.1. While WGS activity at OCV implies that the system is not in kinetic equilibrium between the ceria surface and gas phases, this does not preclude steady-state behavior on the ceria surface.

Figure 3.18 shows impedance spectra for humidified H_2 on the dense, 110 nm ceria anode at 700 ˚C, for current densities ranging from 0 to 31.6 mA/cm^2. Results show two easily resolved arcs, with a possible third arc at very high frequencies ($\omega >$ 10^4 Hz). At currents of 0.0 and 3.16 mA/cm^2, both processes (low frequency and high frequency) contribute significantly to the total polarization resistance (R_{pol}). At open circuit (figure 3.18a), both processes are sensitive to fuel composition for low P_{H2}, with R_{pol} for both processes decreasing with $P_{H2} \leq 0.32$ atm, similar to the nanoporous films. At low currents (i = 3.16 mA/cm^2, figure 7b), the low-frequency process is largely insensitive to P_{H2}, and has a smaller resistance than at OCV. The higher-frequency process dominates at low P_{H2}, and then decreases rapidly with increasing $P_{H2} \leq 0.32$ atm, above which it is insensitive to changes in P_{H2}. Also, the relaxation frequencies for both processes are largely insensitive to variations in both P_{H2} and current density, for low currents. Finally, for a relatively high current density (i = 31.6 mA/cm^2, figure 7c), there are no longer two clearly distinguished arcs. Instead, impedance spectra are dominated by a single arc that changes in magnitude over the entire range of pressures tested. Furthermore, relaxation frequencies vary with P_{H2} and are faster than at lower current densities.

In general, the impedance spectra for low current densities on dense films appear qualitatively similar to those for the nanoporous films. If the two processes at low current densities are consistent with those identified for nanoporous films, the low frequency process is associated with a combination of oxide conduction through the ceria bulk and chemical capacitance, while the higher-frequency process is

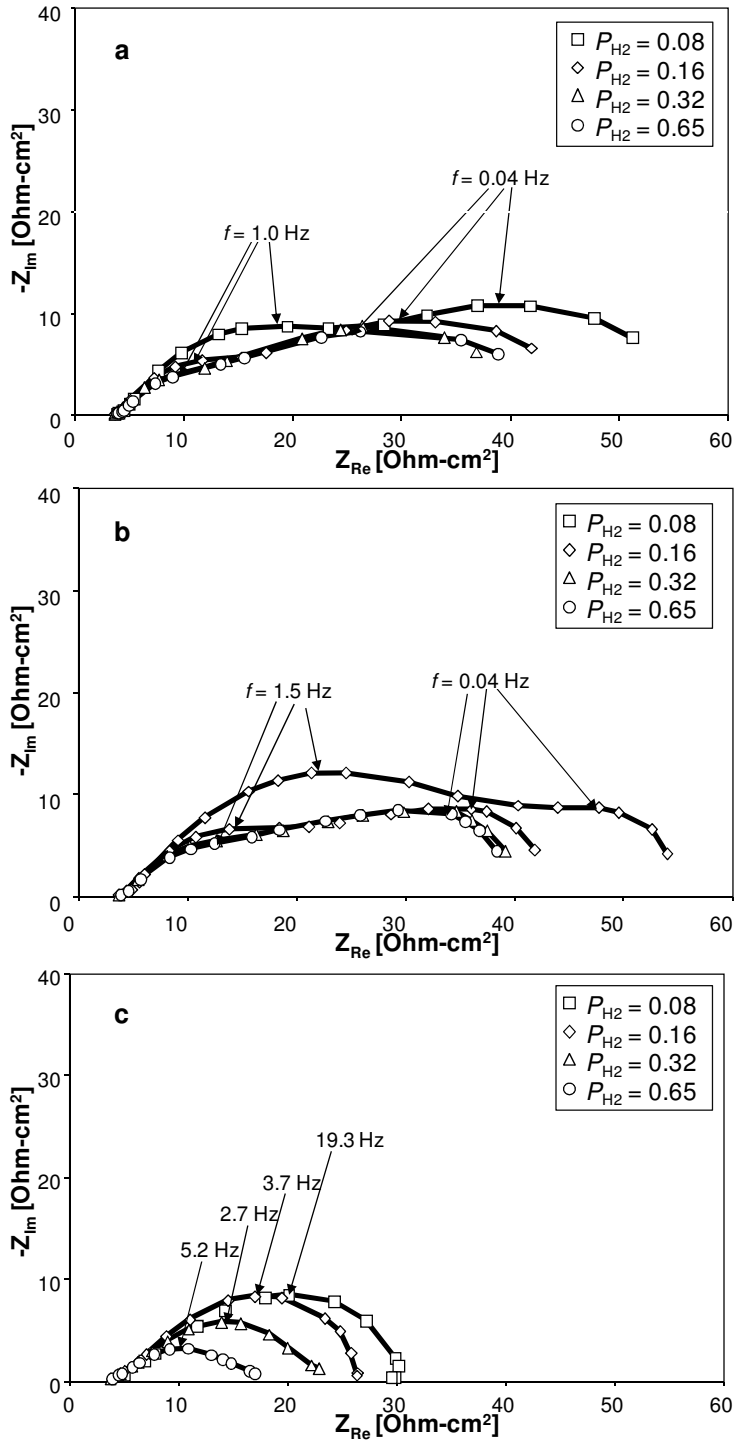

Figure 3.18. Impedance spectra for H_2 oxidation on 110 nm dense ceria anode. T = 700 °C, P_{H2} = 0.03 atm. a) i = 0.0 mA/cm^2; b) i = 3.16 mA/cm^2 c) i = 31.6 mA/cm^2.

associated with surface chemistry. Both arcs, as mentioned, demonstrate the same relationship to P_{H2} as in the nanoporous films. Furthermore, the change in the resistances for each arc between the two film morphologies can be explained by the morphological differences. The high-frequency resistance, possibly associated with surface chemistry, is generally higher in the dense film EIS data, due to the lower overall surface area. Meanwhile, the low frequency resistance, partly associated with solid-state diffusion of ions through the ceria bulk, is generally smaller in these much thinner dense films than in nanoporous films, particularly at low P_{H2}. At higher current densities, the polarization curves show a sudden shift in resistance, possibly indicating a change in oxidation mechanism. Examination of Bode plots, as in figure 3.19, suggests that the decrease in resistance is due primarily to the negligible contribution of the low-frequency process to the polarization resistance. This qualitative shift is not readily explained by common electrochemical models, such as the modified Butler-Volmer equation, and is likely related to the change in ceria valence states with increasing current density. In place of equivalent circuit modeling, the thin-film MIEC SOFC model developed in chapter 2 will be used to fit the dense-film experimental results. The goal will be the derivation of thermokinetic parameters to describe the oxidation of H_2 and CO on CeO_{2-x} anodes.

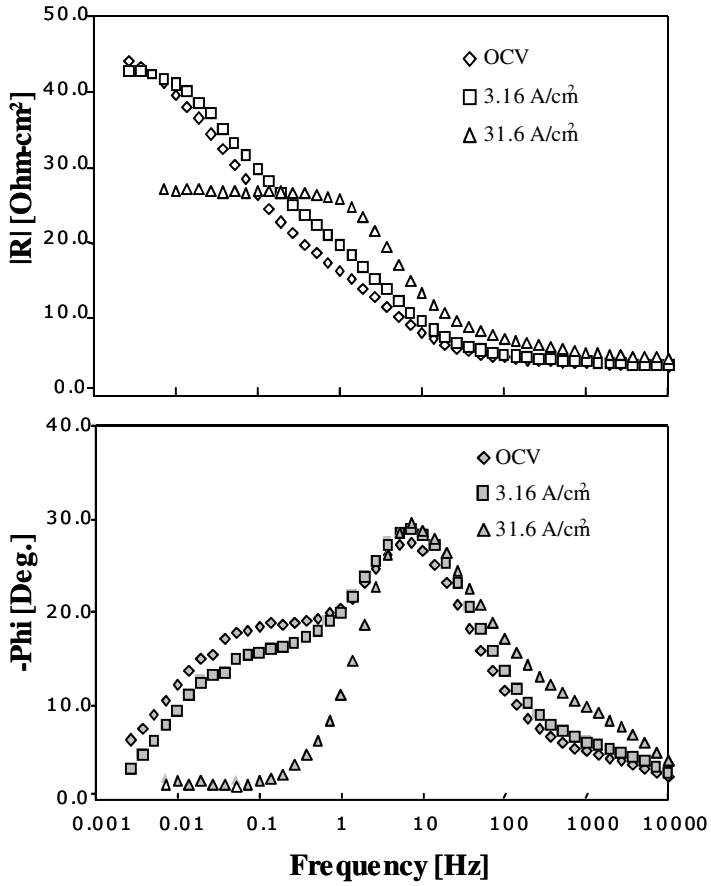

Figure 3.19. Bode plots for varying current density on a 110 nm dense ceria anode. T = 700 ˚C, P_{H2} = 0.16 atm, P_{H2O} = 0.03 atm.

3.3 In situ XPS for Evaluation of Ceria Oxidation States

To help form a more quantitative understanding of Ce oxidation states during SOFC anode operation, this study employs so-called ambient pressure x-ray photoelectron spectroscopy (AP-XPS) at the Advanced Light Source (ALS) at Lawrence Berkeley National Laboratory to characterize a thin-film CeO_{2-x} electrode during electrochemical oxidation of H_2 and reduction of H_2O. Two fundamental changes to the SOFC geometry utilized above were required for this study. First, the

use of XPS requires optical access to the ceria surface, which in previous experiments has been covered with a porous Au current collector. Furthermore, the XPS operating environment only provides a single gas feed, preventing duplication of the two-chamber experiments described above. Thus for this experiment, a single chamber fuel cell was fabricated with a dense CeO_2 film (300 nm thick) as a working electrode and a porous Pt counter electrode – both on the same side of a 1 mm thick YSZ electrolyte, with an Au pattern deposited on top of the CeO_2 for current collection, as illustrated in Figure 3.20a. The thin-film electrodes were characterized using voltammetry and electronic impedance spectroscopy. Analyses of the simultaneous XPS measurements and electrochemical characterization provide valuable insight for the development of a quantitative micro-kinetic mechanism for the oxidation of small fuel species on CeO_{2-x} anodes, as described in chapter 4.

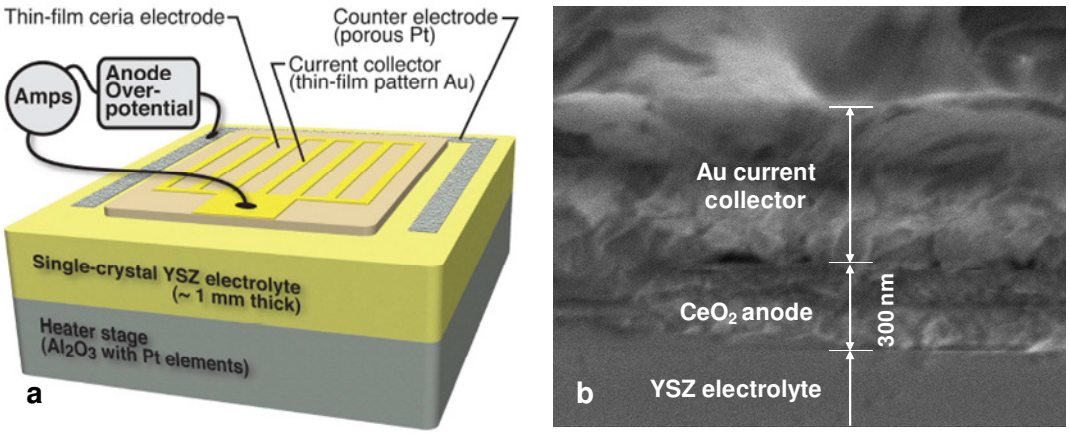

Figure 3.20. Single chamber SOFC. a) Diagram with thin-film ceria electrode and patterned Au current collector and with porous Pt counter electrode. b) SEM cross-section of YSZ electrolyte support, thin-film ceria electrode, and Au current collector.

3.3.1 Experimental Details

3.3.1.1 Ambient Pressure XPS

For the *in situ* characterization of operating thin-film ceria cells, a unique synchrotron-based XPS facility at ALS (Beamline 11.0.2) was operated at a pressure of 0.5 Torr in the presence of H_2O and H_2. Specifications for the ambient-pressure XPS endstation are summarized in Table 3.3. The pressures are not restricted to UHV, owing to the use of differentially pumped pressure zones in the electron spectrometer. This allowed for adequate P_{H2} to cause significant ceria surface, as in reaction 1.7. In order to avoid a shift in the XPS peaks due to variation in the ceria electrode surface Φ, the Au current collector potential was held fixed while the Pt counter electrode was varied in the experiments.

Table 3.3. Characteristics of AP- XPS end station for Beamline 11.0.2 at ALS.

Detector	Phoibos 150 analyzer with 9-channel channeltron line detector
Energy range	95-2000 eV
Monochromator	Variable-included-angle plane gratings
Calculated flux (@ 1.9 GeV, 400 mA)	10^{12}-10^{13} photons/s/0.1% bandwidth
Resolving power ($E/\Delta E$)	2500-7500
Minimum spot size at sample (FWHM)	6×11 μm
Sample environment	$P_{tot} \leq 10$ Torr

3.3.1.2 Cell Fabrication

For this study, a single-chamber cell was created by patterning working and counter electrodes from CeO_2 and platinum on the same side of a 10 mm X 10 mm X 1 mm single-crystal YSZ electrolyte as illustrated in figure 3.20a. Fully dense CeO_2 films (3.0 +/- 30 nm thick, as evaluated by SEM images) were sputter-deposited over a 4 mm X 6 mm area of the YSZ electrolyte support using conditions described previously for dense ceria-film deposition. To deposit the Au current collector on top of the ceria electrodes, patterned masks were used and Au patterns were created with electron beam deposition. The Au pattern consisted of 100 µm wide lines and cross-bars for current collection as illustrated in figure 3.20a. Counter and reference electrodes of porous Pt paste were deposited on the YSZ close to the outer edge of the CeO_2 (as illustrated in figure 3.20a), with Pt mesh pressed onto the Pt electrodes for current collection. The assembly was fired at 800 °C to remove organic solvents and pore former from the Pt paste prior to operation in the XPS chamber. The porous Pt electrode is made with high surface area in hopes to minimize its contribution to the overpotentials at the current densities achieved with the thin-film ceria electrodes.

The ceria films in this study were deposited with a target-to-substrate throw distance of 65 mm with δ_{film} ranging up to 300 nm. As shown in the SEM cross-section figure 3.20b, these films were dense. Post-electrochemical SEM images (figure 3.12b) reveal that the dense structure was maintained during electrochemical testing. The Au current collector, also shown in figure 3.20b, was dense. Although post-electrochemical SEM reveal the formation of significant porosity in the Au

current collector as discussed below, for the tests presented in the current study the Au/ceria interface maintained its integrity for sufficient electronic conductivity.

3.3.1.3 Experimental Set-up and Testing

The cell was mounted in an endstation at beamline 11.0.2 at ALS. The cell was clipped onto a sample holder with an Al_2O_3 heater with internal Pt coils to provide temperatures at the electrode approaching 700 °C at the 0.5 Torr total pressures. The Au current collector was connected directly to the XPS chamber, to ground the CeO_2 electrode at a constant electric potential and thus prevent static shifts in the Ce XPS spectra due to surface charging. Figure 3.21 shows the loaded sample holder before inserting into the test chamber. The XPS chamber at beamline 11.0.2 is not typically used for electrochemical measurement, and so electrical contact to the counter and reference electrodes was maintained by connecting Pt lead wires to thermocouple wires that provided electrical feed-through to the XPS chamber.

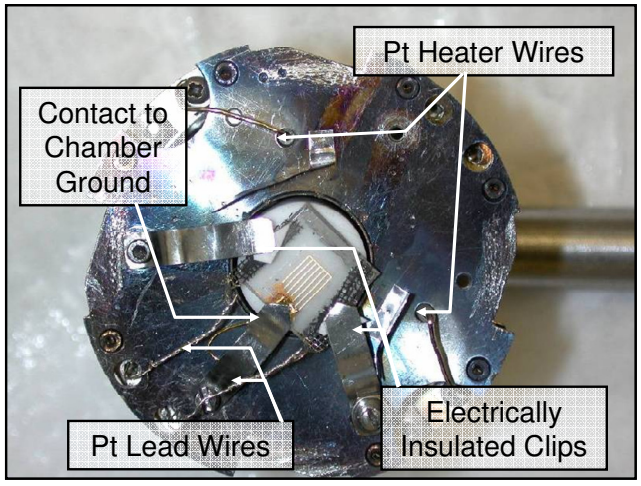

Figure 3.21. Single-chamber SOFC mounted on ALS XPS sample holder

After mounting on the sample holder, the apparatus was inserted into the sample preparation chamber and pumped to UHV. The sample holder was then transferred to the main XPS chamber, where power was supplied to the Al_2O_3 heater, bringing the cell to temperature at a rate of ~5 °C/min. H_2 and H_2O were then back-filled into the XPS chamber to the desired gas composition, with partial pressures monitored via mass spectrometry. Cell temperatures were measured with a pyrometer but the transparency of the materials caused the pyrometer to read the surface of the Al_2O_3 heater underneath. The temperature of the YSZ and ceria were thus determined by the correlation of the bulk resistance R_{bulk} of the cell as a function of temperature, under similar conditions to the ALS experiments. These tests revealed that the ambient pressure XPS tests maintained the cell around 620 °C.

Electrochemical measurements (both voltammetry and EIS) were performed with a Gamry MultiEChem System. The measurements were done at P_{tot} = 0.5 Torr with P_{H2} = 0.25 torr and P_{H2O} = 0.25 torr. The gas mixture presents the opportunity to operate the ceria electrode both in fuel (H_2) oxidation mode as an SOFC anode and in H_2O electrolysis mode as a solid oxide electrolysis cell (SOEC) cathode. The electrochemical measurements compared favorably to similar tests at the University of Maryland with P_{tot} = 1.0 bar and > 99% Ar dilution with very low P_{H2} and P_{H2O}, comparable to the beamline endstation conditions.

Electrochemical measurements at ALS were conducted as 3-probe measurements, with a Pt reference electrode. While the ceria electrode is generally

considered the working electrode in this study, the aforementioned grounding of the Au current collector led to fears that the Gamry workstation would attempt to shift the electric potential of the entire chamber during polarization experiments, were the working electrode connected to the chamber ground. The ceria was thus connected to the counter electrode lead of the Gamry workstation, while the porous Pt counter electrode was connected to the working electrode lead of the Gamry workstation. Unfortunately, wiring the cell in this manner leads to significant uncertainty for the polarization results discussed below. With this configuration, polarization studies measure the electrochemical current between the CeO_{2-x} and Pt counter electrodes as a function of the bias between the reference and the Pt counter electrode, rather than as a function of the bias between the reference and the CeO_{2-x} working electrode. As such, while the currents measured are an accurate representation of the total electrochemical current, the *V-I* curves collected at ALS contain no direct information about the exact electric potential or overpotentials in the ceria electrode. While subsequent 2-probe experiments conducted at UMD produce qualitatively similar results to those at ALS, as seen below, the ceria oxidation state in these measurements should be correlated to the current I_{tot}, rather than to V_{cell}.

At the ALS, simultaneous XPS measurements with the electrochemical activation of the ceria electrodes probed changes in the Ce oxidation state as a function of electrode overpotential and spatial position on the ceria relative to the Au current collector. The focused X-ray beam (diameter < 100 μm) was passed through the chamber at an angle and reflected off of the ceria electrode surface, as illustrated

in figure 3.22a. The XPS signal was captured in a two-stage differentially pumped analyzer with electrostatic focusing optics as also illustrated in figure 3.22a. Figure 3.22b shows a photograph of the analyzer positioned just above the working cell operating at 620 °C at the beamline. The beam and analyzer could be rastered and thus was used to resolve changes in the Ce oxidation state as a function of its proximity to the Au current collector under positive and negative bias. The 100 µm beam spot size is too large to resolve any three-phase boundary chemistry near the Au/CeO_{2-x} interface, but XPS measurements both around and far from the TPB provided some assessment of planar gradients in ceria oxidation states. For measurements at a given bias, the cell voltage was held constant for more than 10 minutes. Constant currents at the individual bias voltages confirmed that the ceria was near steady-state conditions during LSV measurements.

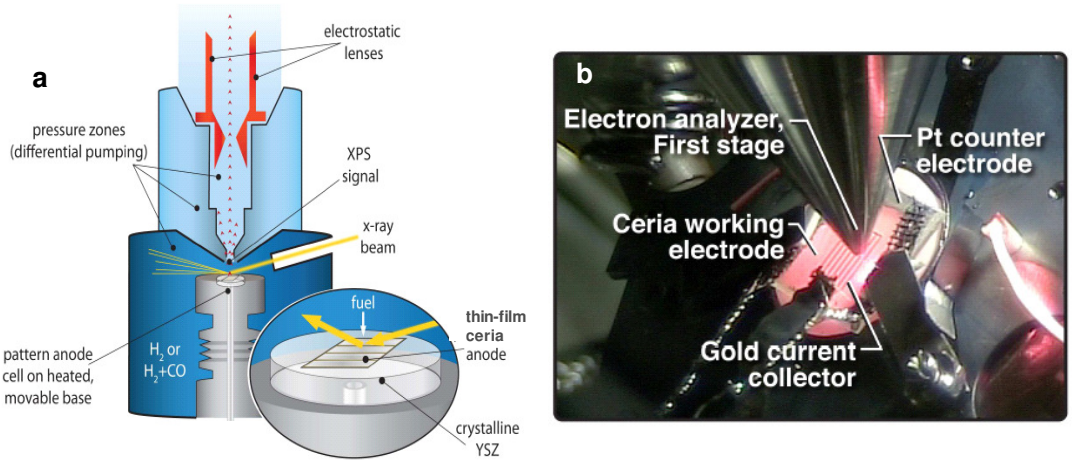

Figure 3.22. a) Diagram of ambient-pressure XPS apparatus for testing single chamber SOFC at Advanced Light Source., and b) photograph of single-chamber SOFC operating in XPS chamber.

3.3.2 Results and Discussion

A *V-I* curve for the single-chamber-cell experiment is shown in figure 3.23a. The curve covers a wide range of currents (I_{tot}) including H_2 oxidation ($I_{tot} > 0$) and H_2O electrolysis ($I_{tot} < 0$) CeO_{2-x} surface. At least three distinct regions of the *V-I* curve are clearly visible in figure 3.23a: 1) a high-resistance region at low current magnitudes and principally small negative voltages, 2) a lower-resistance state at higher negative voltages, and 3) a low resistance state at positive voltages with H_2O electrolysis on the CeO_{2-x}. Since the high-surface area porous Pt electrode is expected to contribute less than the thin-film ceria electrode to the overpotentials for electrolysis or oxidation, the subtraction of IR_{bulk} from V_{cell} in figure 3.23 (where R_{bulk} is taken from high-frequency impedance measurements) can provide an estimate for the overpotentials and resistances of the ceria electrode. The IR_{bulk}-corrected V_{cell} are plotted in figure 3.23a and this correction further highlights the three distinct

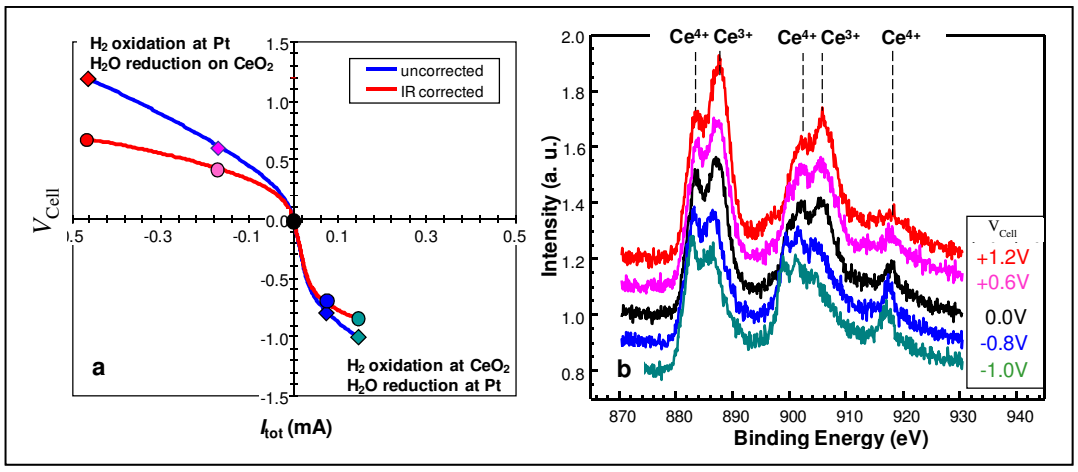

Figure 3.23. Relationship between ceria oxidation state and electrochemical performance. a) Polarization results for H_2 oxidation. $P_{H2} = P_{H2O} = 0.25$ Torr, $T \approx$ 620 ºC. b) *In situ* Ce*3d* XPS spectra for a range of applied biases.

regions of the *V-I* curves. Furthermore, if there is minimal η contribution from the high surface area Pt electrode, it can be expected that sharp changes in resistance with cell current are driven by changes in the electrochemical activity of the ceria electrode either in the bulk or on its surface.

To this end, the *in situ* XPS measurements during electrochemical measurements show significant changes from open circuit conditions in the Ce3d core spectrum as indicated in figure 3.23b. The 3d core spectra in figure 3.23b show relative intensities of XPS peaks associated with the two limiting Ce oxidation states (Ce^{4+} and Ce^{3+}) for various I_{tot} values as marked on the *V-I* curve in figure 3.23a. Figure 3.23b shows the growth in Ce^{3+} peaks as I_{tot} decreases or, similarly, the growth in Ce^{4+} peaks I_{tot} increases during H_2 electrochemical oxidation.

To quantify the changes in the ceria peak intensities varying electrochemical current, reference spectra for both Ce^{4+} and Ce^{3+} in the Ce*3d* core spectrum must be obtained. For the more common Ce^{4+}, reference spectra are available in the literature [133] and are used to fit the data. For the Ce^{3+} Ce*3d* core spectra, the method pioneered by Appel and coworkers [122], was used to self-generate a reference spectrum by subtracting the Ce^{4+} spectrum from the most reduced measured state (at V_{cell} = 1.2V, as in figure 3.23a) until the u‴ peak is completely cancelled. By extrapolating from the most reduced measured state (smallest u‴ peak), the generated spectra minimizes the error from associating u‴ entirely with Ce^{4+} [120].

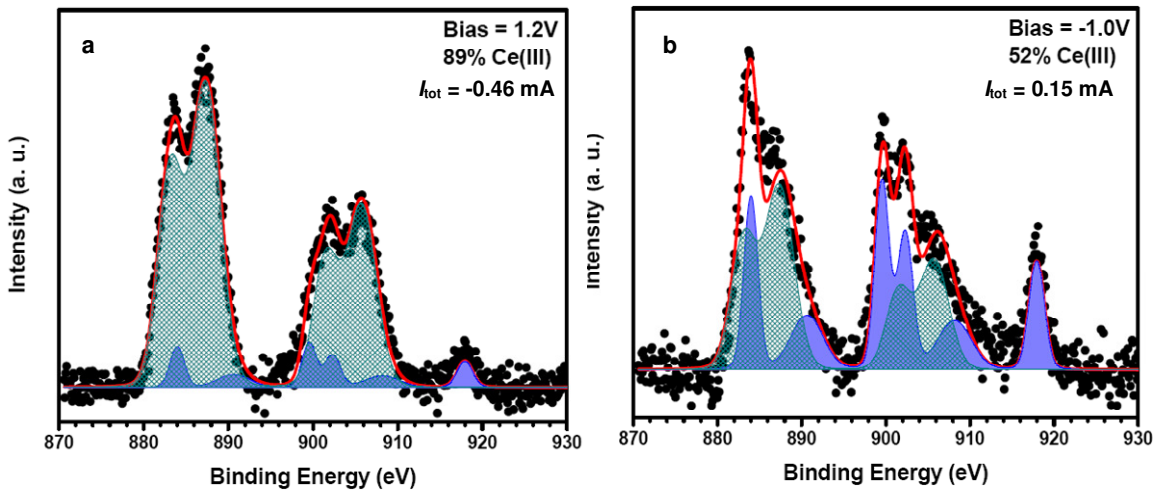

Figure 3.24. Fitting of *Ce3d* core spectra to determine fraction of Ce in different oxidation states at $P_{H2} = P_{H2O} = 0.25$ Torr and $T \approx 620$ ºC for two different ceria electrode overpotential biases a) at +1.2 V with H_2O electrolysis, and b) at –1.0 V for H_2 electrochemical oxidation.

These reference spectra were then used to fit the peaks as indicated in figure 3.24, for the conditions where uncorrected $V_{cell} = 1.2$ V (H_2O electrolysis on the ceria) and –1.0 V (H_2 oxidation on the ceria). The fits for the Ce*3d* core spectra are remarkably good as shown in both fits in figure 3.24. They provide a percentage of Ce^{3+} vs. Ce^{4+} in the near surface region of the electrochemically active ceria film. Figure 3.24 also highlights how the percentage of Ce^{3+} derived from the fits is much higher at positive bias when H_2O electrolysis is occurring. Under such conditions, the O^{2-} ions are pulled from the ceria surface and near sub-surface region into the bulk toward the YSZ electrolyte and Pt cathode (where the balancing H_2 oxidation takes place). The XPS spectra indicate that the ceria surface is reduced until the H_2O dissociative adsorption (reverse of reaction 1.1) rate matches the flux of oxides pulled

into the YSZ. In fact, by looking at the relatively low resistance for the electrolysis on the CeO_{2-x} in figure 3.23a, it is clear that this largely reduced surface has a high activity for H_2O electrolysis. The effectiveness of CeO_{2-x} for H_2O electrolysis remains an unexplored area for further research.

The data in figure 3.24 were taken with the XPS spot placed adjacent to the Au current collector. The XPS beam focus was translated ~100 μm away from the current collector to explore the lateral distribution in the Ce surface oxidation states as identified by fitting the Ce*3d* core spectra. The results in figure 3.25 highlight such measurements, showing that away from the Au current collector, the Ce near the electrode surface is less oxidized, particularly under H_2 electrochemical oxidation conditions. Results show that the two locations behave similarly under positive and zero bias, but diverge as the ceria becomes oxidized under negative applied bias. Under conditions where the CeO_{2-x} is providing H_2 electrochemical oxidation, the surface is more oxidized and thus less amenable for effective electron conduction. Thus, the activity for electrochemical H_2 oxidation may increase with shorter electron conduction paths to the Au current collector. Hence, the H_2 reduction of the CeO_{2-x} surface is stronger near the Au current collector as indicated in figure 3.25 for negative bias voltages. The increased oxidation to Ce^{4+} with negative voltages seems to cause a rapid drop in resistance at bias voltages < -0.6 V. This may be due to improved activity for H_2 with the increased oxygen availability. This argument is supported by the higher degree of oxidation near the Au current collector – the extent of oxidation at 0 V bias represents equilibrium with the gas phase and as such, greater

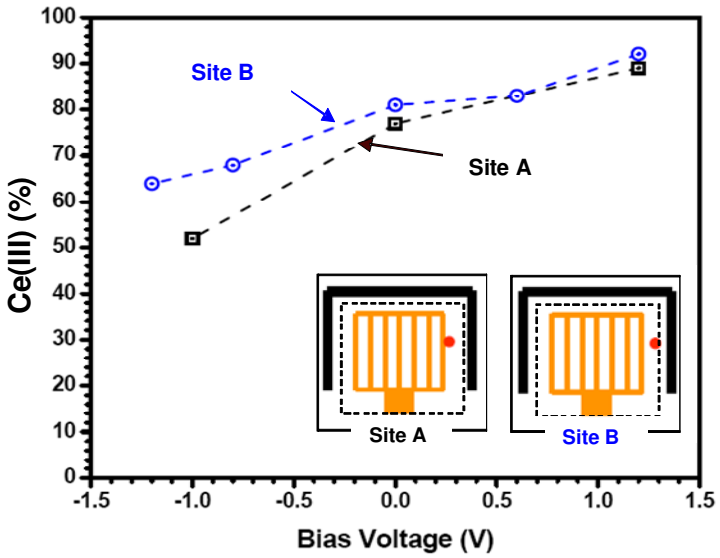

Figure 3.25. Summary of XPS peak fitting for *Ce3d* spectra at locations near the Au current collector and near the ceria/YSZ edge.

deviation from this oxidation state should correspond to higher electrochemical activity – but this remains an issue to be explored.

While shifts in the relative peak intensities are analyzed to determine the distribution of species on the ceria surface, static shifts of the entire spectrum reflect changes in the electric potential of the local surface. Table 3.4 lists the static peak shift, relative to the peak position at OCV, as a function of applied bias for the two locations in figure 3.25. The results show zero shift for the ceria close to the Au current collector, indicating that there is no change in electric potential difference $\Delta\Phi$ between the ceria and Au with varying I_{tot}. These results imply that any possible double-layer charging at the CeO_{2-x} interface is negligible and can be neglected in the model described in chapter 2. At the outer edge of the electrode, roughly 200 μm

Table 3.4. Shifts in ceria surface electric potential for the two locations in figure 3.25, detected by static shifts in XPS Ce*3d* spectra relative to OCV. Results show decreasing potential far from the current collector with increasing oxidation.

	Applied Bias			
	1.2 V	**0.8 V**	**-0.8 V**	**-1.0 V**
Site A	0.0 V	-	-	0.0 V
Site B	0.0 V	0.0 V	-0.6 V	-0.8 V

from the nearest Au current collector bar, significant peak shifting is observed under anodic bias. This shift in electric potential increases with increasing surface oxidation, which correlates with decreasing electrical conductivity. These results support the above argument that decreased electrical conductivity with surface oxidation restricts electrochemical activity under anodic bias to a region near the current collector.

Because of the limited test conditions in the XPS single-chamber environment, additional two-chamber tests were set up where the Pt counter electrode is replaced by a high-surface area LSM/YSZ porous electrode, with fuel dilution by Ar used to replicate the low P_{H2}/P_{H2O} conditions at ALS. As desired for the Pt electrode in the single-chamber experiments, it was determined that the LSM/YSZ high-surface area electrode provided negligibly small contributions to the overall cell overpotential. Thus, these more conventional two-chamber cell arrangements could be readily compared to the single-chamber tests after subtraction of the OCV and

IR_{bulk}, due to the differences in the equilibrium Nernst potential and in R_{bulk} from the different O^{2-}-ion conduction paths through the YSZ electrolyte, respectively.

Figure 3.26 shows just such a comparison with a range of higher P_{H2} and P_{H2O} values. The results indicate that similar changes in resistance occur under higher reactor pressures. While figure 3.26 illustrates that the changes in resistance with Ar dilution are not as distinct as with the low-pressure single-chamber XPS conditions, the 3-probe configuration described above for the ALS measurements under-reports the actual biases applied between the Pt and CeO_{2-x} electrodes. Correcting this discrepancy would increase the agreement between measurements. As with the two-

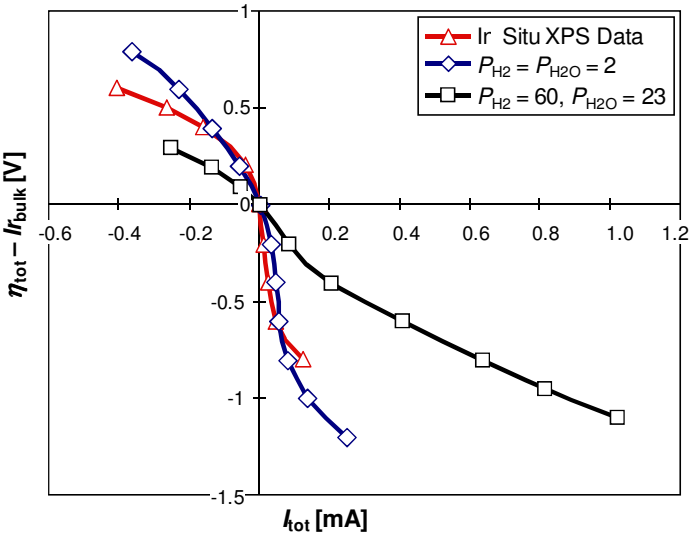

Figure 3.26. Comparison of polarization data from single chamber SOFC in ALS XPS chamber ($T \approx 620$ ºC, $P_{H2} = P_{H2O} = 0.25$ Torr) and from two-chamber SOFC results ($T = 600$ ºC, pressures listed in Torr). OCV and IR_{bulk} is subtracted to eliminate discrepancies in Nernst potential, due to different cathode environments, and R_{bulk}, due to differences in the two geometries, respectively.

chamber experiments described above (figure 3.17b), the transition to low resistance in the CeO_{2-x} electrode as electrochemical H_2 oxidation rates increase appears to occur over a narrow range of current densities, independent of P_{H2}. This result indicates that phenomena observed in the low-pressure, single-chamber cells with the ambient pressure XPS translate well to higher pressures and more conventional fuel cell geometries. As such, this encourages more extensive ambient pressure XPS studies for understanding CeO_{2-x} behavior in both SOFC and SOEC electrode applications.

3.4 Conclusions

In this study, thin-film CeO_{2-x} anodes were electrochemically characterized to identify and analyze the kinetic processes controlling oxidation on ceria in SOFC anodes. Ceria films were sputter-deposited on electrolyte-supported button cells with high surface-area LSM/YSZ cathodes. The results reveal that electrochemical performance is highly sensitive to film morphology, with initial 'nanoporous' films demonstrating qualitatively different performance for varying film thickness. Fabrication of smoother, thinner films led to more consistent performance, albeit with results qualitatively different from those on the nanoporous films.

Analysis of EIS results for nanoporous films revealed three main resistances, in addition to R_{bulk}, including the diffusion of oxides through the ceria bulk, acting in parallel to a capacitive chemical process that is sensitive to P_{H2}, which dominate the

resistance at low currents and low P_{H2}. Additionally, a high-frequency process sensitive to P_{H2} contributes minimally to the total resistance. For both the chemical process and the high-frequency process, the resistance becomes insensitive to P_{H2} above 0.32 atm. Equivalent circuit parameters were used to estimate the oxide diffusion coefficient, with results for $T \leq 700$ °C agreeing with previous results and indicating a modest degree of reduction. Dense films show related trends in the impedance spectra, with two clearly resolved arcs at low currents, both of which are sensitive to P_{H2} below 0.32 atm. At higher currents, impedance spectra on dense films consist of a single arc, which deceases with P_{H2} for the entire range of P_{H2} tested. This corresponds with the observed shift in the electrochemical oxidation behavior, where the total resistance is reduced abruptly with increasing current. The cells also demonstrated stable performance on CO and humidified C_4H_{10}, with no evidence of carbon deposition. Results for CO electrochemical oxidation show a decrease in limiting current with decreasing P_{CO}. In general, overall current densities for humidified CO as well as C_4H_{10} were less than those for humidified H_2, although oxidation of humidified CO showed evidence of water-gas shift reaction through increased current densities over dry CO.

These results suggest a complex interrelation between the SOFC operating conditions (T, P_{H2}, P_{H2O}), the oxidation state of the ceria, and the electrochemical performance. The results for various operating conditions will be analyzed by fitting the data with the thin-film MIEC model described in chapter 2. Analysis will lead to

the formulation of a microkinetic mechanism for oxidation on CeO_2, which will be an important tool for optimizing the micro-structure of SOFCs operating on this MIEC.

In situ AP-XPS was used to evaluate the oxidation state of operating ceria SOFC anodes. These experiments represent the first use of XPS as an *in situ* probe for high-temperature, solid oxide cells. This initial study yielded useful qualitative and quantitative information about the mechanism of H_2 reduction on thin-film ceria anodes. In particular, ceria becomes increasingly oxidized with increasing anodic currents, with the fraction of Ce reduced as Ce^{3+} decreasing from > 80% to ~50% as the measured bias varies from 0.0 to -1.0 V. The extent of Ce oxidation correlates with changes in polarization resistance, although more extensive studies are required to develop a quantitative mechanism. Spatial gradients in the Ce^{3+} fraction across the surface of the ceria electrodes exist with H_2 oxidation, which suggests that with negative bias voltage, electrochemical activity may become more localized due to the reduction in polaron activity with increased oxidation to Ce^{4+}. Furthermore, Ar-diluted tests demonstrate that these single chamber cells with *in situ* XPS results are relevant to phenomena from standard thin-film SOFC results

Further studies are needed to develop a more quantitative and fuller understanding of CeO_{2-x} role in solid oxide cells. The use of XPS to do extensive depth profiling in the ceria will be valuable for understanding the relevance of bulk-phase vs. surface ceria reduction. Furthermore, testing a broader range of fuel partial pressures and temperatures will provide a basis for developing a quantitative

mechanism for CeO_{2-x} materials in more conventional porous composite electrodes. It will also be valuable to expand the XPS studies to include CO and CO_2 and to assess the impact of carbonaceous fuels on the redox cycle of ceria in active high-temperature electrochemical cells. Ultimately, results from the AP-XPS studies will serve as an important measure of validation for the MIEC thin-film model described in chapter 2. Model validation against the various experimental results described above is the subject of the following chapter.

Chapter 4: Modeling Electrochemical Oxidation on Cerium Oxide Anodes – Validation of Thin-film MIEC Model Results

While many researchers have studied ceria-based electrodes [25, 38, 42, 51, 54, 56], little quantitative information exists regarding the oxidation pathways, rate-limiting steps, or thermo-kinetic parameters needed to predict oxidation results for ceria-based SOFC anodes. This lack of information motivates the current study, which aims to derive an oxidation mechanism for undoped ceria SOFC anodes. Preceding chapters have laid the groundwork for this derivation by describing the model formulation for 1-D isothermal simulations and the corresponding experimental characterization of thin-film, undoped ceria SOFC anodes. The use of dense, thin-film anodes effectively isolates the chemistry and overpotentials associated with the ceria while minimizing the impact from phenomena such as gas transport through porous media.

In this chapter, the model parameters described in chapter 2 are adjusted to determine the oxidation mechanism for small fuel species (H_2, CO) on ceria anodes. Model results will be validated using the experimental data of chapter 3, with model parameters adjusted to give the best fits to the polarization and in situ XPS results on the dense CeO_{2-x} films, as described in chapter 3.

4.1 Previous Research

4.1.1 Reduction Thermodynamics in Bulk-phase Ceria

Previous studies of ceria catalysis have explored the equilibrium state of the ceria under varying conditions via numerical and experimental techniques. Adachi and coworkers summarize standard enthalpies and Gibbs free energies of formation for several higher rare earth oxides, including ceria [134]. Reduction thermodynamics are given in terms of the oxygen evolution reaction, written below in Kröger-Vinck notation:

$$2\,\mathrm{Ce}_{\mathrm{Ce}}^{\mathrm{X}} + \mathrm{O}_{\mathrm{O}}^{\mathrm{X}} \leftrightarrow 2\,\mathrm{Ce}_{\mathrm{Ce}}^{'} + \mathrm{V}_{\mathrm{O}}^{\bullet\bullet} + \frac{1}{2}\mathrm{O}_2(\mathrm{g})\,. \qquad \text{(R 4.1)}$$

The authors note that ceria, with a standard enthalpy of reduction $\Delta H^{\mathrm{o}}_{\mathrm{rxn}} = 382$ kJ/mol at ambient temperature (298 K), is the most difficult to reduce of the rare earth oxides. Given the measured standard entropy of reduction $\Delta S^{\mathrm{o}}_{\mathrm{rxn}} = 127.4$ J/mol-K, this corresponds to a standard free energy of reduction $\Delta G^{\mathrm{o}}_{\mathrm{rxn}} = 258$ kJ/mol at $T =$ 700˚ C. While the reaction thermodynamics can change with temperature and with ceria non-stoichiometry, the measurements are of the same order of magnitude as the high-temperature measurements discussed below. These values thus provide a starting estimate for thermodynamic values used in this study, with parameters adjusted from this starting point to provide better fits to the data, as discussed below.

4.1.2 Computer Simulations of Ceria Surface Properties

Numerous researchers have utilized computer simulations to describe the surface properties of stoichiometric ceria, such as the surface energies, anion and cation mobility, and redox behavior. These studies are summarized in a 2002 review by Islam and Balducci [135]. Sayle and coworkers used static lattice methods to calculate the surface energies of the (110), (310), and (111) surfaces [136]. The structures of the (110) and (310) surfaces are similar those described in the model formulation in chapter 2 (figure 2.3) – charge-neutral with stoichiometric amounts of cations and anions in each plane. The (111) surface, meanwhile, terminates with a single anion plane, with three successive planes constituting a charge-neutral repeating unit. The results of Sayle et al. imply that the order of surface stability is ceria(111) > ceria(110) > ceria(310). This result is confirmed by Conesa, who also demonstrates substantial relaxation energies for these surfaces, highlighting their importance in quantitative simulations of ceria surfaces [137]. Vyas and coworkers replicated the same order of surface stabilities using four different interatomic potential models, demonstrating further that the relative surface energies are not sensitive to the potential model used [138].

Additionally, molecular dynamic (MD) and quantum mechanic (QM) studies have explored the behavior of anions and cations for several ceria surfaces. Most notably, NPT ensemble MD simulations by Baudin and coworkers [139] of 20-30 Å surface slabs with 2-D periodicity demonstrate higher mobility for oxide anions

relative to the Ce cations, and demonstrate that the displacement of ions is larger in the out-of-plane direction.

Regarding the redox behavior of the ceria surfaces, atomistic studies by Sayle and coworkers predict that the energy of reduction (R4.1) is approximately 2 – 4 eV lower at the surface than in the ceria bulk, and that this region of more favorable reduction extends ~ 10 Å into the ceria bulk [136, 140]. Furthermore, their results predict that the (110) and (310) surfaces are more easily reduced than the (111) surface. Islam and Balducci note that this increased activity has important implications for materials processing of ceria, and is likely related to the lower stability of the (110) and (310) surfaces, relative to the (111) surface [135].

4.1.3 Non-ideal Energetic Interactions between Reduced Cerium Cations

The thermokinetic model formulation in chapter 2 makes use of mass-action kinetics, which rely upon the assumption that species are dilute and non-interacting. In mass-action kinetics, variations in species concentration contribute to the partial molar free energy only through the configurational entropy, as in eq. 2.18. This assumption also applies to previous models describing charge transport in bulk MIEC materials via eq. (2.17). However, while the use of mass-action kinetics is computationally convenient and is shown to be accurate at low degrees of reduction, experimental measurements on CeO_{2-x} samples demonstrate significant non-ideality, with the Gibbs free energy of reduction departing significantly from dilute solution model predictions [38, 42, 96]. Mogensen and coworkers compile a number of measurements, which correlate the degree of reduction x in the formula CeO_{2-x} with

P_{O2}, via means of thermogravimetry, coulometric titration, and electrical conductivity measurements [38, 42]. The various measurements at 1100 ˚C show a remarkable degree of agreement. The equilibrium P_{O2} value for a given ceria sample relates to the free energy of reduction via the partial molar free energy of O_2:

$$\Delta\overline{G}_{O_2} = \overline{R}\,T \ln\left(\frac{P_{O_2}}{P^o_{O_2}}\right), \qquad \text{(eq. 4.1)}$$

where $P^{\circ}_{O_2}$ represents the standard-state partial pressure of O_2. For these conditions, the ideal gas model requires that the partial molar free energy of O_2 factors into the energy of reduction ΔG_{rxn} via oxygen abstraction (R 4.1):

$$\Delta G_{\text{rxn}} = \frac{1}{2} G^o_{O_2} + \overline{R}\,T \ln\left(\frac{P_{O_2}}{P^o_{O_2}}\right)^{\frac{1}{2}} + G_{Ce_2O_3} - G_{Ce_2O_4}. \qquad \text{(eq. 4.2)}$$

At equilibrium, $\Delta G_{rxn} = 0$, and thus:

$$G_{Ce_2O_3} - G_{Ce_2O_4} = -\frac{1}{2}\left[G^o_{O_2} + \Delta\overline{G}_{O_2}\right]. \qquad \text{(eq. 4.3)}$$

The same argument applies to the partial molar enthalpy and entropy of oxygen. In this manner, the data summarized by Mogensen is used to calculate the enthalpy and entropy of Ce_2O_3 as a function of x, relative to that of Ce_2O_4 [38]. For comparison,

the dilute solution model makes use of the assumption that $X_{Ce2O3} + X_{Ce2O4} = 1$ to predict the free energy of reduction ΔG_{red}, defined as $\Delta G_{red} \equiv G_{Ce2O3} - G_{Ce2O4}$:

$$\Delta G_{\text{red}}\left(T,\, X_{Ce_2O_3}\right) = \Delta G^{o}_{\text{red}} + \overline{R}\, T \ln\left(\frac{2\, X_{Ce_2O_3}}{1 - 2\, X_{Ce_2O_3}}\right). \qquad \text{(eq. 4.4)}$$

Figure 4.1 shows measured values of ΔG_{red} vs. x at T = 700 ˚C, alongside those predicted by the dilute solution model with a standard-state free energy change ΔG^{o}_{red} = 495 J/mol. The figure clearly shows divergence from the dilute solution model with increasing reduction, with agreement in the curve slopes for $x \leq 0.1$. Also notable is the local minimum at x ~ 0.18, related to phase change in the ceria bulk between the α phases $Ce_{10}O_{18}$ and $Ce_{14}O_{26}$, as shown in figure 4.2, adopted from

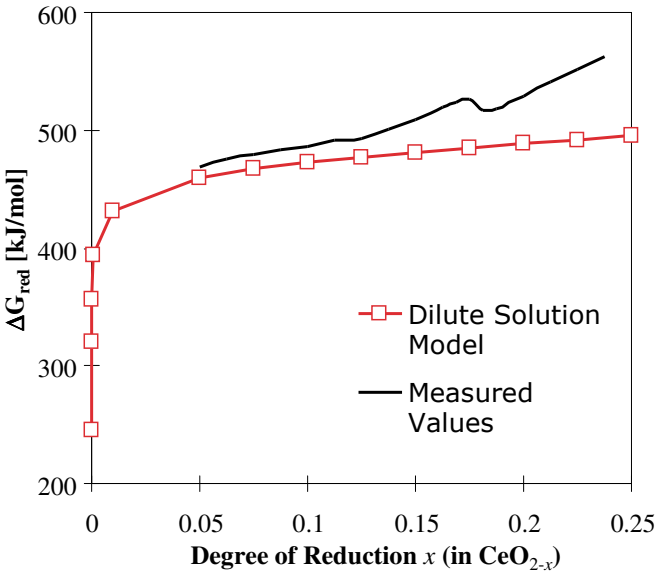

Figure 4.1. Measured values for the Gibbs free energy of ceria reduction, versus values predicted by the dilute solution model. Measured values adapted from [38].

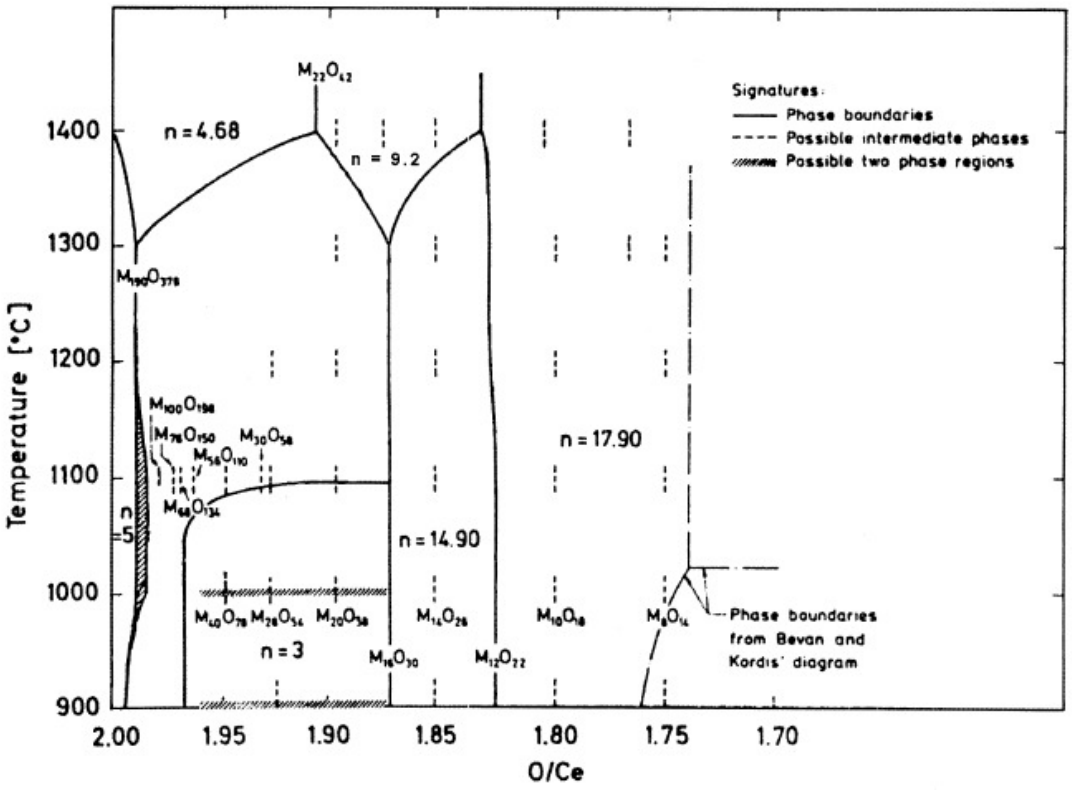

Figure 4.2. Phase diagram for CeO_{2-x}, with $1.70 \leq x \leq 2.00$. Adopted from Mogensen, et al. [38]

Mogensen, et al [38]. Measured values are available only for moderate degrees of reduction, $x \leq 0.25$. Because the degree of reduction in model predictions may exceed this value, the free energy of reduction for $x > 0.25$ is estimated for this study, as discussed below.

As noted above, the non-ideal interaction between reduced ceria cations implies that chemical reactions for moderate and high degrees of reduction are no longer governed by mass-action kinetics. Mass-action kinetics with constant rate coefficients rely on ideal thermodynamics of the reacting species, as in eq. 4.4, to

relate the forward and backward rate coefficients for a particular reaction. Because this form does not apply to the ceria free energy, an alternate rate expression must be derived for reactions involving ceria surface and bulk species.

Adler et al derive several possible rate-law expressions for oxygen exchange on MIEC cathodes, including systems where mass-action no longer applies [93]. The authors demonstrate that careful definition of the standard state and excess free energies allows use of a modified form of mass-action kinetics, such that the forward and reverse rates are proportional to the standard state free energy. In this formulation, the non-ideal interactions are incorporated explicitly into the forward and backward rate coefficients. The rate-of-progress for a reaction is written as:

$$q = k_{\text{fwd}} \prod_k [X_k]^{\nu'} \exp\left(-\frac{(1-\beta_{\text{ex}})\Delta E_{\text{ex}}}{\bar{R}T} \right) - k_{\text{bwd}} \prod_k [X_k]^{\nu''} \exp\left(\frac{\beta_{\text{ex}}\,\Delta E_{\text{ex}}}{\bar{R}T} \right), \quad \text{(eq. 4.5)}$$

where ΔE_{ex} is the shift in the reaction free energy due to non-ideal interactions, relative to the standard state, and β_{ex} is a symmetry parameter related to transition state theory. As illustrated in figure 4.3, β_{ex} dictates how much of ΔE_{ex} affects the energetic barrier to the forward reaction, and how much affects that of the reverse reaction.

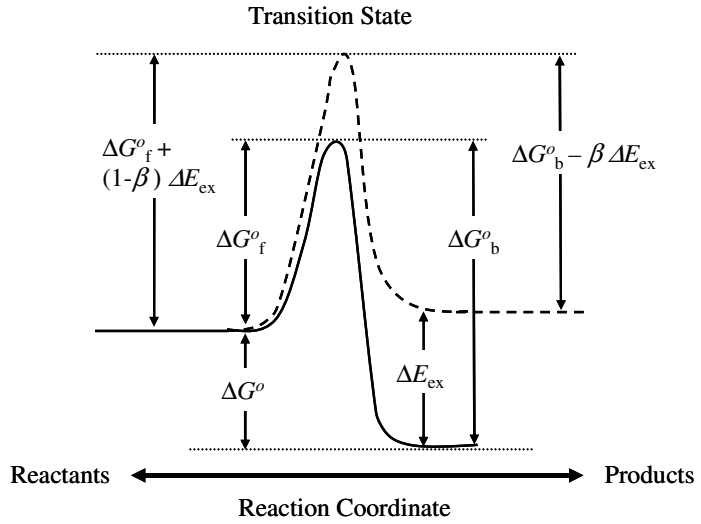

Figure 4.3. Conceptual plot of non-entropic free energy versus reaction coordinate for transition state theory**.** The solid line represents the free energy in the absence of non-ideal interactions. For the dotted line, transition state and product energies are shifted by ΔE_{ex} due to non-ideal interactions. Adapted from ref. [93]

In eq. 4.5, the forward rate coefficient k_{fwd} is user-specified, while k_{bwd} is determined as in mass-action kinetics, with the ratio of k_{fwd} to k_{bwd} determined by the standard-state free energy of reaction:

$$\frac{k_{fwd}}{k_{bwd}} = \exp\left(-\frac{\Delta G^o_{rxn}}{\overline{R}\,T}\right), \qquad \text{(eq. 4.6)}$$

where the standard Gibbs free energy of reaction ΔG^o_{rxn} is defined by Adler as:

$$\Delta G^o_{rxn} = \left(\mu^o_P - \mu^o_R\right) + \left(\varepsilon^o_P - \varepsilon^o_R\right). \qquad \text{(eq. 4.7)}$$

The subscripts P and R refer to products and reactants, respectively, μ^o is the standard-state chemical potential, and ε^o is the standard-state excess energy due to non-ideal interactions. The right-hand side of eq. 4.6, typically referred to as the 'equilibrium coefficient' in mass-action kinetics, is used to describe the ratio of the standard rate coefficients in this study. However, it cannot be used to predict the equilibrium distribution of species, as in systems governed by mass-action, since it neglects non-ideal interactions.

The value of ΔE_{ex} in eq. 4.5 and figure 4.3, then, is defined as the excess energy of reaction due to non-ideal interactions, minus that at standard conditions:

$$\Delta E_{ex} = \left(\varepsilon_{\mathrm{P}} - \varepsilon_{\mathrm{R}}\right) - \left(\varepsilon_{\mathrm{P}}^{o} - \varepsilon_{\mathrm{R}}^{o}\right). \qquad \text{(eq. 4.8)}$$

Using this formulation, non-ideal interactions are incorporated into mass-action type kinetics in a way that preserves thermodynamic consistency. Adler, et al. provides a full derivation of rate laws for systems with non-ideal interactions [93]. The application of eqs. 4.5 – 4.8 to the model described in chapter 2 is described below.

4.2 Derivation of Baseline Thermodynamic and Kinetic Parameters

4.2.1 Thermodynamic Parameters

The baseline set of thermodynamic and kinetic parameters was initially introduced in chapter 2, as tables 2.3 and 2.4. Table 2.3 gives the standard-state

thermodynamics, calculated according to the the baseline set of parameters, at T = 25 ˚C and 700 ˚C. The standard state thermodynamics for bulk and sub-surface species are adapted form the measurements of Adachi and coworkers, as noted above [141]. Previous measurements indicate that the enthalpy of formation for oxide vacancies in the ceria is significantly reduced by trace impurities in the sample [46, 47, 135]. Additionally, researchers have shown that reduction enthalpy reduces significantly for grain sizes less than ~100 nm [46, 47, 113]. For the films in this study, then (δ_{film} ~ 110 nm, δ_g ~ 40 nm) deviation from the measured thermodynamic values is expected, and the enthalpy and entropy of reduction in table 2.3 have been adjusted to give a moderate degree of reduction in the film bulk at equilibrium. Stoichiometric Ce_2O_4 in the bulk and subsurface and O_{Ce}(s) on the ceria surface are considered the reference for all surface and bulk species, and the standard Gibbs free energy for these species are set to zero at 25 ˚C. Using the NASA polynomials for the gas species as an additional set of reference values, the thermodynamic properties of ceria species are calculated using estimated reaction thermodynamic parameters (ΔH_{rxn} and ΔS_{rxn}) [142]. In the absence of pre-existing values for a given reaction or specie, order-of magnitude estimates were obtained by adapting the parameters from similar H_2 and H_2O adsorption reactions on Ni surfaces [2, 58, 66]. Given the superior catalytic activity of Ni relative to ceria, initial estimates for ceria were obtained by adjusting the Ni parameters to reduce the activity for fuel oxidation. While the model allows for thermodynamic differentiation between the bulk and sub-surface phases of the ceria, the baseline case holds the thermodynamics constant for the two phases.

4.2.2 Kinetic Parameters

Table 2.4, reprinted below as table 4.1, gives the baseline forward reaction rate parameters at T = 700 ˚C. Initial estimates were obtained in a manner similar to that described for the thermodynamics above, with order-of magnitude estimates based on similar catalytic reactions on Ni surfaces [2, 58, 66]. As discussed below, the results proved largely insensitive to k_{fwd} values other than k_3, k_6, and k_7. In the case of k_6 and k_7, baseline values were obtained by modifying initial estimates such that model results showed agreement with experimental results at low current density.

4.2.3 Non-ideal Interaction Potentials

While the baseline case results in chapter 2 are based solely on mass-action kinetics, it is expected that non-ideal interactions at moderate and high degrees of reduction will impact results significantly. The above measurements summarized by

Table 4.1. Baseline forward rate parameters for baseline thin-film results, T = 700 ˚C. [a]Sticking coefficient σ^o.

Reaction Equation	Reaction Rate Parameter	k_{fwd} value
Ceria Surface		
$H_2(g) + 2\ O_{Ce}(s) \leftrightarrow 2\ OH_{Ce}(s)$	$k_{1,fwd}$[a]	$1.00*10^{-3}$
$H_2(g) + O_{Ce}(s) + OH_{Ce}(s) \leftrightarrow OH_{Ce}(s) + H_2O_{Ce}(s)$	$k_{2,fwd}$[a]	$4.00*10^{-4}$
$2\ OH_{Ce}(s) \leftrightarrow H_2O_{Ce}(s) + O_{Ce}(s)$	$k_{3,fwd}$	$5.00*10^{9}$
$H_2O(g) + Vac_{Ce}(s) \leftrightarrow H_2O_{Ce}(s)$	$k_{4,fwd}$[a]	$1.00*10^{-4}$
$Ce_2O_4(sb) + Vac_{Ce}(s) \leftrightarrow Ce_2O_3(sb) + O_{Ce}(s)$	$k_{5,fwd}$	$1.00*10^{6}$
Ceria/YSZ Interface		
$O^{2-}_{YSZ} + Ce_2O_3(b) \leftrightarrow V^{\bullet\bullet}_{O,YSZ} + Ce_2O_4(b) + 2\,e^{-}_{Ce}$	$k_{7,fwd}$	$5.00*10^{-8}$

Mogensen are used to calculate the excess energy due to non-ideal interactions ΔE_{ex}, as in eqs. 4.5 and 4.8. For a given state, the free energy of reduction in the ceria bulk (as a function of x and T) is calculated for the ideal solution model. This value is subtracted from the measured value to find ΔE_{ex}. The excess energies of species on the ceria surface rely on the value of x in the sub-surface layer. Originally calculated ΔE_{ex} values were on the order of 10^8, a magnitude that led to unrealistic reaction rates, via eq. 4.5, and thus caused the simulations to fail at very low current densities (< 2 mA/cm^2), either because the tolerances could not be met without reducing step size below the minimum value, or because the ceria became 100% oxidized, and thus could not sustain higher currents. Additional investigation is required to determine the cause of this model failure. Calculated ΔE_{ex} values were thus multiplied by a scaling factor ζ, with $\zeta \sim 0.1$ giving the best results. The use of such a scaling factor may be related to the reports of decreasing free energy of reduction for nano-scaled ceria films, as in Chiang, et al. [113] and the work of Anderson and co-workers [46-49].

Figure 4.4 shows several free energy of reduction profiles utilized in this study, as a function of x. Each profile uses a different approximation for ΔG_{red} at high degrees of reduction, $x > 0.25$. Figure 4.4a uses a linear extrapolation of the $\Delta G_{red} - \log_{10}(x)$ plot to estimate the thermodynamics of highly reduced ceria. While this plot makes use of the available direct measurements, analysis of the phase diagram for CeO_{2-x} reveals a significant phase change at $x \sim 0.29$, between the α phase and various forms of the Θ phase [40]. While the exact value of x for this

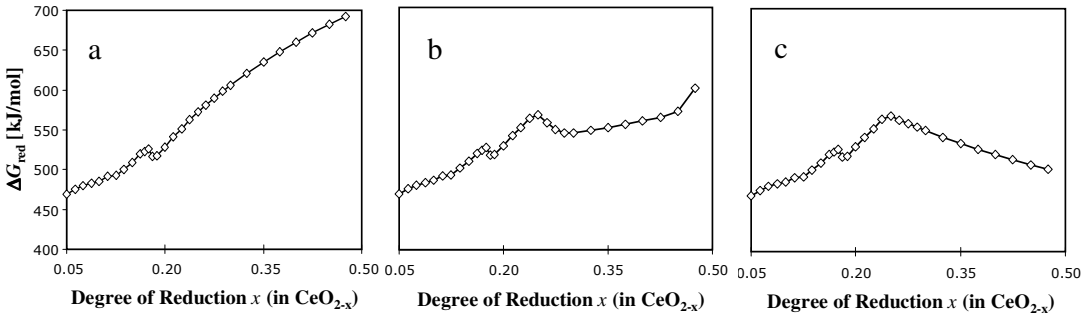

Figure 4.4. Free energy change of ceria reduction ΔG_{red}, vs. degree of reduction (x in CeO_{2-x}). ΔG_{red} estimates for $x > 0.25$: a) linear extrapolation of the ΔG_{red} vs. $\log_{10}(x)$ data for $x \leq 0.25$; b) constant ΔH_{red}, with an increase of 25 J/mol-K in ΔS_{red} at x = 0.25; c) constant increase in ΔS_{red} and constant ΔH_{red} for $x > 0.25$.

phase change varies with temperatures above 1000 ˚C, it is fixed at $x = 0.286$ for T below 1000 ˚C. This region of phase change corresponds with the upper limit of measured x values in reported literature values for $\Delta\overline{G}_{O_2}$. Because previous measurements report free energy barriers to oxidation for phase changes at lower x, figures 4.4b and 4.3c provide two estimates for the free energy of reduction in highly reduced ceria. In figure 4.4b, the slope and curvature of the free energy curve prior to phase change is replicated, but with a shift of 25 J/mol-K in the entropy of reduction curve. In figure 4.4b a more sustained free energy barrier is estimated, where ΔS_{red} increases linearly vs. $\log_{10}(x)$, at a rate of 247 J/mol-K/$\log_{10}(x)$. ΔH_{red} is held constant during both phase-change estimations, similar to the reported phase change at $x \sim 0.2$ [38, 42]. The fits discussed below use the profile in figure 4.4b.

4.3 Results and Discussion

To validate the model parameters, results were compared to the experimental data presented in chapter 3 for T = 700 ˚C. This data represents the most complete and consistent set of data collected on the dense thin-film ceria anodes. As such, temperature-dependent parameters such as reaction rate coefficients $k_{fwd/bwd}$ or ion conduction mobility v_{O2-} are estimated as temperature-independent parameters. The estimation of activation energies for the various processes is left as an extension of this work.

4.3.1 Comparison of Model Predictions and Experimental Results

Figure 4.5 compares model predictions to experimental polarization data for H_2 oxidation on ceria anodes at T = 700 ˚C with varying P_{H2}. The simulation reaction rate parameters have been manually optimized to obtain the closest correspondence between experimental data and model predictions, and are listed in table 4.2. In addition to the modified kinetic parameters, the oxide ion mobility v_{O2-} was reduced by two orders of magnitude from the baseline value, to $2*10^{-9}$ cm^2/V-s. This is most likely to account for surface and grain boundary contributions to the oxide conductivity, which are roughly three orders of magnitude lower than the bulk conductivity [40]. Given the small grain size (d_g = 40 nm) in these films, grain boundary effects have a significant impact on the oxide conductivity through the film thickness. Additionally, the forward symmetry parameter for charge transfer at the

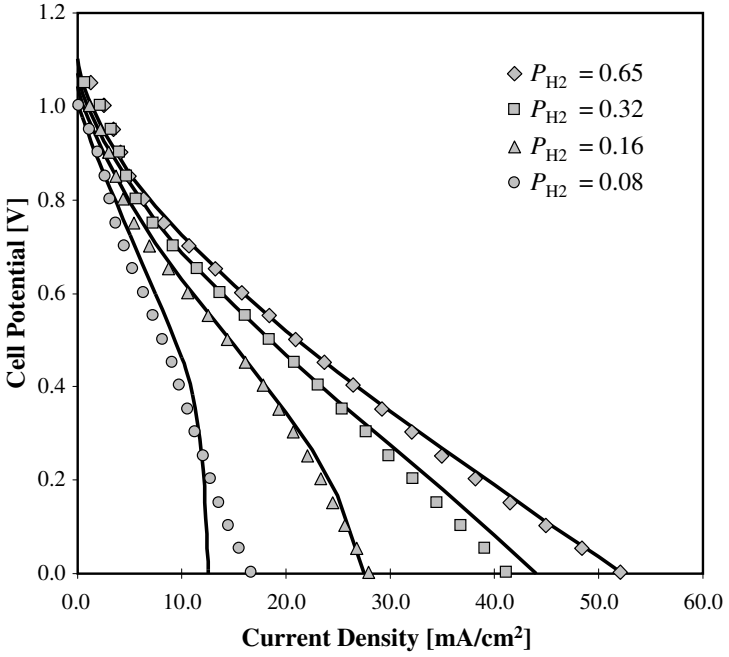

Figure 4.5. Comparison of experimental polarization data (symbols) with model predictions (lines) for H_2 oxidation on dense ceria at T = 700 ˚C. All pressures listed in atm.

Table 4.2. Optimized reaction rate parameters for H_2 oxidation on ceria, as in figure 4.5 [a]sticking coefficient σ^o.

Reaction Rate Parameter	k_{fwd} value
Ceria Surface	
$k_{1,fwd}$[a]	$1.0*10^{-4}$
$k_{2,fwd}$[a]	$3.0*10^{-5}$
$k_{3,fwd}$	$1.0*10^{6}$
$k_{4,fwd}$[a]	$1.0*10^{-3}$
$k_{5,fwd}$	$3.0*10^{6}$
Ceria/YSZ Interface	
$k_{7,fwd}$	$2.0*10^{-9}$

ceria/YSZ boundary was reduced from $\alpha_{fwd} = 0.5$ to $\alpha_{fwd} = 0.42$, to get the best fit to experimental data. Figure 4.5 shows a general qualitative agreement between simulated and experimental results, but with notable differences at low and high current densities, particularly with decreasing P_{H2}. At low current densities ($i_{ext} \leq 5.0$ mA/cm^2) the experimental curves show negative curvature, as the resistance R_{tot} increases rapidly. In the simulated curves, the predicted profiles are consistent with traditional Butler-Volmer kinetics, with high R_{tot} at OCV that decreases gradually as current density increases. Similarly, at moderate current densities for $P_{H2} < 0.65$ atm, experimental data shows a modest and discrete increase in R_{tot}. The best-fit simulation results match the polarization data in these regions by assuming concentration-limited behavior, marked by a gradual but continuous increase in R_{tot}, up to the limiting current density i_{lim}. This limiting current is most noticeable in the prediction for $P_{H2} = 0.08$ atm. Possible explanations for these discrepancies are discussed further below.

Figure 4.6 depicts the distribution of surface species, plus mole fraction of subsurface oxides (O^{2-}(sb)) as a function of current density for varying P_{H2}. The results demonstrate that the ceria surface is dominated by Vac_{Ce}(s) at open circuit. As the current density increases, the concentrations of O_{Ce}(s) and OH_{Ce}(s) increase, while $\theta_{VacCe(s)}$ decreases. The concentration of surface water molecules is in general very low, as in the baseline case (figure 2.5). However, in contrast to the baseline case, $\theta_{H2OCe(s)}$ decreases with increasing current density. This implies that the decrease in the water adsorption rate with decreasing $\theta_{VacCe(s)}$ is stronger than the drop in the

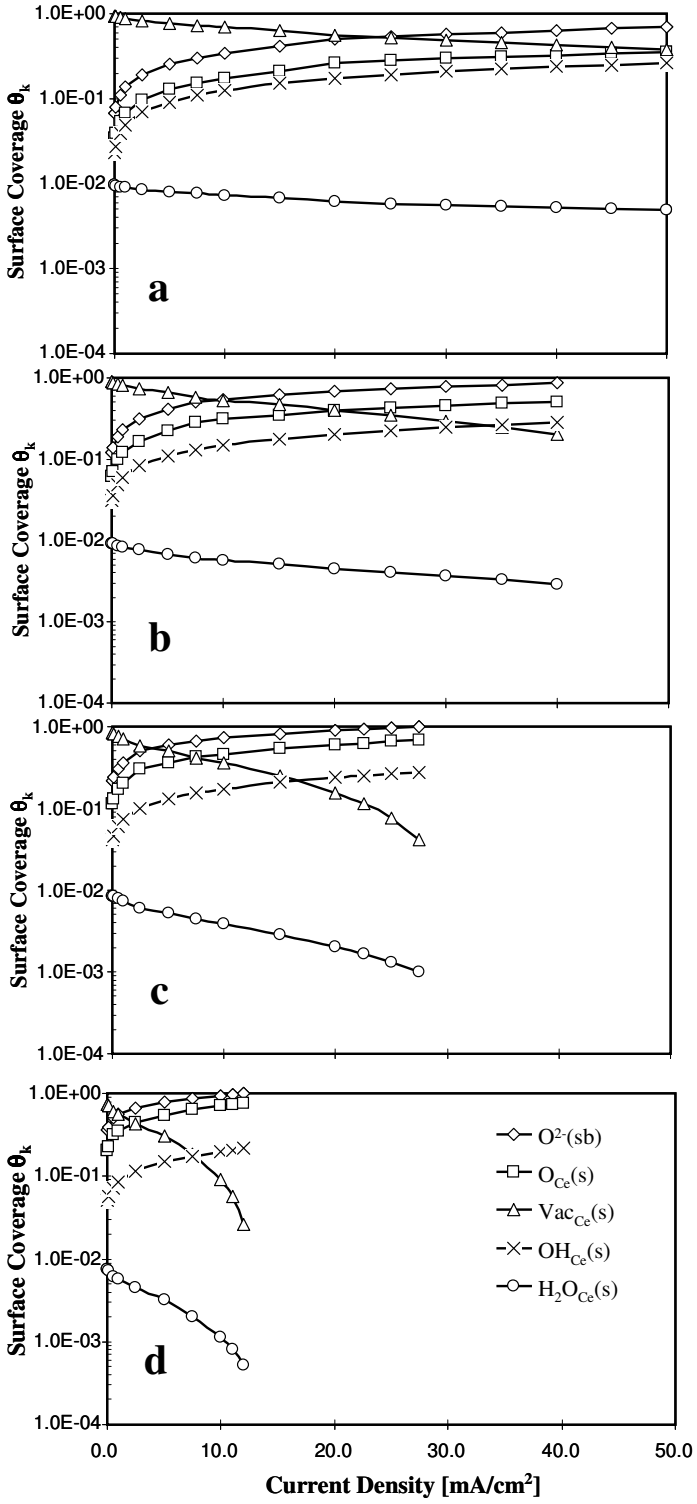

Figure 4.6. Surface and sub-surface species profiles for varying current density. a) P_{H2} = 0.65 atm; b) P_{H2} = 0.32 atm; c) P_{H2} = 0.16 atm; d) P_{H2} = 0.08atm

water desorption rate, since the net rate of desorption must increase proportional to the current density. For $P_{H2} < 0.32$ atm, figure 4.6c and d confirm the concentration-limitations in the model predictions of figure 4.5. As the limiting current approaches, the oxide mole fractions on the surface and in the sub-surface approach 100%, while the $Vac_{Ce}(s)$ and $H_2O_{Ce}(s)$ mole fractions drop precipitously.

Figure 4.7 shows the electric potential in the ceria bulk through the electrode thickness, for $P_{H2} = 0.32$ atm. As with the baseline case, the overall change in electric potential through the film thickness is quite small, although the gradients are quite sizable, due to the thin nature of the electrode. Most of the profiles are nearly linear, as with the baseline case in chapter 2. However, the Φ_{cat} profile for $i_{ext} = 5$ mA/cm^2 is non-monotonic versus the axial coordinate y, with the maximum potential

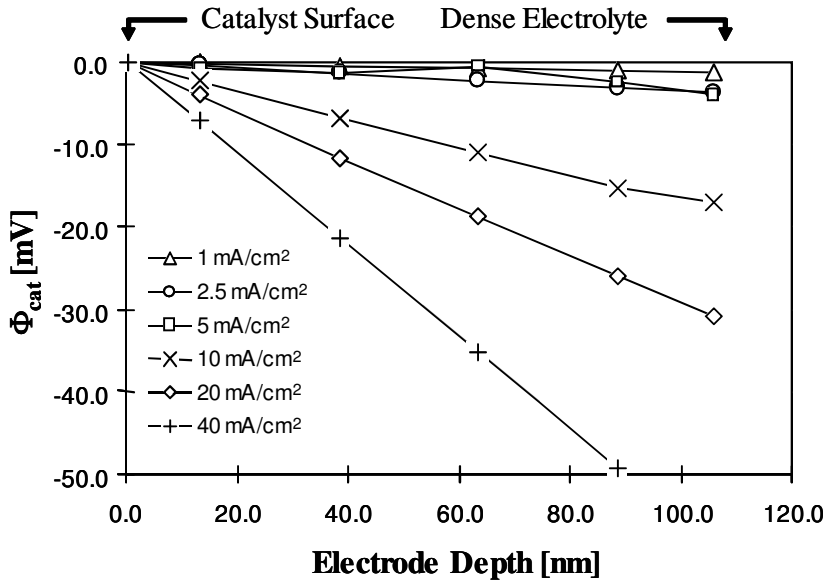

Figure 4.7. Ceria bulk electric potential profile $\Phi_{cat}(y)$ with varying current density.

at y ~ 70 nm from the electrode surface. Furthermore, the total drop in Φ_{cat} across the electrode does not increase from i_{ext} = 2.5 mA/cm^2 to 5.0 mA/cm^2.

This behavior is likely due to the phase change thermodynamics shown in figure 4.4b. As discussed in chapter 2, the value of Φ_{cat} is determined by an algebraic equation that requires charge neutrality in the ceria bulk. In the steady-state calculations of this work, the boundary condition at the ceria/YSZ interface requires that the flux of oxides must be equal to $i_{ext}/2F$ at steady state. Charge neutrality thus dictates that the diffusive flux of polarons (electronic charge, Ce^{3+}) must be zero at steady state. The Φ_{cat} profile at steady state must be such that the electrostatic driving force for polaron diffusion at any point must be equal and opposite the thermodynamic driving force. At a current density of i_{ext} = 0.5 mA/cm^2 and with P_{H2} = 0.32, the predicted mole fraction of oxides in the bulk ranges from 0.507 at the ceria sub-surface (as in figure 4.6b) to 0.587 at the ceria/YSZ interface. While the polaron concentration decreases steadily with y, figure 4.4b shows that the free energy of polarons in this range varies non-monotonically, giving rise to the electric potential profile in figure 4.7. Despite the unique nature of this predicted electric potential profile, it is noted that these deviations are on the order of 1 mV and have negligible impact on the polarization results, as shown in figure 4.5 for P_{H2} = 0.32 atm. Furthermore, any phase changes with variations in the degree of ceria reduction or fully reversible, indicated by the repeatability of the experimental polarization results in chapter 3.

Figure 4.8 shows the average ceria valence state as a function of current density for varying P_{H2}, calculated by multiplying the surface coverage θ_k of each surface species by its valence, as listed in table 2.2. By means of comparison with the *in-situ* XPS measurements discussed in chapter 3, the valence state is given as the percent of total cerium cations that have 3+ valence. As with the polarization results, the model results agree qualitatively with the measured valence states via *in-situ* XPS. At equilibrium/open circuit conditions, the film surfaces show a high degree of reduction (> 75% Ce^{3+}), with the film surfaces becoming increasingly oxidized for 60% reduced) for P_{H2} > 0.3 atm, even when the cell potential reaches 0 V (figure 4.5). increasing anodic current. For low P_{H2} (< 0.3 atm), the film surfaces are only ~20% reduced at limiting current densities, while surfaces show moderate reduction (40 – 60% reduced) for P_{H2} > 0.3 atm, even when the cell potential reaches 0 V (figure 4.4).

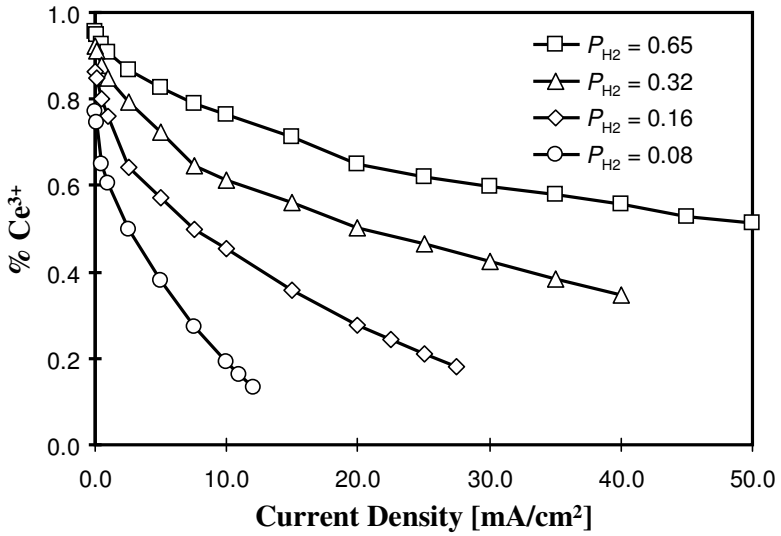

Figure 4.8. Average surface valence state during electrochemical oxidation of H_2 (% Ce^{3+} vs. total Ce cations).

While these predictions show much larger changes in valence state with anodic current than those measured in chapter 3, direct comparisons between the predictions and the measurements in chapter 3 are complicated by a number of differences between the two systems. XPS measurements were conducted at a lower temperature and with a lower P_{H2} value than the experimental results being simulated here. This would imply that the simulated values should always show a higher degree of reduction, with the XPS measurements serving as a lower bound for reasonable average surface valence states. However, one conclusion clearly supported by the measurements in chapter 3 is that the oxidation state is a function of both the experimental conditions *and* the local electrochemical current, with larger currents requiring more significant departure from equilibrium (i.e. higher degrees of oxidation/higher average valence). While the conditions modeled here are more reducing than in the measurements at ALS, the total currents are also significantly larger; higher average valence values are thus a reasonable prediction.

Additionally, direct comparison between model predictions and ALS measurements is complicated by the electrode configuration and cell geometry. As mentioned in chapter 3, the working and counter electrode leads in the ALS experiments were configured incorrectly, leading to uncertainty in the electric potential drop in the ceria anode. Furthermore, the single-chamber configuration relies on lateral charge transport between the two electrodes. This leads to non-uniformity in the distribution of local electrochemical currents, particularly as the film becomes oxidized and the electrical conductivity is diminished under anodic

polarization. Gradients in local electrochemical current on the ceria surface make it difficult to estimate an effective electrode area for normalization of the total current. Furthermore, because measured valence states are averaged over a relatively large spot size (~100 μm), gradients in the local valence state can lead to under-prediction of the maximum degree of oxidation. For these reasons, the *in situ* XPS measurements in chapter 3 remain a qualitative check on model predictions. The ability to conduct *in situ* XPS with a functioning two-chamber SOFC would represent a significant advance in this technique.

One consequence of the large degree of variation in predicted valence states is that the constant values assumed for O^{2-} ion and polaron mobilities in this model are most likely not valid. Previous conductivity measurements demonstrate that the mobilities vary by roughly an order of magnitude with the degree of reduction, with a broad maximum in mobility at approximately 20% reduction [38, 40, 137]. The decrease in mobilities for lower oxidation states is moderate, while the mobilities drop sharply for higher oxidation states. Thus, it is possible that the increase in R_{tot} seen at moderate current densities for low P_{H2} values is more accurately described by a significant reduction in ion mobility with increasing ceria oxidation, rather than the concentration-limited currents seen in the fits of figure 4.5.

4.3.2 Effect of Interaction Potential Model

To assess the impact of the specific thermodynamic model for highly reduced ceria ($x > 0.25$), simulations were run using three separate free energy profiles, as

depicted in figure 4.4. The polarization results for the three free energy profiles, displayed in figure 4.9, show negligible sensitivity to the specific thermodynamic model used. There is some differentiation between the models at very low current density, $i_{ext} < 5$ mA/cm^2, as shown in the inlay of figure 4.9, although at these low currents the difference amounts to several mV at most. It is noted, however, that the excess energy values in these simulations were multiplied by a scaling factor of 0.1, as described above, thereby reducing the potential impact of these separate models. Model refinements are needed, then, to incorporate more significant interaction potential contributions to species thermodynamics.

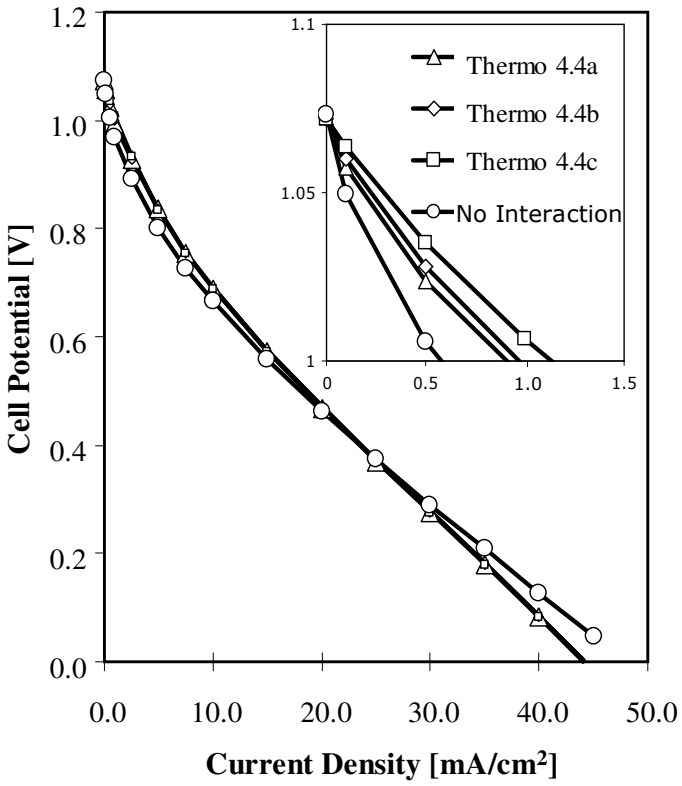

Figure 4.9. Variation of polarization results with varying free energy of reduction for $x \geq 0.25$. Specific models used are depicted in figure 4.4.

Given the insensitivity of results to specific interaction potentials, figure 4.9 also includes results with zero interaction potential. The results show a noticeable difference for zero interaction potential, with larger overpotentials at low currents, but lower overall resistance leading to lower overpotentials at high current densities. Inspection of the variations at low current density in figure 4.9 shows that the performance increases for models that assume lower ΔG_{red} values for $x > 0.25$. While quantitiative measurements of ΔG_{red} in this range have not been reported in the literature, the sesquioxide Θ phase ($x > 0.286$) is known for higher reactivity than phases with lower x values [40]. Significant changes in reactivity with changing degree of reduction, then, provide one possible explanation for the discrepancy between predicted and measured cell voltages near open circuit. The extension of thermodynamic measurements to higher degrees of reduction will thus be important for future simulations of electrochemical oxidation on ceria anodes.

4.3.3 Sensitivity of Model Predictions to Parameter Variation

To assess the sensitivity of model results to simulation parameter values, parameters were varied independently by an order of magnitude in either direction (with the exception of α_{fwd}, which was varied between 0.3 and 0.5) and the simulations for $P_{H2} = 0.32$ were re-run, with all other parameters held at the optimized values used in figure 4.5. The results of this sensitivity assessment are shown in figures 4.10 – 4.12. Each figure shows results for three separate parameter values, with the intermediate value equal to that used in figure 4.4. Reaction rate coefficients k_i refer to the forward rate coefficients $k_{i,fwd}$. Variations in k_1, k_3, and k_4

had negligible effect on simulation results, and so results for these variations are not shown.

Figure 4.10 shows the variation in simulation results with variations in the forward symmetry parameter α_{fwd} for charge-transfer at the ceria/YSZ boundary (R. 2.9). The results show that α_{fwd} has a significant impact on the curvature of the polarization curve, but does not alter the charge-transfer resistance. This result is consistent with electrochemical theory for charge-transfer reactions [94].

Figure 4.11 shows the variation in predicted polarization curves with changes in the oxide ion mobility, v_{O2-}. As one might predict, changes in v_{O2-} have a

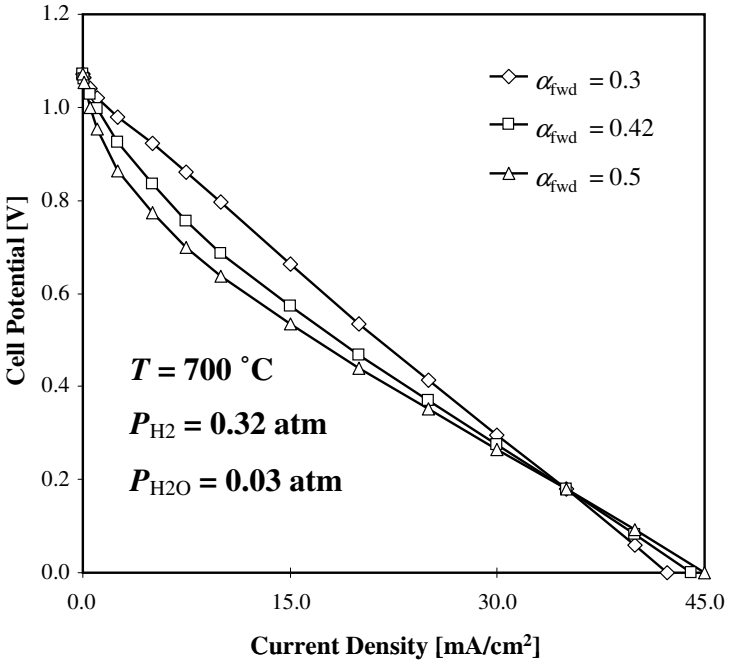

Figure 4.10. Variation of predicted polarization results with varying charge-transfer forward symmetry parameter $\alpha_{fwd.}$

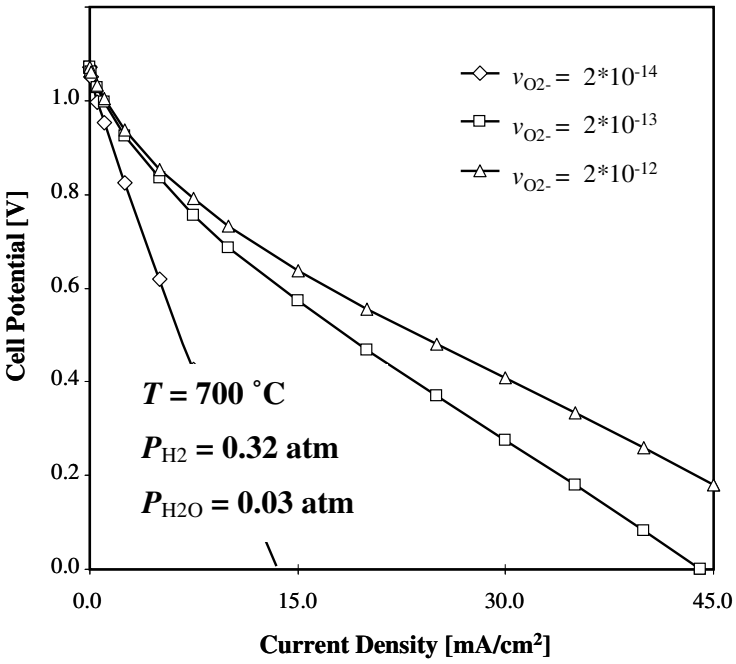

Figure 4.11. Variation of predicted polarization results with varying oxide ion mobility v_{O2-}.

significant impact on the polarization resistance, particularly in the linear portion of the curve. For small v_{O2-} values, this linear resistance is most noticeable at moderate-to-high current densities. For large values of v_{O2-}, however, the resistance to oxide diffusion is the dominant resistance at all current densities, and the total overpotential appears to be proportional to the current density.

Finally, figure 4.12 explores the sensitivity of simulation results to three kinetic parameters. It is noted that, for perturbation of the forward rate coefficients, thermodynamic reversibility requires that the ratio of forward and backward rate coefficients remains constant (in the absence of any changes to the thermodynamic parameters). Thus, any increases to $k_{i,fwd}$ are accompanied by proportional changes

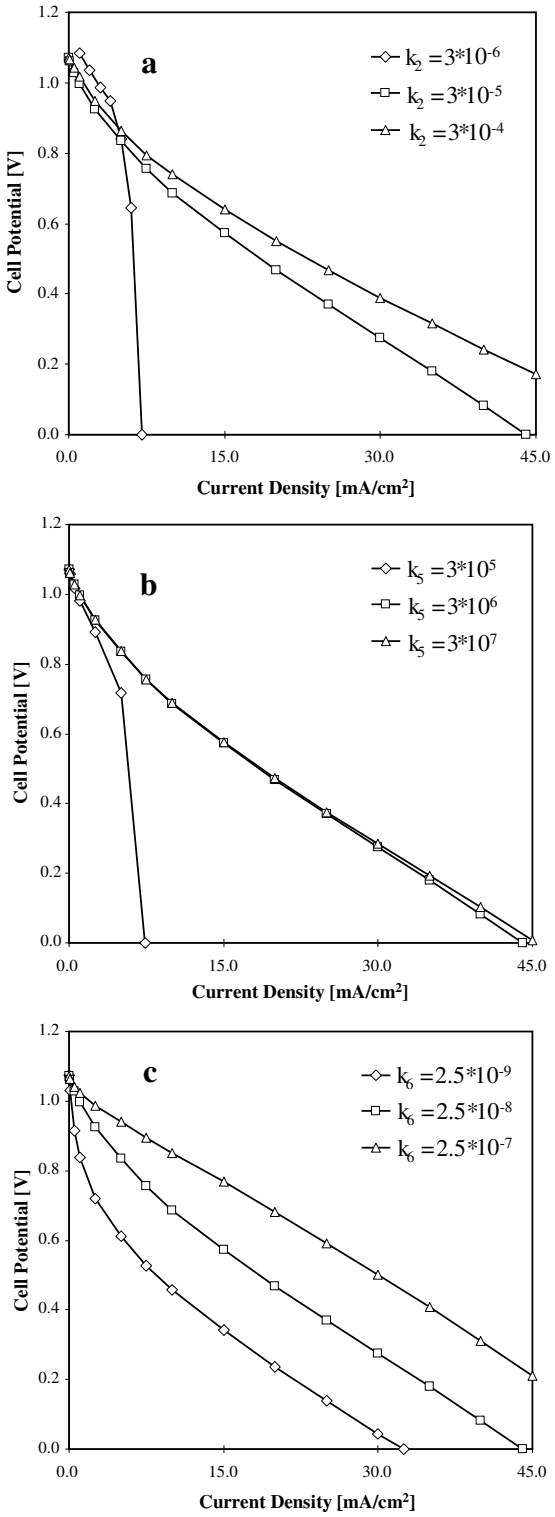

Figure 4.12. Variation of predicted polarization results with varying forward kinetic rate parameters. T = 700 ˚C, P_{H2} = 0.32 atm, P_{H2O} = 0.03 atm, a) k_2; b) k_5; and c) k_6.

in $k_{i,bwd}$. Altering the kinetic parameters, then, simply alters the speed at which a given reaction approaches thermodynamic equilibrium. The rate coefficients k_2, k_5,and k_6 govern the following reactions, reprinted here from chapter 2 for convenience:

- k_2: Gaseous H_2 adsorption:

$$H_2(g) + O_{Ce}(s) + OH_{Ce}(s) \xleftrightarrow{K2} OH_{Ce}(s) + H_2O_{Ce}(s). \qquad \text{(R 2.5)}$$

- k_5: Oxide exchange between ceria surface and sub-surface:

$$Ce_2O_4(sb) + Vac_{Ce}(s) \xleftrightarrow{K5} Ce_2O_3(sb) + O_{Ce}(s). \qquad \text{(R 2.8)}$$

- k_6: Charge-transfer via oxide/ hopping at the ceria/YSZ two-phase boundary:

$$O^{2-}_{YSZ} + Ce_2O_3(b) \xleftrightarrow{K6} V_{\ddot{O},YSZ} + Ce_2O_4(b) + 2e^-_{Ce}. \qquad \text{(R 2.9)}$$

Variations in the H_2 adsorption rate k_2, shown in figure 4.12a have a significant impact on polarization results. Increasing k_2 reduces the overall resistance, while reducing k_2 leads to very low limiting current values. Furthermore, the mismatch in OCV for reduced k_2 implies that the simulation never reaches equilibrium during the simulation, due to the very slow kinetics. Moreover, as the only gas-phase reaction for which parameter variation had a significant impact on simulation results, proper selection of k_2 is necessary in order for the simulation to correctly predict variation of polarization results with varying P_{H2}.

Variations in the subsurface-to-surface oxide hopping reaction coefficient k_5, shown in figure 4.12b, have an effect similar to variations in k_2, though perhaps less severe. Increasing k_5 improves the polarization performance only minimally. Likewise, the simulation with reduced k_5 was able to reach thermal equilibrium at OCV, in contrast to reductions in k_2. Still, reductions in k_5 cause limiting currents at i_{ext} ~ 8 mA/cm^2, implying that proper estimation of k_2 is necessary for accurate simulation results.

Figure 4.12c shows the variations in predicted polarization curves for variations in the charge-transfer reaction rate k_6. Unlike variations in α_{fwd}, changes in k_6 have a significant impact on the magnitude of activation overpotentials at low current density. The R_{tot} values at high current, however, appear unchanged by variations in k_6, and the effect of changing k_6 at high current densities appears simply as a "shift" of the entire curve.

4.4 Conclusions

In this chapter, the comparison of model predictions with experimental results for oxidation of H_2 on dense, thin-film CeO_{2-x} SOFC anodes allows for the estimation of important kinetic parameters governing the electrochemical oxidation process. Model predictions agree qualitatively with both polarization data for varying P_{H2} at T = 700 ˚C and *in situ* XPS data at T ~ 620 ˚C. The results show that the ceria surface is dominated by oxygen vacancies at open circuit, but that the concentration of O_{Ce}(s)

and $OH_{Ce}(s)$ on the ceria surface increase with increasing anodic current. Water vapor covers very little of the ceria surface (approximately 1% at OCV), and the model predicts that this concentration only decreases with increasing current.

Simulation results are sensitive to parameter variations for three main processes—H_2 adsorption on the ceria surface involving $O_{Ce}(s)$ and $OH_{Ce}(s)$, O^{2-} transport through the ceria bulk and to the surface, and charge transfer via oxide hopping at the Ceria/YSZ boundary. The results appear largely insensitive to H_2O adsorption/desorption rates, as well as to the specific thermodynamic model used to describe the free energy of reduction. Furthermore, while electric potential gradients in the ceria bulk can display non-linear and non-monotonic trends, model results predict that these effects have minimal impact on the total cell potential, and that the majority of the potential drop in the thin-film MIEC is at the ceria/YSZ double-layer.

While simulation predictions agree qualitatively with experimental results, discrepancies between the two at very low and moderate-to-high current densities suggest several areas for improvement in model predictions. At OCV, the experimental curves show a brief region of very low resistance that is not predicted by the simulations. At intermediate currents, the simulation accurately predicts the *V-I* relationships with varying P_{H2}. For $P_{H2} < 0.65$ atm, however, polarization curves see a sudden shift to moderately higher resistance as the cell potential drops toward zero. The simulations can correctly predict limiting current for varying P_{H2} due to concentration limitations at high current density, but the shape of the polarization

curve in the region of these limiting currents does not match the slope of the experimental data.

The parameter variations in this chapter focused solely on the effect of kinetic and transport parameters on model predictions for steady-state polarization behavior. While it is possible that further refinement of these parameters plus optimization of the thermodynamic parameters will improve the accuracy of model predictions, it is expected that correction of the model discrepancies described above will involve modeling changes in the ceria properties with changing degree of reduction. One explanation for the low resistance at very low currents involves enhanced reactivity in highly reduced ceria. As the ceria becomes oxidized with increasing anodic currents, the ceria reactivity decreases significantly, leading to polarization curves similar to those predicted by simulations in this chapter. Furthermore, at higher currents it is likely that high levels of oxidation lead to a significant decrease in the mobility of O^{2-} ions, leading to the increase in resistance seen in experimental results. Additional model refinements and improved thermodynamic models for ceria reduction are needed to test these hypotheses. Experimental measurements are published for the free energy of reduction of ceria with varying degrees of reduction, but these measurements do not currently extend to the degree of reduction relevant to this work. Accurate thermodynamic data for ceria with high degrees of reduction—whether from an extension of previous experimental measurements from computer simulation—can have a significant impact, then, on the modeling of ceria-based SOFC anodes.

Chapter 5: 1-D SOFC Model with Porous Electrodes – The Importance of Microstucture in SOFC Modeling

While previous chapters have utilized thin-film electrode geometries to isolate and characterize the role of ceria in fuel oxidation in SOFC anodes, actual SOFC systems will likely make use of ceria as one component in porous composite anodes that contain multiple other phases. Although ceria provides some electronic conductivity, composite metals are incorporated into the porous anodes to provide increased electronic conductivity and, as needed, higher reforming activity for carbonaceous fuels [4, 6, 25, 38, 51, 143]. As such, it is of interest to extend the oxidation mechanism formulated for thin-film ceria electrodes to a working 1-D SOFC model with state-of-the-art porous electrodes. Such a model will differ from the thin-film model described above in several ways, including the microstructure of the ceria particles, variations in gas-phase composition through the electrode thickness, and the chemical interaction with other catalyst phases.

Although much SOFC research focuses on developing new high-performance materials, it is known that electrode structure and microstructure significantly impact SOFC performance. For example, electrode functional layers and functionally graded architectures can be used to enhance SOFC performance [11, 70, 144]. Experiments by Zhao and Virkar show that porosity in Ni–yttria-stabilized zirconia (YSZ) cermet anodes greatly influences performance, especially at high current densities [70].

Recent studies by Barnett and others have shown how barrier-layer architectures can be used to influence non-electrochemical activity as well as overall electrochemical performance [26, 82]. Predictive models that quantitatively represent electrode microstructure can greatly benefit and accelerate the development of new high-performance electrode architectures.

While there have been many recent advances in the ability of SOFC models to predict electrochemical performance, the interrelation between microstructure and electrochemical performance is not sufficiently explained by current models. Changes in electrode microstructure most readily affect gas-transport properties, which in turn primarily affect cell voltage calculations via the concentration overpotential. Due to the frequent use of button-cell geometries, fuel utilization rates and concentration overpotentials in SOFC experiments are typically low. Thus, even within the electrochemically active region of the porous electrode, the verification of model predictions against experimental results does not typically depend on an accurate transport model.

High-performance real-world SOFC systems, however, will encounter significant fuel utilization rates, particularly as fuel flows reach the end of flow channels, as predicted by two-dimensional SOFC model results [111, 145, 146]. The optimization of electrode microstructures for real-world systems must therefore make use of models that accurately describe the dependence of electrochemical performance on gas-transport effects. Williford, et al, document the failure of

previous models to accurately predict this dependence, observing the unrealistic parameter assumptions made by many models in order to match experimental results with significant fuel utilization [80, 81].

The primary objective of this chapter is to determine the interrelationships of electrode microstructural parameters that affect SOFC performance. The chapter will first describe the formulation for a 1-D isothermal SOFC button cell model with porous composite electrodes. The model will then be validated against experimental data for the oxidation of H_2/H_2O on Ni-YSZ SOFC anodes as a function of varying anode microstructure. Zhao and Virkar report experimental button-cell performance using humidified H_2 over a wide range of Ni–YSZ anode support-layer porosities, but with fixed structures for the anode functional layer, cathode, and electrolyte [70]. The present study uses these insightful experiments as a vehicle to validate models and to explore how microstructural parameters (principally porosity φ_g and tortuosity τ_g) are interrelated. Validation against the Ni-YSZ data is useful, because the oxidation thermodynamics and chemistry for H_2/H_2O on these materials are relatively well-understood [20, 64, 66], allowing the model validation to focus on the estimation of microstructural parameters, which have a higher degree of uncertainty. Understanding the correct interrelationship between microstructure and electrochemistry will have a significant impact on the modeling of composite ceria anodes, in Chapter 6, as well as on the field of SOFC modeling, in general.

5.1 Previous SOFC Modeling Efforts

Published models present a wide range of general approaches to SOFC modeling. An overview of these approaches is given in chapter 2 of this work. The model presented in this chapter makes use of the approach described therein, including the use of transient numerical simulation and reversible elementary-step chemistry. As such, the review below focuses on modeling efforts that couple porous-media transport with electrochemical oxidation in SOFC anodes.

5.1.1 Characterization of Porous Media Microstructures

Models of porous composite electrodes are typically formulated in terms of phenomenological parameters to characterize the porous-media structure [7, 20, 58, 63, 82]. Key microstructural parameters are illustrated in Figure 5.1. Tortuosity τ_g is the average path length of diffusing gas molecules, normalized by the electrode thickness. Porosity φ_g is the volume fraction of the gas phase. Utilization thickness δ_{util} is the thickness of the electrochemically active portion of the electrode. The balloon shows relevant electrochemical parameters: electrochemically active surface areas a_{cat} and a_{elec}, and length of three-phase boundary, l_{TPB}. Although the parameters are often specified independently, results below show that they are in fact correlated.

There are significant challenges in acquiring the data necessary to fully characterize the microstructure and performance of porous electrode architectures. Electrochemical polarization data can provide important measures of how electrode microstructure can influence cell performance [70]. Performance measurements can

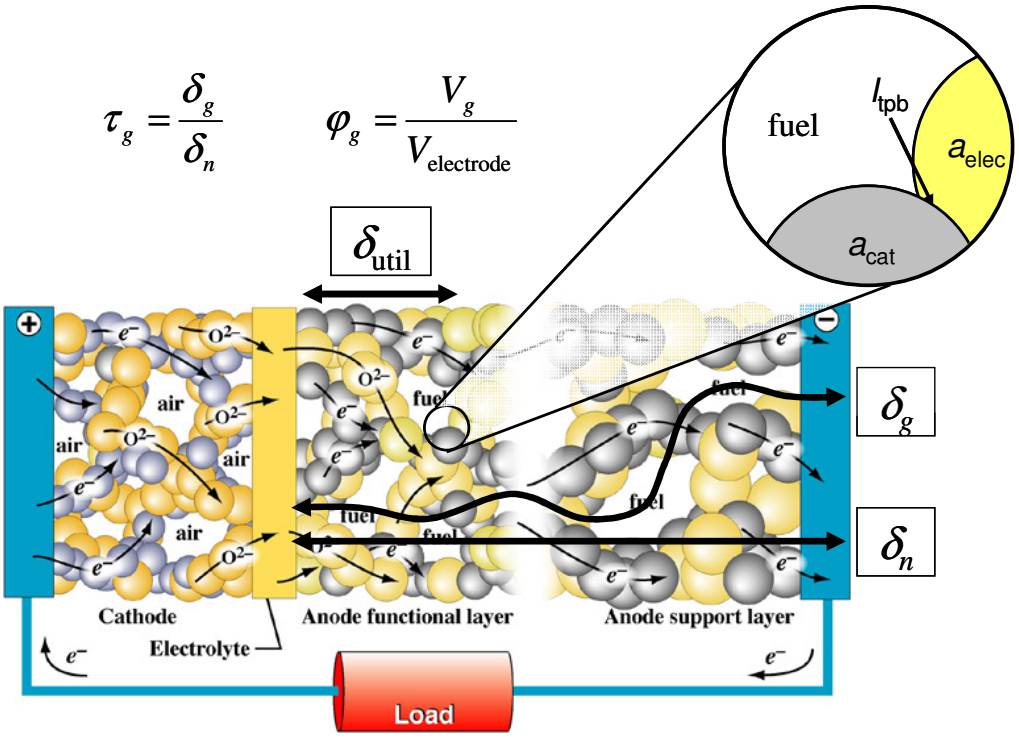

Figure 5.1. Illustration of key microstructural parameters related to modeling of porous SOFC electrodes. Modified from Kee, et al. 2008 [147].

be substantially augmented by direct microscopic observations, such as three dimensional tomographic reconstructions of electrode microstructure using dual-beam focused ion beam-scanning electron microscopy [148]. Although such mapping provides a detailed picture of electrode microstructure, practical SOFC computational models must still rely upon average phenomenological parameters to characterize porous-media transport and chemistry, given the disparities in length scale in a full SOFC membrane-electrode assembly (MEA). The model described below thus relies on macroscopic averaging over representative electrode volumes to obtain effective microstructural properties, as in previous models [1, 64, 65].

5.1.2 Gas-phase Transport in Porous SOFC Electrodes

The Knudsen number *Kn*—the ratio of the mean free-path length of the gas molecules to a representative length scale, such as pore diameter—serves as an important indicator of rate-limiting phenomena for gas diffusion in porous media. For $Kn >> 1$, molecule-wall collisions dominate transport phenomena, whereas for $Kn << 1$, molecule-molecule collisions dominate. In the pores of typical SOFC anodes, $Kn \sim 1$, and so both bulk gas-phase diffusion and Knudsen diffusion as well as pressure-driven Darcy flow must be considered. A number of approaches have been developed to describe diffusion in SOFC porous media. On the simplest level, transport is treated as a multi-component diffusion problem, with effective diffusion coeffcients calculated as:

$$D_{kl}^{e} = \frac{\varphi_g}{\tau_g} D_{kl}, \qquad \text{(eq. 5.1)}$$

where D_{kl} is the ordinary binary diffusion coefficient for species k and l. Greater accuracy is achieved by models that incorporate the effects of all three diffusion phenomena. Several such models have been developed, such as the mean pore transport model (MPTM) [149] and cylindrical pore interpolation model [62, 78], but perhaps the most commonly used model is the so-called 'Dusty Gas Model' (DGM) [1, 2, 7, 63, 65].

The DGM provides an implicit relationship between molar fluxes, molar concentrations, concentration gradients and pressure gradients that considers bulk and

Knudsen diffusion in parallel with Darcy flow [91, 150]. The multi-component transport model derived from kinetic theory treats the porous matrix as a stationary and uniformly distributed species and may be used over the entire range of *Kn* values [2]. The transport equations, summarized below, are illustrated in a series of papers by Zhu and Kee, who demonstrate qualitative agreement between model results and experimental results, and have used the DGM to explore a variety of fuel mixtures and cell architectures [1, 2, 63, 65, 82, 83].

5.1.3 Distributed Electrochemistry Models

Many previous SOFC models represent charge transfer reactions as taking place at the two-dimensional interface between the electrode and electrolyte [65]. These interface models assume that the resistance to oxide diffusion through the electrolyte particles in composite electrodes restricts electrochemical activity to a vanishingly small region near the dense electrolyte. In reality, O^{2-} ions diffuse into the depth of the composite electrode, and electrochemical reactions are distributed across a finite "utilization thickness" δ_{util}, as depicted in figure 5.1 [68]. Given the disparity in length scales between δ_{util} (< 20 μm) and the total electrode thickness (on the order of 1 mm), the interface assumption gives reasonably accurate predictions of diffusion and electrochemical phenomena.

While the interface model is accurate within a limited range of operating conditions, recent efforts have included a more detailed description of the underlying physical and electrochemical phenomena in anode utilization regions. One reason for

this development is the trend toward thinner MEA architectures, as documented by Zhu and Kee [65]. For thinner anodes, the utilization region represents a more significant portion of the total electrode, and cannot be neglected. Furthermore, while variations on the order of several microns in δ_{util} will not significantly impact the total resistance to gas diffusion, results below demonstrate that increasing the O^{2-} diffusion length on the order of microns represents a significant increase in the total Ohmic resistance of the MEA. As such, separate models by Bessler [64] and by Zhu and Kee [65] outline a framework for simulation of porous SOFC electrodes with distributed electrochemistry. The current model largely follows the approach for heterogeneous chemistry/electrochemistry of these recent studies, but this study differs significantly by implementing these approaches to fit model parameters for representing experimentally observed characteristics. This provides a basis for evaluating how microstructural parameters influence SOFC performance and, in particular, Ni–YSZ anode performance.

5.2 Model Formulation

The model is based on physical conservation laws that are derived as continuum partial-differential equations and then discretized with a finite-volume method and solved computationally. As illustrated in figure 5.2, the membrane MEA is composed of seven distinct elements: (*i*) fuel chamber, (*ii*) porous anode support layer (ASL), (*iii*) porous anode functional layer, (*iv*) dense electrolyte membrane, (*v*) porous cathode functional layer, (*vi*) porous cathode support layer, and (*vii*) air chamber.

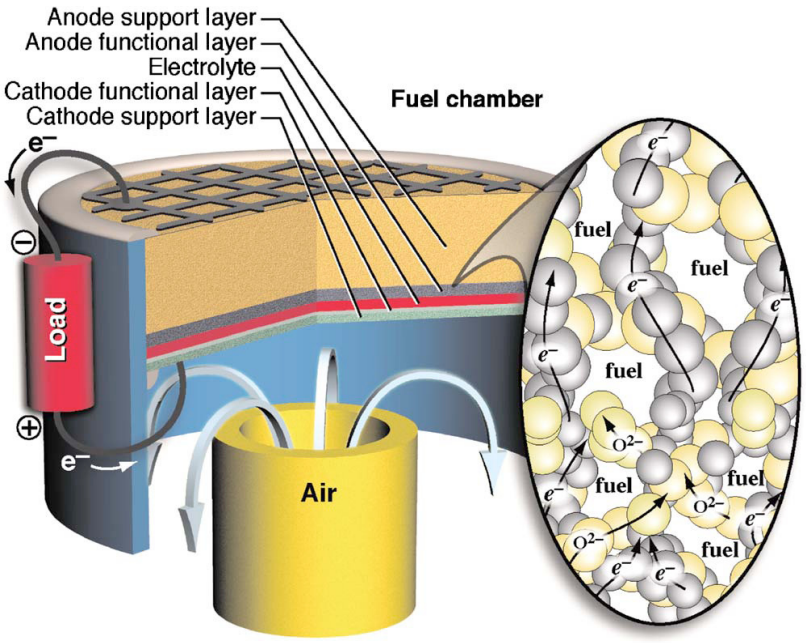

Figure 5.2. Layout of a typical button cell. The balloon illustrates ion and electron current paths near the interface between the anode support layer and anode functional layers. Particle sizes are typically smaller in the functional layer, where charge-transfer chemistry proceeds.

The Ni–YSZ anode provides structural support with a relatively thick (1.0 mm here) ASL whose relatively high porosity provides low resistance to gaseous transport. Between the ASL and the dense electrolyte, a thin (20 μm in this study) Ni–YSZ functional layer has low porosity and high surface area to promote electrochemical reactions. There is a similarly thin (20 μm) functional layer for the lanthanum strontium manganite (LSM)–YSZ cathode, which has a relatively thin support layer (50 μm) that facilitates gaseous O_2 transport and current collection. The high specific catalyst and electrolyte areas (a_{cat} and a_{elec}) and high three-phase

boundary length per unit volume l_{TPB} in the functional layers facilitate the surface and charge-transfer reactions necessary for electrochemical oxidation of the fuel in the anode or reduction of O_2 in the cathode.

In this study, H_2 and H_2O are the only gases in the anode feed, and thus all non-equilibrated chemistry (including charge-transfer reactions) is confined to the electrode functional layers. Although thermal surface chemistry can occur throughout the electrode thickness, the high resistances associated with adsorbate surface diffusion and bulk ion transport significantly limit the spatial extent of the charge-transfer regions. Non-electrochemical surface chemistry, such as hydrocarbon-reforming or water-gas-shift processes, can occur in the support layers [2]. However, in the present study with H_2/H_2O anode feeds and air as the cathode-side oxidizer, the heterogeneous surface reactions outside of the electrochemically active region are in equilibrium under steady-state conditions, and thus do not impact voltage–current relationships.

The governing conservation equations capture the following physical phenomena for both the anode and the cathode: (*i*) convective and diffusive transport from the bulk gas chambers to the electrode surfaces, (*ii*) gas transport through porous electrode structures, described by DGM, (*iii*) reversible heterogeneous chemistry, including adsorption/desorption and charge-transfer reactions, and (*iv*) transport of O^{2-} ions in the electrolyte phase (YSZ) and electrons in the electrodes (Ni or LSM) as described by Ohm's law. The model is isothermal, and as such does not include any

formulation of the energy equation. While non-isothermal effects may become important in SOFC systems with internal reforming, where endothermic reforming reactions utilize the heat provided by exothermic oxidation reactions, previous non-isothermal models for H_2 oxidation indicate extremely low temperature gradients in the through-cell direction [151].

5.2.1 Gas-phase Mass and Species Conservation

Assuming ideal gas behavior, the gaseous state is defined by temperature T, density ρ_g, and the gas-phase mass fractions Y_k. The gas-phase species and overall mass-continuity equations are written as

$$\varphi_g \frac{\partial \rho}{\partial t} = \sum_{k_g=1}^{K_{gas}} \left(-\nabla J_{k,g} + W_k \left(a_{cat} \dot{s}_{k,g,cat} + a_{elec} \dot{s}_{k,g,elec} \right) \right); \qquad \text{(eq. 5.2)}$$

$$\varphi_g \rho \frac{\partial Y_k}{\partial t} = -\nabla J_{k,g} + W_k \left(a_{cat} \dot{s}_{k,g,cat} + a_{elec} \dot{s}_{k,g,elec} \right)_k - Y_k \sum_{k_g=1}^{K_{gas}} \left(-\nabla J_{g,k} + W_k \left(a_{cat} \dot{s}_{k,g,cat} + a_{elec} \dot{s}_{k,g,elec} \right) \right) . \qquad \text{(eq. 5.3)}$$

$J_{k,g}$ are the gas-phase mass fluxes for gas-phase species k, whose evaluation is discussed in a subsequent section. The molar production rates of gas-phase species k by heterogeneous reactions on the catalyst and electrolyte surfaces are represented as

$\dot{s}_{k,g,cat}$ and $\dot{s}_{k,g,elec}$, respectively. The specific areas (area per unit volume) available for catalytic and electrochemical charge-transfer chemistry are a_{cat} and a_{elec}, respectively. The molecular weight for species k is W_k. K_{gas} represents the total number of gas-phase species. The independent variables are time t and the spatial coordinate y. The species and overall continuity equations are not all independent. Thus, the species-continuity equations are applied for all but one of the species, and the remaining species mass fraction is evaluated as

$$Y_{K_{gas}} = 1 - \sum_{1}^{K_{gas}-1} Y_k \ . \qquad \text{(eq. 5.4)}$$

5.2.2 Conservation of Surface Species

On the catalyst and electrolyte surfaces, the surface coverages $\theta_{\text{k,m}}$ for species k on phase m (electrolyte or electrode) are represented as

$$\frac{\partial \theta_{k,m}}{\partial t} = \frac{1}{\Gamma_m}\left(\dot{s}_{k,m} + \frac{l_{\text{TPB}}}{a_m} \dot{s}_{k,m,tpb} \right) \ . \qquad \text{(eq. 5.5)}$$

In this equation, Γ_m is the available surface sites per unit area, and $\dot{s}_{k,m}$ and $\dot{s}_{k,m,tpb}$ are surface production rates per unit area a_m and charge-transfer reaction rates per unit length of three-phase boundary l_{TPB}. In general, the reaction rates depend on local gas-phase state (i.e., temperature, density, and composition), surface-species

coverages, and electric-potential differences between phases. Reaction rate equations are discussed in greater detail, below.

5.2.3 Charge Conservation

Two separate approaches toward distributed electrochemistry are described in this chapter. The initial approach assumes that all charge-transfer reactions take place within a single finite volume adjacent to electrode/electrolyte interfaces. In such a formulation, one half the thickness of this volume serves as δ_{util}, and is prescribed by the model inputs. As discussed below, fitting Zhao and Virkar's experimental data with this model identifies δ_{util} as a critical parameter for explaining the link between microstructure and electrochemical performance [73]. As such, relying on a user-specified, constant δ_{util} neglects the forces that influence this parameter, and limits the usefulness of this model as predictive tool for microstructure optimization.

With this in mind, a second model was developed to allow charge-transfer reactions in all volumes, with the state variables determining the local ionic, electronic, and charge-transfer (Faradaic) currents. This model follows closely the frameworks outlined by previous efforts [64, 65]. The first model is henceforth referred to as the "fixed δ_{util} model," while the second formulation is referred to as the "distributed electrochemistry model." For both models, the charge balance in a given volume must incorporate the sources and sinks due to the Faradaic current i_{far} and the currents due to electric-potential gradients. Equation 5.6 describes the conservation of charge in these electrochemically active regions [66] as

$$C_{dl}\,\frac{\partial \Delta\Phi_{\mathrm{el}}}{\partial t} - \frac{\partial}{\partial y}\left(\sigma^{e}_{\mathrm{cat}}\,\frac{\partial \Phi_{\mathrm{cat}}}{\partial y}\right) = \pm l_{\mathrm{tpb}}\, i_{\mathrm{far}}\,. \qquad \text{(eq. 5.6)}$$

The electric-potential difference between the catalyst-phase electric potential Φ_{cat} and the electrolyte-phase electric potential $\Phi_{\mathrm{electrolyte}}$ is defined as $\Delta\Phi_{\mathrm{el}} \equiv \Phi_{\mathrm{cat}} - \Phi_{\mathrm{electrolyte}}$. The effective conductivity of phase *m* per unit of geometric area is σ^{e}_{m}. The double-layer capacitance per unit total volume C_{dl} [F/m^3] can be extracted from equivalent-circuit modeling of experimental data [68, 152]. The actual value of C_{dl} only impacts transient calculations and thus has no effect on the steady-state polarization curves reported herein. Thus, estimated values of C_{dl} are sufficient. The Faradaic current density i_{far} (i.e., the local charge-transfer rate between phases at the three-phase boundaries) is calculated from the charge-transfer reaction rates $\dot{s}_{k,m,tpb}$, as discussed below. The ± on the left side of equation 5.6 depends on whether the catalyst phase in the composite electrode has a Faradaic current that produces or consumes electrons.

While charge can be capacitively stored in the double-layer at the electrode/electrolyte interface, the double-layer itself is a charge-neutral entity—the charge stored in one phase is matched by an equal and opposite charge in the other phase. Local charge neutrality thus leads to equation 5.7.

$$\frac{\partial}{\partial y}\left(\sigma^{e}_{\text{cat}}\frac{\partial \Phi_{\text{cat}}}{\partial y}\right) = -\frac{\partial}{\partial y}\left(\sigma^{e}_{\text{electrolyte}}\frac{\partial \Phi_{\text{electrolyte}}}{\partial y}\right). \qquad \text{(eq. 5.7)}$$

Under steady-state conditions in the fixed δ_{util} model, $i_{\text{far}} = 0$ and $i_{O}{}^{2-} = 0$ outside of the electrochemically active region, and hence $\partial\Phi_{\text{electrolyte}}/\partial y = 0$. Thus, the electric potential in the catalyst phase collapses to Ohm's law, for this model:

$$i_{\text{ext}} = -\sigma^{e}_{m}\frac{\partial \Phi_{m}}{\partial \text{y}}. \qquad \text{(eq. 5.8)}$$

Here, i_{ext} is the external current density, a user-specified boundary condition for the simulation. In the current study, σ^{e}_{m} for the porous electrode structures are calculated using a simple Bruggman correlation where $\sigma^{e}_{m} = \varphi_{m}^{3/2}\cdot\sigma_{m,\text{bulk}}$, where φ_{m} is the volume fraction of conductive phase m and $\sigma_{m,\text{bulk}}$ is the bulk conductivity of phase m. Along with eq. 5.8, the user-specified i_{ext} determines the gradient in Φ_{cat} at the fuel/air chamber interface. Furthermore, application of eq. 5.7 over the entire electrode volume requires that i_{O2-} at the electrode/electrolyte interface matches i_{ext}. Therefore, eq. 5.8 and i_{ext} determine the gradient in $\Phi_{\text{electrolyte}}$ at this interface.

For the fixed δ_{util} model, integration of eq. 5.6 in the electrochemically active region and the application of eq. 5.8 throughout the rest of the electrode and electrolyte thicknesses determine the steady-state cell potential $V_{\text{cell}} = \Phi_{\text{cathode,int}} - \Phi_{\text{anode,int}}$, where the subscript 'int' refers to the electrode interface with the fuel/air

chamber. For the distributed electrochemistry model, integration of eq. 5.6 and application of eq. 5.7 are used to determine V_{cell}.

The current study, like many previous SOFC modeling studies, assumes that equilibration time scales in the electrolyte are much faster than electrode processes. Thus, transient changes in local bulk electrolyte composition can be neglected. Given the correspondence between the measured high frequency impedance and the electrolyte resistance, as discussed in chapter 3, this assumption is reasonable. This implies that the total charge-transfer currents at the two electrodes must be equal at any given time, which is always true for steady-state conditions. Thus, the voltage gradient across the dense-electrolyte membrane can be calculated from Ohm's law according to eq. 5.8 for a given i_{ext}, where $\sigma^{e}_{\text{electrolyte}} = \sigma^{e}_{\text{electrolyte,bulk}}$, as the electrolyte is assumed to be a fully dense and pure ionic conductor.

5.2.4 Gas-phase Transport Equations

As noted above, the DGM is an implicit relationship among the gas-phase molar concentrations, concentration gradients, molar fluxes, and the pressure gradient [1, 91]. This relationship can be inverted [1] to provide the gas-phase species mass flux J_{k} as

$$J_{k,g} = -W_k \left[\sum_l \left(D_{DGM,kl} \nabla [X_l] \right) + \sum_l \left(\frac{D_{DGM,kl} [X_l]}{D^{e}_{Kn,l}} \right) \frac{B_g}{\mu} \nabla P \right]. \quad \text{(eq. 5.9)}$$

In this equation, $[X_l]$ is the molar concentration of species l, B_g is the permeability (evaluated according to the Cozeny–Karman relationship [1]), μ_g is the mixture dynamic viscosity, P is the pressure, and $D^e_{Kn,l}$ is the effective Knudsen diffusion coefficient for species l. The effective DGM diffusion coefficients [1] are determined as a matrix inverse $D_{\mathrm{DGM},kl} = H^{-1}$, where the elements of the matrix H are

$$h_{kl} = \left[\frac{1}{D^e_{Kn,k}} + \sum_m \frac{X_m}{D^e_{km}} \right] \delta_{kl} + (\delta_{kl} - 1) \frac{X_k}{D^e_{kl}} . \qquad \text{(eq. 5.10)}$$

The effective ordinary multi-component diffusion coefficients are evaluated as in eq. 5.1, where the coefficients D_{km} are determined from the binary diffusion coefficients in the usual way [98]. The Knudsen diffusion coefficients $D^e_{Kn,k}$ are evaluated as

$$D^e_{Kn,k} = \frac{2}{3} \frac{\varphi_g}{\tau_g} r_p \sqrt{\frac{8RT}{\pi W_k}} , \qquad \text{(eq. 5.11)}$$

where r_p is the pore radius and R is the universal gas constant. Note that both the ordinary and Knudsen diffusion coefficients are modified by the ratio φ_g/τ_g. This ratio reflects two impacts of the porous media on diffusion velocities: (*i*) Multiplication by φ_g reflects the fact that only a portion of the electrode geometric area is available for gas diffusion, and (*ii*) division by τ_g correlates the actual diffusion velocity inside the tortuous pores with the diffusion velocity in the axial direction.

Equations 5.2, 5.3, 5.5, and 5.6 form a boundary-value problem whose solution requires boundary conditions related to Y_k, T, Φ_{cat} and $\Phi_{electrolyte}$ at the interfaces with the dense electrolyte and the bulk-gas compartments. Because the dense electrolyte is impervious to gas transport, $J_k = 0$ at the electrode/electrolyte interfaces. At the gas-compartment interfaces, the mass transfer is determined by considering a gas-phase mass-transfer boundary layer in the bulk gas. The flux-continuity at the interface is expressed as

$$J_{k,\text{int}} - Y_{k,\text{int}} \sum_l J_{l,\text{int}} = \frac{Sh_k \; D_{k,\text{mix}}}{L_{\text{ch}}} \left(\rho_{\text{ch}} Y_{k,\text{ch}} - \rho_{\text{int}} Y_{k,\text{int}} \right). \quad \text{(eq. 5.12)}$$

In this expression the subscript 'int' indicates the electrode/gas-channel interface and the subscript 'ch' indicates the gas composition in the flow channel far from the interface. The mixture-averaged diffusion coefficient of species k with respect to the mixture composition in the gas compartment is $D_{k,\text{mix}}$. The Sherwood numbers Sh_k are related to the flow field, generally scaling with a Reynolds number. The characteristic length scale L_{ch} may be taken as the distance between an inlet tube (illustrated on the air side in Figure 5.1) and the electrode interface. For the results shown in this paper the Sherwood numbers are fixed as $Sh_k = 3.5$. Because the resistance to gas transport in the bulk-gas boundary layer is small compared to the porous-media resistance, the results are found to be insensitive to the Sherwood number. Moreover, the interface composition is found to be nearly equal to the bulk-gas composition.

5.2.5 Surface and Electrochemical Reaction Rates

All surface reactions are simulated as reversible reactions, with rates calculated using the Cantera software package according to mass-action kinetics [153]. For reversible reactions, Cantera uses user-specified forward-reaction rate coefficients and thermodynamics to evaluate the reverse reaction rate coefficients [66, 98]. For adsorption–desorption reactions, forward (adsorption)-rate coefficients are calculated as sticking coefficients

$$k_{\mathrm{fwd}} = \frac{s^0}{\Gamma_m^{\nu}} \sqrt{\frac{RT}{2\pi W_k}}\,, \qquad \text{(eq. 5.13)}$$

where s^0 is the sticking probability and ν is the sum of the surface adsorbates' stoichiometric coefficients [98]. The forward-rate expressions for other surface reactions are described in Arrhenius form as

$$k = AT^{\beta} \exp\left(-\frac{E_a}{RT}\right). \qquad \text{(eq. 5.14)}$$

As described by Bessler et al.. [20], the rate expressions for reactions involving charge transfer follow from mass-action kinetics as

$$k_{\text{fwd}} = k_{\text{fwd}}^{*} \exp\left(\frac{\alpha_{\text{fwd}} n_{\text{elec}} F \ \Delta\Phi_{\text{el}}}{RT} \right); \qquad \text{(eq. 5.15)}$$

$$k_{\text{bwd}} = k_{\text{bwd}}^{*} \exp\left(-\frac{\alpha_{\text{bwd}} n_{\text{elec}} F \ \Delta\Phi_{\text{el}}}{RT} \right). \qquad \text{(eq. 5.16)}$$

The thermal component of the rate expressions, k_{bwd}^{*} and k_{fwd}^{*}, are expressed in Arrhenius form, as in eq. 5.14. The Faraday constant is F. The forward and backward symmetry parameters are α_{fwd} and α_{bwd}. In this study, the charge transfer reaction rates follow the stipulation for elementary reactions that $\alpha_{\text{fwd}} + \alpha_{\text{bwd}} = 1$ [99]. The number of electrons transferred in a reaction is given as n_{elec}.

The net rate of species production $\dot{s}_k$ depends upon summing the rate-of-progress q_{i} over all reactions

$$\dot{s}_k = \sum_i \nu_{i,k} q_i \ , \qquad \text{(eq. 5.17)}$$

where $\nu_{i,k} = \nu'_{i,k} - \nu''_{i,k}$ is the net stoichiometric coefficient of species k in reaction i. The reaction rate-of-progress is evaluated as

$$q_i = k_{\text{i,fwd}} \prod_k^K [X_k]^{\nu'_{ik}} - k_{\text{i,bwd}} \prod_k^K [X_k]^{\nu''_{ik}} \ , \qquad \text{(eq. 5.18)}$$

where $\nu'_{i,k}$ and $\nu''_{i,k}$ are the stoichiometric coefficients of species k for reaction i in the forward and backwards directions, respectively, and $[X_k]$ is the generalized activity of species k. The generatlized activity for gas-phase species is the molar concentration, and the activity for surface species is the site density [98]. That is, for surface species

$$[X_k] = \frac{\theta_k \Gamma_m}{\zeta_k}, \qquad \text{(eq. 5.18)}$$

where ζ_k is the number of sites occupied by species k. In the present study, each surface species occupies one site, $\zeta_k = 1$.

Thermodynamic consistency is necessary to ensure microscopic reversibility and hence to assure that $k_{i,fwd}$ and $k_{i,bwd}$ are consistent with the asymptotic approach to chemical equilibrium. In elementary electrochemistry, this consistency includes the prediction of open-circuit potential [66]. Many fuel cell models incorporate the notion of an equilibrium Nernst potential, from which various overpotentials are subtracted (as in eq. 2.1). Here, however, when elementary charge-transfer chemistry is used, there is no need to evaluate the Nernst potential. Rather, the faradaic current density (i_{far} in eq. 5.6) for a given volume is simply $\dot{s}_k$ for the electron in the Ni bulk multiplied by F. Predicting open-circuit potential (i.e., cell potential when there is no current flow) is thus the natural result of thermodynamic consistency.

In the present effort, thermodynamic properties and reaction-rate expressions are derived from a number of sources. As described by Bessler et al., forward and backward reaction rates are used to derive reaction thermodynamic parameters $\Delta H^{o}_{\mathrm{rxn}}$ and $\Delta S^{o}_{\mathrm{rxn}}$, both of which are assumed constant [20]. Using the NASA polynomials as a set of reference thermodynamics for gas-phase species, and setting surface and bulk vacancies to selected reference values, in the same manner described by Goodwin, reaction thermodynamic parameters are used to calculate the unknown thermodynamics for surface and bulk species [66, 142].

For the non-electrochemical reactions on the Ni anode catalyst, kinetic rate parameters are adopted from Janardhanan and Deutschmann [58]. The forward kinetic parameters and thermodynamics for charge-transfer reactions on a Ni–YSZ anode and for surface reactions on the YSZ surface are taken from studies by Goodwin and Bessler [20, 64, 66]. Finally, the kinetic rate parameters for O_2 reduction on an LSM–YSZ cathode are derived from data reported by Jiang et al [15]. Table 5.1 provides thermodynamic properties for all species at 25°C and 800°C. Table 5.2 lists all reactions and associated forward-rate parameters.

Table 5.1. Thermodynamics of species at 25 °C and 800 °C.

	$h^0_{k,25^\circ C}$ [kJ/gmol]	$s^0_{k,25^\circ C}$ [J/gmol*K]	$h^0_{k,800^\circ C}$ [kJ/gmol]	$s^0_{k,800^\circ C}$ [J/gmol*K]
Gas Phase Species				
O_2	1.63e-8	204.15	25.27	246.06
H_2	1.33e-8	130.68	22.90	168.38
H_2O	-241.83	188.82	-212.77	235.69
Ni Surface Species				
$[\,]_{Ni}$	0.0	0.0	20.02	33.08
O_{Ni}	-237.48	19.36	-204.82	72.90
H_{Ni}	-40.61	28.33	-9.14	80.25
OH_{Ni}	-214.62	18.31	-173.75	85.05
H_2O_{Ni}	-302.62	87.58	-253.54	167.52
YSZ Bulk and Surface Species				
$[\,]_{YSZ(s)}$	0.0	0.0	47.75	78.91
$O^{2-}_{YSZ(s)}$	-182.63	29.54	-122.25	128.91
$[]_{YSZ(b)}$	0.0	0.0	47.75	78.91
$O^{2-}_{YSZ(b)}$	-182.63	29.54	-122.25	128.91
OH^-_{YSZ}	-244.09	47.70	-172.25	165.91
$H2O_{YSZ}$	-294.06	51.24	-217.25	177.01
LSM Surface Species				
$[]_{LSM}$	0.0	0.0	32.22	53.24
O_{LSM}	-84.35	19.46	-39.50	93.16

Table 5.2. Reactions and forward rate parameters used in simulations.
[a]Sticking coefficient s^o.

Reaction Equation	A_{fwd} [gmol, cm, s]	β	$E_{act,fwd}$ [kJ/mol]	α_{fwd}	Source
Ni Surface					
1. $H_2 + 2\,[]_{Ni} \leftrightarrow 2\,H_{Ni}$	1.00e-02[a]	0	0		[154]
2. $O_2 + 2\,[]_{Ni} \leftrightarrow 2\,O_{Ni}$	1.00e-02[a]	0	0		[154]
3. $H_2O + []_{Ni} \leftrightarrow H_2O_{Ni}$	1.00e-01[a]	0	0		[154]
4. $O_{Ni} + H_{Ni} \leftrightarrow OH_{Ni} + []_{Ni}$	5.00e+22	0	97.9		[154]
5. $H_2O_{Ni} + []_{Ni} \leftrightarrow OH_{Ni} + H_{Ni}$	2.27e+21	0	91.76		[154]
6. $2\,OH_{Ni} \leftrightarrow O_{Ni} + H_2O_{Ni}$	3.00e+21	0	100.00		[154]
LSM Surface					
7. $O_2 + 2\,[]_{LSM} \leftrightarrow 2\,O_{LSM}$	1.00e-04[a]	0	0		[15]
YSZ Surface					
8. $H_2O + []_{YSZ(s)} \leftrightarrow H_2O_{YSZ(s)}$	1.00e+00[a]	0	0		[92]
9. $O^{2-}_{YSZ(b)} + []_{YSZ(s)} \leftrightarrow []_{YSZ(b)} + O^{2-}_{YSZ(s)}$	5.00e+07	0	0		[92]
Ni/YSZ Three-phase boundary					
10. $H_{Ni} + O^{2-}_{YSZ(s)} \leftrightarrow []_{Ni} + OH_{YSZ} + e^-_{Ni(b)}$	1.00e+16	0	90.0	0.5	[92]
11. $H_{Ni} + OH^-_{YSZ} \leftrightarrow H_2O_{YSZ} + e^-_{Ni(b)}$	1.00e+15	0	90.0	0.5	[92]
LSM/YSZ Three-phase boundary					
12. $O_{LSM} + []_{YSZ(s)} + 2\,e^-_{LSM(b)} \leftrightarrow O^{2-}_{YSZ(s)} + []_{LSM}$	5.00e+17	0	158.2	0.65	[15]

5.3 Simulation Procedure

Simulating an SOFC polarization curve requires a series of steady-state calculations for a range of specified current densities i_{ext}. In transient form and after finite-volume discretization of the spatial operators, the system of governing equations forms a system of differential-algebraic equations (DAEs). The DAE system is solved within the Matlab framework using the function ODE 15s. For each i_{ext} the solution is determined by integrating the transient system to a steady state. For the baseline set of 'fixed δ_{util} model' parameters, the simulation completed a sweep of 28 steady-state calculations, with $i_{ext} \leq 2.5$ A/cm^2, in a time of 2.5 h on a 3.6 GHz processor.

Many physical and chemical parameters are needed to describe a particular MEA. Some parameters, such as physical dimensions, are easily established from the cell structure. Table 5.3 lists the parameters used to represent the baseline cell. The anode support layer is discretized into eight equal finite-volume cells, while the anode functional layer, cathode functional layer, and cathode support layer are discretized separately into four equal finite-volume cells.

In the active electrode functional layers, surface areas for the electrocatalyst and electrolyte, a_{cat} and a_{elec}, respectively, are estimated by assuming an average primary particle for each phase to be a 2.5 μm diameter hemisphere. This estimate provides a basis for specifying the values in table 5.3. The value for l_{TPB} per unit

Table 5.3. Model parameters for baseline cell.

	Anode	Cathode
TPB length, l_{TPB} [m^{-2}]	3e13	3e13
Average pore radius, r_p [μm]	0.5	0.5
Average particle diameter, d_p [μm]	2.5	2.5
Utilization thickness, δ_{util} [μm]	5	5
Support layer thickness [μm]	1000	50
Support layer porosity, φ_g	0.32	0.45
Support layer tortuosity, τ_g	3.5	2.9
Functional layer thickness [μm]	20	20
Functional layer porosity, $\varphi_{g,int}$	0.23	0.26
Functional layer tortuosity, $\tau_{g,int}$	4.5	4.5
Catalyst fraction of solid phase	0.6	0.5
Catalyst surface site density, Γ_{cat} [mol/cm^2]	1.66e-9	1.66e-9
Catalyst surface area a_{cat} [m^{-1}]	1e7	1e7
Electrolyte surface site density, Γ_{elec} [mol/cm^2]	1e-9	1e-9
Electrolyte surface area, a_{elec} [m^{-1}]	1e7	1e7
Double layer capacitance, C_{dl} [F/m^3]	0.003	0.2

volume in table 5.3 is estimated by assuming the 2.5 μm particles are well mixed. The final value for l_{TPB} is adjusted such that the low overpotential activation losses fit the experimental measurements of Zhao and Virkar [70].

As mentioned above, another important parameter used in this simulation is derived from the concept of a "utilization region," which Adler discusses with regard to SOFC cathodes in a 2004 review paper [68]. This region is the thickness δ_{util} of the electrode in which ionic current is converted to electronic current by charge-transfer reactions (or vice versa, in the case of O_2 reduction in the cathode). In the case of composite Pt–YSZ cathodes, Adler observes that δ_{util} can range from 0.4 to 20 μm,

with typical values from 3 to 5 μm. The value of δ_{util} can be influenced by the thickness of the functional layer, which explains why Zhao and Virkar observed reductions in overpotential with increases in the cathode functional layer thickness up to 20 μm but not with increases beyond 20 μm [70]. Temperature and species composition can also influence δ_{util}, and thus δ_{util} is not necessarily equal to the thickness of the functional layer [68]. Physically, any increase in δ_{util} provides additional l_{TPB}, a_{cat}, and a_{elec} for charge transfer and other key surface reactions, but also increases the average path length of migrating O^{2-} ions. Although functional-layer microstructures are identical for all cells modeled here, δ_{util} may vary as a function of $\varphi_{g,anode}$ due to its dependence on gas-phase transport and H_2 concentration in the electrochemically active region. Because the cathode microstructure is held fixed in this study, the $\delta_{util,cathode}$ remains constant for all simulations.

5.4 Results

Zhao and Virkar report experimental results concerning the influence of electrode microstructure on button-cell performance [70]. They studied MEAs with varying anode support-layer porosity $\varphi_{g,anode}$, anode support-layer thickness δ_{anode}, electrolyte thickness $\delta_{electrolyte}$, and cathode functional-layer thickness. Varying $\varphi_{g,anode}$ was found to influence cell performance greatly. The present effort uses this study to quantify the direct and indirect influences of $\varphi_{g,anode}$ on polarization characteristics. Figure 5.3 (which is a reproduction of Zhao and Virkar's figure 9) shows the measured polarization characteristic for widely varying $\varphi_{g,anode}$, with the

characteristics of the anode functional layer held constant. These experiments were operated at T = 800°C and P = 1 atm. The cathode was supplied with dry air and the anode with humidified hydrogen (i.e., 97% H_2 and 3% H_2O). The external current density i_{ext} was varied from 0 to 3.5 A/cm^2. The anode support layer provides the bulk of the MEA thickness for typical SOFC designs, and as such $\varphi_{g,anode}$, $\tau_{g,anode}$, and other anode geometrical parameters can greatly impact mass transport and electrochemical performance. To explore the impact of these geometric parameters, this study focuses on anode-side microstructural variations while fixing the cathode side parameters according to the baseline-cell conditions listed in table 5.3. In this sense, the present study follows the experimental exploration of Zhao and Virkar,

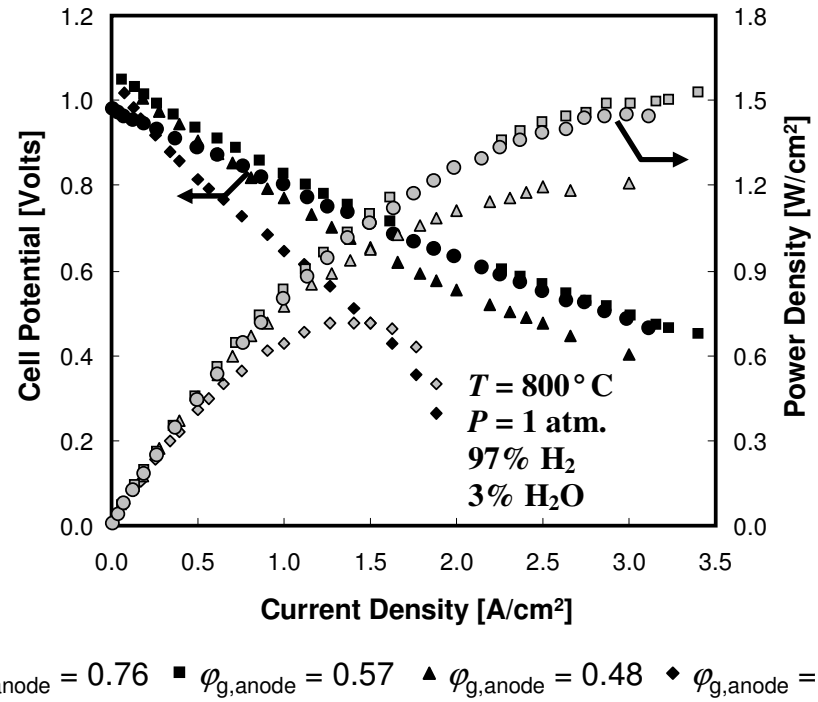

Figure 5.3. Experimental polarization and power-density measurements with varying anode support porosity $\varphi_{g,anode}$. From Zhao and Virkar [70].

who systematically varied φ_g in the anode support layer while holding all other parameters fixed, including those in the anode functional layers. However, other microstructural parameters, such as $\tau_{g,anode}$, may be covariant with $\varphi_{g,anode}$, and thus it becomes important to establish those relationships for SOFC model validation and design.

5.4.1 Fixed δ_{util} model

Before attempting to model the experimental data of figure 5.3, $\varphi_{g,anode}$ and $\tau_{g,anode}$ are varied independently from to assess the sensitivity. Figure 5.4 shows the

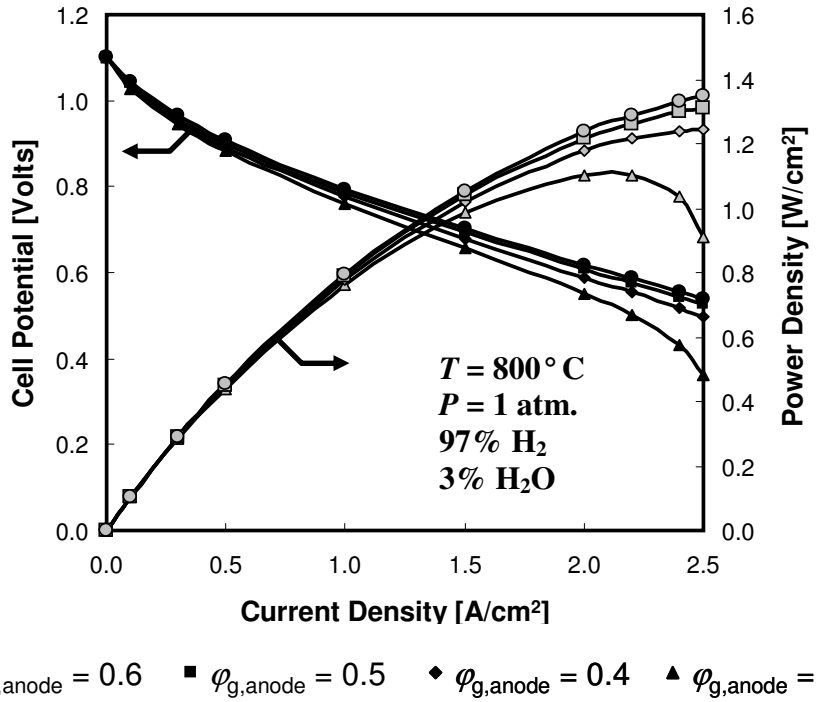

Figure 5.4. Simulated polarization and power density with varying anode support porosity but with all other parameters fixed at baseline values.

impact of varying $\varphi_{g,anode}$ from 0.30 to 0.60, a range that is typical of practical MEA architectures [70, 81, 155]. As illustrated in figure 5.4, the simulation shows a relatively weak dependence on $\varphi_{g,anode}$ alone. At low-to-moderate i_{ext} (i.e., <1.5 A/cm^2), V_{cell} for the entire porosity range differs by less than 50 mV. For the lowest porosity ($\varphi_{g,anode}$ = 0.30), gas diffusion becomes rate-limiting for i_{ext} > 1.5 A/cm^2, and there is a rapid increase in concentration overpotentials, resulting in V_{cell} dropping off quickly. However, $\varphi_{g,anode}$ does not have a significant impact on the other polarization curves. By contrast, the experimental evidence in figure 5.3 shows that porosity has a significant impact on polarization. For the model to explain these data, there must be other significant parameter(s) of the anode microstructure that vary with $\varphi_{g,anode}$.

One such co-varying parameter is likely $\tau_{g,anode}$. Williford et al. report experimentally determined $\tau_{g,anode}$ vs $\varphi_{g,anode}$ curves for SOFC MEAs with Ni–YSZ cermet anodes using various measurement techniques [81]. Their results suggest two reasonable conclusions about $\tau_{g,anode}$: (*i*) $\tau_{g,anode}$ generally ranges from 2.0 to 4.5, and (*ii*) $\tau_{g,anode}$ decreases as $\varphi_{g,anode}$ increases. The negative correlation between $\tau_{g,anode}$ and $\varphi_{g,anode}$ makes intuitive sense, because removing solid particles to increase the void fraction should decrease the average path length of diffusing molecules.

Figure 5.5 shows the predicted effects of varying $\tau_{g,anode}$ while holding all other parameters at their baseline condition. In figure 5.5a, property gradients in the diffusive transport equations are calculated according to the distance between the

centers of adjacent finite volumes. Using this approach, high values of $\tau_{g,anode}$ (i.e., between 16 and 20) are needed to predict the measured transport-limited current densities below ~ 3 A/cm^2 [70]. This supports the observations of Williford et al., who note that models have required $\tau_{g,anode}$ as high as 17 to match experimental results with significant concentration polarization [81]. A number of approaches have been reported to correct this discrepancy in previous SOFC models:

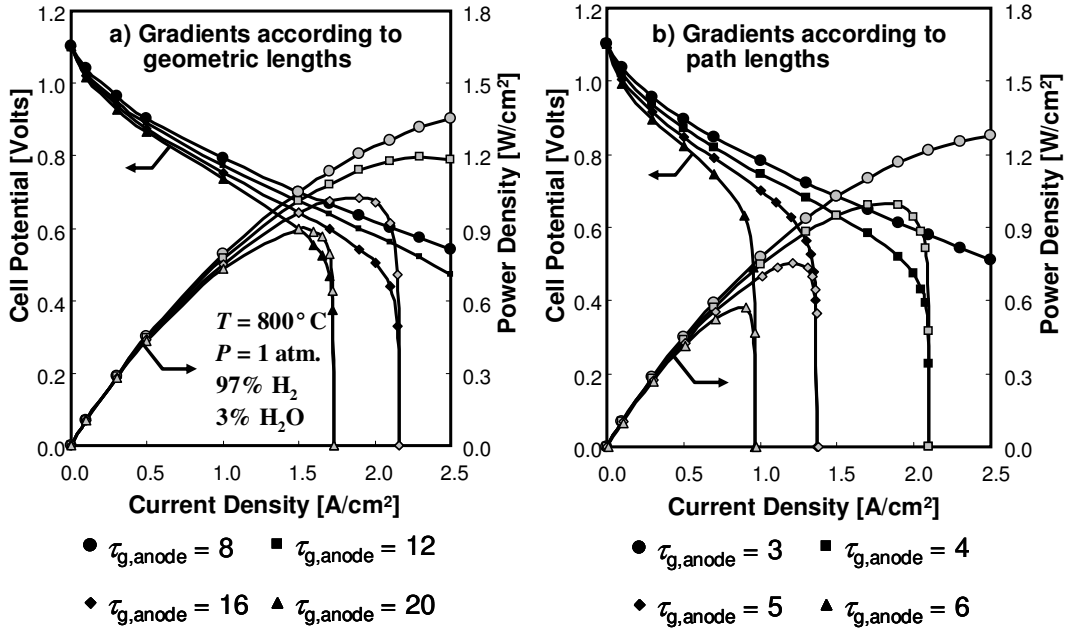

Figure 5.5. Simulated polarization and power density with varying anode support tortuosity. All other parameters are fixed at baseline values. a) Gas-phase composition gradients computed using the physical coordinate. b) Gas-phase composition gradients computed using the actual path lengths according to tortuosity.

- Williford and coworkers suggest that the anomalously high $\tau_{g,anode}$ are compensating for the absence of surface diffusion effects and propose a surface-diffusion mechanism based on the Vignes concept [80, 81].

- A similar approach is advocated by O'Hayre et al., who describe a semi-empirical method for modeling the impact of surface diffusion on the effective width of the triple-phase boundary [156].

- Zhu et al. use an effective $\varphi_{g,anode}$ less than the experimentally measured value by approximately 35% [2]. They reason that the Kozeny–Carman relationship for the electrode permittivity is based on randomly packed spherical particles, while micrographs reveal that the sintered particles are clearly not spherical. Thus, their model uses $\varphi_{g,anode} = 0.35$ to qualitatively match data from Jiang and Virkar [157] for an MEA with an experimentally determined $\varphi_{g,anode} = 0.54$.

- Haberman and Young derive a porous transport model with effective diffusion coefficients $D^e = \frac{\varphi}{\tau^2} D$, rather than those employed in eqs. 5.1 and 5.11 [62]. In agreement with Haberman and Young, Epstein posits that finite-difference approximations of local gradients of any property Ψ in porous media should employ the actual path length for the differencing distance $\tau \Delta y$ [158]. In other words:

$$\nabla\Psi = \frac{\Delta\Psi}{\Delta L} = \frac{\Delta\Psi}{\tau\Delta y}, \qquad \text{(eq. 5.19)}$$

where Δy is the distance between the centers of adjacent finite volumes. (Epstein notes that the failure to distinguish between pore and axial gradients was introduced by Kozeny in 1927 and explicitly corrected by Carman in 1956. Nevertheless, the initial error has been propagated by numerous researchers [158].)

Each of the above approaches has merit and is attempted in the current study. Surface-diffusion effects may certainly be significant at high i_{ext} [80, 81]. However, this approach is not attempted here due to the high degree of uncertainty surrounding physical models of surface diffusion and the magnitude of diffusion coefficients. It is expected that development and inclusion of surface-diffusion models will improve modeling capabilities, but it is unclear how the competition between surface diffusion and adsorption–desorption near the TPB impacts the need for such improved surface-diffusion models.

Of all the approaches mentioned above, the use of eq. 5.19 to evaluate diffusive gradients in the porous matrix provides the most effective means to match experimental data using values for $\tau_{g,anode}$ that are within the range of measured values for Ni–YSZ anodes [81]. Figure 5.5b shows the effect of $\tau_{g,anode}$ when gradients are

evaluated using eq. 5.19. While evaluating gradients using the physical coordinates (i.e., figure 5.5a) requires $\tau_{g,anode}$ = 16 to predict reasonable limiting current density, the corrected porous-media gradients require $\tau_{g,anode}$ = 4 to achieve experimentally observed current densities. Thus, it appears likely that the method for evaluating gradients is responsible for unusually high tortuosities used in some earlier models to predict the effects of concentration polarization.

As discussed earlier, a negative correlation between $\tau_{g,anode}$ and $\varphi_{g,anode}$ in porous SOFC electrodes should be expected. It is therefore interesting to co-vary these two parameters in predicting the influence of porosity on cell performance. Figure 5.6 shows the polarization curves for specific combinations of $\varphi_{g,anode}$ and $\tau_{g,anode}$. Model results are shown for the values of $\varphi_{g,anode}$ used in the Zhao and Virkar experiments [70] and are compared to the experimental measurements. The tortuosity $\tau_{g,anode}$ increases from 2.4 to 4.1 as $\varphi_{g,anode}$ decreases from 0.57 to 0.32, in order for the model to give reasonable agreement with the experimental data. Data for $\varphi_{g,anode}$ = 0.76 are not modeled here because, as Zhao and Virkar note, that particular cell suffered from leakage current [70].

Figure 5.6 shows that the simulations for $\varphi_{g,anode}$ = 0.57 agree well with the experimental data. The model also correctly predicts the limiting current density for $\varphi_{g,anode}$ = 0.32. Nevertheless, there are significant discrepancies between the experimental and simulated results. Most noticeably, the curves for $\varphi_{g,anode}$ = 0.32 and 0.48 significantly underpredict the overpotentials for all current densities. Thus, while

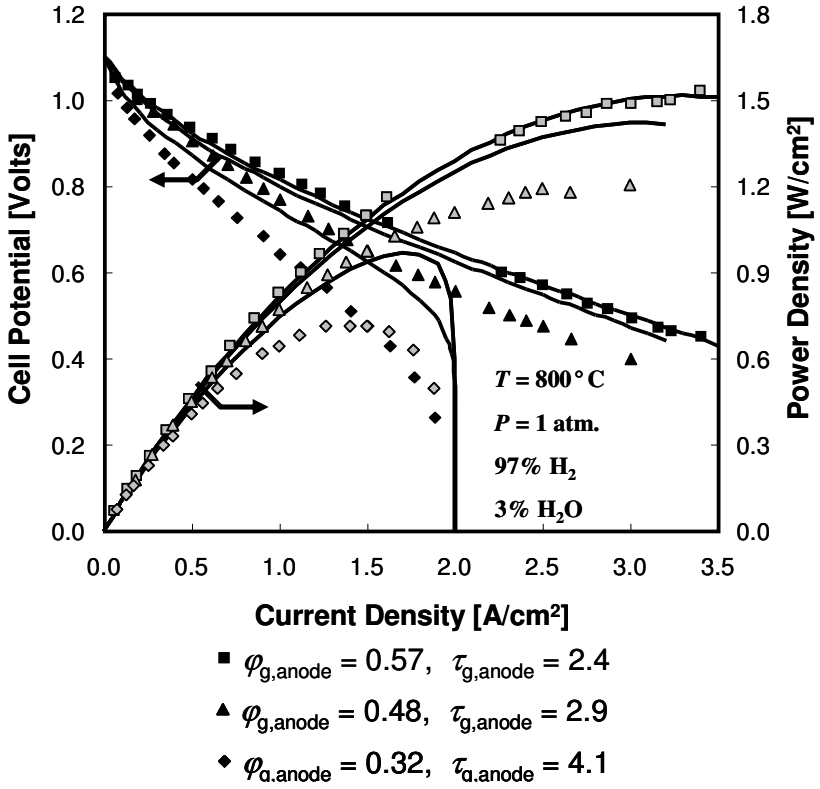

Figure 5.6. Simulated polarization and power density with covarying anode support porosity and tortuosity. Symbols are experimental data from Zhao and Virkar [70]. The utilization thickness is fixed at 5 μm for all cases.

the limiting current density for $\varphi_{g,anode}$ = 0.32 is essentially correct, the maximum power density for this cell is predicted to be 0.97 W/cm^2, while the measured value is 0.71 W/cm^2. Despite capturing some aspects of the measured polarization, it is evident from figure 5.6 that this combination of $\varphi_{g,anode}$ and $\tau_{g,anode}$ provides a poor overall representation of the data. For example, at 1.5 A/cm^2, comparing the cell potentials for $\varphi_{g,anode}$ = 0.32 and $\varphi_{g,anode}$ = 0.57 shows a difference of only 170 mV, while figure 5.3 shows a difference of about 240 mV. Attempts to further manipulate $\tau_{g,anode}$ to fit the experimental data would involve either decreasing the tortuosity for

$\varphi_{g,anode}$ = 0.57 or increasing the tortuosity for $\varphi_{g,anode}$ = 0.32. The former would likely lead to disagreement between the model and experiment at higher current densities, while the latter would cause a discrepancy between the observed and predicted limiting current densities. Because of this, it may be hypothesized that yet another parameter may co-vary with $\varphi_{g,anode}$ and $\tau_{g,anode}$.

The utilization thickness parameter $\delta_{util,anode}$ may also tend to vary with changes in $\varphi_{g,anode}$. Changes in $\delta_{util,anode}$ are derived from changes in mass-transport resistance, which impact diffusion rates and thus surface activity within the anode functional layer. Figure 5.7 shows the polarization and power density curves with co-varying $\varphi_{g,anode}$, $\tau_{g,anode}$, and $\delta_{util,anode}$, with the intent of comparing the modeling results with the experimental data from figure 5.3. Figure 5.7 shows that the model results agree with the experiments by allowing $\delta_{util,anode}$ to increase with decreasing $\varphi_{g,anode}$. The cell with $\varphi_{g,anode}$ = 0.57 has the least resistance to gas-phase diffusion and thus the highest P_{H2} in the electrochemically active region for a given current density (at i_{ext} = 2 A/cm^2, the model predicts P_{H2} = 0.768 atmospheres in the electrochemically active region near the electrolyte interface). Higher P_{H2} increases net charge-transfer rates and thereby reduces the distance (i.e., $\delta_{util,anode}$) required for O^{2-} conduction from the electrolyte into the porous anode functional layer. For this high $\varphi_{g,anode}$, a reasonable value of $\delta_{util,anode}$ = 5 μm provides a good match to the experimental data.

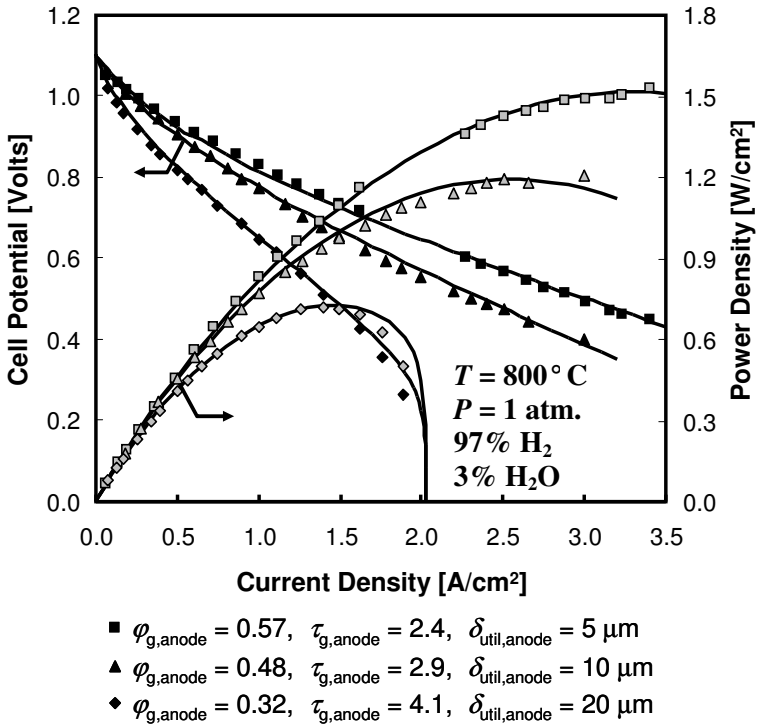

Figure 5.7. Simulated polarization and power density with covarying anode support porosity, tortuosity, and utilization thickness. Symbols are experimental data from Zhao and Virkar [70].

Decreasing porosity $\varphi_{g,anode}$ increases gas-phase diffusion resistance, which reduces P_{H2} in the electrochemically active region. For example, at i_{ext} = 2 A/cm^2, the model used for figure 5.7 predicts P_{H2} = 0.651 and 0.031 atmospheres for $\varphi_{g,anode}$ = 0.48 and 0.32, respectively. Reducing H_2 concentration reduces local charge-transfer rates and thus suggests the need for increasing $\varphi_{g,anode}$ to support high current densities (i.e., by increasing the total amount of l_{TPB} available for charge-transfer reaction, the current per unit length of l_{TPB} is decreased). As noted elsewhere, the decrease in P_{H2} has a thermodynamic effect on Butler–Volmer kinetics, which increases the activation overpotentials (i.e., the charge-transfer polarization

resistance) [20]. In light of this reasoning, it is not surprising that for the model to predict the experimental data in figure 5.7, $\delta_{util,anode}$ increases to 10 and 20 μm for the cells with $\varphi_{g,anode}$ of 0.48 and 0.32, respectively.

As a means of comparing the implementation of the DGM used in this study to previous modeling efforts, figure 5.8 shows species and pressure profiles through

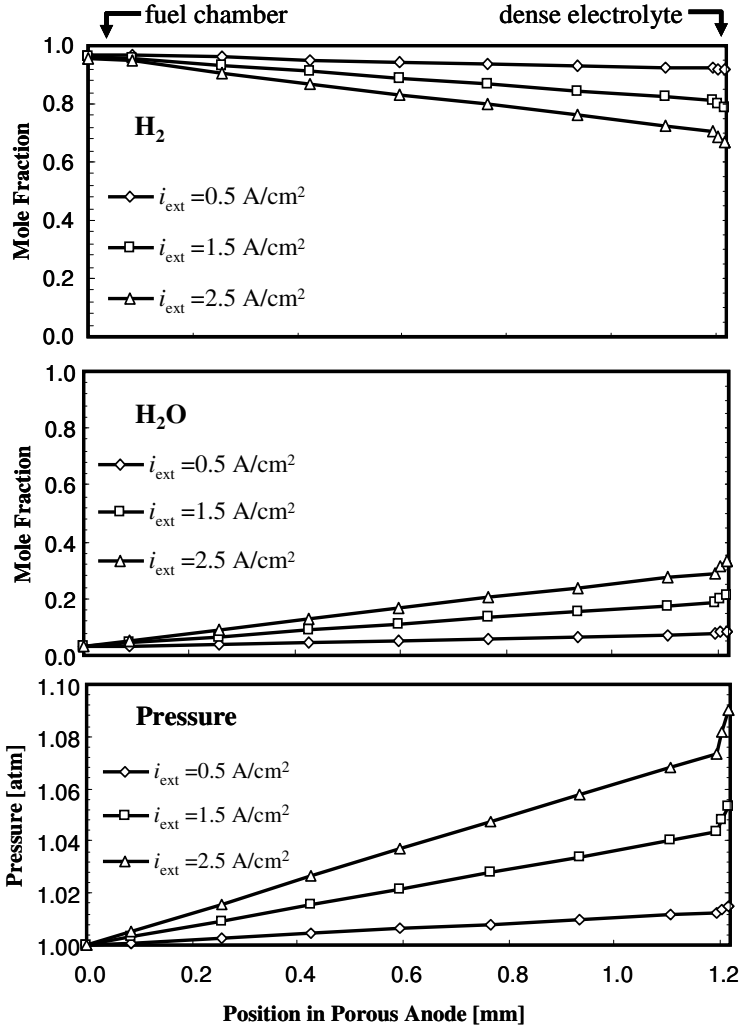

Figure 5.8. H_2, H_2O, and P profiles through the porous anode thickness at selected current densities. In all cases, $\varphi_{g,anode} = 0.57$, $\tau_{g,anode} = 2.4$, and $\delta_{util,anode} = 5\mu m$

Table 5.4. Pressure and concentration gradients in the anode support layer with $\varphi_{g,anode} = 0.57$, $\tau_{g,anode} = 2.4$, and $\delta_{util,anode} = 5$ μm

i_{ext} [A/cm^2]	$\partial P/\partial y$ [atm/m]	$\partial[H_2]/\partial y$ [kmol/m^4]	$\partial[H_2O]/\partial y$ [kmol/m^4]
0.5	1.26	-0.35	0.51
1.5	4.41	-1.23	1.80
2.5	7.52	-2.11	3.09

the anode thickness for current densities of 0.5, 1.5, and 2.5 A/cm^2. As expected for the binary H_2–H_2O system, the profiles are linear. However, within the 20 μm functional layer (which has lower porosity) the gradients are significantly higher than in the support layer. The magnitudes of all gradients increase as the current density increases. Table 5.4 summarizes the predicted gradients in the anode support layer for the solutions illustrated in figure 5.8. While it is difficult to make direct comparisons between different modeling efforts, given the large number of parameters involved, the nominal pressure and concentration gradients should be comparable. Zhao and Virkar present a parametric modeling study of their experimental observations[70]. Lehnert et al. [159] and Gemmen and Trembley [7] model SOFCs operating on reformed methane, but with operating conditions similar to the present investigation. The results of the present study are consistent with these previous investigations.

5.4.2 Distributed Electrochemistry Model

The above results show the importance of assessing the extent of the electrochemically active region $\delta_{\text{util,anode}}$ within the electrode structure. Variation in $\delta_{\text{util,anode}}$ for alternative MEA architectures suggests the importance of establishing l_{TPB}, a_{cat}, and a_{elec} as functions of functional-layer microstructure. These parameters are derived from the variation in depth of the active region. The above results allow $\delta_{\text{util,anode}}$ to be a fitting parameter. However, $\delta_{\text{util,anode}}$ should be established from a more rigorous approach that allows for electrochemistry to occur throughout the depth of the electrode, even beyond the functional layer. Such an approach has been implemented in past SOFC models wherein the electrochemistry was handled by a single-step Butler–Volmer reaction [160-164]. As such, these models did not capture the complex supporting surface chemistry on both the catalyst and electrolyte phases. Distributed electrochemically active regions using the elementary kinetic models are presented here to explore how $\delta_{\text{util,anode}}$ varies with operating conditions, as well as microstructural properties. For these results, eq. 5.7 is used to capture the variation in electric potential in the catalyst and electrolyte phases through the thickness of the electrode.

While the intent of the current study is to comment on the impact of various microstructural parameters on SOFC overpotentials, some modification of the surface thermodynamics and/or chemical kinetics is necessary to fit distributed electrochemistry model results to the data in figure 5.3. As discussed above, expansion of the utilization region increases some overpotentials, while reducing

others. The diffusion path length for O^{2-} ions increases, thus increasing η_{ohm}. Simultaneously, increases in δ_{util} reduce the total current density per unit length l_{TPB}, which decreases η_{act}. Additionally, gas-phase concentration gradients in the functional layer, particularly at moderate-to-high current densities, result in higher gas-phase reactant activities further from the dense electrolyte. This serves to decrease local η_{act} as distance form the dense electrolyte interface increases. Competition between a reduction in η_{act} and an increase in η_{ohm} determines the physical extent of the utilization thickness. When the resistance ($\partial\eta_{tot}/\partial i_{ext}$) associated with increasing current density for a fixed δ_{util} is larger than the Ohmic resistance associated with increasing O^{2-} diffusion lengths, δ_{util} will increase.

The previous results, which keep δ_{util} fixed as a function of current, should predict significant increases in $\eta_{act,anode}$, particularly for cells with low $\varphi_{g,anode}$ as P_{H2} reduces (and P_{H2O} increases) in the electrochemically active region. Figure 5.6, where $\varphi_{g,anode}$ and $\tau_{g,anode}$ are co-varied with a fixed $\delta_{util,anode}$, clearly does not predict the increases in $\eta_{act,anode}$ that would lead to the changes in $\delta_{util,anode}$ seen at moderate current densities. Using the same set of thermodynamic and kinetic parameters in a distributed electrochemistry model is thus unlikely to predict the proper increase in $\delta_{util,anode}$.

As mentioned, the kinetic and thermodynamic parameters in tables 5.1 and 5.2 come from multiple sources. While the parameters related to thermo-chemistry on Ni surfaces are the result of experimentally verified surface studies [58], the YSZ surface

parameters adapted from Goodwin are only meant to provide reasonable accuracy in the demonstration of a patterned-anode simulation, tested under a limited range of gas concentrations [66]. Figure 5.9 shows the surface coverages (θ_k) on the YSZ surface for the baseline set of parameters.

As described by eq. 5.18, changes in the gas-phase activity will impact the activation overpotentials by changing the activity (via the surface coverage θ_k) of species involved in charge transfer reactions. On the YSZ surface, this implies that θ_k for charge-transfer products $H_2O_{YSZ(s)}$ and $OH^-_{YSZ(s)}$ increases as the gas-phase composition changes with current density. As shown in figure 5.9, while the concentrations of product species on the YSZ do increase by more than an order of

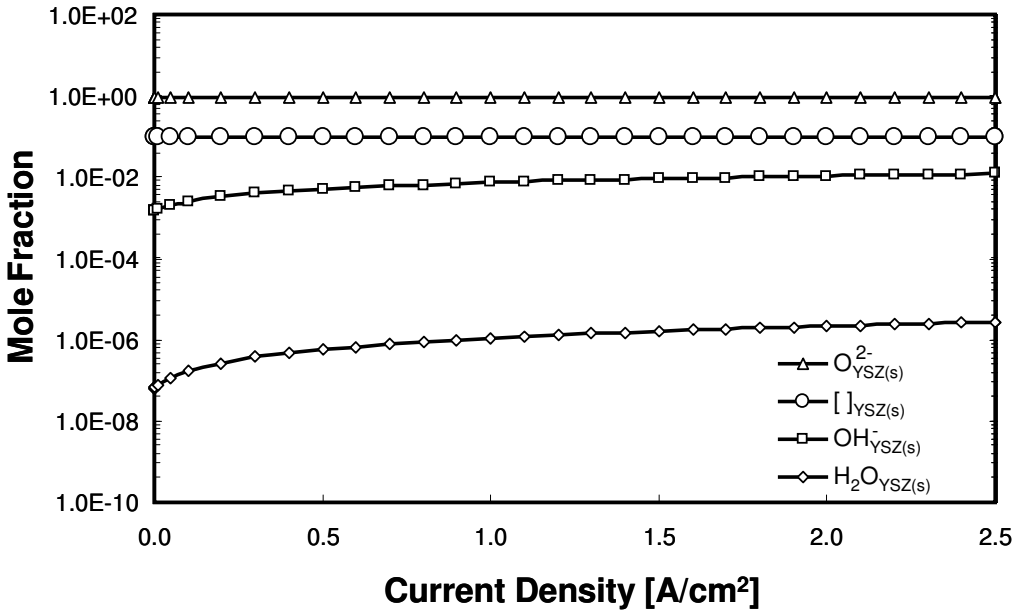

Figure 5.9. Predicted YSZ surface species coverages θ_{YSZ} in the electrochemically active region as a function of i_{ext} for baseline cell parameters.

magnitude with increasing i_{ext}, the very small magnitude of these surface coverages renders these changes insignificant with regard to charge-transfer resistance. Thus, while gas-phase reaction products (H_2O vapor) builds up in the electrochemically active region at high current densities (as in figure 5.8), this build up does not have a significant effect on charge-transfer reaction rates.

To improve the accuracy of distributed electrochemistry model predictions, the thermodynamics for species $H_2O_{YSZ(s)}$ and $OH^-_{YSZ(s)}$ were adjusted by changing ΔH_{rxn} for reactions 8 and 10 in table 5.2. Thermodynamics were shifted to increase θ_k such that model results were sensitive to θ_k for these species. The best fit achieved with the distributed electrochemistry model is shown in figure 5.10. While the model produces a good qualitative fit to the data in figure 5.3, predictions are not as accurate as those for the fixed δ_{util} model (figure5.7). Model predictions are particularly accurate for $i_{ext} \leq 2.5$ A/cm^2, but predicted polarization curves beyond this current density are more linear than those measured by Zhao & Virkar, and predict higher values for the polarization resistance R_p. Several possible reasons for this discrepancy are discussed further below. To produce the fits of figure 5.10, several parameters were varied from the baseline case parameters described in tables 5.1-5.3. Table 5.5 provides values for geometric parameters used in the distributed electrochemistry model. One significant change is that separate support and functional layer values are stored for the average pore radius and particle diameter (r_p and d_p, respectively). As mentioned above, smaller particles are utilized in the functional layer, to provide greater l_{TPB} and surface areas (i.e. a_{cat} and a_{elec}) per unit

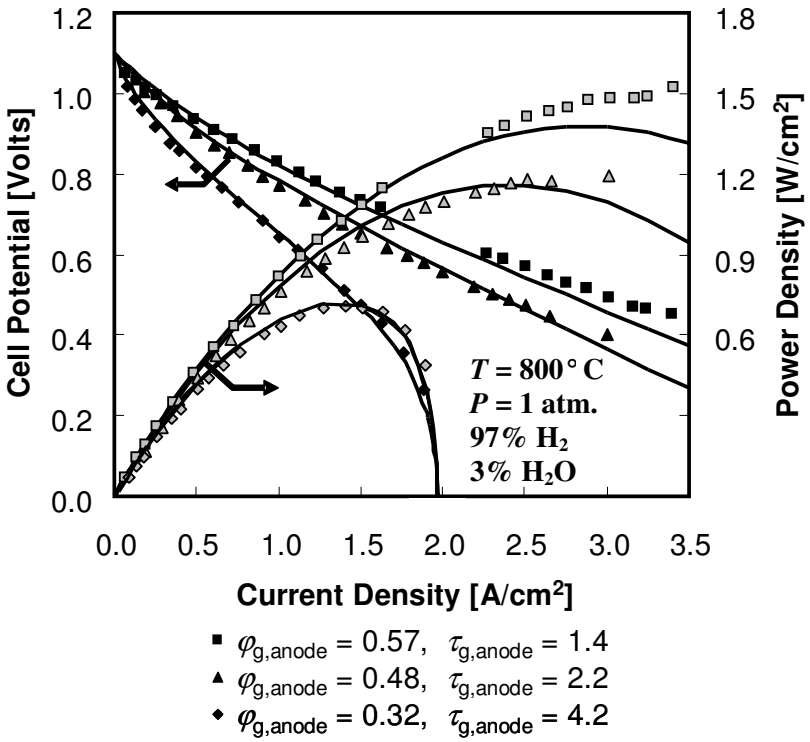

Figure 5.10. Simulated polarization and power density with co-varying anode support porosity and tortuosity for distributed electrochemistry model. Symbols are experimental data from Zhao and Virkar [70]. The utilization thickness is allowed to vary with cell operating conditions.

volume. Values for r_p and d_p are thus expected to be smaller in the functional layer, and are estimated from visual inspection of SEM imaging reproduced in Zhao & Virkar [70]. Parameters utilized are consistent with predictions from random-packing numerical studies of composite SOFC electrodes [165].

Table 5.5. Model parameters for distributed electrochemistry model.

	Anode	Cathode
Support layer TPB length, l_{TPB} [m^{-2}]	3e10	3e10
Average support layer pore radius, r_p [μm]	0.5	0.5
Average support layer particle diameter, d_p [μm]	2.5	2.5
Support layer thickness [μm]	1000	50
Catalyst fraction of solid phase, support layer	0.45	1.0
Functional layer TPB length, $l_{TPB,int}$ [m^{-2}]	1e13	1e13
Average functional layer pore radius, $r_{p,int}$ [μm]	0.15	0.2
Average functional layer particle diameter, $d_{p,int}$ [μm]	0.5	0.5
Functional layer thickness [μm]	20	20
Catalyst fraction of solid phase, functional layer	0.45	0.4
Functional layer porosity, $\varphi_{g,int}$	0.23	0.26
Functional layer tortuosity, $\tau_{g,int}$	4.5	4.5
Catalyst surface site density, Γ_{cat} [mol/cm^2]	1.66e-9	1.66e-9
Catalyst surface area a_{cat} [m^{-1}]	1e5	2e6
Electrolyte surface site density, Γ_{elec} [mol/cm^2]	1e-9	1e-9
Electrolyte surface area, a_{elec} [m^{-1}]	1e5	1e5
Double layer capacitance, C_{dl} [F/m^3]	0.003	0.2

Tables 5.6 and 5.7 summarize kinetic and thermodynamic parameters for the distributed electrochemistry model. The thermodynamics for the YSZ surface species were changed to reflect an updated mechanism by the original author [20]. As mentioned, the thermodynamics for YSZ surface species were modified via changes to the reaction enthalpies on the YSZ surface. It is also noted that table 5.6 contains an additional reaction (reaction 10), where $H_2O_{YSZ(s)}$ and $O^{2-}_{YSZ(s)}$ react to form two OH^-_{YSZ} species, with the reaction rate adopted from a distributed electrochemistry model by Bessler, et al [64]. Furthermore, the change in surface reactions will change the calculated reverse reaction rates, and thus the surface species equilibrium.

Table 5.6. Thermodynamics of distributed electrochemistry model at 25 and 800 °C.

	$h^0_{k,25^\circ C}$ **[kJ/gmol]**	$s^0_{k,25^\circ C}$ **[J/gmol*K]**	$h^0_{k,800^\circ C}$ **[kJ/gmol]**	$s^0_{k,800^\circ C}$ **[J/gmol*K]**
Gas Phase Species				
O_2	1.63e-8	204.15	25.27	246.06
H_2	1.33e-8	130.68	22.90	168.38
H_2O	-241.83	188.82	-212.77	235.69
Ni Surface Species				
$[\,]_{Ni}$	0.0	0.0	20.02	33.08
O_{Ni}	-237.48	19.36	-204.82	72.90
H_{Ni}	-40.61	28.33	-9.14	80.25
OH_{Ni}	-214.62	18.31	-173.75	85.05
H_2O_{Ni}	-302.62	87.58	-253.54	167.52
YSZ Bulk and Surface Species				
$[\,]_{YSZ(s)}$	0.0	0.0	47.75	78.91
$O^{2-}_{YSZ(s)}$	-247.3	-13.82	-186.9	85.5
$[]_{YSZ(b)}$	0.0	0.0	47.75	78.91
$O^{2-}_{YSZ(b)}$	-247.3	-13.82	-186.9	85.5
OH^-_{YSZ}	-302.2	40.7	-230.4	158.9
$H2O_{YSZ}$	-422.9	90.2	-346.1	215.8
LSM Surface Species				
$[]_{LSM}$	0.0	0.0	32.22	53.24
O_{LSM}	-84.35	19.46	-39.50	93.16

Table 5.7. Reactions and forward rate parameters used in distributed electrochemistry model. [a]Sticking coefficient s^o.

Reaction Equation	A_{fwd} [gmol, cm, s]	β	$E_{act,fwd}$ [kJ/mol]	α_{fwd}	Source
Ni Surface					
1. $H_2 + 2\,[]_{Ni} \leftrightarrow 2\,H_{Ni}$	1.00e-02[a]	0	0		[154]
2. $O_2 + 2\,[]_{Ni} \leftrightarrow 2\,O_{Ni}$	1.00e-02[a]	0	0		[154]
3. $H_2O + []_{Ni} \leftrightarrow H_2O_{Ni}$	1.00e-01[a]	0	0		[154]
4. $O_{Ni} + H_{Ni} \leftrightarrow OH_{Ni} + []_{Ni}$	5.00e+22	0	97.9		[154]
5. $H_2O_{Ni} + []_{Ni} \leftrightarrow OH_{Ni} + H_{Ni}$	2.27e+21	0	91.76		[154]
6. $2\,OH_{Ni} \leftrightarrow O_{Ni} + H_2O_{Ni}$	3.00e+21	0	100.00		[154]
LSM Surface					
7. $O_2 + 2\,[]_{LSM} \leftrightarrow 2\,O_{LSM}$	1.00e-03[a]	0	0		[15]
YSZ Surface					
8. $H_2O + []_{YSZ(s)} \leftrightarrow H_2O_{YSZ(s)}$	1.00e+00[a]	0	0		[92]
9. $O^{2-}_{YSZ(b)} + []_{YSZ(s)} \leftrightarrow []_{YSZ(b)} + O^{2-}_{YSZ(s)}$	1.00e+11	0	0		[92]
10. $H_2O_{YSZ(s)} + O^{2-}_{YSZ(s)} \leftrightarrow 2\,OH^-_{YSZ(s)}$	1.00e+19	0	0		[64]
Ni/YSZ Three-phase boundary					
10. $H_{Ni} + O^{2-}_{YSZ(s)} \leftrightarrow []_{Ni} + OH_{YSZ} + e^-_{Ni(b)}$	1.00e+15	0	90.0	0.5	[92]
11. $H_{Ni} + OH^-_{YSZ} \leftrightarrow H_2O_{YSZ} + e^-_{Ni(b)}$	1.00e+14	0	90.0	0.5	[92]
LSM/YSZ Three-phase boundary					
12. $O_{LSM} + []_{YSZ(s)} + 2\,e^-_{LSM(b)} \leftrightarrow O^{2-}_{YSZ(s)} + []_{LSM}$	5.00e+17	0	158.2	0.65	[15]

To confirm the expansion of the utilization thickness with increasing current density, figure 5.11 shows effective $\delta_{util,anode}$ values (calculated according to eq. 5.21, below), for the model curves in figure 5.10. For $\varphi_{g,anode} = 0.57$ and $\varphi_{g,anode} = 0.48$, where diffusion resistance is minimal, results show a very slight increase in $\delta_{util,anode}$ with i_{ext}. When $\varphi_{g,anode} = 0.32$, however, the gas-phase composition in the functional layer changes significantly, leading to the increase in $\delta_{util,anode}$ discussed above.

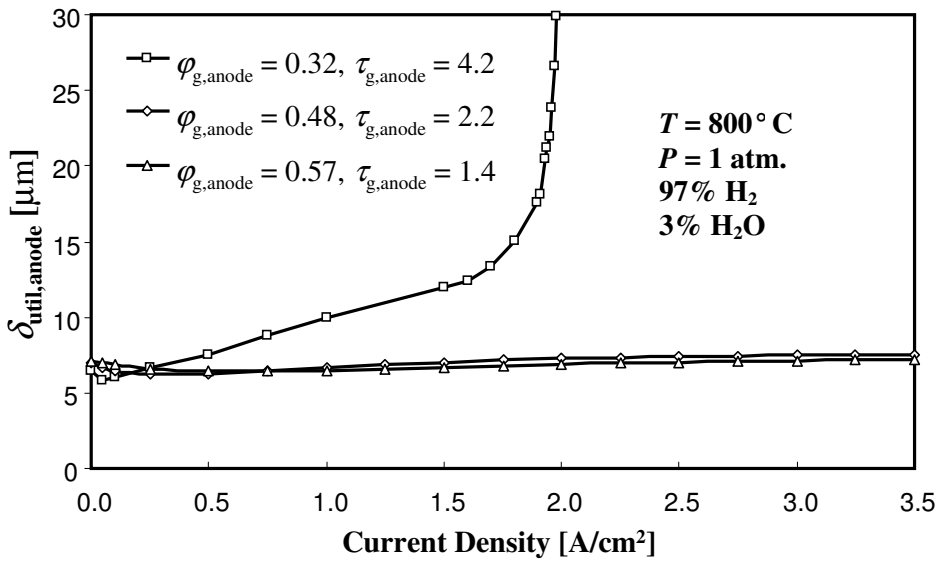

Figure 5.11. Predicted $\delta_{util,anode}$ values for varying support layer composition.

To explore the growth of $\delta_{util,anode}$ more fully in the $\varphi_{g,anode} = 0.32$ cell, figure 5.12 shows the local Faradaic current i_{far} in this cell (normalized by i_{ext}) as a function of distance from the dense electrolyte for varying i_{ext}. At low current densities ($i_{ext} \leq$ 1.5 A/cm^2), results show a majority of the charge-transfer current restricted to within 15 μm of the dense electrolyte. However, as current densities increase toward the limiting current of i_{lim} = 2.0 A/cm^2, the distribution of i_{far} shifts further and further towards the support layer. For currents very near i_{lim} ($i_{ext} \geq$ 1.95 A/cm^2), model results show significant electrochemistry in the support layer and a growing region at the interface with the dense electrolyte that is electrochemically inactive, confirming the results presented in figure 5.11.

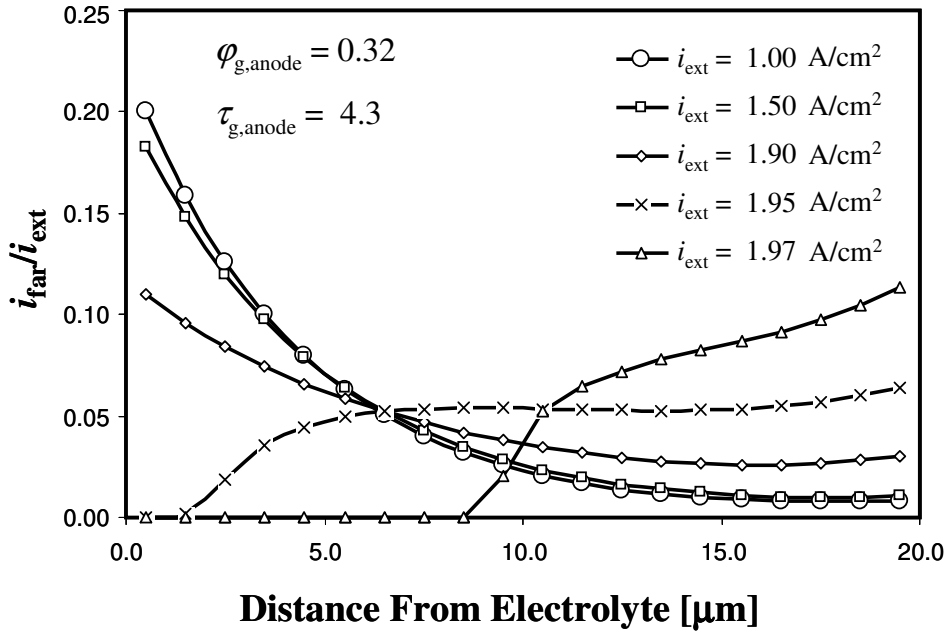

Figure 5.12. Predicted distribution of faradaic current in the anode functional layer

5.5 Discussion

This study reveals the importance of considering physical correlations among several microstructural parameters that describe porous electrodes. The results also emphasize the importance of considering the full range of current densities (i_{ext}) when determining the microstructural parameters that best represent cell polarization characteristics. The present study focuses especially on physical porous-media characteristics without exploring fully other uncertain characteristics such as surface thermodynamics and chemical kinetics. Rather, these thermodynamic and kinetic parameters are based on previous literature values. Nevertheless, from the model studies presented here, it is clear that reasonable variation of those parameters alone would not provide adequate sensitivity to match the rapid fall-off in the polarization characteristics near the limiting current densities (which vary greatly with $\varphi_{g,anode}$).

Because activation overpotentials dominate at low i_{ext}, relative to concentration overpotentials, it is possible to predict polarization behavior at low current density even with significant errors in the mass-transport model parameters [81]. Polarization behavior at high current density provides a more rigorous test of mass-transport models and fits for the microstructure parameters, such as $\varphi_{g,anode}$ and $\tau_{g,anode}$, that significantly impact transport.

Although much can be learned from model-based interpretation of polarization characteristics, the approach provides only indirect measures of the controlling microstructural characteristics. Because porous-media transport is important to cell performance, especially at high current density or high fuel utilization, it is important to find independent measures of the critical parameters. Three-dimensional tomographical reconstruction of electrode materials provides an important, direct route to establish needed microstructural parameters [148].

5.5.1 Comparison of Predicted and Measured R_{bulk} Values

One means of evaluating fitting parameters is to predict how bulk resistance R_{bulk} varies with $\varphi_{g,anode}$. Because R_{bulk} depends almost exclusively on the resistance to O^{2-} ion current in the electrolyte phase, its value increases (or decreases) with $\delta_{util,anode}$ due to the increase (or decrease) in average diffusive path length of O^{2-} ions into the anode functional layer. For the fixed δ_{util} model, the diffusion lengths for each phase (catalyst and electrolyte phases in anode and cathode, dense electrolyte)

are known *a priori* from model input parameters, and so R_{bulk} is simply determined according to eq. 5.20:

$$R_{bulk} = \sum_m R_m \delta_m \qquad \text{(eq. 5.20)}$$

where R_m is the resistivity and δ_m is the average diffusion path length for charged species (electrons or O^{2-} ions) in phase m. For the distributed electrochemistry model, there is no set value for δ_{util}, as nonzero values for i_{far} are possible throughout the entirety of the electrode. Values for the effective δ_{util} are calculated for each current density by the normalized i_{far} for each volume times the distance from the dense electrolyte, over the span of the electrode:

$$\delta_{util}^{e} = \frac{\sum_j i_{far}(j)\delta_{O^{2-}}(j)}{i_{ext}} \qquad \text{(eq. 5.21)}$$

where $i_{far}(j)$ is the Faradaic current for volume j and δ_{O}^{2-} is the distance from the center of the volume to the dense electrolyte (i.e., the axial diffusion length for O^{2-} ions). R_{bulk} for each current density is then calculated according to eq. 5.20. Given the changes in δ_{util}^{e} apparent in figure 5.11, the identification of a single R_{bulk} value oversimplifies the nature of oxide conduction in the utilization thickness. However, in order to compare model predictions with experimental results, R_{bulk} is calculated for a given microstructure by averaging R_{bulk} over the linear portion of the

polarization curve. In this manner, R_{bulk} values correspond to those of Zhao and Virkar [70], who used a linear fit of Ohmic overpotentials vs. current density (as measured by current-interruption) to calculate R_{bulk} for the various microstructures..

As shown in table 5.8, the calculated R_{bulk} for the simulations in figure 5.7 and 5.10 compare favorably with the variation in R_{bulk} measured by Zhao and Virkar [70]. The significant variation in R_{bulk} illustrates the importance of the functional layer and the associated $\delta_{util,anode}$ in determining the net bulk resistance. The distributed electrochemistry model, in general, over-predicts R_{bulk} values. It is worth noting, however, that the predicted that subtracting constant value (0.04 Ω-cm^2) from the R_{bulk} values predicted by the distributed electrochemistry model gives an exact match to the measured R_{bulk} values for $\varphi_{g,anode}$ = 0.32 and $\varphi_{g,anode}$ = 0.57, with only a 10% error (0.01 Ω-cm^2) for the $\varphi_{g,anode}$ = 0.48 R_{bulk} value. Thus, there is likely some parameter error common to all three $\varphi_{g,anode}$ predictions (such as in the cathode) that leads to this over-prediction.

Table 5.8. Comparison of R_{ohm} values from experiment and from model predictions for varying anode microstructures.

	R_{ohm} [Ω cm^2]		
$\varphi_{g,anode}$	Zhao and Virkar [70]	This work, figure 5.7	This work, figure 5.10
0.32	0.156	0.182	0.196
0.48	0.104	0.113	0.135
0.57	0.090	0.079	0.130

For the fixed $\delta_{util,anode}$ model, the agreement between experimental and simulation R_{bulk} values removes much of the uncertainty surrounding the absolute values of $\delta_{util,anode}$ and $l_{TPB,anode}$. While the values of $l_{TPB,anode}$ were tuned to fit the low-polarization characteristics of the experimental data, this fitting was performed with an arbitrarily assumed value of $\delta_{util,anode}$ = 5 μm. Because the total TPB length for an electrode depends on the product of l_{TPB} and δ_{util}, a different assumption for $\delta_{util,anode}$ would affect the fitting of the $l_{TPB,anode}$ variable. The modest agreement between R_{bulk} values, however, lends validity to the absolute values of $\delta_{util,anode}$ used in this simulation as well as the overall magnitude of $l_{TPB,anode}$.

5.5.2 Possible Sources of Model Error

It is important to re-emphasize that this study is not intended to provide exact measures of the fitted parameters; rather, the model is used to explore the effect of several microstructural parameters on electrochemical performance and their inter-relationships. As such, several improvements to the fits in figure 5.10 were not explored. For example, the pore radius and particle diameter values in the anode support layer, $r_{p,ASL}$ and $d_{p,ASL}$ respectively, will vary with $\varphi_{g,anode}$, similar to the manner in which they vary between the support and functional layers in table 5.5. However, in the absence of any experimentally measured values these parameters would assume the role of free-fitting parameters (similar to $\tau_{g,anode}$). The distributed electrochemistry model demonstrates conceptually the expansion of δ_{util} with changing operating conditions rather than providing exact measures for the fitted

parameters, and thus tripling the number of free-fitting parameters was not seen as worth the modest improvement to the model fits.

The direct co-variation of $r_{p,ASL}$ and $d_{p,ASL}$ with $\varphi_{g,anode}$ would thus serve to increase gas-transport resistance in MEAs with low $\varphi_{g,anode}$. Neglecting this impact of varying $\varphi_{g,anode}$ leads to the overcompensation by some other source in order to get the qualitative fits in figure 5.10. One such 'overcompensation' can be seen in the surface coverage of H_2O_{YSZ} . Predicted surface coverages on the YSZ surface, shown in figure 5.12 for $\varphi_{g,anode}$ = 0.48, indicate that the YSZ surface is almost entirely covered by H_2O_{YSZ}, even at low current densities. While ΔH^{o}_{ads} for H_2O on the YSZ surface was adjusted to give the best fit to the data, such high surface coverage is inconsistent with prior knowledge of the YSZ surface, which indicates that H_2O_{YSZ} coverage at 800 °C should be much lower [20, 64, 166].

Given the modest sensitivity of results to variations in r_p and d_p (not shown here), it is not likely that unrealistic values for $\theta_{H2O,YSZ}$ are due entirely to the lack of co-variation in ASL parameters. Rather, a more comprehensive exploration of the thermodynamic and kinetic parameter space for surface species and reactions, particularly on the YSZ surface, would likely improve the quality of the fits. Such an exploration, however, is beyond the scope of this work. Rather, such parameters are more effectively determined from experimental studies that isolate surface kinetic effects, such as patterned-anode studies [9, 66, 167, 168]. The inclusion of surface diffusion may also improve the model (and lead to higher activity for H_2O_{YSZ} near the

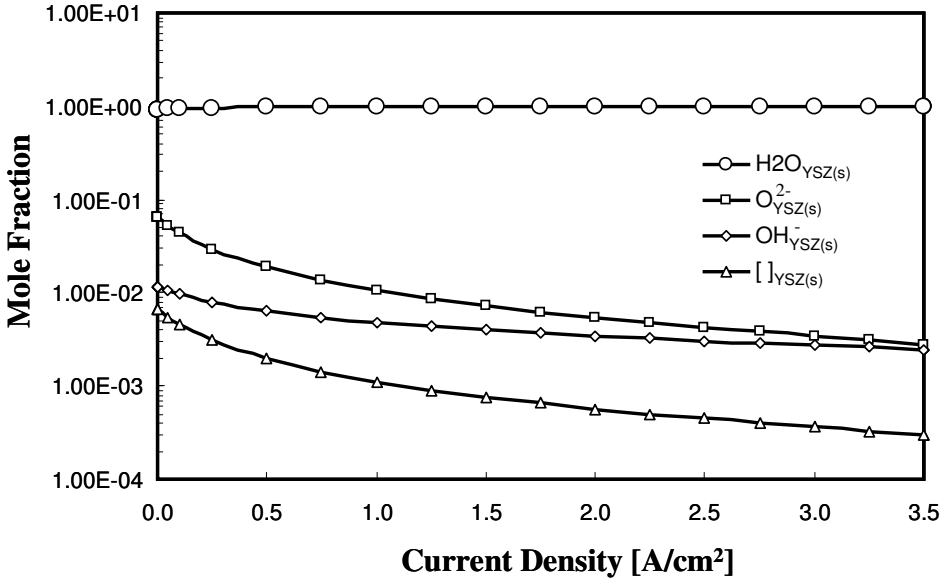

Figure 5.12. Predicted YSZ surface species coverages θ_{YSZ} in the electrochemically active region as a function of i_{ext} for $\varphi_{g,anode}$ = 0.48, $\tau_{g,anode}$ = 2.2. Calculations performed with distributed electrochemistry model.

TPB), but more work is needed to measure (or estimate) surface diffusivities and length scales before these models can be effective [81]. Modeling patterned-anode experiments with well-defined geometries is likely to prove helpful in the development of both surface-diffusion and charge-transfer models and thus contribute to improving MEA models [20, 66].

5.6 Conclusions

The comparison of model predictions and experimental data of Zhao and Virkar [70] provides the basis for assessing how key microstructural parameters in porous Ni–YSZ anodes are inter-related. Predicting the experimental observations

requires physically reasonable correlations between $\varphi_{g,anode}$, $\tau_{g,anode}$, and $\delta_{util,anode}$. These correlations enabled the accurate prediction of button-cell polarization characteristics using physical parameters whose values are consistent with independent measurements. Values of tortuosity $\tau_{g,anode}$ between 2 and 5 are facilitated by correcting the transport-gradient calculations according to Epstein [158].

Furthermore, distributed electrochemistry modeling predicts the increase in $\delta_{util,anode}$ with varying microstructure and with varying gas-phase composition in the anode functional layer. While additional model improvements are needed to improve the accuracy of the distributed electrochemistry fits, the models show the importance of porous-electrode microstructural characteristics on cell performance. Thus, to assist continuing development of model-based cell design and optimization, it is important to establish underpinning functional relationships for needed physical parameters. In addition to modeling polarization behavior, as in the present paper, experiments such as patterned electrodes and tomographic reconstructions can play a valuable role in the independent measurement of critical functional relationships and physical parameters.

Chapter 6: Conclusions and Outlook

The overarching concern of this work has been to quantify the role of cerium oxide as an electrocatalyst in SOFC anodes. Ceria has proven useful in a number of SOFC systems, particularly in the oxidation of hydrocarbon fuels. The intent of this study was to provide a framework for the optimization of ceria-based composite SOFC anodes. This was organized into three major tasks: (*i*) Experiments on thin-film ceria button-cell anodes (chapter 3), including electrochemical characterization and *in-situ* XPS to evaluate the distribution of surface oxidation states; (*ii*) The development of a 1-D isothermal thin-film MIEC model (chapter 2), and the comparison of model predictions with experimental results to obtain important thermodynamic and kinetic parameters for H_2 oxidation on ceria (chapter 4); and (*iii*) the development and validation of a 1-D isothermal porous media SOFC model that can describe state-of-the-art SOFC anodes (chapter 5). While much has been learned about the role of ceria in SOFC anodes, several open questions remain. The conclusions drawn from this study, followed by an analysis of open questions and future work, are summarized below for each task.

6.1 Experimental Characterization of Thin-film CeO_2 Anodes

6.1.1 Conclusions

The fabrication and electrochemical characterization of dense, thin-film ceria anodes was the focus of chapter 3. The results revealed that electrochemical activity

was very sensitive to film morphology. Initial films displayed nano-scale pores, with porosity and surface roughness increasing with film thickness. For these films, electrochemical results showed little consistency, with nominally identical films giving qualitatively different polarization curves. Successive fabrications and inspection via SEM were used to optimize the sputtering conditions, with increased throw distance leading to smooth, dense films that gave consistent, repeatable results. The results on these films, while self-consistent, were qualitatively different than those on the thicker, rougher films.

Analysis of EIS results for nanoporous films revealed three main contributions to the polarization resistance, including the diffusion of oxides through the ceria bulk, acting in parallel to a capacitive chemical process that is sensitive to P_{H2},. These two processes dominate the resistance at low currents and low P_{H2}. Additionally, a high-frequency process sensitive to P_{H2} contributes a small amount to the total resistance. For both the chemical process and the high-frequency process, the resistance becomes insensitive to P_{H2} above 0.32 atm. Equivalent circuit parameters were used to estimate the oxide diffusion coefficient, with results for $T \leq 700$ °C agreeing with previous results and indicating a modest degree of reduction. Dense films show related trends in the impedance spectra, with two clearly resolved arcs at low currents, both of which are sensitive to P_{H2} below 0.32 atm.

The cells also demonstrated stable performance on CO and humidified C_4H_{10}, with no evidence of carbon deposition. Results for CO electrochemical oxidation

show a decrease in limiting current with decreasing P_{CO}. In general, overall current densities for humidified CO as well as C_4H_{10} were less than those for humidified H_2, although oxidation of humidified CO showed evidence of water-gas shift reaction through increased current densities over dry CO. These results suggest a complex interrelation between the SOFC operating conditions (T, P_{H2}, P_{H2O}), the oxidation state of the ceria, and the electrochemical performance. .

In situ ambient pressure X-ray photoelectron spectroscopy (AP-XPS) was used to evaluate the oxidation state of operating ceria SOFC anodes. These experiments represent the first use of XPS as an *in situ* probe for high-temperature, solid oxide cells. This initial study yielded useful qualitative and quantitative information about the mechanism of H_2 reduction on thin-film ceria anodes. In particular, ceria becomes increasingly oxidized with increasing anodic currents, with the fraction of Ce reduced as Ce^{3+} decreasing from > 80% to ~50% as the measured total current varies from 0.0 to 150 μA. The extent of Ce oxidation correlates with changes in polarization resistance, although more extensive studies are required to develop a quantitative mechanism. Spatial gradients in the Ce^{3+} fraction across the surface of the ceria electrodes exist with H_2 oxidation, which suggests that with negative bias voltage, electrochemical activity may become more localized due to the reduction in polaron activity with increased oxidation to Ce^{4+}. Furthermore, Ar-diluted tests demonstrate that these single chamber cells with *in situ* XPS results are relevant to phenomena from standard thin-film SOFC results. In addition to providing qualitative information about oxidation mechanisms, these results provide a

rare direct measure of the distribution of valence states. At open circuit, where thermodynamic equilibrium between the surface and gas phase is assumed, these results are useful for determining the thermodynamic parameters needed for a quantitative oxidation mechanism. These results establish AP-XPS as a powerful *in situ* analytical tool for high-temperature electrochemical devices.

Further studies are needed to develop a more quantitative and fuller understanding of CeO_{2-x} role in solid oxide cells. The use of XPS to do extensive depth profiling in the ceria will be valuable for understanding the relevance of bulk-phase vs. surface ceria reduction. Furthermore, testing a broader range of fuel partial pressures and temperatures will provide a basis for developing a quantitative mechanism for CeO_{2-x} materials in more conventional porous composite electrodes. It will also be valuable to expand the XPS studies to include CO and CO_2 and to assess the impact of carbonaceous fuels on the redox cycle of ceria in active high-temperature electrochemical cells. Ultimately, results from the AP-XPS studies will serve as an important measure of validation for the MIEC thin-film model described in chapters 2 and 4.

6.1.2 Looking Forward

While a detailed study of the relation between deposition conditions and film characteristics was beyond the scope of this study, a better understanding of and greater degree of control over deposited film characteristics would certainly benefit extensions of this work. Previous authors have shown the sensitivity of ceria redox

behavior to film properties, particularly as dimensions (film thickness and grain diameter) approach 100 nm and less, as in this study [42, 46, 113]. While the thin, dense films prepared in this study gave more consistent results than the thicker films, it is as yet unclear whether the thermodynamics and kinetics related to electrochemical oxidation on these nanometer-scaled films are relevant to conditions seen in ceria-based composite anodes.

Similarly, a useful extension of this work would involve the testing of a broader range of material combinations that better reflect those seen in real-world SOFC systems, particularly gadolinium-doped ceria (GDC). Doping with gadolinium is typically included in composite ceria anodes to improve mechanical stability by reducing the significant lattice expansion observed with ceria reduction [38, 40], and is known to affect the ability of ceria to participate in redox cycling. As such, characterization of electrochemical oxidation on GDC represents a valuable contribution to the SOFC community, as well as an interesting comparison to the results presented in this study.

Finally, while the *in situ* use of AP-XPS promises to be a valuable technique for the analysis of high-temperature reacting systems, some refinement of the initial experiments will be valuable in capitalizing on the promise of the technique, both in terms of the general application of the technique, and for measurements on the $CeO_{2-x}/H_2/H_2O$ system described in this study. For the overall technique, accurate and verifiable temperature measurements are necessary to correlate results accurately with

quantitative models of oxidation on ceria. Also, the ability to use the AP-XPS technique for *in situ* measurements with two-chamber fuel cells would represent a significant advance in the technique. The use of separate gas environments for the working and counter electrode will allow for more uniform current distribution in the ceria electrode, determination of the active electrode area for scaling of measurements, and the use of higher gas pressures on the counter electrode to minimize its contribution to overpotentials. Finally, the extension of these surface results to the measurement of the distribution of valence states in the ceria bulk would provide valuable information for the validation of ceria models, both for ceria electrodes as well as ceria-based electrolytes. This information can be obtained possibly via XPS measurements of the fluorescence yield, or from alternate *in situ* techniques such as neutron reflectivity studies.

Other improvements to these experiments involve the fabrication of the single-chamber SOFC. Most notably, degradation of the Pt counter-electrode currently limits the durability of the single-chamber SOFC, and subsequent measurements not presented here imply that the resistance of this electrode represents a substantial portion of the total cell resistance. Improvements to the counter electrode thus benefit these measurements. Furthermore, initial measurements indicated significant contamination with Si, likely due to the bonding agent in Kapton tape masks, which prevented observation of the XPS peaks for the O*1s* spectra. The use of stainless-steel shadow masks for has been shown to mitigate this concern in initial follow-up measurements, although fabrication techniques are still being

optimized. Finally, future measurements on the ceria system described in this work should explore a greater range of conditions, to confirm and complement the AP-XPS measurements included in this study. Measurement of ceria valence states as a function of temperature and PH2, even without any electrochemical current, will help to predicting the thermodynamics of the ceria film, while measurement the distribution of valence states under electrochemical oxidation with varying temperature will be useful in determining activation energies for important processes.

6.2 Isothermal 1-D Thin-film MIEC Simulations

6.2.1 Conclusions

Chapters 2 and 4 focused on the formulation and validation of a 1-D isothermal SOFC model with a thin-film MIEC anode. By comparing model predictions and experimental results from chapter 3, important kinetic parameters were estimated for the oxidation of H2 on undoped ceria anodes at 700 ˚C. The results agree qualitatively with the experimental polarization data, and identified critical parameters for charge-transfer, O2- diffusion, and H2 adsorption on the ceria surface. With a few exceptions, the model correctly predicts changes in electrochemical activity with varying PH2, and the predicted shifts in surface valence states are consistent with those observed in in-situ XPS measurements. These results establish the effectiveness of the model in describing H2 oxidation in SOFC anodes with moderate current densities, where high-performance SOFCs are most likely to operate.

6.2.2 Looking Forward

While the model predictions qualitatively agree with experimental results, additional refinement of simulation parameters is needed to improve model accuracy at very low and at high current densities. The model currently predicts significant changes in the degree of reduction (x in CeO_{2-x}) in the ceria bulk under anodic polarization; it is hypothesized that these changes in x are associated with significant changes in the ceria properties (such as reactivity, energetics of Ce^{3+}, or O^{2-} mobility) and that these changes in ceria properties lead to some of the discrepancies between experimental and simulated polarization data. Extensions of this work will test this hypothesis by incorporating more accurate models of how ceria properties vary with the degree of reduction.

Additionally, this study leaves as future work the formulation of an oxidation mechanism for CO on CeO_{2-x}. The procedure should follow much in the same vein as that described here for H_2. Given the relative weak dependence of polarization and EIS results on P_{CO}, it is likely that the oxidation mechanism for CO involves fewer critical parameters than the H_2 mechanism. The validation of the H_2 and CO mechanisms will represent an important first step in the development of oxidation mechanisms for larger hydrocarbons on ceria anodes.

6.3 Isothermal 1-D Porous-media SOFC Simulations

6.3.1 Conclusions

The description and validation of a 1-D SOFC model with bi-layer porous electrodes was the focus of chapter 5. By comparing model predictions and the experimental data of Zhao and Virkar [70], this study was able to describe the likely interrelation between key microstructural parameters. In the 'fixed utilization thickness ($\delta_{util,anode}$)' model, the best fit to the experimental measurements required physically realistic correlation between the porosity $\varphi_{g,anode}$, tortuosity, $\tau_{g,anode}$, and $\delta_{util,anode}$. Additionally, correct implementation of the tortuosity factor on transport-gradients, as per Epstein [158], allows for the utilization of $\tau_{g,anode}$ values between 2 and 5, in agreement with measured values [81].

Furthermore, the correlation between fixed microstructural parameters $\varphi_{g,anode}$, and $\tau_{g,anode}$, and $\delta_{util,anode}$, which varies with electrochemical activity and Ohmic resistance, provides important insight into how transport and electrochemical activity are interrelated. In contrast to models that subtract activation, concentration, and ohmic overpotentials as independent entities, these results show that at high fuel utilization, correct interrelation of all three overpotentials is required to correctly predict SOFC performance. In the presented 'distributed electrochemistry' model, transport and electrochemistry are correctly interrelated by enforcing thermodynamic consistency in reversible chemistry written as elementary-step reactions, while Ohmic losses are correctly predict by enforcing charge neutrality through the depth of the electrode. Rather than relying on $\delta_{util,anode}$ as an input, the distributed

electrochemistry model predicts increasing Ohmic resistance with varying microstructure, as seen in the measurements of Zhao & Virkar [70] and predicted by the 'fixed $\delta_{util,anode}$' fits.

6.3.2 Looking Forward

While additional model improvements are needed to improve the accuracy of the distributed electrochemistry fits, the models show the importance of porous-electrode microstructural characteristics on cell performance. Thus, to assist continuing development of model-based cell design and optimization, it is important to establish underpinning functional relationships for needed physical and thermo-kinetic parameters. In addition to modeling polarization behavior, as in the present paper, experiments such as patterned electrodes and tomographic reconstructions can play a valuable role in the independent measurement of critical functional relationships and physical parameters.

Finally, this study leaves as future work the integration of the two SOFC models explored in this work. Incorporating an MIEC such as ceria into a porous-media SOFC model involves more than simply replacing the nickel oxidation kinetics and thermodynamics described in chapter 5 with those derived for ceria in chapters 2 and 4. While the dense films used in this study prevented significant electronic current in the axial direction, porous ceria allows true MIEC behavior, as in figure 1.3, with ionic and electronic currents acting in parallel. Additionally, the relative importance of the bulk oxidation pathways in this study and the three-phase boundary

mediated pathways of traditional SOFC models are currently unknown. As such, the mechanism presented in this study is meant to represent an initial step toward fully understanding the role of ceria in SOFC anodes. As a follow-on study, modeling of composite systems such as Cu-CeO_2-YSZ will be able to address some of these open questions by comparing initial model results to experimental results on similar systems. Successful predictions on such simple composite systems will provide a basis for predictions on some of the more complex composite ceria systems found in the literature, such as Ni-CeO_2-YSZ. By use of a distributed electrochemistry model, such as that described in this work, such models can correlate electrochemical performance with changes to anode microstructural design, and thus make valuable contributions to the working knowledge and optimization of composite ceria anodes.

Glossary of Symbols Used

t	Time
T	Temperature
ρ	Mass density
P	Gas-phase pressure
P_{k}	Partial pressure of species k
P_k°	Standard-state partial pressure of species k
W_{k}	Molar weight of species k
Y_{k}	Mass fraction of gas-phase species k
θ_{k}	Surface coverage of species k
Γ_m	Surface site density for surface phase m
μ	Gas-phase dynamic viscosity
Φ_{cell}	Cell electric potential
Φ_{cat}	Electric potential of local catalyst phase
$\Phi_{\mathrm{electrolyte}}$	Electric potential of local electrolyte phase
$\Delta\Phi_{\mathrm{el}}$	Electric potential difference between local catalyst and electrolyte phases
i_{o}	Exchange current density
$\beta_{wd/bwd}$	Forward/reverse symmetry parameter for a given charge transfer reaction
η_{ct}	Overpotential associtated with a given charge-transfer step

C_{dl}	Double layer capacticance for composite electrode, per unit total volume.
η	Overpotential
η_{act}	Activation overpotential
η_{Ohm}	Ohmic overpotential
η_{conc}	Concentration overpotential
R_b	Total Ohmic resistance to current conduction
i_{ext}	External current density
I_{tot}	Total cell current
i_{Far}	Local Faradaic current
V_{cell}	Cell voltage
V_{OCV}	Open-circuit cell voltage
G_k	Gibbs free energy of species k
G°	Standard-state Gibbs free energy
ΔG_{red}	Gibbs free energy of ceria reduction
ΔG_i°	Standard-state Gibbs free energy of reaction *i*
$\Delta \overline{G}_{O_2}$	Partial molar free energy of O_2
ΔH_i	Enthalpy of reaction for reaction *i*
ΔH_i°	Standard-state enthalpy of reaction for reaction *i*
ΔS_i	Entropy of reaction for reaction *i*
ΔS_i°	Standard-state entropy of reaction for reaction *i*
h_k°	Standard-state molar enthalpy of species k

s_k°	Standard-state molar entropy of species k
a_{k}	Activity coefficient for species k
a_k°	Standard-state activity coefficient for species k
μ_{k}	Chemical potential of species k
μ_k°	Standard-state chemical potential of species k
F	Faraday constant
$\overline{R}$	Universal gas constant
n_{elec}	Number of electrons transferred for a given charge-transfer process
v_{k}	Net stoichiometric coefficient for species k for the global half-cell reaction
$v_{i,\mathrm{k}}$	Net stoichiometric coefficient for species k for reaction *i*
$v'_{i,\mathrm{k}}$	Stoichiometric coefficient for species k in forward reaction *i*
$v''_{i,\mathrm{k}}$	Stoichiometric coefficient for species k in reverse reaction *i*
q_i	Rate-of-progress for reaction *i*
$k_{\mathrm{i,fwd/bwd}}$	Forward/reverse rate coefficient for reaction *i*
$A_{i,fwd/bwd}$	Pre-exponential reaction rate coefficient for forward/reverse reaction *i*
$E_{a,i,fwd/bwd}$	Forward/reverse activation energy for reaction *i*
σ°	Sticking coefficient
$\dot{s}_{\mathrm{k,g,m}}$	Net molar production rate of gas-phase species k from heterogeneous surface reactions on phase *m*
$\dot{s}_{\mathrm{ion,\,j}}$	Molar production rate of Oxide ions from heterogenous surface reactions in discretized cell *j*

B_g	Porous electrode permeability
φ_g	Porosity
τ_g	Tortuosity
l_{TPB}	Length of three-phase boundary, per unit total electrode volume
r_p	Average pore radius of porous electrode
d_p	Average particle diameter of porous electrode
δ_m	Total thickness of element *m*
d_g	Grain size
Δy_m	Thickness of fuel cell element *m* (anode, cathode, or electrolyte)
Δy_j	Axial thickness of discretized cell *j*
a_m	Surface area of phase *m* (catalyst or electrolyte) per unit volume
N_k	Molar diffusive flux of gas-phase species k
$J_{g,k}$	Diffusive mass flux of gas-phase species k
i_{O2-}	Ionic current due to oxide ion transport in ceria bulk
i_{el}	Electronic current due to polaron transport in ceria bulk
v_{O2-}	Mobility of oxide ions in ceria bulk
v_{el}	Mobility of polarons in ceria bulk
$i_{j+1/2}$	Local current between discretized cells *j* and *j* + 1
J_{O2-}	Molar flux of O^{2-} oxide ions
$D_{DGM,kl}$	Effective binary Dusty Gas Model diffusion coefficients
$D^e_{Kn,l}$	Effective Knudsen diffusion coefficient for species *l*
D^e_{kl}	Effective multi-component binary diffusion coefficient for species *k* and *l*

$D_{k,mix}$	Mixture-averaged diffusion coefficient for gas-phase species *k*
σ_{elec}	Electronic conductivity
σ_{ion}	Ionic conductivity
σ^{e}	Effective conductivity
Q	Charge density
N_{Ce3+}	Molar concentration of Ce_2O_3 in ceria bulk
$\Gamma_{bulk,m}$	Molar concentration of species in bulk phase *m*
X_k	Mole fraction of species k
$[X_l]$	Molar concentration of species *l*
$[X_l^\circ]$	Standard-state molar concentration of species *l* $\tilde{\mu}_k$ Electrochemical potential of species k
z_k	Valence of species k
t_d	Sputtering deposition time
Z_{Re}	Real component of cell impedance
Z_{Im}	Imaginary component of cell impedance
R_{tot}	Total cell resistance
R_{ion}	Resistance to O^{2-} ion conduction in ceria bulk
W_{ion}	Warburg impedance element related to O^{2-} ion conduction in ceria bulk
R_{chem}	Resitance related to chemical processes on ceria surface
σ_{chem}	Effective conductivity related to chemical processes on ceria surface
C_{chem}	Capacitance related to chemistry in ceria electrodes
R_{hf}	Resistance related to high-frequency processes in ceria electrodes

σ_{hf}	Effective conductivity related to high-frequency processes in ceria electrodes
Q_{hf}	Constant-phase element related to high-frequency processes in ceria electrodes
C_{hf}	Pseudo-capacitance related to high-frequency processes in ceria electrodes
j	Imaginary number $\sqrt{-1}$
ω	Perturbation frequency for impedance measurements
E_{act}	Activation energy for resistive impedance elements
A	Area for ionic conduction
D_{O2-}	Diffusion coefficient for oxide ions in ceria bulk
D_{p}	Diffusion coefficient for polarons in ceria bulk
β_{ex}	Symmetry parameter related to interaction potential effects on forward and reverse reaction rates
ΔE_{ex}	Shift in reaction free energy due to non-ideal species interaction potentials
ε_k°	Standard-state excess energy of species k due to non-ideal interactions
ζ	Scaling factor for excess energy interactions
Kn	Knudsen number
δ_{util}	Utilization thickness
Sh	Sherwood number
ζ_k	Number of surface sites occupied by species k

Bibliography

1. H.Y. Zhu and R.J. Kee, *J. Power Sources*, **117,** 1-2 (2003).
2. H.Y. Zhu, R.J. Kee, V.M. Janardhanan, O. Deutschmann, and D.G. Goodwin, *Journal Of The Electrochemical Society*, **152,** 12 (2005).
3. S.P. Jiang and S.H. Chan, *J. Mat. Sci.*, **39,** (2004).
4. A. Atkinson, S. Barnett, R.J. Gorte, J.T.S. Irvine, A.J. McEvoy, M. Mogensen, S. Singhal, and J. Vohs, *Nat. Mater.*, **3,** (2004).
5. A. Weber, B. Sauer, A.C. Muller, D. Herbstritt, and E. Ivers-Tiffee, *Solid State Ionics*, **152,** (2002).
6. O. Costa-Nunes, J.M. Vohs, and R.J. Gorte, *J. Electrochem. Soc.*, **150,** 7 (2003).
7. R.S. Gemmen and J. Trembly, *Journal Of Power Sources*, **161,** 2 (2006).
8. S. McIntosh, H.P. He, S.I. Lee, O. Costa-Nunes, V.V. Krishnan, J.M. Vohs, and R.J. Gorte, *Journal Of The Electrochemical Society*, **151,** 4 (2004).
9. A.M. Sukeshini, B. Habibzadeh, B.P. Becker, C.A. Stoltz, B.W. Eichhorn, and G.S. Jackson, *Journal Of The Electrochemical Society*, **153,** 4 (2006).
10. M.C. Williams, *Fuel Cells*, **7,** 1 (2007).
11. A. Weber and E. Ivers-Tiffee, *J. Power Sources*, **127,** 1-2 (2004).
12. S.C. Singhal, *Solid State Ionics*, **135,** 1-4 (2000).
13. Y.H. Du and N.M. Sammes, *Journal Of Power Sources*, **136,** 1 (2004).
14. Y.J. Leng, S.H. Chan, K.A. Khor, and S.P. Jiang, *International Journal Of Hydrogen Energy*, **29,** 10 (2004).
15. Y. Jiang, S.Z. Wang, Y.H. Zhang, J.W. Yan, and W.Z. Li, *Solid State Ionics*, **110,** 1-2 (1998).
16. P. Hjalmarsson, M. Sogaard, and M. Mogensen, *Solid State Ionics*, **179,** 27-32 (2008).
17. J. Chen, F.L. Liang, L.N. Liu, S.P. Jiang, B. Chi, J. Pu, and J. Li, *Journal Of Power Sources*, **183,** 2 (2008).
18. H. Kishimoto, N. Sakai, T. Horita, K. Yamaji, M.E. Brito, and H. Yokokawa, *Solid State Ionics*, **179,** 27-32 (2008).
19. A. Martinez-Amesti, A. Larranaga, L.M. Rodriguez-Martinez, A.T. Aguayo, J.L. Pizarro, M.L. No, A. Laresgoiti, and M.I. Arriortua, *Journal Of Power Sources*, **185,** 1 (2008).
20. W.G. Bessler, J. Warnatz, and D.G. Goodwin, *Solid State Ionics*, **177,** (2007).
21. Z.L. Zhan and S.A. Barnett, *Science*, **308,** 5723 (2005).
22. E.P. Murray, T. Tsai, and S.A. Barnett, *Nature*, **400,** (1999).
23. S. McIntosh and R.J. Gorte, *Chemical Reviews*, **104,** 10 (2004).
24. R.J. Kee, H.Y. Zhu, A.Y. Sukeshini, and G.S. Jackson, *Comb. Sci. Tech*, **180,** 6 (2008).
25. R.J. Gorte and J.M. Vohs, *Journal Of Catalysis*, **216,** 1-2 (2003).
26. Y.B. Lin, Z.L. Zhan, J. Liu, and S.A. Barnett, *Solid State Ionics*, **176,** 23-24 (2005).
27. B.D. Madsen and S.A. Barnett, *Solid State Ionics*, **176,** 35-36 (2005).
28. J. Liu, B.D. Madsen, Z. Ji, and S.A. Barnett, *Electrochemical and Solid State Letters*, **5,** 6 (2002).

29. V.V. Krishnan, S. McIntosh, R.J. Gorte, and J.M. Vohs, *Solid State Ionics*, **166,** 1-2 (2004).
30. Z.L. Zhan and S.A. Barnett, *Solid State Ionics*, **176,** 9-10 (2005).
31. M. Molinelli, D. Larrain, N. Autissier, R. Ihringer, J. Sfeir, N. Badel, O. Bucheli, and J. Van Herle, *J. Power Sources*, **154,** 2 (2006).
32. N.M. Tikekar, T.J. Armstrong, and A.V. Virkar, *J. Electrochem. Soc.*, **153,** 4 (2006).
33. Z. Cheng and M.L. Liu, *Solid State Ionics*, **178,** 13-14 (2007).
34. Y. Matsuzaki and I. Yasuda, *Solid State Ionics*, **132,** 3-4 (2000).
35. M.B. Pomfret, J.C. Owrutsky, and R.A. Walker, *Anal. Chem.*, **79,** 6 (2007).
36. D. Sarantaridis, R.A. Rudkin, and A. Atkinson, *Journal Of Power Sources*, **180,** 2 (2008).
37. H.H. Mobius and B. Rohland, U. S. Patent no. 3 377 203, April 9, 1968, filed Nov. 18, 1964
38. M. Mogensen, N.M. Sammes, and G.A. Tompsett, *Solid State Ionics*, **129,** 1-4 (2000).
39. T. Takahashi, H. Iwahara, and Y. Suzuki. in *Third Int. Symp. on Fuel Cells*. (1969). Brussels: Presses Academiques Europeennes.
40. A. Trovarelli, *Structural Properties and Nonstoichiometric Behavior of CeO_2*, in *Catalysis by Ceria and Related Materials*. (2002), London: Imperial College Press.
41. H. Tuller, *Solid State Ionics*, **131,** (2000).
42. M. Mogensen, *Ceria-based Electrodes*, in *Catalysis by Ceria and Related Mateials*, A. Trovarelli, Editor. (2002), London: Imperial College Press. p. 453 - 481.
43. F.S. Baumann, J. Fleig, H.U. Habermeier, and J. Maier, *Solid State Ionics*, **177,** 11-12 (2006).
44. C. Sun and U. Stimming, *J. Power Sources*, **171,** (2007).
45. H. Yokokawa, T. Horita, N. Sakai, K. Yamaji, M.E. Brito, Y.P. Xiong, and H. Kishimoto, *Solid State Ionics*, **174,** 1-4 (2004).
46. H.U. Anderson, W. Heuebner, and I. Kosacki, *Low Temperature Cathode Supported Electrolytes*. US Dept. of D.o. Energy, (2001).
47. I. Kosacki, T. Suzuki, H.U. Anderson, and P. Colomban, *Solid State Ionics*, **149,** 1-2 (2002).
48. T. Suzuki, I. Kosacki, and H.U. Anderson, *Solid State Ionics*, **151,** 1-4 (2002).
49. T. Suzuki, I. Kosacki, H.U. Anderson, and P. Colomban, *J. Amer. Ceramic Soc.*, **84,** 9 (2001).
50. X.D. Zhou, W. Huebner, I. Kosacki, and H.U. Anderson, *J. Amer. Ceramic Soc.*, **85,** 7 (2002).
51. O.A. Marina, C. Bagger, S. Primdahl, and M. Mogensen, *Solid State Ionics*, **123,** 1-4 (1999).
52. T. Kim, K. Ahn, J. Vohs, and R.J. Gorte, *J. Power Sources*, **164,** (2007).
53. K.Y. Ahn, H.P. He, J.M. Vohs, and R.J. Gorte, *Electrochem. Solid State Lett.*, **8,** 8 (2005).
54. H.P. He, R.J. Gorte, and J.M. Vohs, *Electrochemical And Solid State Letters*, **8,** 6 (2005).

55. H.P. He, J.M. Vohs, and R.J. Gorte, *J. Electrochem. Soc.*, **150,** 11 (2003).
56. O.A. Marina and M. Mogensen, *Applied Catalysis A-General*, **189,** 1 (1999).
57. A. Bieberle-Hutter, M. Sogaard, and H.L. Tuller, *Solid State Ionics*, **177,** 19-25 (2006).
58. V.M. Janardhanan and O. Deutschmann, *J. Power Sources*, **162,** 2 (2006).
59. S. Griesser, G. Buchinger, T. Raab, D.P. Claassen, and D. Meissner, *J. Fuel Cell Sci. Tech.*, **4,** 1 (2007).
60. J.R. Izzo, A.S. Joshi, K.N. Grew, W.K.S. Chiu, A. Tkachuk, S.H. Wang, and W.B. Yun, *J. Electrochem. Soc.*, **155,** 5 (2008).
61. J. Malzbender and R.W. Steinbrech, *J. Power Sources*, **173,** 1 (2007).
62. B.A. Haberman and J.B. Young, *Journal Of Fuel Cell Science And Technology*, **3,** 3 (2006).
63. H.Y. Zhu and R.J. Kee, *Journal Of The Electrochemical Society*, **153,** 9 (2006).
64. W.G. Bessler, S. Gewies, and M. Vogler, *Electrochim. Acta*, **53,** 1782 (2007).
65. H.Y. Zhu and R.J. Kee, *Journal Of The Electrochemical Society*, **155,** 7 (2008).
66. D. Goodwin. in *Solid Oxide Fuel Cells IX*. (2005): the Electrochemical Society Proceedings Series.
67. J. Mizusaki, T. Saito, and H. Tagawa, *J. Electrochem. Soc.*, **143,** 10 (1996).
68. S.B. Adler, *Chem. Rev.*, **104,** 10 (2004).
69. C.D. Baertsch, K.F. Jensen, J.L. Hertz, H.L. Tuller, S.T. Vengallatore, S.M. Spearing, and M.A. Schmidt, *J. Mater. Res.*, **19,** 9 (2004).
70. F. Zhao and A.V. Virkar, *J. Power Sources*, **141,** 1 (2005).
71. S.J. Rosenberg, *Nickel and Its Alloys*. US Dept. of N.B.o. Standards, (1968).
72. P. Jawlik, *M. S. Thesis*. University of Maryland, College Park, (2008)
73. S.C. DeCaluwe, H. Zhu, R.J. Kee, and G.S. Jackson, *Journal Of The Electrochemical Society*, **155,** 6 (2008).
74. A. Bieberle, *Ph. D. Thesis*. Swiss Federal Institute of Technology, Zurich, (2000)
75. B. Habibzadeh, *Ph. D. Thesis*. The University of Maryland, College Park, (2007)
76. Q. Hu, S.R. Wang, and T.L. Wen, *Solid State Ionics*, **179,** 27-32 (2008).
77. M. Suzuki, N. Shikazona, K. Fukagata, and N. Kasagi, *Journal Of Power Sources*, **180,** 1 (2008).
78. B.A. Haberman and J.B. Young, *Journal Of Fuel Cell Science And Technology*, **5,** 1 (2008).
79. J. Rossmeisl and W.G. Bessler, *Solid State Ionics*, **178,** 1694 (2008).
80. R.E. Williford and L.A. Chick, *Surface Science*, **547,** 3 (2003).
81. R.E. Williford, L.A. Chick, G.D. Maupin, S.P. Simner, and J.W. Stevenson, *J. Electrochem. Soc.*, **150,** 8 (2003).
82. H.Y. Zhu, A.M. Colclasure, R.J. Kee, Y.B. Lin, and S.A. Barnett, *Journal Of Power Sources*, **161,** 1 (2006).
83. H.Y. Zhu and R.J. Kee, *Journal Of Power Sources*, **161,** 2 (2006).
84. W.G. Bessler, *Solid State Ionics*, **176,** 11-12 (2005).
85. G.W. Coffey, L.R. Pederson, and P.C. Rieke, *Journal Of The Electrochemical Society*, **150,** 8 (2003).
86. J. Deseure, Y. Bultel, L. Dessemond, and E. Siebert, *Solid State Ionics*, **176,** 3-4 (2005).

87. D.S. Mebane, Y.J. Liu, and M.L. Liu, *Journal Of The Electrochemical Society*, **154,** 5 (2007).
88. M.Y. Zhou, H.M. Deng, and B. Abeles, *Solid State Ionics*, **93,** 1-2 (1996).
89. I. Riess, *Journal Of The Electrochemical Society*, **128,** 10 (1981).
90. I. Riess, *Solid State Ionics*, **157,** 1-4 (2003).
91. M. Kaviany, *Principles of Heat Transfer in Porous Media*. 2nd ed. Mechanical Engineering Series, New York: Springer, (1995).
92. D. Goodwin. *A Pattern Anode Model with Detailed Chemistry*. in *SOFC IX*. (2005). Quebec City, Canada: the Electrochemical Society Proceedings Series.
93. S.B. Adler, X.Y. Chen, and J.R. Wilson, *Journal Of Catalysis*, **245,** 1 (2007).
94. I. Riess, *Electrochemistry of Mixed Ionic-Electronic Conductors*, in *The CRC Handbook of Solid State Electrochemistry*, P.J. Gellings and H.J.M. Bouwmeester, Editors. (1997), New York: CRC Press.
95. H.Y. Zhu, R.J. Kee, V.M. Janardhanan, O. Deutschmann, and D.G. Goodwin, *J. Electrochem. Soc.*, **152,** 12 (2005).
96. S.R. Wang, H. Inaba, H. Tagawa, M. Dokiya, and T. Hashimoto, *Solid State Ionics*, **107,** 1-2 (1998).
97. D.G. Goodwin, *Cantera*, http://www.cantera.org, (2001-2007).
98. R.J. Kee, M.E. Coltrin, and P. Glarborg, *Chemically Reacting Flow: Theory and Practice*, Hoboken, NJ: John Wiley & Sons, (2003).
99. A.J. Bard and L.R. Falkner, *Electrochemical Methods; Fundamentals and Applications*, New York: John Wiley & Sons, (1980).
100. S.C. DeCaluwe, A.M. Sukeshini, and G.S. Jackson. *Experimental Characterization of Thin-film Ceria Solid Oxide Fuel Cell Anodes*. in *214th Biannual Meeting of the Electrochemical Society*. (2008). Honolulu, HI: The Electrochemical Society Proceedings Series.
101. M. Dudek, *Journal Of The European Ceramic Society*, **28,** 5 (2008).
102. A. Atkinson, S.A. Baron, and N.P. Brandon, *Journal Of The Electrochemical Society*, **151,** 5 (2004).
103. H.C. Park and A.V. Virkar, *Journal Of Power Sources*, **186,** 1 (2009).
104. V. Gil, J. Tartaj, and C. Moure, *Ceramics International*, **35,** 2 (2009).
105. S. Omar, E.D. Wachsman, and J.C. Nino, *Solid State Ionics*, **179,** 33-34 (2008).
106. X. Hongmei, Y. Hongge, and C. Zhenhua, *Solid State Sciences*, **10,** 9 (2008).
107. J. Di, C.Y. Wang, M.M. Chen, and B. Zhu, *Journal Of Inorganic Materials*, **23,** 3 (2008).
108. S. Omar, E.D. Wachsman, and J.C. Nino, *Solid State Ionics*, **178,** 37-38 (2008).
109. S.H. Jo, P. Muralidharan, and D.K. Kim, *Solid State Ionics*, **178,** 39-40 (2008).
110. P. Briois and A. Billard, *Surface & Coatings Technology*, **201,** 3-4 (2006).
111. E.S. Hecht, G.K. Gupta, H.Y. Zhu, A.M. Dean, R.J. Kee, L. Maier, and O. Deutschmann, *Applied Catalysis A-General*, **295,** 1 (2005).
112. R.J. Kee, H.Y. Zhu, A.Y. Sukeshini, and G.S. Jackson, *Submitted for publication to Combustion Science and Technology*, (2007).
113. Y.M. Chiang, E.B. Lavik, I. Kosacki, H.L. Tuller, and J.Y. Ying, *Journal Of Electroceramics*, **1,** 1 (1997).

114. E.L. Brosha, R. Mukundan, D.R. Brown, Q.X. Jia, R. Lujan, and F.H. Garzon, *Solid State Ionics*, **166,** 3-4 (2004).
115. G.J. La, J. Hertz, H. Tuller, and Y. Shao-Horn, *Journal Of Electroceramics*, **13,** 1-3 (2004).
116. A.F. Jankowski and J.P. Hayes, *Surface & Coatings Technology*, **76,** 1-3 (1995).
117. Y.Z. Jiang, H.Z. Song, Q.L. Ma, and G.Y. Meng, *Thin Solid Films*, **510,** 1-2 (2006).
118. C. Peters, A. Weber, and E. Ivers-Tiffee, *Journal Of The Electrochemical Society*, **155,** 7 (2008).
119. D. Teschner, A. Pestryakov, E. Kleimenov, M. Havecker, H. Bluhm, H. Sauer, A. Knop-Gericke, and R. Schlogl, *Journal of Catalysis*, **230,** 1 (2005).
120. J.C. Conesa, M. Fernandez-Garcia, and A. Martinez-Arias, *Studies of Ceria-Containing Catalysts Using Magnetic Resonance Imaging and X-ray Spectroscopies*, in *Catalysis by Ceria and Related Materials*, A. Trovarelli, Editor. (2002), London: Imperial College Press. p. 169 - 216.
121. P. Burroughs, A. Hamnett, A.F. Orchard, and G. Thornton, *Journal Of The Chemical Society-Dalton Transactions*, 17 (1976).
122. L.G. Appel, A. Frydman, C.A.C. Perez, J.G. Eon, D.G. Castner, C.T. Campbell, and M. Schmal, *Physica Status Solidi B-Basic Research*, **192,** 2 (1995).
123. S.W. Gaarenstroom, *Applied Surface Science*, **26,** 4 (1986).
124. J.P. Holgado, R. Alvarez, and G. Munuera, *Applied Surface Science*, **161,** 3-4 (2000).
125. J.P. Holgado, G. Munuera, J.P. Espinos, and A.R. Gonzalez-Elipe, *Applied Surface Science*, **158,** 1-2 (2000).
126. M. Romeo, K. Bak, J. Elfallah, F. Lenormand, and L. Hilaire, *Surface And Interface Analysis*, **20,** 6 (1993).
127. J.Z. Shyu, W.H. Weber, and H.S. Gandhi, *Journal Of Physical Chemistry*, **92,** 17 (1988).
128. J.Z. Shyu and K. Otto, *Journal Of Catalysis*, **115,** 1 (1989).
129. C.M. Kleinlogel, *Ph. D. Thesis*. Swiss Federal Institute of Technology, (1999)
130. J.H. Park and R.N. Blumenthal, *Journal of the Electrochemical Society*, **136,** 10 (1989).
131. A.J. Bard and L.R. Faulkner, *Electrochemical Methods -- Fundamentals and Applications*, New York: John Wiley & Sons, (1980).
132. M. Mogensen, *Ceria-Based Electrodes*, in *Catalysis by Ceria and Related Materials*, A. Trovarelli, Editor. (2002), London: Imperial College Press.
133. D.R. Mullins, S.H. Overbury, and D.R. Huntley, *Surface Science*, **409,** (1998).
134. S. Bernal, G. Blanco, J.M. Gatica, J.A. Perez-Omil, J.M. Pintado, and H. Vidal, *Chemical Reactivity of Binary Rare Earth Oxides*, in *Binary Rare Earth Oxides*, G. Adachi, N. Imanaka, and Z.C. Kang, Editors. (2004), Boston: Kluwer Academic Publishers. p. 9-88.
135. M.S. Islam and G. Balducci, *Computer Simulation Studies of Ceria-based Oxides*, in *Catalysis by Ceria and Related Materials*, A. Trovarelli, Editor. (2002), London: Imperial College Press. p. 281-309.
136. T.X.T. Sayle, S.C. Parker, and C.R.A. Catlow, *Surface Science*, **316,** 3 (1994).

137. J.C. Conesa, *Surface Science*, **339,** 3 (1995).
138. S. Vyas, R.W. Grimes, D.H. Gay, and A.L. Rohl, *Journal Of The Chemical Society-Faraday Transactions*, **94,** 3 (1998).
139. M. Baudin, M. Wojcik, and K. Hermansson, *Surface Science*, **468,** 1-3 (2000).
140. T.X.T. Sayle, S.C. Parker, and C.R.A. Catlow, *Journal Of Physical Chemistry*, **98,** 51 (1994).
141. G. Adachi and N. Imanaka, *Chemical Reviews*, **98,** 4 (1998).
142. S. Gordon and B.J. McBride, *NASA reference publication 1311*, Houston, TX, (1994).
143. K. Kammer and M. Mogensen, *Electrochemical And Solid State Letters*, **8,** 2 (2005).
144. B. Kenney and K. Karan, *Solid State Ionics*, **178,** 3-4 (2007).
145. K. Tseronis, I.K. Kookos, and C. Theodoropoulos, *Chemical Engineering Science*, **63,** 23 (2008).
146. K.M. Walters, A.M. Dean, H.Y. Zhu, and R.J. Kee, *Journal Of Power Sources*, **123,** 2 (2003).
147. R.J. Kee, H.Y. Zhu, A.M. Sukeshini, and G.S. Jackson, *Combustion Science And Technology*, **180,** 6 (2008).
148. J.R. Wilson, W. Kobsiriphat, R. Mendoza, H.Y. Chen, J.M. Hiller, D.J. Miller, K. Thornton, P.W. Voorhees, S.B. Adler, and S.A. Barnett, *Nature Materials*, **5,** 7 (2006).
149. T. Ackmann, L.G.J. de Haart, W. Lehnert, and D. Stolten, *Journal Of The Electrochemical Society*, **150,** 6 (2003).
150. E.A. Mason and P. Malinauskas, *Gas Transport in Porous Media: The Dusty-Gas Model*, New York: American Elsevier, (1983).
151. L. Pisani and G. Murgia, *Journal Of The Electrochemical Society*, **154,** 8 (2007).
152. A. Mitterdorfer and L.J. Gauckler, *Solid State Ionics*, **117,** 3-4 (1999).
153. D.G. Goodwin. in *Chemical Vapor Deposition XVI and EUROCVD 14*. (2003).
154. V.M. Janardhanan and O. Deutschmann, *Journal Of Power Sources*, **162,** 2 (2006).
155. T.S. Lai and S.A. Barnett, *Journal Of Power Sources*, **147,** 1-2 (2005).
156. R. O'Hayre, D.M. Barnett, and F.B. Prinz, *Journal Of The Electrochemical Society*, **152,** 2 (2005).
157. Y. Jiang and A.V. Virkar, *Journal Of The Electrochemical Society*, **150,** 7 (2003).
158. N. Epstein, *Chemical Engineering Science*, **44,** 3 (1989).
159. W. Lehnert, J. Meusinger, and F. Thom, *Journal Of Power Sources*, **87,** 1-2 (2000).
160. S.H. Chan and Z.T. Xia, *Journal Of The Electrochemical Society*, **148,** 4 (2001).
161. J. Divisek, R. Jung, and I.C. Vinke, *Journal Of Applied Electrochemistry*, **29,** 2 (1999).
162. P. Costamagna, P. Costa, and V. Antonucci, *Electrochimica Acta*, **43,** 3-4 (1998).

163. C.W. Tanner, K.Z. Fung, and A.V. Virkar, *Journal Of The Electrochemical Society*, **144,** 1 (1997).
164. T. Kenjo, S. Osawa, and K. Fujikawa, *Journal Of The Electrochemical Society*, **138,** 2 (1991).
165. V.M. Janardhanan, V. Heuveline, and O. Deutschmann, *Journal Of Power Sources*, **178,** 1 (2008).
166. S. Raz, K. Sasaki, J. Maier, and I. Riess, *Solid State Ionics*, **143,** 2 (2001).
167. A. Bieberle and L.J. Gauckler, *Solid State Ionics*, **146,** 1-2 (2002).
168. A. Bieberle, L.P. Meier, and L.J. Gauckler, *Journal Of The Electrochemical Society*, **148,** 6 (2001).